Sorption-cooled Miniature Dilution Refrigerators for Astrophysical Applications

Gustav Teleberg

A Thesis submitted to
Cardiff University
for the degree of
Doctor of Philosophy

September 2006

ProQuest LLC
789 East Eisenhower Parkway
P.O. Box 1346
Ann Arbor, MI 48106-1346

Author: Gustav Teleberg

Title: Sorption-cooled Miniature Dilution Refrigerators for Astrophysical Applications

Date of submission: September 2006

Address: School of Physics & Astronomy
Cardiff University
5 The Parade
Cardiff, CF24 3YB
Wales, UK

Typesetting: LaTeX 2ε using MiKTeX 2.4 and WinEdt 5.3.
Figures: Origin Pro 7.5, SolidWorks 2004 and AutoCad 2005
Fonts: Adobe Garamond Pro, equations in Computer Modern


16 JAN 2007

To: Stig

Abstract

The next generation of balloon-borne and ground-based mm/sub-mm astronomy experiments will require operating temperatures near or below 0.1 K. When these experiments are operated remotely on platforms or at sites with limited infrastructure and maintenance support, a compact and reliable dilution refrigerator becomes essential. We have investigated two different dilution refrigerators in order to evaluate which system is most suitable for these applications.

We have carried out a feasibility study of the simplest of the two technologies, a single-shot dilution refrigerator. A thermal model for predicting its performance has been developed, and a first prototype which achieved temperatures of about 70 mK was built. We discuss advantages and disadvantages of a single-shot system and show how minor changes to the current design can make it useful for many astronomy applications.

The second dilution refrigerator is based on the principle of condensation pumping. We have built and integrated such a refrigerator with a pulse-tube cooler in order to create a completely cryogen-free system. Temperatures below 50 mK have been achieved, and temperatures below 100 mK have been maintained for more than 10 hours with several micro-Watt of cooling power. Using two ^{3}He sorption coolers and gas-gap heat switches we have also demonstrated how this cooler can be operated in a continuous mode. The entire system is fully automatic in operation and can be controlled and monitored remotely through a standard http protocol. We show how existing thermal models can be used to predict the cooling power and lowest achievable temperatures of the refrigerator. Experimental results are analysed and used to estimate the condensation efficiency, the performance of the heat exchangers and the ^{3}He circulation rate.

Acknowledgements

First of all, thanks to my supervisor Lucio Piccirillo for giving me the opportunity to do a PhD in Cardiff, for your support throughout the project, your enthusiasm and optimistic approach to any problems and for giving me more responsibility than what I probably deserve. Also, thanks to Kate Isaak for all your help and many valuable comments on this thesis.

Special thanks to Simon Chase, without whom this project would never have left the drawing board. Thanks for many valuable conversations, debates and comments to my work. Your experience and knowledge has played a key part throughout this project, and I look forward to any future collaboration... and whiskey sessions.

Thanks to Rob Tucker for helping me out with numerous electronic problems. If it was not for you, I would probably still be confused with grounding issues and all sorts of EMI and RF pickup.

Thanks to Brian Kiernan, Jeff Trivett and Glynn Summers for all your engineering support and for keeping up with my repeated requests for urgent bits and pieces to be machined. I have certainly learned to appreciate skilled and flexible engineering work, and realized the importance of such knowledge in any cryogenic project. Also, thanks to Olivier Mallie for patiently answering all my questions about SolidWorks and IDEAS, and for your help with tensile testing of G10 samples.

Thanks to Michael Zemcov, Simon Doyle, Bruce Sibthorpe, Robbie Auld and Douglas Haigh for being such reliable Tut'n Shive comrades. May the sun always shine on the god-blessed building which became our second home. Thanks to Lois Smallwod for help in typesetting and grammar, and for every now and then reminding me about the world outside the lab.

Tack mamma och pappa för erat stöd och för att ni har uppmuntrat mig till att fortsätta läsa och jobba, även när jag valt att göra det lång hemmifrån — ni är världens bästa föräldrar!

CONTENTS

1 **Introduction** 1
- 1.1 Scientific Background . . . 1
  - 1.1.1 Astronomy at mm/sub-mm wavelengths . . . 1
  - 1.1.2 Detector technologies . . . 3
  - 1.1.3 Noise Fundamentals of Bolometers . . . 5
- 1.2 Mechanical Coolers . . . 7
  - 1.2.1 Pulse-tube Coolers . . . 9
  - 1.2.2 The PTC thermal cycle . . . 11
- 1.3 Cryogenic Systems for sub-Kelvin Applications . . . 13
  - 1.3.1 Properties of liquid helium . . . 13
  - 1.3.2 Adsorption . . . 14
  - 1.3.3 Sorption coolers . . . 15
  - 1.3.4 Adiabatic demagnetization refrigerators . . . 19
  - 1.3.5 Dilution refrigerators . . . 21
- 1.4 Candidates for a Miniature Dilution Refrigerator . . . 25
- 1.5 About this Thesis . . . 28

2 **Cryogen-free Sorption Coolers** 31
- 2.1 Introduction . . . 31
- 2.2 PTC Cryostat . . . 32
  - 2.2.1 Cryostat assembly . . . 32
  - 2.2.2 Thermal conductivity of support structure . . . 34
  - 2.2.3 Thermal conduction of copper straps . . . 36
  - 2.2.4 FE analysis of support structure . . . 38
  - 2.2.5 Analytical analysis of support structure . . . 38
  - 2.2.6 Compression and tension tests of support structure . . . 42
- 2.3 Sorption coolers . . . 45
  - 2.3.1 Pumping speed . . . 45
  - 2.3.2 Thermal model . . . 47
  - 2.3.3 Best-fit of thermal model to experimental data . . . 48
- 2.4 Conclusions . . . 51

3 **Heat Switches** 53
- 3.1 Introduction . . . 53
- 3.2 Overview of different heat switch technologies . . . 54
  - 3.2.1 Superconducting heat switches . . . 54

3.2.2 Gas-gap heat switches . . . 56
3.2.3 Liquid-gap heat switches . . . 56
3.2.4 Mechanical heat switches and thermal contact resistance . . . 57
3.3 Thermal model of the gas-gap heat switch . . . 59
3.3.1 Mean-free path . . . 59
3.3.2 Heat transport in the laminar regime . . . 60
3.3.3 Heat transport in the molecular regime . . . 62
3.3.4 Off-conductance . . . 63
3.4 A Heat switch for Operation Below 0.5 K . . . 64
3.4.1 Design . . . 64
3.4.2 Experiments . . . 66
3.4.3 Results . . . 67
3.5 A Heat Switch Optimized for Pre-cooling of Large Thermal Loads . . . 69
3.5.1 Design . . . 70
3.5.2 Experiments . . . 72
3.5.3 Results . . . 72
3.6 Conclusions . . . 74

4 A Condensation Pumped MDR 75
4.1 Introduction . . . 75
4.2 Thermodynamic Properties of ^{3}He-^{4}He Mixtures . . . 76
4.2.1 Phase separation . . . 77
4.2.2 Landau–Pomeranchuk theory . . . 78
4.2.3 Osmotic pressure . . . 81
4.3 Dilution Refrigerators . . . 82
4.3.1 ^{3}He circulation rate . . . 82
4.3.2 Cooling power estimates . . . 84
4.3.3 Continuous heat exchangers . . . 85
4.4 Design of the MDR . . . 87
4.4.1 Heat exchanger calculations . . . 87
4.4.2 Design Details . . . 88
4.5 Initial Tests in a LHe Cryostat . . . 92
4.5.1 Experiment . . . 93
4.5.2 Results . . . 94
4.6 Detailed tests in a PTC cryostat . . . 97
4.6.1 Experiment . . . 97
4.6.2 Results . . . 99
4.7 MDR in continuous operation . . . 106
4.7.1 Experiment . . . 106
4.7.2 Results . . . 106
4.8 Software Control . . . 109
4.9 Conclusions . . . 109

5 A Single-shot MDR 113
5.1 Introduction . . . 113
5.2 Thermal Model . . . 115
5.3 ssMDR Design . . . 119
5.4 Experiments . . . 121
5.5 Results . . . 122
5.5.1 Cycle procedures . . . 122
5.5.2 Cooling power and circulation rate . . . 124
5.5.3 Extended duty cycle . . . 126
5.5.4 Impeded ^{3}He-circulation phenomena . . . 127
5.6 Future Design . . . 130
5.7 Conclusions . . . 131

6 Conclusions and Final Remarks 133
6.1 Cryogen-free Sorption Coolers . . . 133
6.2 Gas-gap heat switches . . . 133
6.3 Condensation Pumped Dilution Refrigerators . . . 134
6.4 Single Shot Dilution Refrigerators . . . 136

Appendices 139

A Derivations 139
A.1 Partial Chemical Potential . . . 139
A.2 The Perfect Heat Exchanger Model . . . 141

B Low-Temperature Thermometry 143
B.1 Errors associated with temperature measurements . . . 143
B.2 Cryogenic sensors . . . 144

References 155

List of Tables

1.1 A selection of past, ongoing and future sub-mm/mm experiments 5
1.2 A comparison between a selection of pulse-tube coolers 10

2.1 Measured thermal conductivity of epoxy and G10 rods 36
2.2 Measured thermal conductance of copper braid samples 38
2.3 Dimensions of compression and tension test samples 43
2.4 Measured modulus of elasticity in comparison with data from manufacturer 43
2.5 Pumping line dimensions 48

3.1 Superconducting transition temperatures of some metals 55

4.1 A selection of important design parameters of the continuous MDR 93

5.1 Defined notations for the thermal analysis of the ssMDR 116
5.2 Design parameters of the ssMDR 122

List of Figures

1.1 Relative contributions to the extragalactic background radiation 2
1.2 CMB anisotropy from COBE-DMR 3
1.3 Principle operation of a spider-web bolometer 4
1.4 Typical *COP* for mechanical coolers 9
1.5 Recent development of pulse-tube coolers 10
1.6 The PTC thermal cycle in comparison with the Sterling cycle 12
1.7 P-V and T-S diagrams of the Sterling cycle. 12
1.8 Vapour pressure of liquid ^{4}He and liquid ^{3}He 14
1.9 Schematic of a single stage ^{3}He sorption cooler 16
1.10 Schematic of a double stage (^{4}He-^{3}He) sorption cooler 17
1.11 A triple stage (^{4}He-^{3}He-^{3}He) sorption cooler 18
1.12 Principle schematic of an ADR 21
1.13 ^{3}He-^{4}He phase diagram 22
1.14 Principle schematic of a conventional dilution refrigerator 23
1.15 A comparison of the cooling power of the dilution refrigerator and the ^{3}He sorption cooler 24
1.16 The Edel'man dilution refrigerator 26
1.17 Schematic of the Sivokon dilution refrigerator 27
1.18 Principle schematic of the system developed during this project 29

2.1 PTC cryostat assembly 33
2.2 Pictures of the cryostat assembly and the PTC 33
2.3 Pictures of the thermal straps and the vacuum can 34
2.4 Thermal conductivity experiment on G10 and epoxy rods 35
2.5 Thermal conduction measurements of thermal straps 37
2.6 FE displacement analysis of 3 K support structure 39
2.7 FE buckling analysis of 3 K support structure 39
2.8 Schematic for estimating the moment of inertia of the G10 support structure 40
2.9 Euler length in various buckling scenarios 41
2.10 A picture of G10 and Epoxy rods samples 43
2.11 G10 and epoxy compression test results 44
2.12 G10 and epoxy tension test results 44
2.13 Schematic of a typical system of pumping lines in an evaporation cryostat . . 47
2.14 Measured and theoretical cooling power of the sorption coolers used during this project 49
2.15 Adsorption isotherms of ^{3}He on activated charcoal 50

3.1 Thermal conductivity of s.c. Nb 55
3.2 The mean-free path of the gas inside a gas-gap heat switch 61
3.3 Thermal conductivity of ^{3}He gas 63
3.4 Thermal conductance of an ideal heat switch 64
3.5 Photograph of a heat switch for operation below 0.5 K 65
3.6 Schematic of a heat switch for fast switch-off times 66
3.7 Measured on-conductance at 0.4 K of gas-gap heat switches 67
3.8 Measured switch-off time at 0.4 K of gas-gap heat switches 68
3.9 Specific heat of some common material 70
3.10 Schematics of thermal contraction gas-gap heat switches 71
3.11 Gap size of heat switch as a function of temperature 72
3.12 Measured conductance of the thermal contraction heat switch 73

4.1 ^{3}He-^{4}He phase diagram 77
4.2 Chemical potential of a ^{3}He atom in a mixture of ^{3}He and ^{4}He 80
4.3 Definition of the osmotic pressure 81
4.4 Lowest achievable temperature as a function of the ^{3}He circulation rate . . . 89
4.5 A comparison of the cooling power as predicted by the perfect heat exchanger model with that predicted by the high temperature approximation . 89
4.6 Two pictures of the MDR developed during this project 90
4.7 Detailed desciption of the MDR 90
4.8 Measured cooling power of the MDR in a LHe cryostat 95
4.9 Cool-down of the MDR from liquid helium temperatures 96
4.10 Temperature oscillations of the still 96
4.11 A picture of the experimental setup for semi-continuous operation in a PTC 97
4.12 Example of an MDR cycle from 50 mK back to 50 mK 100
4.13 Measured cooling power in comparison with thermal model 101
4.14 Measured cooling power using 625 μW to the still 101
4.15 Measured cooling power using 225 μW to the still 103
4.16 The condensation efficiency as a function of temperature 103
4.17 Measured circulation rate as a function of the still power 104
4.18 Measured circulation rate in comparison with thermal model 104
4.19 Measured m.c. temperature as a function of the tilt angle 105
4.20 Principle schematic of the MDR operating in continuous mode 107
4.21 Continuous operation of the MDR 108
4.22 MDR continuous operation, using two different cycle procedures 108
4.23 The MDR cycle scheme 110

5.1 Enthalpy diagrams of diluted and concentrated ^{3}He 115
5.2 Calculated performance of the single-shot MDR 118
5.3 Principle schematic of the ssMDR 119
5.4 Pictures of the ssMDR 120
5.5 Photograph of the double-stage sorption cooler 120
5.6 A cool-down of the ssMDR to 73 mK 123
5.7 A cool-down of the ssMDR to 73 mK 123
5.8 Measured cooling power of the ssMDR 125

5.9 Theoretical prediction of the cool-down time 126
5.10 Extended operation at 100 mK 127
5.11 Observed phenomena of the still temperature 129
5.12 Future design of the ssMDR 131

A.1 Illustration of the perfect heat exchanger model 142

1 INTRODUCTION

In this chapter we give a brief introduction to far infra-red and mm/sub-mm astronomy, which together with a discussion on relevant detector technologies provide the scientific background of this project. We describe current technologies for achieving the cryogenic temperatures required for mm/sub-mm astronomy; in particular we discuss the advantages and disadvantages of existing dilution refrigerators, and justify the development of new systems. We also describe in some detail the fundamental principle of two cryogenic technologies which are of particular interest for future ground-based and balloon-borne astronomy experiments: condensation pumped and single-shot dilution refrigerators.

1.1 SCIENTIFIC BACKGROUND

1.1.1 ASTRONOMY AT MM/SUB-MM WAVELENGTHS

The mm/sub-mm and far infra-red (FIR) wavebands play host to a large number of different observational tools with which to study both the local and distant universe. Studies of continuum broad-band emissions and narrow-band spectroscopy provide complementary information: for example, broad-band instruments provide insight into the formation and structure of planets, stars, galaxies and galactic clusters. They also measure the geometry, structure and content of the early universe. In contrast, narrow-band spectroscopy can provide insight into the kinematics, mass distribution and physical conditions within a given source [1].

Shown in figure 1.1 is a plot of the extragalactic background radiation. It is clear that the dominant contribution is from the cosmic microwave background[†] (CMB), and the

[†]The CMB origins from when the Universe was only 380 000 years old, and therefore holds crucial information about the geometry and content of the early universe. Such information is essential for the understanding of big bang, and how matters and the structures of the Universe we observe today were formed

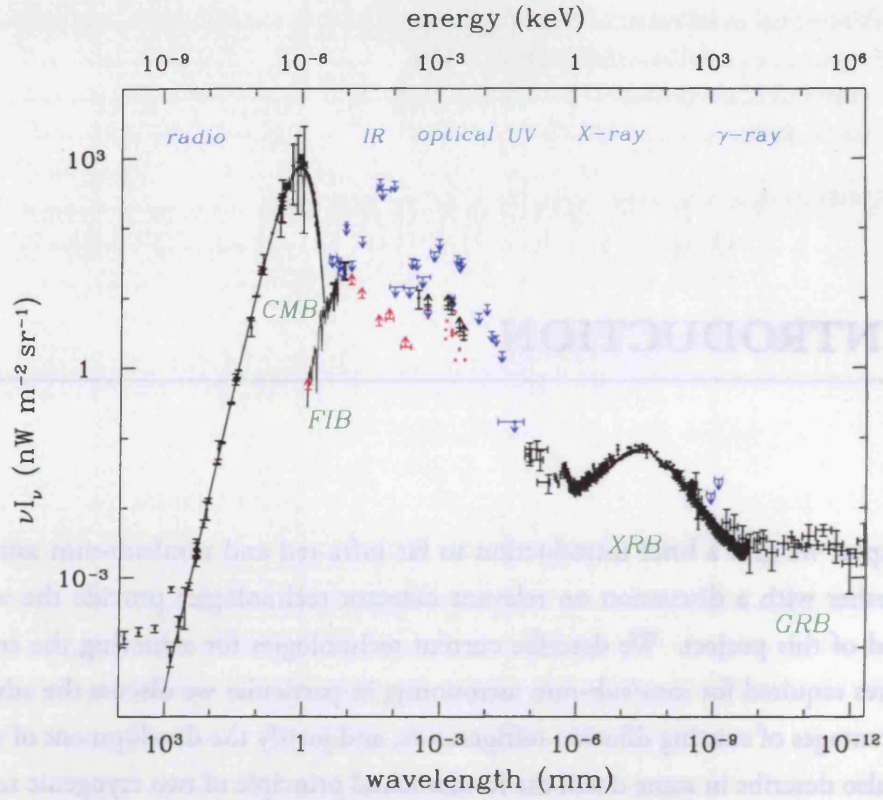

Figure 1.1: Relative contributions to the total energy distribution of the extragalactic background radiation, where I_ν is intensity and ν is frequency. [2]

next most significant wavebands are optical and infra-red [2]. Almost half of all the light in the universe is found at mm/sub-mm wavelengths. Astronomy in this part of the spectrum is, however, still a very young and unexplored field, and there is much more to be learned about the universe at these wavelengths.

Considerable progress has been made in mm/sub-mm instrumentation during the past 20 years; primarily due to the development of large detector arrays and new detector technologies such as low-noise bolometers, High Electron Mobility Transistors (HEMTs) as well as local oscillators for Heterodyne Mixers. The two satellite missions IRAS (1983) and COBE (1992) are spectacular examples of how astronomy instrumentation has revolutionized the field. An almost full-sky survey by IRAS discovered more than half a million sources, many of which are still awaiting identification. COBE measured the spectrum of the CMB, showing it to have exactly the expected form of a 2.7 K black body. Another key contribution of COBE was the discovery of anisotropies (figure 1.2) which observers had been searching for more than two decades [3]. Ever more sophisticated ground-based, balloon-borne and satellite experiments have been employed since: SCUBA, DASI, BOOMERANG and WMAP to mention a few of them of them.

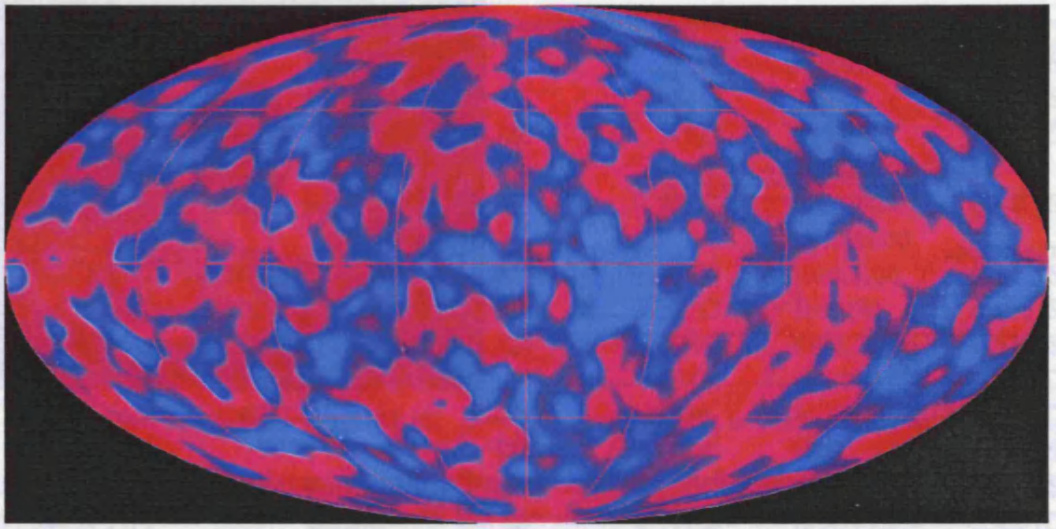

Figure 1.2: CMB anisotropy after elimination of the galaxy signal; the tiny fluctuations in the sky brightness are at a level of a part in one hundred thousand. Courtesy of the NASA/COBE-DMR Science Team.

A complication of observing at mm/sub-mm and FIR wavelengths is the opacity of the Earth's atmosphere. Observations therefore have to be done from very dry sites at high altitudes, or ultimately from space. As a result, space missions achieve the highest sensitivities and generally lead to the biggest break-throughs. However, satellite missions are extremely expensive and will only use well developed technologies, while ground-based and balloon-borne experiments will adopt any new technology long before it is realized in space.

Both continuum broad-band and narrow-band spectroscopic instruments require very sensitive and cryogenically cooled detectors. Future experiments will, however, require more than just an increased sensitivity of individual detectors: the development of more sophisticated detector *systems* including cryogenic coolers, cooled optics, signal modulation and multiplexed read-out electronics will become essential [4]. Large detector arrays require advanced fabrication methods and multiplexing to reduce the number of signal wires, but also more powerful coolers which can absorb the dissipated heat.

1.1.2 DETECTOR TECHNOLOGIES

Extrinsic photoconductors are used at mid and far infra-red wavelengths; for example gallium-doped germanium cooled to temperatures below 2 K are sensitive out to 110 μm. In such semiconductors, photons with energies larger than impurity-atom ionization energies excite either electrons into the conduction band or holes into the valance band. Thus, when voltage biased, the resulting current is a measure of the photon energy. The upper bound can be extended by the application of stress along the appropriate crystal axis, which lifts the

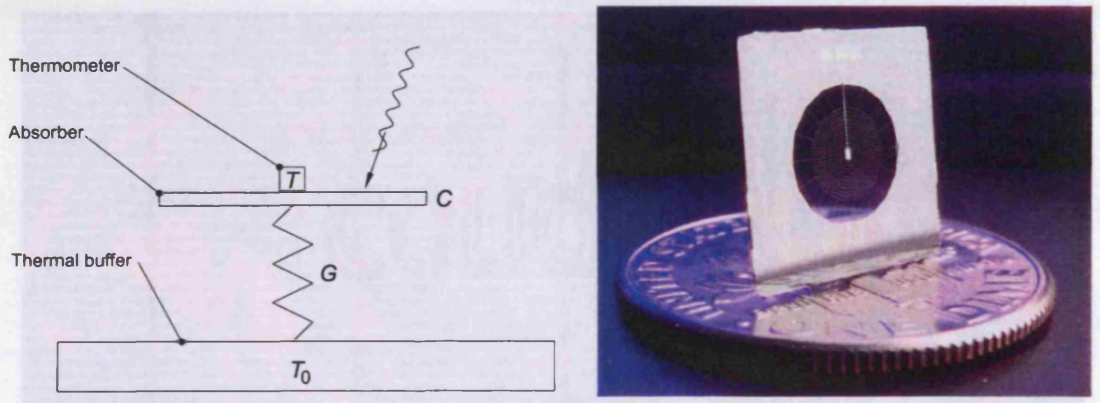

(a) Principle schematic of a bolometer

(b) Picture of a spider-web bolometer

Figure 1.3: The structure of the web is much smaller than the wavelength of the incoming radiation. This avoids incoming cosmic rays and minimizes G without compromising absorption efficiency.

valence band degeneracy and so extends the cutoff wavelength to 200 μm.

Bolometers, for mm/sub-mm detectors, distinguish themselves from those used at shorter wavelengths in that they are thermal detectors rather than photoconductors. As such, they are limited by the phonon fluctuations in the device, and state-of-the-art performance requires temperatures typically between 0.1 and 0.3 K. In bolometers, the electron excitation caused by absorbed photons produce a temperature rise that can be sensed by a thermometer (see figure 1.3). Usually the thermometer consists of a neutron transmutation doped (NTD) germanium or silicon chip which, when current biased, produces a steep temperature dependent voltage signal. Junction field-effect transistors (JFETs) operated near 100 K are used to amplify the signal from the high-impedance (5–20 MΩ) thermometer. However, hand assembly, thermal complexity, a small amplifier noise margin and an inability to multiplex the output signal make the construction of large NTD bolometer arrays challenging.

Voltage biased transition edge superconducting (TES) bolometers do not require individual wires to each and every detector, instead an entire row of detectors can be read out at the same time. In addition, they are also significantly easier to manufacture in bulk quantities through deposition and etching. For example, SCUBA 2 uses a TES array with over 10,000 pixels which is well over an order of magnitude more than any detector array based on NTD technology. The resistance of a superconducting thermometer increases rapidly with temperature at the transition. Consequently, when a fixed bias voltage is placed across the TES, the bias power produces a strong negative electrothermal feedback. The negative feedback dramatically improves linearity and bandwidth and also makes the detector significantly less sensitive to changes in the optical power and temperature fluctuations of the heat sink. CMB experiments using TES technology have already been designed and

Project	Year	Site	Nr. Detectors	Bolometers	$\lambda(\mu m)$	Cryogenics
UKT14	1986	JCMT	1	NTD	450,850	0.3 K (SC)
SHARC	1996	CSO	20	NTD	350	0.3 K (SC)
SCUBA	1997	JCMT	128	NTD	350,450	0.1 K (DR)
					750,850	
BOOMERANG	1998	balloon	16	NTD	1000,1400	0.3 K (SC)
					2100,3000	
BOLOCAM	2000	CSO	144	NTD	1100,2100	0.3 K (SC)
SHARC II	2002	CSO	384	NTD	350,450	0.3 K (SC)
APEX	2004	Atacama	324	TES	1400, 2000	0.3 K (SC)
SCUBA 2	2006	JCMT	10240	TES	450,850	0.1 K (DR)
CLOVER	2007	Atacama	320/520	TES	3300/2000	0.1 K (DR)
			520	TES	1400	0.3 K (SC)
SPIRE	2007	satellite	270	NTD	250,350,500	0.3 K (SC)
PLANCK HFI	2007	satellite	48	NTD	100,143,217	0.1 K (DR)
					353,545,857	
EBEX	2008	balloon	1320	TES	670, 860	0.3 K (SC)
					1200, 2000	

Table 1.1: A selection of past, ongoing and future sub-mm/mm experiments. The number of detectors are for each sub-Kelvin cooler. For example, CLOVER uses three separate coolers: two dilution refrigerators (DR) and one ^{3}He sorption cooler (SC).

commissioned and several projects are scheduled for the next few years which will operate at temperatures from 50 mK to 300 mK (see table 1.1). Although TES detectors can be designed to become superconductive at an arbitrary temperature, the transition width decreases with temperature and hence the sensitivity increases. To increase the dynamic range of the detector, the heat sink temperature also needs to be well below the superconducting transition, the bias voltage then balances the detector near the transition edge.

1.1.3 NOISE FUNDAMENTALS OF BOLOMETERS

The two most important parameters for a bolometer are the thermal time constant, τ, and the noise equivalent power, NEP. The time constant is a measure of the bolometer response time to incoming radiation. The NEP is a measure of the sensitivity of a bolometer and is defined as the signal power which gives a signal-to-noise ratio of unity for an integration time of 0.5 s. This gives the NEP units of $Ws^{0.5}$, or alternatively in terms of the post-detection bandwidth, units of $WHz^{-0.5}$. Each of the NEP terms is an uncorrelated noise source and so these can be added together in quadrature [5]:

$$NEP^2 = \underbrace{NEP^2_{\text{Johnson}} + NEP^2_{\text{Phonon}}}_{\text{Detector noise}} + \underbrace{NEP^2_{\text{Photon}}}_{\text{Background noise}} . \tag{1.1}$$

A number of publications have described the different noise sources in bolometers in detail [6–9]. Here we give a brief summary of the topic and for clarity, use the simplest form of the fundamental equations and ignore any effects of a time varying signal. For an ideal bolometer, the detector noise contributions should arise from only two sources: Johnson noise and phonon noise. Johnson noise is due to the random motion of electrons in a device of resistance R and can (in units of $\mathrm{WHz}^{-0.5}$) be written as

$$NEP^2_{\mathrm{Johnson}} = 4k_{\mathrm{B}}T\frac{R}{S^2} \tag{1.2}$$

where S is the responsivity and T is the temperature at which the device is operated. In the case of a current biased bolometer, S is the change in output voltage per absorbed power (V/W). Phonon noise is due to the quantization of phonons that transport energy between the absorber and the heat sink along the thermal conductance G:

$$NEP^2_{\mathrm{Phonon}} = 4k_{\mathrm{B}}T^2\gamma G\,, \tag{1.3}$$

The background contribution to the overall NEP arises from the sky, telescope and instrument. This photon noise, due to the statistical fluctuations of the photon arrival rate, is ultimately limited by the observed source only. If the Rayleigh-Jeans approximation is valid ($h\nu < k_{\mathrm{B}}T$) and the radiation passband is limited to a frequency interval $\Delta\nu$ around a central frequency ν_0, then the photon noise contribution to the NEP is dominated by the poisson noise component:

$$NEP^2_{\mathrm{Photon}} = 2Qh\nu_0, \tag{1.4}$$

where Q, the absorbed incident power is given by $Q = A\Omega B_\nu(\nu_0, T_{\mathrm{b}})\eta\epsilon\Delta\nu$. Here A is the telescope primary area and Ω the beam solid angle, thus $A\Omega$ is the telescope throughput. $B_\nu(\nu_0, T_{\mathrm{b}})$ is the Planck function, T_{b} the temperature of the background radiation, η is the overall transmission of the system and ϵ the emissivity of the background. In reality, the background temperature is not well defined since the incoming radiation is affected by all the optical components from telescope mirrors to filters and lenses. In the case of a ground based experiment, the background temperature is dominated by the atmosphere.

Achieving the lowest possible overall NEP requires minimizing R, T and G, and maximizing S. However, since the thermal time constant $\tau = C/G$, where C is the heat capacity, there is a trade-off between NEP and τ in terms of the selection of G. For this reason, it is common to use the value of $NEP\sqrt{\tau}$ as a figure of merit when optimizing a detector system.

The importance of the cryogenic system is clear from equations 1.2, 1.3 and 1.4. Lowering the detector temperature as well as the background temperature decreases the overall NEP and results in a more sensitive instrument. In particular, given a fixed response time and given equation 1.3, the intrinsic detector NEP of an optimally biased bolometer is proportional to $TC^{1/2}$. Typical bolometers have materials which have heat capacities proportional to T (metals) or T^3 (dielectrics) and so the intrinsic NEP is proportional $T^{3/2}$ or $T^{5/2}$ [10].

The detector's dynamic range is another important parameter which puts requirements on the operating temperature of the detectors. In a superconducting bolometer array, the maximum power seen before saturation is $P_{\text{sat}} = GT/\alpha$, where $\alpha \sim 10$ is a temperature rise factor [11]. Therefore, in order to ensure $NEP_{\text{Phonon}} \ll NEP_{\text{Photon}}$, equation 1.3 and 1.4 using $Q = P_{\text{sat}}$ give: $2k_{\text{B}}T\alpha \ll h\nu_0$. For example, with $\nu_0 = 1\,\text{THz}$ a temperature $\sim 250\,\text{mK}$ would be required. Of course, yet lower temperatures are required at longer wave lengths; other noise sources than just the poisson noise component (equation 1.4) will however contribute to the photon noise outside the Rayleigh-Jones region.

The required noise performance of the detector system is dictated by the background noise from the telescope and the atmosphere. Ground based experiments are carried out at very dry sites at the highest possible altitude to minimize the effect of the atmosphere. From this perspective, the two most suitable sites on earth are the South Pole in Antarctica (2900 m) and Atacama in Chile (5000 m). The next generation mm/sub-mm astronomy experiments will use increasingly sensitive detectors and cryogenically cooled optics to further decrease the instrumental photon noise. To remain background limited, the detector system therefore needs to operate at yet lower temperatures.

In addition to the need of an improved sensitivity, larger detector arrays require a higher cooling power. More detectors dissipate more heat and the mechanical structure to hold the arrays also becomes more bulky. Inevitably this leads to a larger heat load on the coldest parts of the system. Further to this tough constraints on reliability, weight and temperature stability must be fulfilled too. All this necessitates improvements of the current and/or development of new cryogenic systems, in order to meet the requirements of future astronomy experiments.

1.2 MECHANICAL COOLERS

With a demand and usage of helium quickly increasing and with a world supply of helium diminishing, there is a need to find alternative ways of cooling. The cost of liquid helium is also a significant cost burden to a project and to make regular transfers to a cryostat can be tedious as well as impractical, in particular for experiments carried out at remote

sites. For these reasons, a lot of effort has been invested in the development of mechanical coolers (also referred to as cryocoolers) such as pulse-tube coolers, sorption coolers, Stirling coolers, Gifford-McMahon coolers and Joule-Thompson coolers. They all use compressed gas and through varies thermal cycles and different geometries, they can achieve cryogenic temperatures. Gifford-McMahon (G-M) coolers are a low cost variation of a Stirling cooler and are the most common type of cryogenic refrigerator sold industrially. For example, Sumitomo has developed a powerful double stage G-M cooler with 1.5 W of cooling power at 4 K. But the most promising method for applications at and below 4 K, is the two-stage pulse-tube cooler (PTC) which benefits from no moving cold parts and hence low vibrations and high reliability which is important for detector applications in astrophysics. On the down side, most mechanical coolers are rather inefficient so the compressor package becomes bulky and expensive to operate, with several kW of electric power required. The overall coefficient of performance, *COP*, is defined as the ratio of cooling power to input electrical power. In figure 1.4 the *COP* of a few mechanical coolers is compared with the Carnot *COP*: the Carnot efficiency is typically 20% for coolers operating above 20 K, but decreases to less than 1% at 4 K.

The coupling of dilution refrigerators, ADRs and other sub-Kelvin refrigerators to pulse-tube coolers is obviously a field which now attracts attention. The design of these systems usually needs to be altered in order to operate in a 'dry' cryostat. Also, RF and EMI noise, vibrations and temperature fluctuations from the PTC needs to be addressed carefully in a system operating with detectors.

The development of pulse-tube coolers has accelerated since Mikulin [13] showed that their efficiency could be increased by introducing an orifice and a reservoir at the hot end. This observation led to the Orifice Pulse-Tube which nowadays is the standard design for all modern pulse-tube coolers. Double stage 4 K pulse-tube coolers are today commercially available through a number of companies: for example CryoMech[†] and VeriCold[‡]. CryoMech can offer the most powerful version with up to 1 W at 4 K plus 40 W at 45 K. Vericold on the other hand, can offer a version with extremely low level of vibration: $<$ 10 nm at the second stage. This makes the Vericold PTC very useful for optical spectroscopy but its relatively weak first stage makes it less suitable for the large cryostats typically used in astronomy experiments. Problems with RF and EMI and can be limited by separating the rotary valve from the motor head: mechanically as well as electrically. Such modifications have been made by both VeriCold and CryoMech. Nowadays, the main problem is the temperature oscillations at the second stage which can be as large as $\pm$ 0.2 K each second. These temperature fluctuations also give rise to the mechanical vibrations of the cold head as

[†]CryoMech, 113 Falso Drive, Syracuse, New York 13211, USA, http://www.cryomech.com
[‡]VeriCold Technologies GmbH, Bahnhofstrasse 21, 85737, Ismaning, Germany, http://www.vericold.com

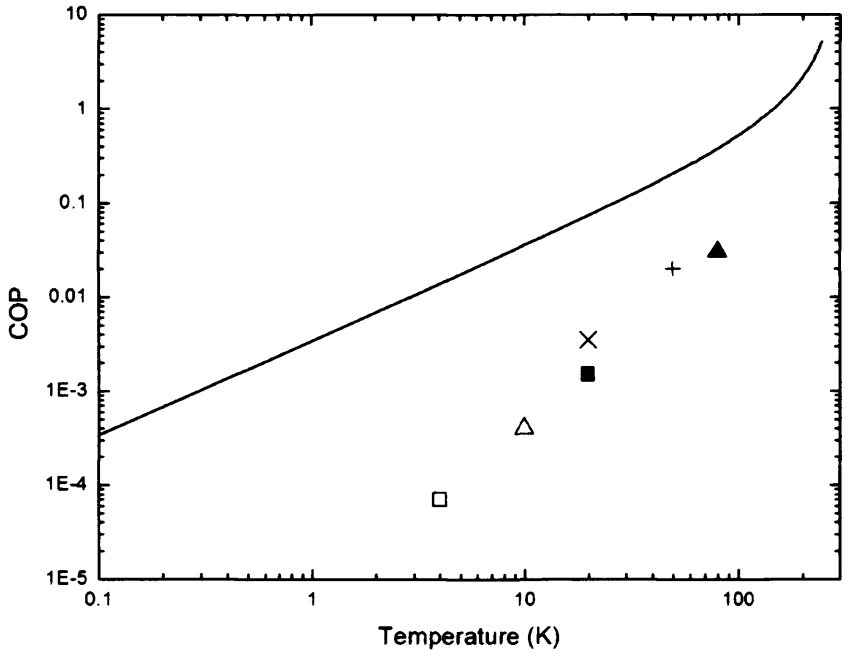

Figure 1.4: Typical *COP* for mechanical coolers in comparison with the Carnot *COP* (solid line): MMS 4 K cooler (□), MMS 10 K (△), MMS 20 K (■), Planck 20 K (×), MMS 50 K (+) and TRW PTC (▲). [12]

the pulse-tube expands and contracts with the change of temperature. Cryomech have measured the vibrations on their PT-405 cooler and compared it with a Sumitomo G-M cooler. They measured the displacement amplitude and by means of a load cell, mounted under the room temperature flange of the coolers, they also measured the mounting force amplitude. The mounting force from the G-M cooler was 38 times that of the pulse-tube cooler and the displacement was 4 times greater. In table 1.2 we summarize the characteristics of a few common 4 K pulse-tube coolers from two different manufacturers. For comparison we also include a Sumitomo 4 K G-M cooler, distributed by Janis[†].

1.2.1 PULSE-TUBE COOLERS

Figure 1.5 shows the progress of pulse-tube coolers in recent years. Today's world record is held by a group from Giessen University who reached 1.3 K in a two stage machine using ^{3}He gas. Several groups are also working on three stage machines but they have so far not been able to outperform the best two-stage coolers. Today's commercially available 4 K pulse-tube coolers are optimized for vertical operation and will degrade significantly when tilted

[†]Janis Research Company Inc., 2 Jewel Drive, Wilmington, MA 01887-0696, USA, http://www.janis.com

	VeriCold	PT-405	PT-410	RDK-415D
Distributor	VeriCold	CryoMech	CryoMech	Janis
Thermal cycle	pulse-tube	pulse-tube	pulse-tube	modifed G-M
Cooling power	0.5 W at 4.2 K + 6.5 W at 50 K	0.5 W at 4.2 K + 16 W at 50 K	0.8 W at 4.2 K + 45 W at 50 K	1.5 W at 4.2 K + 35 W at 50 K
Orientation	± 45°	± 45°	± 50°	any
Separated motor	yes	yes	yes	no
Vibrations	0.01 μm	11 μm, 4.5 N	N/A	42 μm, 170 N
Input power (kW)	6.0	4.1	7.0	6.5
Weight (kg)	13.6	14	15	17.6
Price ($)	44,600	33,500	38,700	36,000

Table 1.2: A comparison between a selection of pulse-tube coolers and one G-M cooler. Orientation refers to the maximum tilt angle which gives a stable performance. The estimated prices (excl. VAT) are based on quotes acquired in 2005 and includes the compressor package. Weight refers to the weight of the pulse-tube itself and its motor head, excluding flexi-lines and compressor. For more information, see text.

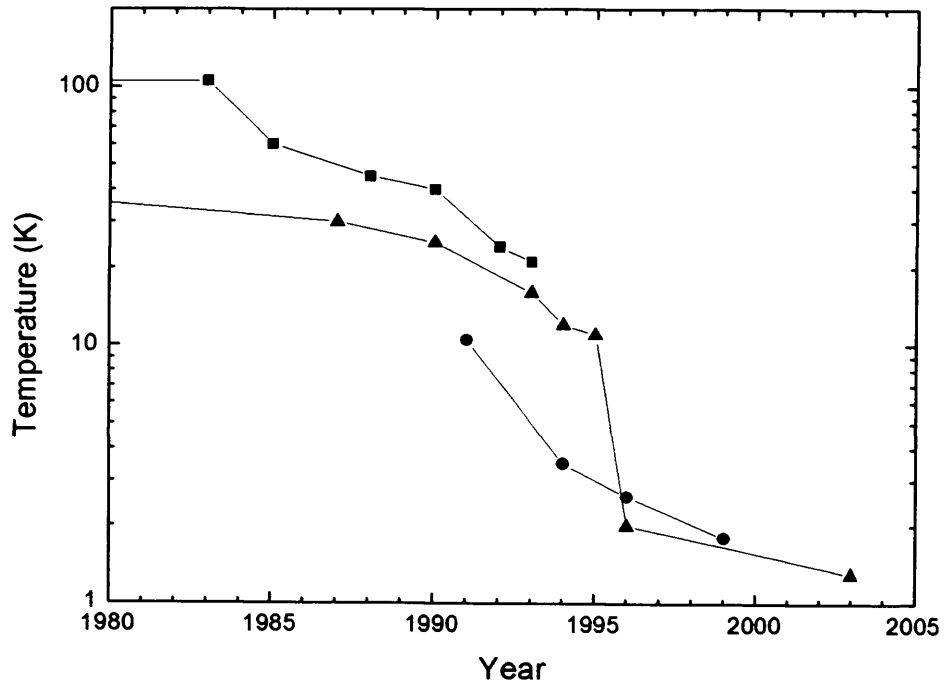

Figure 1.5: Temperatures reached with single stage (■), double stage (▲) and triple stage (●) pulse-tube coolers in recent years. [14]

to an angle above 50 degrees. This is due to gravitationally induced convection whenever the pulse-tube diameter is larger than 10 mm [15]. Since this effect is only prevalent in gravity, pulse tubes can operate in space and they have been used in satellite experiments like EOS-AIRS.

The development of pulse-tube coolers is very much of interest to the development of miniature dilution refrigerators: a powerful pulse-tube cooler capable of operating at temperatures below 2 K would reduce the complexity, cost and size of the sub-Kelvin system. The temperature stability of the dilution refrigerator is also correlated to the temperature stability of the pulse-tube cooler.

1.2.2 THE PTC THERMAL CYCLE

There are several good publications describing the thermal cycle and the rather complicated theoretical modelling of a PTC [16–18]. However, anything but a simplified discussion would be well outside the scope of this thesis. Here we describe the thermal cycle, in essence as it was presented by Yuan and Jung [19].

The thermal cycle of the PTC is basically the same as that of the Sterling refrigerator, with the cold piston replaced by a surge volume and an orifice, see figure 1.6. The regenerator is a matrix material which acts as a buffer to absorb heat from the hot gas as it arrives from the compressor (left flow). It then returns the heat to the cold gas as the gas moves from the cold tip back to the compressor (right flow).

The piston compresses from (1) to (2) The pressure in the system increases. Very little gas is transferred into the surge volume, however, as the initial pressure difference across the orifice is small. In the Sterling cycle, the cold piston is stationary.

The piston compresses further from (2) to (3) More working gas passes through the orifice into the surge volume. In the Sterling cycle, the cold piston is displaced, resulting in a near-isochoric process. In both the PTC and the Sterling cycle, gas flows to the left and heat is transferred from the gas to the regenerator.

The piston becomes stationary between (3) and (4) As the compressor piston reaches its maximum stroke, expansion occurs because gas continues to flow into the low-pressure surge volume. As a result, the pressure within the pulse-tube system decreases. An equivalent process occurs in the Sterling cycle, due to the cold piston being displaced further.

The piston returns to (1) A combination of gas exiting the surge volume and the expansion of the compression space results in another near-isochoric processes as the system

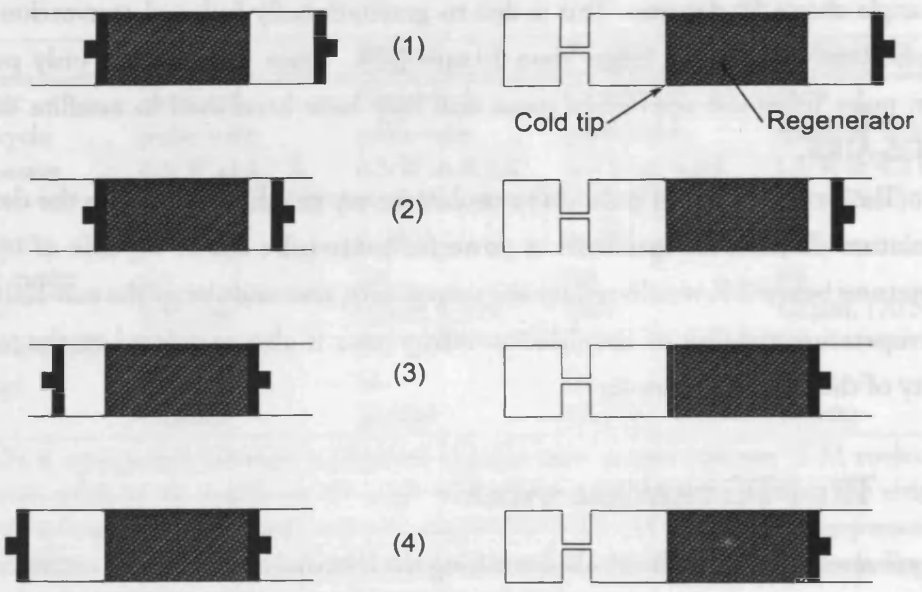

(a) The Stirling cycle (b) The PTC cycle

Figure 1.6: In a PTC refrigerator, the cold piston used in the Stirling refrigerator has been replaced by a surge volume and an orifice.

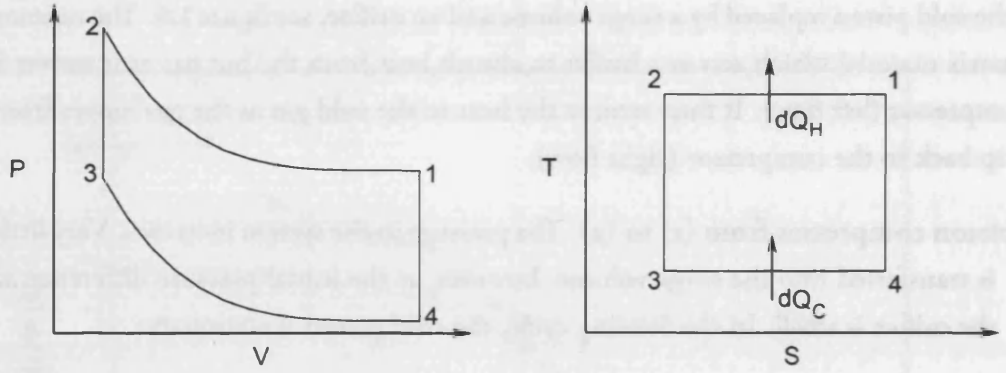

Figure 1.7: P-V and T-S diagrams of the Sterling cycle.

returns to its initial state. During this phase, heat is released from the regenerator and absorbed by the working gas.

With subindex H and C for the hot and cold end respectively; an amount of heat $\mathrm{d}Q_\mathrm{H} = T_\mathrm{H}\,\mathrm{d}S$ is rejected from the compressor while $\mathrm{d}Q_\mathrm{C} = T_\mathrm{C}\,\mathrm{d}S$ is absorbed at the cold tip in accordance with figure 1.7.

The advantage of the pulse-tube cooler over the Sterling cooler is obvious from figure 1.6. With no moving cold parts, the system becomes more reliable and vibrations are significantly reduced. The price for this is a decreased efficiency due to the dissipation of heat in the orifice. The overall coefficient of performance, COP, is defined as the ratio of cooling

power to input electrical power, and for an ideal PTC this reduces to $COP_{\text{ideal}} = T_C/T_H$ [20]. This can be compared with COP of an ideal Stirling cooler, which equals that of the Carnot cycle: $COP_{\text{Carnot}} = T_C/(T_H - T_C)$. Therefore, the Carnot efficiency of an ideal PTC is given by:

$$\eta_{\text{ideal}} \equiv \frac{COP_{\text{ideal}}}{COP_{\text{Carnot}}} = \frac{T_H - T_C}{T_H}. \tag{1.5}$$

This shows that the efficiency of an ideal PTC is less than that of ideal coolers such as the Stirling cooler. Close to room temperature, this difference is big but at temperatures in the range of liquid nitrogen and below the difference is insignificant. Of course, in reality the system is far from ideal with entropy production from several sources. One of them is due to axial heat conduction in the regenerator and the heat exchangers. This is a result of heat conduction in the gas, gas-wall interactions and a limited heat exchange between the gas and the matrix. A second important source of entropy production is gas flow over a pressure difference. This occurs predominately in the orifice, in the regenerator and in the rotary valve.

1.3 CRYOGENIC SYSTEMS FOR SUB-KELVIN APPLICATIONS

1.3.1 PROPERTIES OF LIQUID HELIUM

Liquid nitrogen (LN_2) with a boiling point of 77.4 K and liquid helium (LHe) with a boiling point of 4.2 K are the two most common refrigerants in cryogenic applications. Temperatures above 4.2 K are usually achieved through cooling by the vapour from a LHe bath, and temperatures down to 1 K are achieved by operating the LHe cryostat at sub-atmospheric pressures by means of a pumping system. The cooling power and lowest achievable temperature in such an evaporation refrigerator is limited by the liquid's vapour pressure and latent heat of evaporation. The lower vapour pressure, the more difficult it becomes to remove any of the remaining molecules from the vapour.

There is a strong correlation between the boiling point, the latent heat of evaporation and the vapour pressure of a liquid. Helium has the lowest latent heat of evaporation of all the elements due to two different effects. Firstly, the Van der Waals' forces between the atoms are weak because of the closed electronic s-shell, giving rise to the absence of static dipole moments. Secondly, due to the small atomic mass, m, helium has a large quantum mechanical zero-point energy, $E_0 \propto 1/m$. The large zero-point energy also gives a large zero-point vibration amplitude, meaning the that the molecules will be less confined by its neighbors. On the one hand, the weak interatomic forces gives a low latent heat of evaporation and the LHe refrigerator a very modest cooling power. But on the other, it

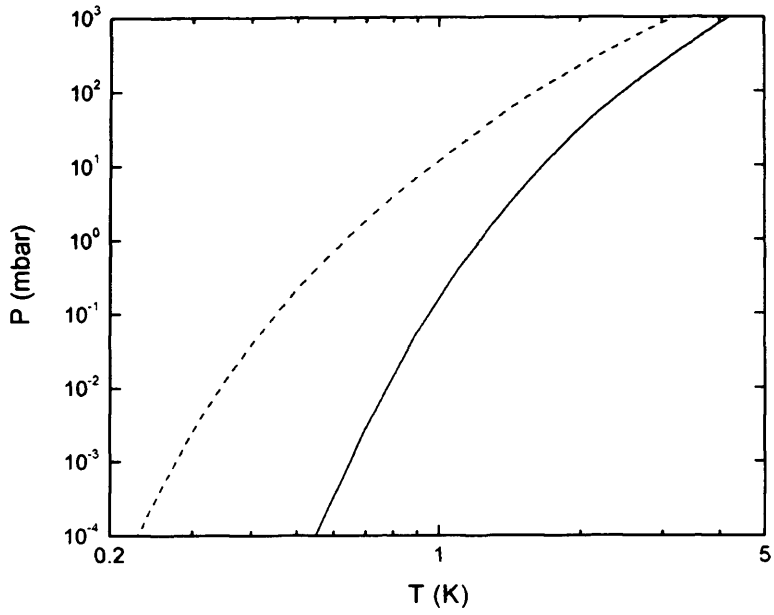

Figure 1.8: Vapour pressure of liquid ^{4}He (solid line) and liquid ^{3}He (dashed line)

means helium remains liquid down to absolute zero with a relatively large vapour pressure.

The common stable isotope is ^{4}He. With a nucleus consisting of two protons and two neutrons, each with antiparallel spin orientations, ^{4}He is a boson particle since the total nuclear spin $I = 0$. The more rare isotope ^{3}He is a Fermion particle due to one less neutron in its nucleus which results in $I = 1/2$. The different statistics of the two isotopes cause substantial differences in their low-temperature behaviour, some of which will be discussed in section 4.2. Since ^{3}He is lighter than ^{4}He, it has a larger zero-point energy and hence lower boiling point (3.2 K), smaller latent heat of evaporation and larger vapour pressure. The larger vapour pressure makes it more suitable as a refrigerant at low temperatures. Figure 1.8 shows the vapour pressure of the two helium isotopes down to temperatures close to the practical limit of refrigeration. Unfortunately, the low abundance of ^{3}He in the atmosphere makes it a very expensive gas. The ^{3}He used in cryogenics today is collected as a byproduct of tritium manufacture in nuclear reactors and costs approximately £150/L (STP) of gas.

1.3.2 ADSORPTION

Sorbents are materials that can attract and hold gases or liquids. A qualitative distinction is usually made between chemical adsorption (chemisorption) and physical adsorption (physisorption), in terms of the relative binding strengths and mechanisms. In chemisorption, a strong chemical bond is formed between the molecule and the adsorbent. Energies of a few eV/atom are typical of chemisorption. Physisorption, which is of interest to us, is weaker and the energy of interaction (typically tens of meV/atom) is largely due to the van der Waals'

force. Although adsorption is a universal process that occurs spontaneously on all surfaces at all temperatures and pressures, even at temperatures above the critical temperature of the adsorbed gas, it is significantly more effective at low temperatures. When gases or vapour are adsorbed, their molecules lose a degree of freedom and the energy released is in the order of the heat of condensation. Adsorption is a continuing, reversible process with the molecules constantly being adsorbed and others desorbed from the adsorbent surface. When the rate of molecule adsorption onto the surface is equal to the rate of molecule desorption, the system is in adsorption equilibrium.

It is easy to see how adsorption can be used in a cryogenic refrigerator; the vapour above a liquid can be adsorbed using a suitable material and the liquid will effectively cool as a result of the strong temperature dependence of its vapour pressure. Adsorption pumps are very powerful with a pumping speed comparable with the best turbo-molecular pumps. Because of their simplicity, reliability and cheap design, adsorption pumps have found widespread use in refrigeration, vacuum technologies and purification of gases.

1.3.3 SORPTION COOLERS

The name sorption cooler is generally used for any cryogenic refrigerator utilizing pumps containing an adsorbing material. They are used in applications at temperatures ranging from hundreds of Kelvin down to temperatures below 100 mK depending on what working gas, or mixture of gases, is being used. A large number of materials can be used as adsorbents; silica gel, zeolite, activated carbon or indeed any metal structure kept at sufficiently low temperature and with large enough surface area. From now on we will refer to sorption coolers as sub-Kelvin refrigerators using activated carbon adsorbents and various isotopes of helium gas.

The main advantage of using adsorption pumps inside the cryostat is the absence of serious pressure drops in the pumping line and the fact that no external pumps are needed. By an adequate arrangement of the adsorbent very high pumping speeds can be obtained. A further advantage is that no capillaries can be blocked by impurities which greatly improves the reliability of the system. Several early designs of cryostats using adsorption coolers have been described elsewhere [21–25].

Figure 1.9 shows the schematic of a sorption cooler in its simplest form. By means of a liquid helium bath, all parts of the refrigerator is cooled to 4.2 K, at which temperature the gas is confined to the charcoal pump. In order to achieve an efficient condensation, the bath temperature needs to be below the critical temperature of the gas (5.2 K for ^{4}He or 3.3 K for ^{3}He). For this reason it may be advantageous to first pump on the helium bath to reduce the temperature of the condenser further. The heat switch is then switched off and the charcoal

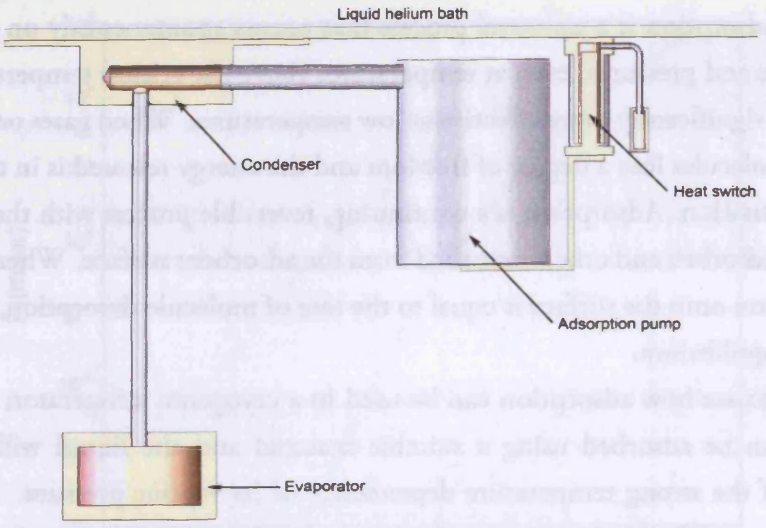

Figure 1.9: Schematic of a single stage ^{3}He sorption cooler.

pump heated up. The gas will start desorbing from the charcoal grains at approx 10 K and most of it will have been desorbed at 25 K. As the charcoal pump is heated up further, the pressure inside the refrigerator increases, the gas liquifies inside the condenser and gravity pulls it down to the evaporator. The condensation efficiency is given by the vapour-pressure curve in figure 1.8. The heat switch is then switched on and so the charcoal pump cools down again. When its temperature falls below 25 K, the charcoal starts adsorbing molecules from the vapour and hence acts as an efficient pump. As the vapour pressure decreases, so does the boiling point of the liquid and when the temperature of the pump is below 5 K, the evaporator reaches its lowest temperature (typically 800 mK for ^{4}He or 320 mK for ^{3}He). The lowest achievable temperature in a sorption cooler is limited by four factors: (i) the total heat load on the evaporator, (ii) the pumping speed of the system, (iii) the Kapitza resistance of the evaporator and (*iv*) the vapour pressure of the liquid which obviously justifies the use of ^{3}He. In the case of ^{4}He there is an additional factor since the liquid goes superfluid below 2.177 K and, unless precautions are taken, the superfluid film-flow will effectively increase the thermal load on the evaporator.

Although a ^{3}He cooler can be cycled from a pumped helium bath, it is generally better to use a double-stage ^{3}He-^{4}He cooler. Consider the cooling of a liquid ^{4}He bath from 4.2 K to 2.5 K. This cooling will require the removal of

$$Q = \int_{2.5\mathrm{K}}^{4.2\mathrm{K}} C_\mathrm{p}(T)\, dT \simeq 38\,\mathrm{J/mol}\,. \tag{1.6}$$

Comparing this value with the average molar latent heat of vaporization (90 J/mol) shows that approximately 40% of the liquid will evaporate during the cooling. Hence, by using a

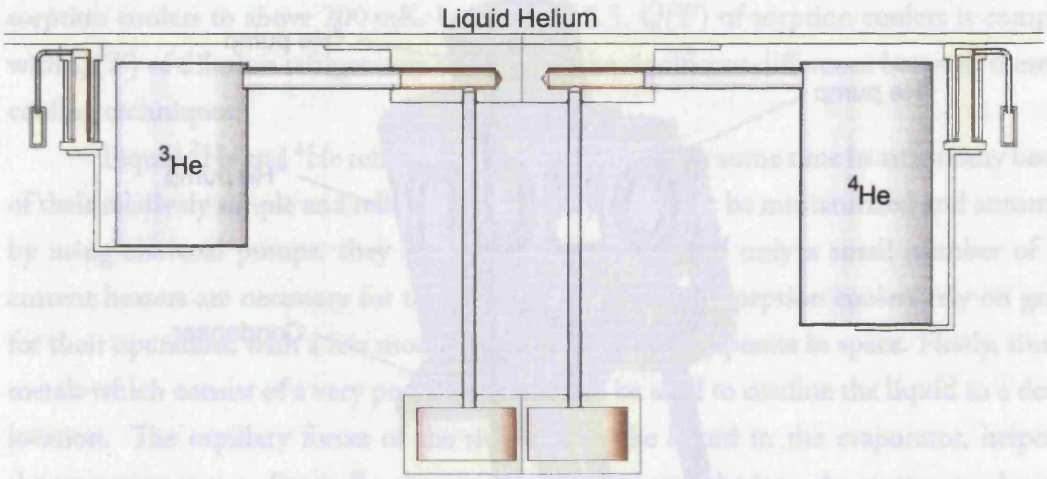

Figure 1.10: Schematic of a double stage (^{4}He-^{3}He) sorption cooler. The ^{4}He stage is used to condense the ^{3}He straight into the evaporator.

separate sorption cooled ^{4}He stage, one can save a lot of expensive liquid helium, time and effort since only a much smaller amount of helium will have to be cooled, see figure 1.10. This arrangement will also increase the condensation efficiency of the ^{3}He stage since a sorption cooled ^{4}He stage can generally reach lower temperatures (< 0.9 K) than a mechanically pumped helium bath.

The system can be improved further by introducing a third stage [26], figure 1.11 shows a commercial triple stage cooler from Chase Research Cryogenics Ltd.[†]. (CRC). A double stage cooler, operating at 350 mK is used as a buffer stage to decrease the thermal load on the third (^{3}He) stage, thus allowing it to reach 220 mK. An additional buffer stage, using the enthalpy of the evaporated gas operates at approximately 1.5 K. This particular refrigerator is designed for operation with a pulse-tube cooler which is why the charcoal pumps are positioned above the condenser. This has the advantage of suppressing convection and also helps to reduce thermal radiation from the pumps during the condensation phase. One could argue that by introducing a fourth or even a fifth stage, even lower temperatures could be reached. Although this is true in principle, it is hardly worth the effort since the cooling power below 200 mK would be too small to be useful in any real experiment.

Sorption coolers are single-shot systems in that they can provide cooling for a limited time only. Eventually all the liquid in the evaporator has boiled off and the system has to be recycled. This means an interruption in the experiment of typically 1–5 hours depending on the complexity of the design, the mass of the cold components, cycling procedures, etc. The total run-time of the system is still long in comparison with the time it takes to recycle

[†]Chase Research Cryogenics Ltd., 140 Manchester road, Sheffield, S10 5DL, UK, http://www.chasecryogenics.com

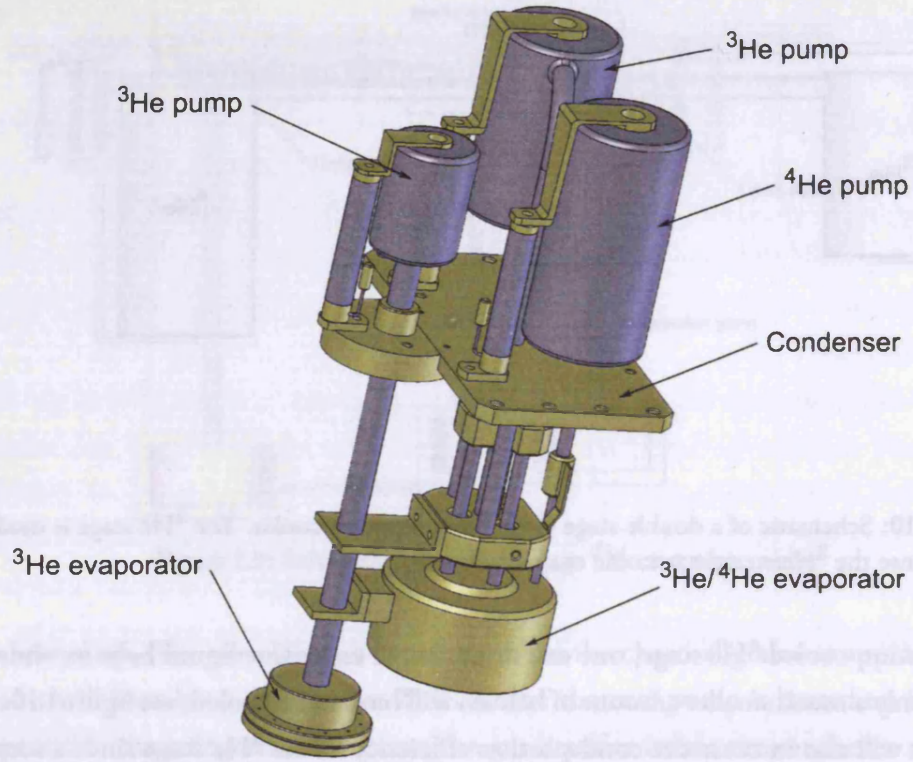

Figure 1.11: A commercial triple stage (^{4}He-^{3}He-^{3}He) sorption cooler, developed and distributed by Chase Research Cryogenics. The total height of this cooler is approximately 300 mm.

it so a duty cycle efficiency of at least 90% is generally easy to achieve.

The cooling power of a liquid helium refrigerator is given by $\dot{Q} = \Delta H \dot{n}$ where ΔH is the difference in the (molar) enthalpy of the vapour and the enthalpy of the liquid. The number of moles of helium molecules being removed from the liquid each unit of time, $\dot{n}$, is proportional to the vapour pressure. The slope of the vapour pressure curve can be calculated using the Clausius-Clapeyron equation $\mathrm{d}P/\mathrm{d}T = \Delta S/\Delta V_\mathrm{m}$, where S is entropy and V_m the molar volume. Since the molar volume of the gas is much larger than that of the liquid, $\Delta V_\mathrm{m} \simeq RT/P$ where the ideal gas approximation has been used. With $\Delta S = L/T$, where L is the latent heat of evaporation, the Clausius-Clapeyron equation can be written as

$$\frac{\mathrm{d}P}{\mathrm{d}T} \simeq \frac{LP}{RT^2} \Rightarrow \ln P = -L/RT + C\,, \tag{1.7}$$

where C is a constant. Very accurate, empirical [27–29] as well as analytical [30], vapour-pressure expressions have been derived and are used for international temperature standards. For our purpose, however, it is enough to notice that P and therefore also $\dot{Q}$ is proportional to $\exp(-L/RT)$. This very strong temperature dependence effectively limits the use of

sorption coolers to above 200 mK. In section 1.3.5, $\dot{Q}(T)$ of sorption coolers is compared with $\dot{Q}(T)$ of dilution refrigerators to illustrate the significant difference between these two cooling techniques.

Liquid ^{3}He and ^{4}He refrigerators have been used for some time in astronomy because of their relatively simple and reliable design. They can easily be miniaturized and automated by using charcoal pumps, they have no moving parts and only a small number of low-current heaters are necessary for their operation. Although sorption coolers rely on gravity for their operation, with a few modifications they can also operate in space. Firstly, sintered metals which consist of a very porous material can be used to confine the liquid to a desired location. The capillary forces of the sinter holds the liquid in the evaporator, helped by the vapour pressure. Secondly, the gas is condensed straight into the evaporator by using a heat switch, thus making the condensation phase independent of gravity. Such systems are now well developed [31–34] and have found applications on satellite experiments like Herschel-SPIRE.

Although double stage coolers are more common for operation from 4.2 K, it is worth pointing out that single stage ^{3}He coolers can actually be operated from 4.2 K. This is because of the adiabatic expansion taking place in the evaporator as the charcoal pump cools down. This will cool the gas and a fraction of it will liquify straight into the evaporator. In fact, this method can be used to condense ^{3}He at a base temperature above its critical temperature. It has been shown [35] that a condensation efficiency as high as 48% is possible to achieve in a single stage ^{3}He cooler, operated from 4.2 K.

Sorption coolers are likely to play an important role also in the future since they can provide the necessary base temperature for new technologies such as solid state micro-coolers [36] and miniature dilution refrigerators.

1.3.4 ADIABATIC DEMAGNETIZATION REFRIGERATORS

The adiabatic magnetization refrigerator (ADR) has been used extensively in astronomy. This very mature technology, first proposed in 1920, uses the magnetic enthalpy of various salt pills to reach temperatures below 0.1 K. Just like liquid helium refrigerators, they are 'single-shot' systems which means they only operate for a limited time before they have to be recycled, during which time the experiment has to be halted. An ADR uses very strong magnetic fields (typically 4 T) which constantly change in magnitude so extreme care has to be taken to shield the detector system. Passive and active shielding methods have been developed but not yet demonstrated in a system with large detector arrays [37]. High current leads are required for the magnet resulting in large thermal loads on the 4 K stage. Further

to this, there is a small chance that the superconducting magnet will quench[†], resulting in a disastrous dissipation of heat. Nevertheless, ADR refrigerators have been very successful and used on several balloons (MAXIMA, MAXIPOL) and rockets (XQC). It is also the chosen technology for some future satellite missions (XRS, XEUS). Their main advantages are: (*i*) a natural ability to work in zero gravity, (*ii*) an efficient cooling cycle which is typically 90 percent of the Carnot cycle, (*iii*) they can operate from a base temperature as high as 8 K and (*iv*) there are no gases or liquid cryogens to leak.

Several projects aiming at developing a continuous ADR are ongoing and the most recent effort [38, 39], developed for the satellite mission Constellation-X, has achieved an impressive 6 μW of cooling power at 50 mK. The design of a continuous ADR is however very elaborate, expensive and at least ten times bigger and heavier than a liquid helium sorption cooler. A 50 mK continuous ADR [40] under development for a satellite experiment (XEUS) has a weight of 45 kg and in comparison, the weight of a typical sorption cooler is 2–3 kg.

Figure 1.12 shows the schematic of a single-shot ADR using only one salt pill. The superconducting magnet generates a strong magnetic field which interacts with the paramagnetic dipoles of the salt pill, orienting them in the same direction. This isothermal magnetization decreases the entropy and the heat of magnetization is released from the salt and absorbed by the buffer stage through the heat switch. During the next phase, the heat switch is open to thermally isolate the salt from the buffer stage. The magnetic field is decreased to allow for the adiabatic demagnetization to cool the salt pill to its operating temperature. The temperature can be kept stable by decreasing the magnetic field further to balance the entropy production against the heat leak. Eventually, when the magnetic field equals zero, the salt pill warms up and has to be re-cycled.

There are a number of different paramagnetic salts which can be used in an ADR. The most common high-temperature salt is ferric ammonium alum (FAA) which can be used down to about 30 mK. Cerium magnesium nitrate (CMN) can be used to achieve temperatures below 10 mK. The lowest achievable temperature is limited by the magnetic ordering temperature of the salt. For example, at a temperature of 20 mK the interactions between the FAA ions generates an internal field which causes the ions to self-align. The fundamental difference between a FAA and a CMN salt is the much weaker interactions between the Cerium ions which gives the CMN salt its lower magnetic ordering temperatures. Because the CMN salt has a rather low entropy at high temperatures, it is usually combined with a high-temperature salt connected in series. In such a double stage configuration the high-temperature salt pill acts as a thermal buffer for the low-temperature salt.

[†]The applied current may drive the superconducting magnet normal, should the current exceed the superconductor's critical current. As a result, the electrical resistance increases dramatically.

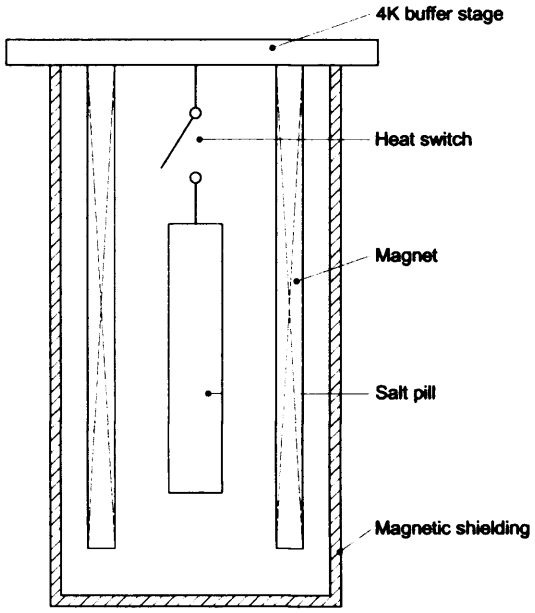

Figure 1.12: Principle schematic of a single-shot ADR using only one salt pill.

1.3.5 DILUTION REFRIGERATORS

The detailed theory of dilution refrigeration (DR) will be discussed in chapter 4, here we give a very brief introduction to the subject and describe a few important applications.

A mixture of liquid ^{3}He and ^{4}He, cooled to a temperature below 700 mK will separate into two phases as shown in figure 1.13. A layer of concentrated ^{3}He will float on top of a layer of almost concentrated ^{4}He. The entropy of mixing must decrease with temperatures and so the two liquids should be completely separated at $T = 0$. Due to the different statistics of Fermions and Bosons, however, there is a finite solubility of about 6% of ^{3}He in the ^{4}He rich phase. The ^{4}He rich layer is usually referred to as the diluted phase. This finite solubility is of utmost important for dilution refrigeration and came as a great surprise for scientists when it was discovered. Crucially, the molar enthalpy of ^{3}He in the diluted phase is larger than in the concentrated phase, meaning that when a ^{3}He molecule crosses the boundary from the concentrated layer to the ^{4}He rich layer it produces cooling. By continuously removing ^{3}He from the diluted phase, molecules from the concentrated phase are forced to cross the boundary between the two phases. Obviously, the ^{3}He molecules removed from the diluted phase have to be returned to the concentrated phase in order to close the loop and achieve a continuous cooling.

Figure 1.14 shows the main components in a dilution refrigerator. Phase separation occurs in the mixing chamber (m.c.). By means of a pump connected to an evaporator (still) operated at a much higher temperature, ^{3}He atoms can be removed from the diluted phase. The temperature of the still is generally 0.6–0.7 K, hot enough to allow for a reasonable

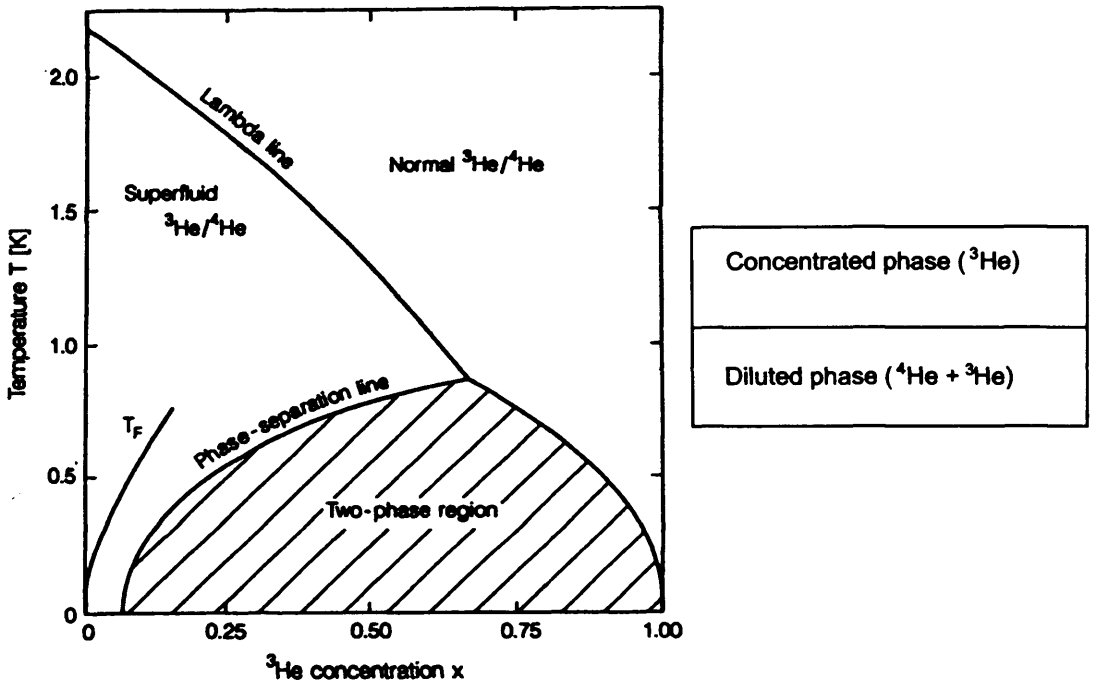

Figure 1.13: ^{3}He-^{4}He phase diagram. [41]

circulation rate of ^{3}He but low enough to avoid too much ^{4}He to be circulated in the system. Essentially, the vapour pressure of ^{3}He should be as high as possible but the vapour pressure ratio of ^{4}He/^{3}He should be low. At for example 0.7 K, the vapour typically contains 3% of ^{4}He. In the still, the ^{3}He molecules are evaporated and removed by a powerful pump operated outside the cryostat. The evaporation decreases the ^{3}He concentration in the still and drives ^{3}He atoms from the diluted phase in the m.c. up to the still. The ^{3}He are returned to the mixing chamber through a condensation stage (^{4}He evaporator), and a number of heat exchangers. The enthalpy of the up-flowing ^{3}He molecules is used to cool the returning liquid.

The cooling power of the DR is given by $\dot{Q} = \Delta H \dot{n}_3$ where ΔH is the difference in molar enthalpy of pure ^{3}He and diluted ^{3}He, and $\dot{n}_3$ is the ^{3}He circulation rate (mol/s). The molar enthalpy of pure and diluted ^{3}He is given by

$$H(T) = H(0) + \int_0^T C(T)\, dT, \tag{1.8}$$

and can be calculated through theoretical estimates or experimental measurements of the specific heat, C. More details on the cooling power will be discussed in chapter 4, but it is clear that the temperature dependence of $\dot{Q}$ only depends on ΔH since $\dot{n}$ is independent of temperature due to the finite solubility of ^{3}He in ^{4}He. In both phases, of course, the specific heat $C \propto T$ because ^{3}He are Fermi particles whether they are diluted or not. As a result,

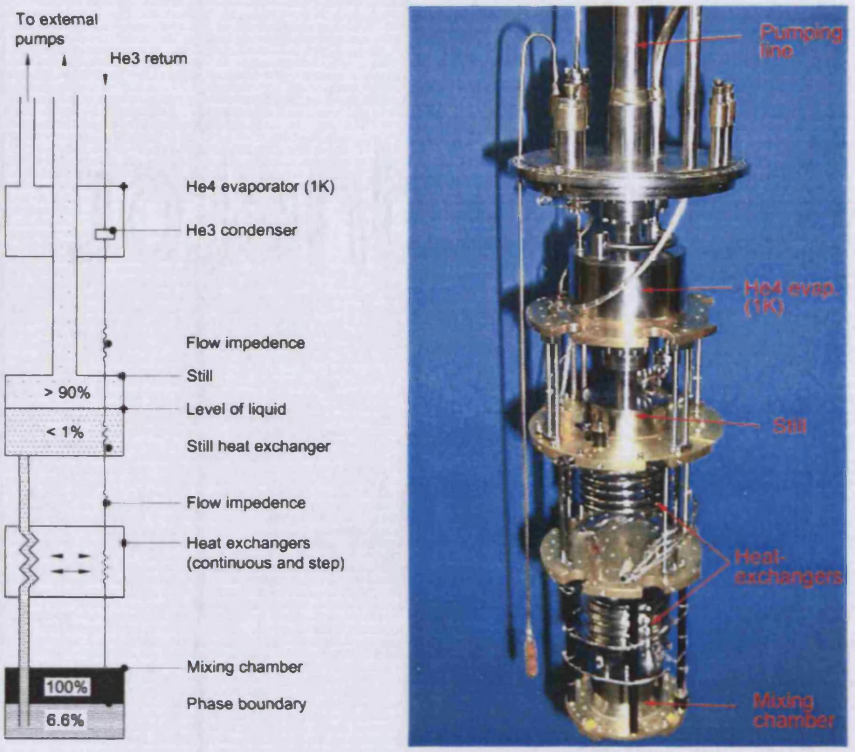

Figure 1.14: Principle schematic of a conventional dilution refrigerator (left) and a picture of a commercial machine (JDR500) from Janis Research Company Inc. (right).

the cooling power will depend on the temperature as $\dot{Q}(T) \propto T^2$. In comparison with evaporation cooling discussed in section 1.3.3, this is a very weak temperature dependence which makes dilution cooling powerful even at very low temperatures. A comparison of the cooling power of a DR and a ^{3}He evaporation cooler is shown in figure 1.15.

The dilution refrigerator has been the workhorse of cryogenics for the last 30 years. It was originally suggested by London in 1951 [42, 43] and experimentally demonstrated by Das *et. al.* in 1965 [44] reaching 0.22 K. Improved versions of this designed by Neganov and Hall, soon reached 25 mK. The development of advanced heat exchangers by Frossati made dilution refrigeration below 3 mK possible, and the current world record is 1.75 mK. Dilution cooling is today the most important refrigeration technology for sub-Kelvin applications and the only refrigeration method to achieve continuous cooling at temperatures below 300 mK. They are today developed to a point where it is not practically possible to lower the operating temperature further. Dilution refrigeration has also made nuclear magnetic refrigeration possible, a method very similar to magnetic refrigeration of salt (ADR) , which relies on a powerful dilution cooler to provide the base temperature. Nuclear magnetic refrigeration is still the only way of achieving temperatures in the micro-Kelvin range and has allowed scientists to explore various superfluid phenomena, crystalized helium and

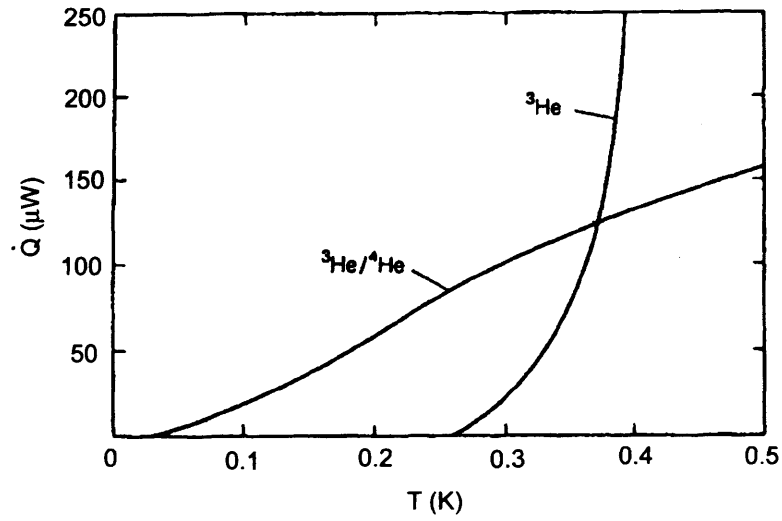

Figure 1.15: A comparison of the cooling power of the dilution refrigerator and the ^{3}He sorption cooler. A room-temperature pumping system with a capacity of 5 L/s has been assumed. Given the vapour pressure of ^{3}He when the refrigerators are in operation (a fraction of a mbar), this corresponds to a circulation rate of 30 μmol/s in the dilution refrigerator and the ^{3}He cooler at 0.5 K. [41]

negative temperatures.

Most sub-Kelvin experiments carried out in a laboratory environment take use of the dilution refrigerator. It benefits from a high cooling power, can operate at temperatures below 10 mK and is naturally continuous in operation which avoids any interruption of the experiment. Dilution refrigerators have found applications in a whole range of fields from condensed matter physics and biology to dark matter astronomy, CMB experiments and gravitational wave detectors. On the down side, conventional systems are expensive and bulky and usually require a fair bit of cryogenics knowledge to install as well as to operate. Problems with leaks and blocks are common and can be very tedious to resolve. It is only very recently they have become useful in astronomy and PLANCK will be the first mission to operate a dilution refrigerator in space.

The PLANCK cooler [45] has already been successfully used for the balloon experiment ARCHEOPS and reached 75 mK [46]. Due to its open-cycle operation, the ^{3}He flow was limited to give a very moderate 200 nW of cooling power at 100 mK. Evens so, it will consume a massive 4876 L STP of expensive ^{3}He gas (plus 21600 L STP of ^{4}He gas) during its 2 years lifetime. The originality of the Planck open cycle cooler is that pure ^{3}He and ^{4}He gas are separately injected under pressure into the cryostat. They are pre-cooled, liquified and passed through a heat exchanger, and mix together to produce cooling once they reached the coldest part of the system. Therefore, the process does not need an evaporator (a still) to separate the ^{3}He from the mixture. Unlike conventional dilution refrigerators, the two

liquids are not separated into two layers. Instead the concentrated phase forms bubbles in the diluted phase and the cooling takes place at the surface of the bubbles, a process which is independent of gravity.

In analogy with the sorption coolers developed for space, attempts have been made to use sintered materials in a single-shot dilution refrigerators to confine the liquid [47]. The ultimate goal of that project has been to develop a dilution refrigerator with a continuous cycle for operation in zero-gravity [48]. The main challenge in this refrigerator is to keep the ^{3}He rich phase separated from the diluted phase and to assure that only ^{3}He from the diluted phase is pumped off from the still. Although some progress have been reported on the single-shot version with a lowest temperature of 50 mK and a maintained performance at tilted angles, the work appears to have stalled on the continuous version.

1.4 CANDIDATES FOR A MINIATURE DILUTION REFRIGERATOR

In conventional dilution refrigerators, the ^{3}He gas is pumped off the still using powerful pumps at room temperature outside the cryostat. It is then recycled back to the mixing chamber through a number of heat exchangers and a condensation stage. This method offers a very high circulation rate (hundreds of μmol/s) and hence cooling power but is impractical for many astronomy applications. It requires an external gas handling and pumping system which would be impossible to upkeep on for example a balloon-borne experiment. There are also problems associated with the necessity of introducing large-diameter exhaust pipes into the cryostat, purification of ^{3}He from oil decomposition products, protection from vibrations generated by pumps, and so on.

A far more compact and reliable design, first suggested by London *et. al.* [49] and later constructed by Edel'man [50], circulates the ^{3}He internally without the need of any external mechanical pumps. Figure 1.16 shows the principle of this method. Here the condensation stage itself, cooled by a ^{3}He evaporation stage, acts as a pump since it is kept at a temperature below that of the still: for example the vapour pressure at 0.4 K is 50 times lower than at 0.7 K, a significant pressure drop which ensures the circulation of ^{3}He. As long as the condensation efficiency is high enough, that is as long as the condenser is kept significantly colder than the still and the surface area of the condenser is sufficiently large, circulation rates of the order tens of micro-mol per second can be achieved. This is more than enough to achieve a cooling power of several micro-Watt at 0.1 K.

The most recent effort on this design [51, 52] showed that dilution refrigeration using condensation pumping can operate at temperatures of 35–50 mK or even lower at

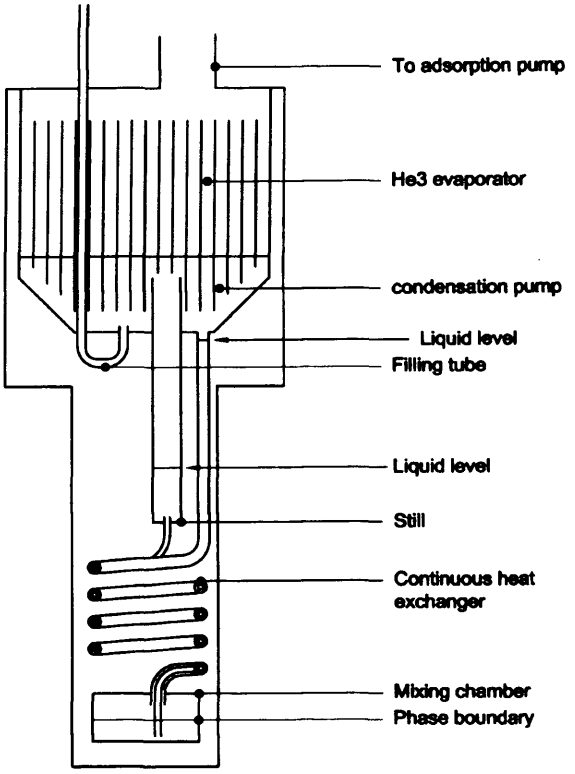

Figure 1.16: The Edel'man dilution refrigerator. The condensation pump and the ^{3}He evaporator have a developed surface area (vertical lines) for improved thermal contact between the two chambers.

circulation rates of only 1 μmol/sec. Interestingly enough, because the still is the hottest part of the system, any superfluid film flow is naturally suppressed and so the design of the still can be significantly simplified and the system will still circulate almost pure ^{3}He. Another advantage is the fact that no fine capillaries are necessary which eliminates problems with blocks which otherwise could develop as a result of impurities. The entire system can also easily be computer automated using only a few low-power heaters. There is however one serious problem with the Edel'man cooler in that it is not fully continuous since it relies on a continuous cooling of its condenser. With the required heat load, today's sorption coolers can only operate for about 20–30 hours without becoming impractically large, slow in operation and expensive.

In order to operate the Edel'man cooler in a fully continuous mode, two separate condensers can be used (figure 1.17). It is then easy to ensure that at any one time, at least one of the condensers is cold which will guarantee a continuous ^{3}He circulation. This method of operation was first realized by Mikheev *et. al.* [54, 55] and later improved by Bunkov *et. al.* [56]. The most advanced version of this design [53], achieved a lowest temperature of 10 mK. Such a low temperature could be reached due to the additional step heat exchangers

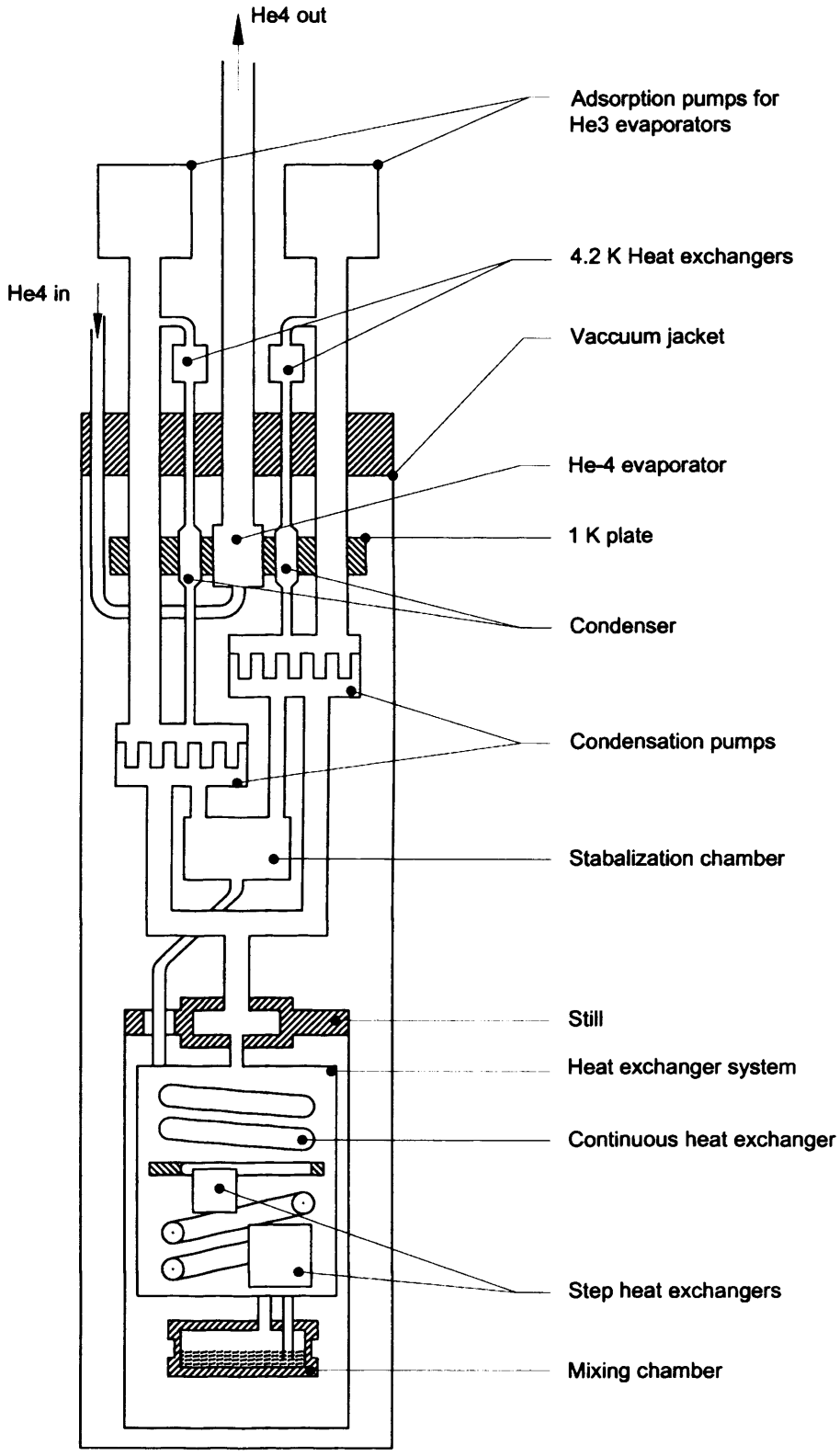

Figure 1.17: Schematic of the Sivokon dilution refrigerator. Using two separate condensation pumps and a stabilization chamber, a continuous operation is achieved. [53]

introduced below the continuous heat exchanger. Although this principle allows for a fully continuous operation, it has another serious problem in that it relies on a 1 K stage and an external pump. This makes it impossible to operate the system in a pulse-tube cooler without introducing an additional liquid helium bath which would have to be refilled on a regular basis. Nevertheless this design remains a very feasible candidate for astronomy applications since minor modifications to the design could allow it to function without such a 1 K stage.

For short-term experiments only requiring a limited run time, a single-shot dilution stage could be combined with a double or triple stage sorption cooler. Basically, the third stage in figure 1.11 could be replaced by a dilution stage. Such a configuration could prove very valuable since it offers a cheap and simple way of achieving extremely low temperatures. In fact without the need of any heat exchangers, the lowest achievable temperature is only limited by viscous heating, conducting through the liquid, thermal radiation and any mechanical support structure. Whether or not it could find applications in astronomy depends on how efficient a cool-down phase one could achieve; once the mixing chamber has reached the required temperature, there must be a significant amount of ^{3}He left in order to achieve an appreciable duty time. This issue will be discussed in more detail in chapter 5.

1.5 ABOUT THIS THESIS

We have investigated two different dilution refrigerators in order to evaluate which system is most suitable for applications in astronomy. The focus of this thesis is on a condensation pumped dilution refrigerator: here we opted for a novel concept combining the single-condenser Edel'man cooler with two separate double stage ^{3}He-^{4}He sorption coolers, as shown in figure 1.18. For us, the advantage of this system was the simplicity of the dilution unit, which is where our group had least experience, whilst there was significant experience in designing sorption coolers for operation in pulse-tube coolers as well as for balloon-borne experiments.

In chapter 2 we describe the design of a cryogen-free 300 mK system which represents the platform on which the MDR has been developed. We also present thermal conductivity and thermal conduction measurements on some critical parts of the assembly, and investigate the performance of ^{3}He sorption coolers.

To operate the MDR in a continuous manner, heat switches for operation below 0.5 K was developed. Our work on heat switches, presented in chapter 3, also includes a heat switch specifically designed for cooling of large thermal loads. Such a switch is essential for any larger experiment where the detector assembly is generally rather heavy and therefore can take a very long time to cool from room temperatures.

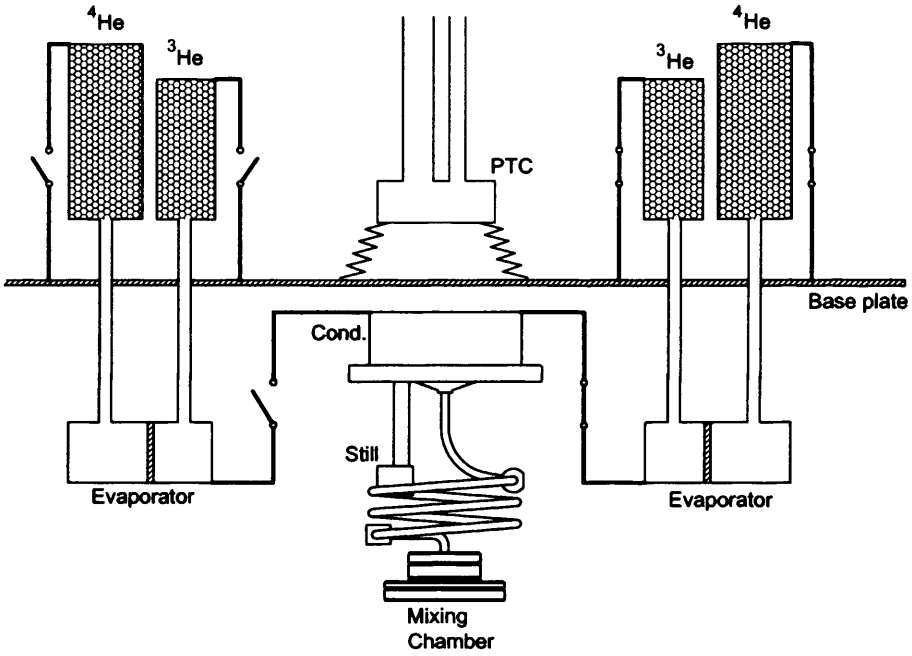

Figure 1.18: Principle schematic of the system developed during this project. The PTC is coupled to the base plate using flexible copper straps. Two double stage sorption coolers are used together with two heat switches to ensure a continuous operation of the dilution unit.

The condensation pumped MDR, chapter 4, was characterized in detail with measurements of the condensation efficiency, temperature stability, tilted operation and lowest attainable temperature as a function of the still power.

In parallel to the development of the continuous MDR, we also chose to investigate the feasibility of a single-shot MDR. The design and testing of this system is presented in chapter 5; a thermal model is used to identify the critical parameters of the design and to evaluate the experimental results.

For clarity, the word 'we' will strictly refer to the author's own work and opinions, any other work will be referred to in third person. SI units and style conventions are used consistently throughout this thesis.

2 Cryogen-free Sorption Coolers

In this chapter the design and integration of a cryogen-free cryostat with sorption coolers is described. The purpose of this work was to provide the continuous MDR (chapter 4) with a 300 mK base temperature. We present measurements on thermal conductivity and mechanical strength of the support structure, as well as the thermal impedance of copper straps in different configurations. We also investigate the performance of the ^{3}He sorption cooler and compare it with a theoretical model and other existing systems.

2.1 Introduction

The integration of various sub-Kelvin systems with pulse-tube coolers now attracts attention. The reason for this is the many advantages of a cryogen-free system, financial as well as practical. A small laboratory using 100–200 L of liquid helium per week pays around £6 per litre inc. VAT.[†] This can add up to a significant cost burden for a project unless the laboratory is equipped with a liquid helium recycle unit. Such recycle units are, however, very expensive and hardly worth the investment unless very large amounts of helium are used on a regular basis.

Assume a cryogenic system operating at 300 mK is required. Further to this, assume a triple stage sorption cooler like the one described in section 1.3.3 is used together with a standard LHe cryostat. Provided that the sorption cooler is recycled ones every 24 h, such a system will consume approximately 6 L of liquid helium per day of operation. The monthly cost for the 300 mK system would be about £1200. Now, a PT405 from CryoMech, see table 1.2, in combination with a 10 kW water cooler would consume a total of 14 kW of electricity. Assuming an electricity price of 5 pence per kWh, the PTC system would cost about half as

[†]Taken from Cardiff University's Rolling Grant Renewal Application 2005, which declared an average cost for past 12 months. The price therefore includes boil-off from the LHe storage dewar and also assumes a necessary safety margin for any unforeseen usage. The actual cost per litre was £3.71 inc. VAT.

much as the liquid helium cryostat. Here we have ignored the fact that the system most likely would have to be warmed up on a regular basis to change whatever samples are under test. The cool-down consumes a significant amount of LHe which will add to the operational costs of the 'wet' system. Of course, astronomy experiments are usually carried out on sites where the cost of liquid helium is significantly higher than in a laboratory environment. Also, to make regular LHe transfers can be time consuming and awkward, and may interrupt the ongoing experiment.

Based on the arguments above, the aim of this project was to integrate the 100 mK system with a PTC. As was described in section 1.5, two double stage sorption coolers were required. A PT405 pulse-tube cooler from CryoMech was integrated with a cryostat to hold the sub-Kelvin system. We designed the cryostat in such a way it could be used as a cryogenic testbed for another project (CLOVER) which means that the dimensions of the complete system are significantly larger than what was required for our purposes. The two double stage sorption coolers from Chase Research Cryogenics were charged with 8 L (STP) of ^{3}He gas plus 10 L (STP) of ^{4}He gas.

2.2 PTC CRYOSTAT

2.2.1 CRYOSTAT ASSEMBLY

Figure 2.1 shows the assembly of the cryostat. A 14" base plate is coupled to the second stage of the PTC by means of flexible OFHC copper braid. This provides a good thermal contact, and reduces vibrations and temperature oscillations from the PTC. A 16" base plate is coupled to the first stage of the PTC in a similar manner (figures 2.2 and 2.3). As will be shown in section 2.2.3, the braid should ideally be silver soldered into copper blocks, the blocks could then be gold plated and bolted to the end plates. Unfortunately, problems with soldering the rather large braids prevented us from using this configuration; instead the braids were clamped straight to the PTC cold head as well as to the base plate.

G10 rods[†] were used to support both the first stage and the second stage base plates. The rods were glued with Stycast 1266 into aluminium blocks which allows the support assembly to be bolted to the base plates.

Both base plates were made from OFHC copper and gold plated without any nickel interposer (see discussion on goldplating in section 3.2.4). The radiation shields were made from Aluminium Al-6082, a high-conductivity alloy to minimize the temperature gradient across the shields. In general, the temperature dependence of the thermal conductivity of

[†]Acculam™ G10 Glass Reinforced Epoxy from Accurate Plastics Inc., 18 Morris Place, Yonkers, NY 10705, US

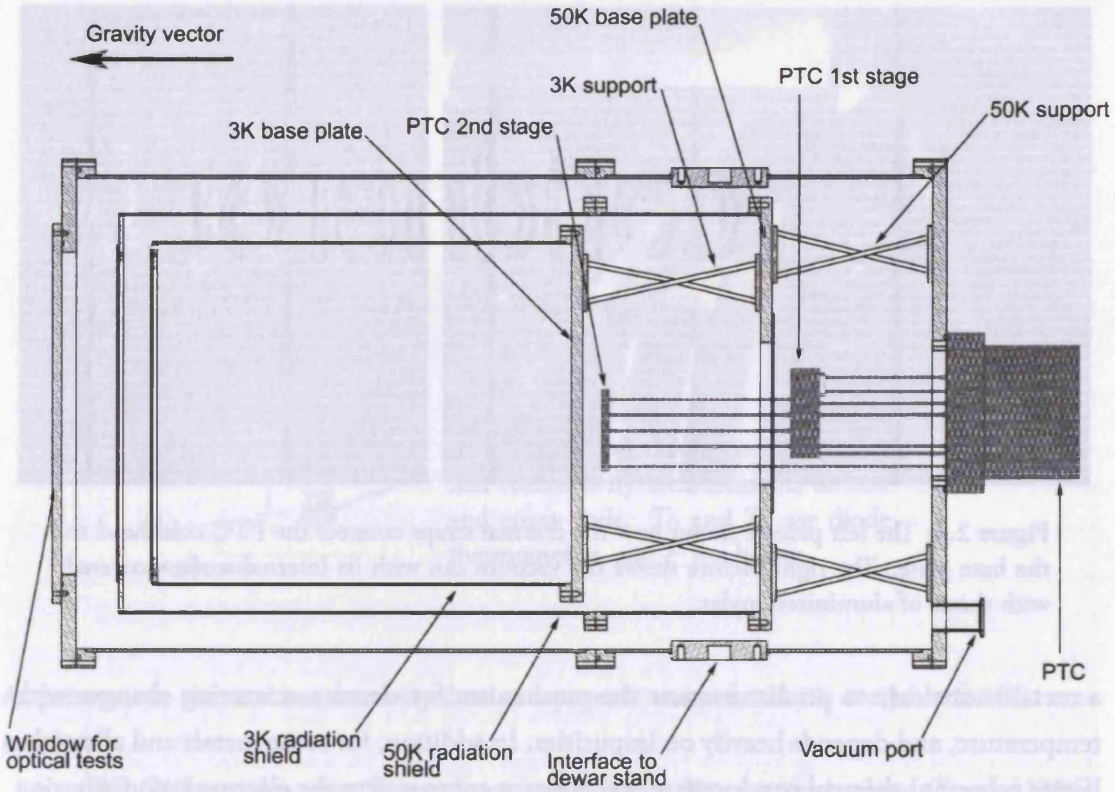

Figure 2.1: The principle components of the PTC cryostat assembly. Notice the gravity vector.

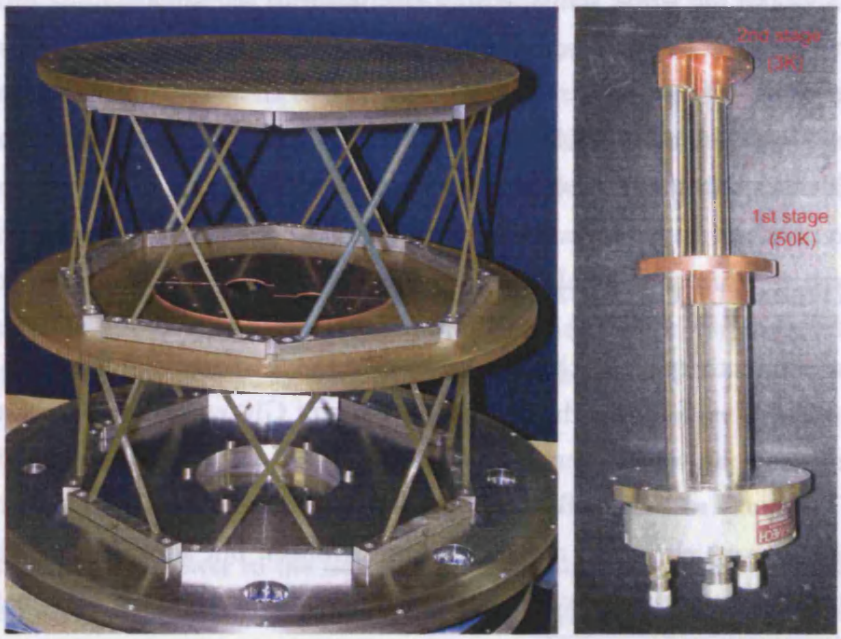

Figure 2.2: Left picture shows the 3 K base plate (top), the 50 K base plate (middle) and the vacuum shield (bottom) together with the G10 support structures. The right picture shows the PTC with its first and second stage cold heads.

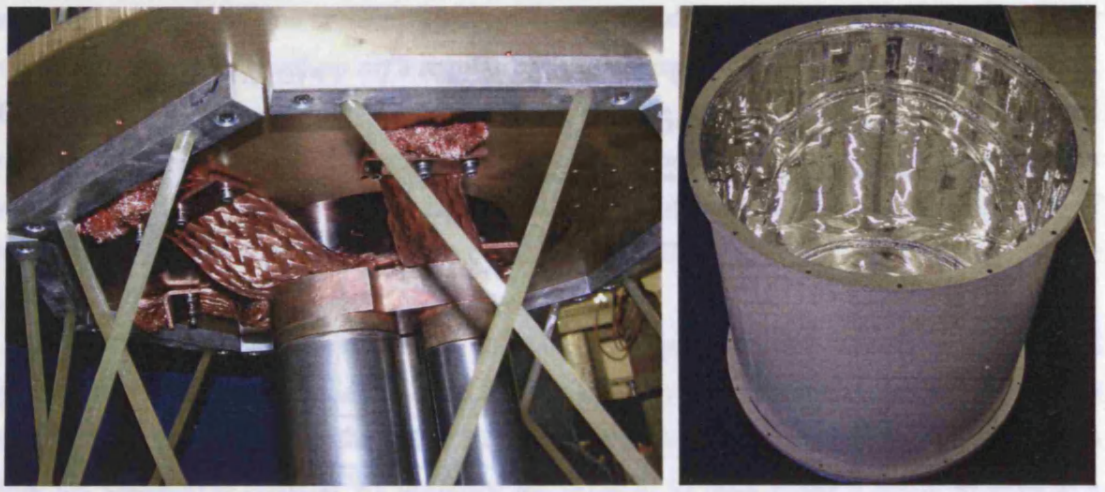

Figure 2.3: The left picture shows how the thermal straps connect the PTC cold head to the base plate. The right picture shows the vacuum can with its internal surface covered with sheets of aluminized mylar.

a metal is not easy to predict because the mechanism for electron scattering changes with temperature, and depends heavily on impurities. In addition, for some metals and alloys the lattice (phonon) thermal conductivity is significant compared to the electronic contribution to the thermal conductivity at room temperature. For Aluminium alloys, however, it turns out that the thermal (or electrical) conductivity at room temperature immediately gives the conductivity in the whole temperature range down to the superconducting transition temperature[†] [57].

The inside surfaces of the radiation shields as well as the vacuum tank are covered by sheets of aluminized mylar to reduce the emissivity. In addition, the outer surfaces of both radiation shields are covered by five layers of super-insulation.

2.2.2 THERMAL CONDUCTIVITY OF SUPPORT STRUCTURE

The thermal conductivity of G10 has been measured [58] but may vary from one manufacturer to another. Therefore, the thermal conductivity of G10 samples were measured from 4 K to room temperatures and compared with samples of epoxy-reinforced glassfibre from Bastion[‡]. The epoxy rods from Bastion is of a similar material to G10 but with a higher contents of epoxy which makes them stiffer and stronger, but also gives a higher room-temperature thermal conductivity. The epoxy rods are also significantly cheaper than G10.

[†]The reason for why this method works for Aluminium alloys and not for other metal alloys is not understood. In fact, there is no reason for why this method should work at all for any metals.

[‡]Pultruded epoxy-reinforced glassfibre rods from Bastion Glassfibre rod & Sections Ltd., 12 Harvey close, Crowther, NE38 OAB, UK

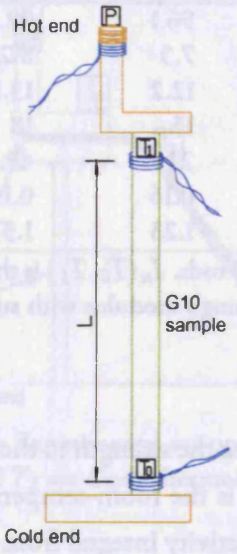

Figure 2.4: Experimental set-up for thermal conductivity measurements of G10 and epoxy rods. T_0 and T_1 are diode thermometers, and P is a heater.

At present, no thermal conductivity data at cryogenic temperatures is available for this material.

All G10 samples were 50 mm long, and 3.5 mm diameter rods glued (Stycast 1266) into copper blocks. The 'hot end' of the sample had a heater mounted to it and the thermometers were positioned in accordance with figure 2.4. Notice how the position of the thermometers and the heater is such that the glue does not affect the results in any way. The three heater wires were a combination of copper and constantan. The copper wire helps thermalizing the heater to the sample whereas the constantan wire isolates the hot end from the base plate. A 3-wire heater configuration is used to eliminate the lead resistance. Each (diode) thermometer was first calibrated against a LakeShore RhFe thermometer (see Appendix B for more information about low-temperature thermometry) and read out using a 4-wire configuration. The samples were mounted in a LHe cryostat and data were taken at LN_2 temperatures and LHe temperatures. By applying heat to the hot end of the sample, the integrated thermal conductivity is measured in accordance with

$$P = \frac{A}{L}\int_{T_0}^{T_1} \kappa(T)\, dT\,, \tag{2.1}$$

where P is the applied power to the heater, L the distance between the thermometers, A the cross-section of the sample, κ the thermal conductivity, and T_0 and T_1 are the measured temperatures.

Table 2.1 gives a summary of the results and compares the results of our G10 sample with calculated values using data from literature [58, 59]. As a figure of merit, FOM, of how

	Epoxy sample	G10 sample	G10 theoretical
$I_\kappa(79.5, 293)$ (W/m)	5000	96.1	92.5
$I_\kappa(3.5, 50.7)$ (W/m)	12.9	7.5	8.23
$I_\kappa(4.1, 70.0)$ (W/m)	29.1	12.2	13.1
E_C (GN/m^2)	27	15	18
E_T (GN/m^2)	30	22	49.6
$FOM(79.5, 293)$ (GNW^{-1}m^{-1})	0.054	0.16	0.19
$FOM(4.1, 70)$ (GNW^{-1}m^{-1})	0.928	1.23	1.37

Table 2.1: Measured thermal conductivity of epoxy and G10 rods. $I_\kappa(T_0, T_1)$ is the thermal conductivity integral between T_0 and T_1, and E is the Young's modulus with subindex C for compressions and T for tension.

useful the material is as a cryogenic support structure, we use the strength to thermal conductivity ratio: $FOM(T_0, T_1) = E_C/I_\kappa(T_0, T_1)$ where E_C is the room-temperature Young's module of compression and $I_\kappa(T_0, T_1)$ the thermal conductivity integral from equation 2.1. The values for E_C and E_T are from the compression/tension test described in section 2.2.6. It is clear that the support structure for both the PTC first stage and second stage should be made out of G10 rather than the Epoxy sample (FOM 0.16 for G10 vs. 0.054 for Epoxy), but the benefit from using G10 for the second stage support structure is much smaller (FOM 1.23 for G10 vs. 0.928 for Epoxy).

2.2.3 THERMAL CONDUCTION OF COPPER STRAPS

The PTC cold head is connected to the base plate by means of flexible copper straps. These straps are important to the overall system performance since their thermal conductance dictates the condensation efficiency of the sorption coolers. If their conductance is poor, the base plate will operate at a significantly higher temperature than the PTC cold head. This will make it difficult to cycle the sorption coolers and will result in an unnecessarily large thermal load on the colder parts. As will be shown in chapter 4, the thermal straps will also affect the temperature stability of the dilution refrigerator.

The thermal conductivity of bulk copper can be very high, but widely divergent values for the same material are often reported in literature. For comparatively pure materials, the differences are due mainly to slight material differences that have large effect on transport properties at cryogenic temperatures. At 10 K, the thermal conductivity of commercial oxygen free copper for two samples can be different by more than a factor of 20, while the same samples at room temperature would be within a few percent. It is also not uncommon for some experimental results to have uncertainties as high as 50%. The copper braid we used in our thermal straps is a oxygen-free high-conductivity (OFHC, C103) copper with a bulk conductivity of about 1000 W/m/K at 4 K [58]. But equally important for our application

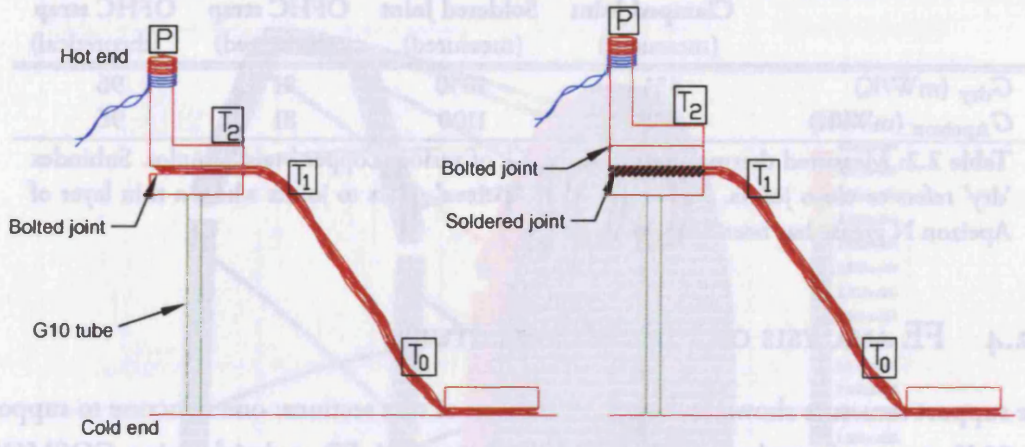

Figure 2.5: Experimental set-up for thermal conduction measurements of thermal straps. T_0, T_1 and T_2 are diode thermometers, and P is a heater.

is the thermal impedance at the interfaces between the straps and the plates it connects to. The thermal conductance of such pressed copper contacts will be discussed in more detail in section 3.2.4. Here we present measurements on the thermal conductance of such straps in various configurations in order to achieve best possible contacts at low temperatures.

We have evaluated four different configurations: clamped 'dry' contacts, clamped contacts with a thin layer of grease, soldered contacts and soldered contacts with grease. In the clamped configuration, the braid was bolted straight to the copper interface in accordance with figure 2.5. In the soldered configuration, a small sample of braid was first silver-soldered to a copper block, and the copper block was then bolted to the copper interface. Each configuration was tested with and without a thin layer of grease applied to the bolted joint. The total cross-section of each sample was 15 mm^2 and the length was 130 mm. All bolted interfaces used 4-40 stainless steel screws, tightened with a torque of 120 Ncm. Thermometers and heaters were mounted in accordance with figure 2.5, and both samples were tested at 4 K using a PTC from VeriCold. The temperature of the joints were about 8.2 K with the applied thermal load. The same thermometer and heater read-out scheme as described in section 2.2.2 was used.

The results of the thermal conductance tests are summaries in table 2.2. Here we also include the theoretical values of the copper braid using thermal conductivity data of OFHC copper from literature [58].

We conclude that the soldered braid is about twice as good as the clamped braid, and that a small amount of Apeizon^{TM} N grease only gave a very small improvement on the thermal conductance. It is likely that the thermal conductance can be improved further by better preparation of the copper blocks: for example, by gold plating and a more careful machining of the parts to ensure the surfaces are flat.

	Clamped Joint (measured)	Soldered Joint (measured)	OFHC strap (measured)	OFHC strap (theoretical)
G_{dry} (mW/K)	431	1050	81	96
$G_{Apeizon}$ (mW/K)	498	1100	81	96

Table 2.2: Measured thermal conductance, G, of various copper braid samples. Subindex 'dry' refers to clean joints, whilst subindex 'Apeizon' refers to joints where a thin layer of Apeizon N grease has been applied.

2.2.4 FE ANALYSIS OF SUPPORT STRUCTURE

The support structure shown in figure 2.2 consists of two sections: one structure to support the 50 K stage and another to support the 3 K stage. A FE analysis[†] (using COSMOS-SolidWorks) was carried out on each section separately. It turns out that the warmer structure is very rigid in comparison with the colder; a maximum deflection of 0.1 mm is easily achieved due to the larger diameter rods used for 50 K support. Also, the diameter-to-length ratio of these rods is large enough to avoid buckling. From this perspective, the analysis of the 3 K structure was more important; the results are shown in figure 2.6 and 2.7, where a 500 N was load applied along the horizontal axis. The analysis showed a maximum deflection of 0.44 mm and a safety margin to buckling of 2.04. These results corresponds to a worse-case scenario since the cryostat will never operate at angles greater than 45° with respect to the vertical axis.

In the FE analysis, the deflection of the Stycast was assumed to have a negligible impact on the overall deflection. To confirm that this simplification was sound, we also carried out a number of compression and tension tests on glued G10 samples (section 2.2.6).

2.2.5 ANALYTICAL ANALYSIS OF SUPPORT STRUCTURE

Any FE analysis should be complemented with analytical calculations. In this section we will use equations which can be found in most relevant text books (see for example Shigley and Mischke [60]).

Consider figure 2.8 which shows an approximate cross-section schematic of the assembly. Here we have ignored the fact that the rods are not actually vertically orientated. These calculations therefore represent a lower limit of the assembly stiffness. Given the moment of inertia, $I_x = \pi d^4/64$, of each rod's cross-section, the overall moment of inertia of

[†]In a finite element analysis, the structure is represented by a geometrically similar model consisting of multiple, linked, simplified representations of discrete regions: that is, finite elements on an unstructured grid. Equations of equilibrium, in conjunction with applicable physical considerations are applied to each element, and a system of simultaneous equations is constructed and solved through an iterative algorithm.

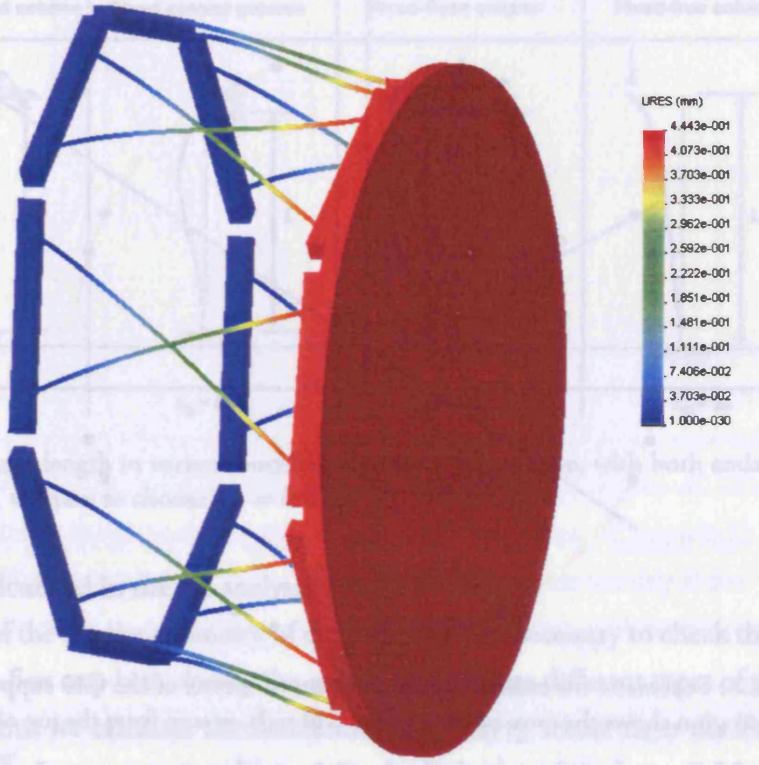

Figure 2.6: FE displacement analysis of the 4 K support structure. A 500 N load is applied horizontally on the 3 K base plate to simulate the weight of the base plate itself plus 30 kg of cryogenic components. The result shows a maximum deflection of 0.44 mm.

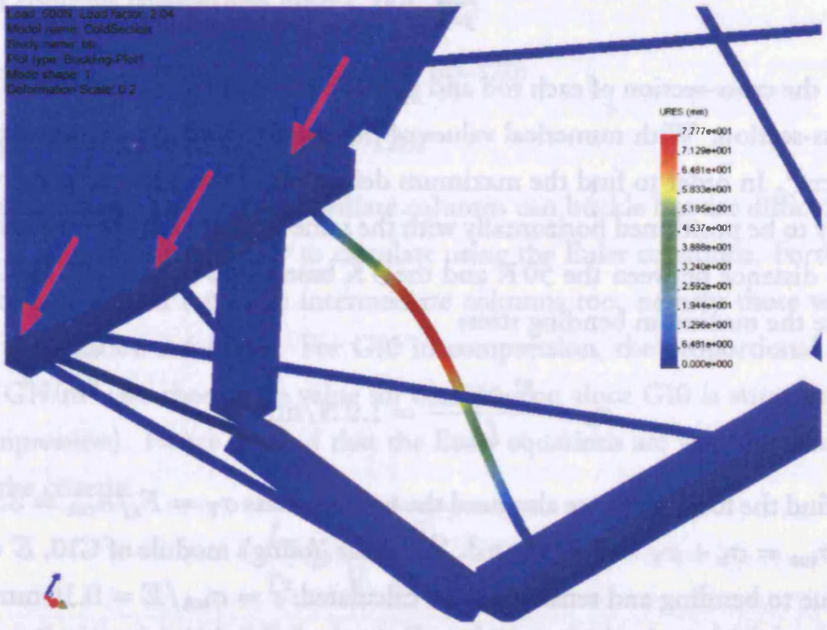

Figure 2.7: FE buckling analysis of the 3 K support structure. The figure shows how one of the components in the assembly buckles under a horizontal force of 1020 N. Given a nominal force of 500 N, the safety margin to buckling is 2.04.

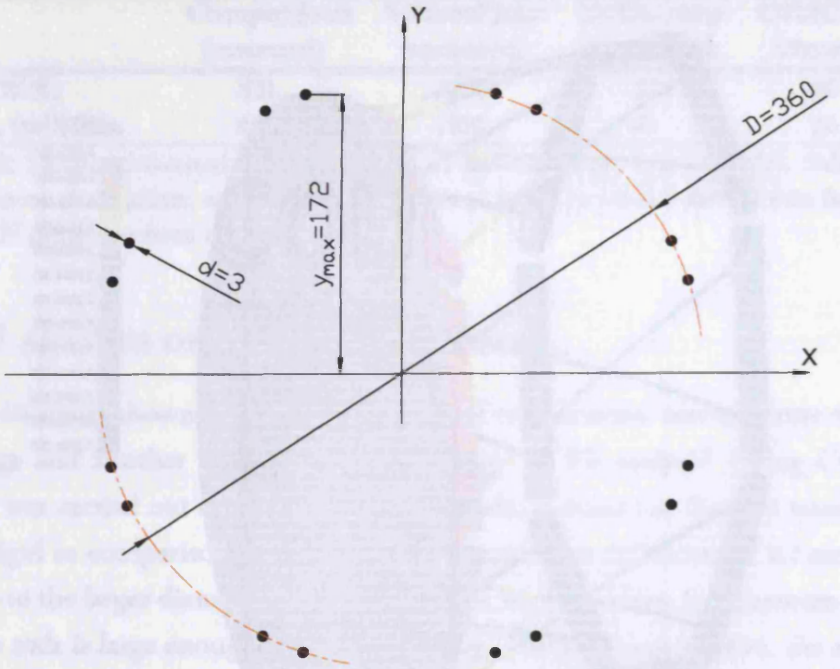

Figure 2.8: Schematic for estimating the moment of inertia of the G10 support structure. The illustration shows the cross-section of the G10 rods, as seen from the top of the cryostat.

the entire assembly, I_{xx}, can be calculated as

$$I_{xx} = \sum_{j=1}^{n} I_x + A_j y_j^2 , \tag{2.2}$$

where A_j is the cross-section of each rod and y_j is the distance from the x-axis to the centre of each cross-section. With numerical values of the cross-section and dimensions, we find $I_{xx} = 394\,\mathrm{cm}^4$. In order to find the maximum deflection of the 3 K base plate, we assume the assembly to be positioned horizontally with the same load used in the FE analysis: $F_x = 500\,\mathrm{N}$. The distance between the 50 K and the 3 K base plates is $z = 190\,\mathrm{mm}$. Thus, we can calculate the maximum bending stress

$$\sigma_b = \frac{F_x z y_{max}}{I_{xx}} = 1.9\,\mathrm{N/mm}^2 . \tag{2.3}$$

To find the total stress, we also need the tension stress $\sigma_T = F_x/A_{tot} = 3.9\,\mathrm{N/mm}^2$. Therefore, $\sigma_{tot} = \sigma_b + \sigma_T = 5.8\,\mathrm{N/mm}^2$. Using the Young's module of G10, $E = 18\,\mathrm{GPa}$, the strain due to bending and tension can be calculated: $\varepsilon = \sigma_{tot}/E = 0.16\,\mathrm{mm}$. Here we have ignored that fact that each individual rod may also bend slightly as a result of non-axial forces. This would explain why the analytical calculations give a somewhat smaller deflection

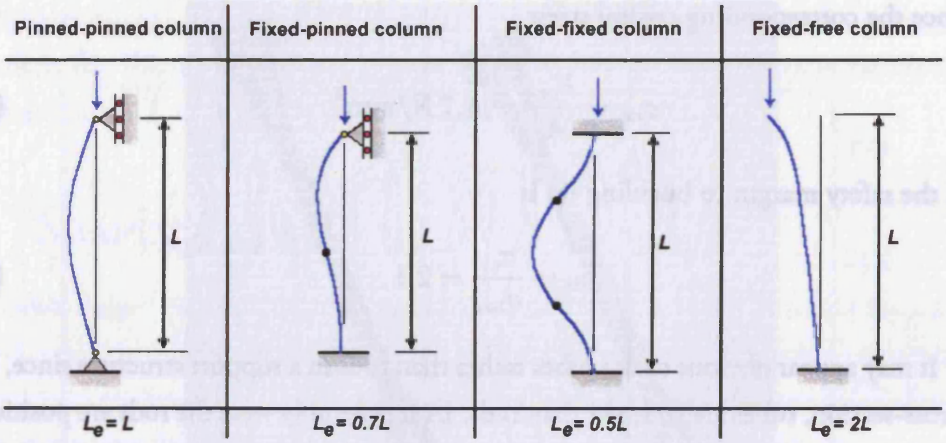

Figure 2.9: Euler length in various buckling scenarios. In our case, with both ends of the G10 rod fixed, we have to choose $L_e = 0.5L$.

than what was calculated in the FE analysis.

Because of the slender geometry of the rods, it is also necessary to check the assembly for buckling. The first step is to classify the rods as one of three different types of slenderness columns. To do this we calculate the slenderness ratio L_e/r_x where L_e is the Euler length and $r_x = \sqrt{I_x/A}$. In our case (see figure 2.9), the Euler length is $L_e = 0.5L$ where L is the free length of the column. Thus we find a slenderness ratio $L_e/r_x = 74.5$ which means our rods are classified as *intermediate columns* in accordance with the following definition:

1. Short columns (slenderness ratio < 60)
2. Intermediate columns (slenderness ratio 60–120)
3. Long columns (slenderness ratio > 120)

Short columns can not buckle; intermediate columns can buckle but are difficult to model analytically. Long columns are easy to calculate using the Euler equations. Fortunately the Euler equations are valid for some intermediate columns too, namely those which fulfill the criteria of equation 2.4 below. For G10 in compression, the proportional limit stress $\sigma_p = 0.68\,\mathrm{GN/m^2}$ (we choose the value for compression since G10 is stronger in tension than in compression). Hence we find that the Euler equations are valid for our rods since they fulfill the criteria:

$$\frac{L_e}{r_x} \geqslant \sqrt{\frac{\pi^2 E_C}{\sigma_p}} = 50.7\,. \tag{2.4}$$

We can now calculate the critical Euler load, F_{cr}, which is the load at which buckling occur.

$$F_{cr} = \frac{\pi^2 E_C I_x}{L_e^2} = 83\,\mathrm{N} \tag{2.5}$$

and hence the corresponding critical stress

$$\sigma_{cr} = \frac{F_{cr}}{A} = 11.7\,\mathrm{N/mm^2}\,. \tag{2.6}$$

Finally, the safety margin to buckling n_b is

$$n_b = \frac{\sigma_{cr}}{\sigma_{tot}} = 2.1\,. \tag{2.7}$$

It may appear obvious to use tubes rather than rods in a support structure since, for a given cross-section, tubes are stronger than rods. In an assembly were the rods are positioned on a large diameter, however, the benefit of using tubes instead of rods would be very small. This is because the overall stiffness of the assembly is much more dependent of the diameter D (figure 2.8) than of the small rod diameter, d. This argument obviously ignores the effect of buckling which puts some requirements on the rod diameter too. Provided that d is large enough to avoid buckling, however, there is little or nothing to gain from using tubes.

2.2.6 COMPRESSION AND TENSION TESTS OF SUPPORT STRUCTURE

Figure 2.10 shows the G10 and epoxy rod samples, glued into stainless steel caps using Stycast 1266. The dimensions of each sample are given in table 2.3

The testing machine[†] applied a compression and tension load, F, along the axis of the sample and measured the resulting deformation, ΔL. The results from these measurements are shown in figure 2.12 and 2.11. The initial deflection which occurred at small loads were due to slight misalignments of the assembly and the testing machine, and is ignored in the following analysis. Young's modulus is defined for the elastic region, *i.e.* for loads small enough to avoid permanent deformation of the material. Therefore, only the slope of the linear region is of interest here.

Given a sample's cross-section, A, and length L, we can calculate the Young's modulus of elasticity, $E \equiv \Delta\sigma\Delta L/L$, from the measured load curves. Using the definition of stress, $\sigma \equiv F/A$:

$$E = \frac{L}{A}\frac{\Delta F}{\Delta L}\,, \tag{2.8}$$

where $\Delta F/\Delta L$ is the slope of the linear region from the load curves. The resulting modulus of elasticity in compression and tension respectively are given in table 2.4.

Visual inspection of the tension test samples showed that the glue failed before the samples failed for both G10 and epoxy. A more important conclusion, however, is that the

[†]A NEXYGEN LRXplus-5K single column testing machine.

Figure 2.10: A picture of the G10 (green) and Epoxy (yellow) rod samples used for the tension test. The compression test samples were plain rods without any end caps.

	G10 tension (tension)	Epoxy (tension)	G10 (compression)	Epoxy (compression)
Rod diameter (mm)	6.0	6.0	6.0	6.0
Free length (mm)	128.6	127.2	215.1	215.4
Glued (yes/no)	yes	yes	no	no
Steel cap diameter (mm)	6.5	6.5	-	-
Steel cap length (mm)	19,0	19,1	-	-

Table 2.3: Dimensions of compression and tension test samples.

glue appears to have had an effect on the overall modulus of elasticity in tension. This can be seen by comparing the results from the tension tests with the data from the manufacturer: both the epoxy and G10 rods were found to have a lower value of E_T than was expected. The measured values of E_C, however, are similar or even exceeds the values provided by the manufacturer.

When we estimated the total deflection of the assembly, we assigned a single value for the modulus of elasticity rather than one for tension and another for compression. This simplification made the analysis much easier and by choosing the lowest of the two values, E_C, an extra safety margin was naturally added to the results. Although the compression and

	G10 (measured)	Epoxy (measured)	G10 (literature)	Epoxy (literature)
E_T (GPa)	22.4	30.2	35.5	49.6
E_C (GPa)	15.0	27.0	14.5	18.0

Table 2.4: Measured modulus of elasticity in comparison with data from manufacturer.

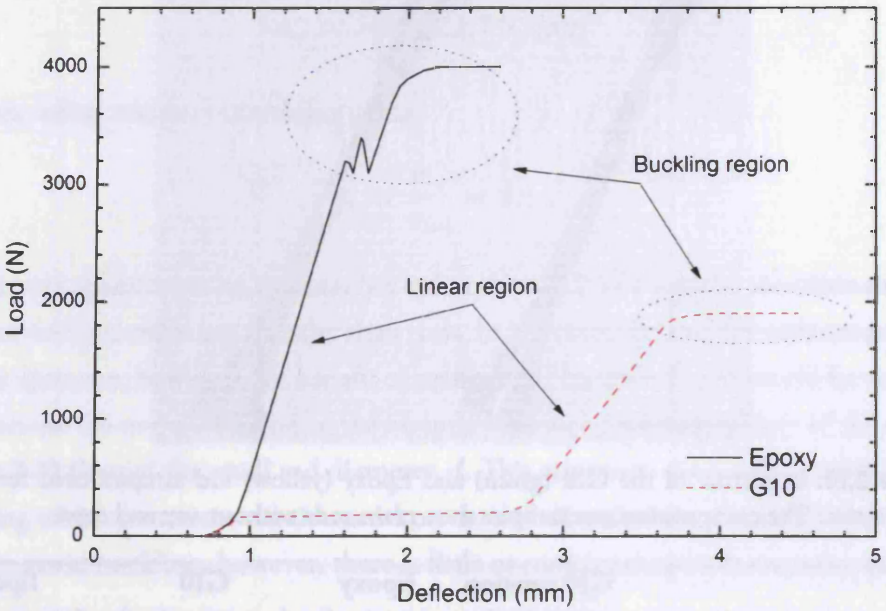

Figure 2.11: G10 and epoxy compression test results

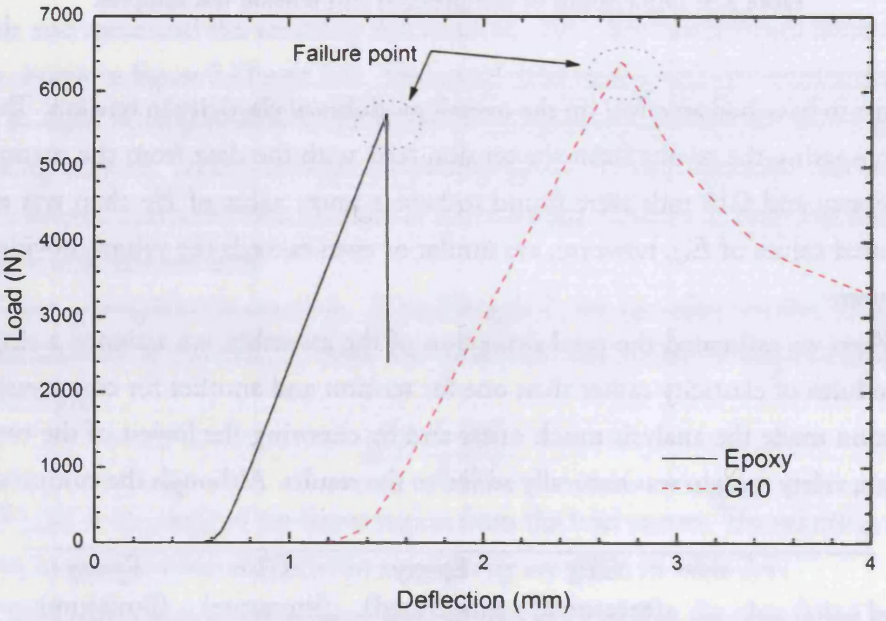

Figure 2.12: G10 and epoxy tension test results

tension tests showed that E_T was reduced as a result of the glue, E_T was always found to be larger than E_C. We can therefore conclude: since we used E_C in both analytical calculations as well as in the FE analysis, it was safe to ignore the effect of the glue.

2.3 SORPTION COOLERS

The double stage ^{3}He-^{4}He sorption cooler, discussed in section 1.3.3, was integrated with the PTC cryostat. The performance of this system is critical to the operation of the dilution refrigerator; a thermal model of the sorption cooler is therefore a very useful diagnostic tool. In this section we develop a very simple model and compare it with experimental results in order to investigate what limits the performance of our sorption coolers. We will limit our analysis to the capacity of the pumping lines; the capacity of the charcoal pumps are far more complicated to model and would require detailed (and commercially sensitive) information about their internal design.

2.3.1 PUMPING SPEED

The fundamental design and operation of sorption coolers has already been described in section 1.3.3. Here we describe the pumping system of sorption coolers together with some useful expressions for estimating their performance. More details about pumping speed and conductance in the molecular flow regime can be found elsewhere [61].

The conductance F of a pumping line is defined as

$$F \equiv \Phi/(P_1 - P_2)\,, \tag{2.9}$$

where P_1 and P_2 are pressures at the upstream and downstream end of the system respectively. The volumetric throughput, Φ, is defined as $\Phi \equiv P\,\mathrm{d}V/\mathrm{d}t$, where $\mathrm{d}V/\mathrm{d}t$ is the volume of gas crossing a plane perpendicular to the flow per unit time, and P is the pressure at which the flow rate is measured. For most cryogenic applications, however, the mass flow Φ_m is a more convenient quantity than the volumetric flow. If the gas is assumed to be ideal, then

$$\Phi = k_B T \dot{N} = \Phi_m \frac{k_B T}{m}\,, \tag{2.10}$$

where $\dot{N}$ is the flow rate in molecules per second, and m is the molecular mass. The units of Φ_m is then g/s. In the molecular flow regime, where the mean-free path of the molecules is greater than the dimension of the pumping line, the conductance of a straight cylindrical

tube of radius r, length l and temperature T is given by [62]

$$F = \frac{4r^3}{3l}\sqrt{\frac{2\pi k_B T}{m}}. \tag{2.11}$$

Although it is possible that the gas flow in ^{3}He refrigerator is not strictly molecular, the conductance given by the equation 2.11 always gives the lower limit. That is, if we use this equation to design our refrigerator we can be sure that the cooling power will be slightly larger than what we have estimated. Equation 2.11 is only valid for long tubes, that is for $l \gg r$, but as will be described in the next section, this can be corrected for in simple way.

For a section of tube at constant temperature, equations 2.9, 2.10 and 2.11 yields

$$\Phi_m = \frac{4r^3}{3l}\sqrt{\frac{2\pi m}{k_B T}}\,(P_1 - P_2)\,. \tag{2.12}$$

If both the temperature and the pressure are allowed to vary along the tube, then [62, 63]:

$$\Phi_m = \frac{4r^3}{3l}\sqrt{\frac{2\pi m}{k_B}}\left(\frac{P_1}{\sqrt{T_1}} - \frac{P_2}{\sqrt{T_2}}\right). \tag{2.13}$$

In general, the pumping lines in a ^{3}He refrigerator looks like in figure 2.13. If the gas flow is in a steady state, then Φ_m will be the same throughout the whole series and equation 2.13 can be used for each section of tube

$$\begin{aligned}
\frac{P_0}{\sqrt{T_0}} - \frac{P_1}{\sqrt{T_1}} &= A\frac{l_1}{r_1^3} \\
\frac{P_1}{\sqrt{T_1}} - \frac{P_2}{\sqrt{T_2}} &= A\frac{l_2}{r_2^3} \\
&\vdots \\
\frac{P_{n-1}}{\sqrt{T_{n-1}}} - \frac{P_n}{\sqrt{T_n}} &= A\frac{l_n}{r_n^3},
\end{aligned}$$

where $A = \frac{3}{4}\Phi_m\sqrt{k_B/(2\pi m)}$. Finally, by adding all these equations together, only the terms involving the pressure and temperature at the extreme ends of the entire pumping line remain [63]:

$$\frac{P_0}{\sqrt{T_0}} - \frac{P_n}{\sqrt{T_n}} = A\sum_{i=1}^{n}\frac{l_i}{r_i^3}. \tag{2.14}$$

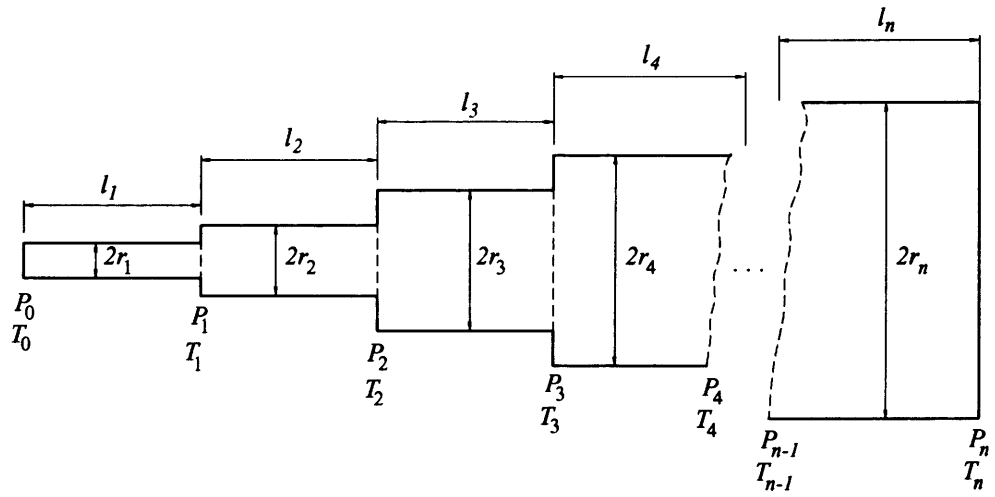

Figure 2.13: Schematic of a typical system of pumping lines in an evaporation cryostat. The diameter of each section should increase towards the higher temperature end to accommodate for the expanding gas.

2.3.2 THERMAL MODEL

We will now apply the general equations above to our sorption coolers. In order to do this, we first need to make an important modification to take into account the small geometries of our system. In a ^{3}He sorption cooler, the pumping line can be split into three sections; a first section from the evaporator to the vapour-cooled heat exchanger, a second from the heat exchanger to the base plate and a third from the base plate to the cryopump. Each one of these tubes is too short for the $l \gg r$ approximation used above to be valid. Fortunately, there is an easy way to deal with this problem. Let F_t be the conductance calculated using equation 2.11. The actual conductance of the tube is then given by [62]

$$F = \frac{3l}{8a} K_f F_t \,, \tag{2.15}$$

where K_f is the Clausing's factor which takes into account the effect of short tubes. The Clausing's factor is given by [64]

$$K_f(x) = \frac{0.98441 + 0.00466x}{1 + 0.46034x} \,, \tag{2.16}$$

where $x = l/r$. Following the same steps as above, we find the corresponding equation to 2.14, this time without the $l \gg r$ approximation:

$$\frac{P_0}{\sqrt{T_0}} - \frac{P_n}{\sqrt{T_n}} = B \sum_{i=1}^{n} \frac{1}{K_f(l_i/r_i)\, r_i^2} \,, \tag{2.17}$$

Pumping line sections	Length (mm)	Diameter (mm)	Thickness (mm)	Nr. tubes
Evaporator - Heat exch. 1	62	2.4	0.125	3
Heat exch. 1 - Heat exch. 2	44	4.7	0.125	1
Heat exch. 2 - Base plate	75	3.15	0.125	2
Base plate - Charcoal pump	105	4.0	0.175	1

Table 2.5: Dimensions of the sorption cooler's pumping line. There are two thermal breaks between the evaporator and the base plate; we refer to the colder and hotter one of these breaks as heat exchanger 1 and heat exchanger 2 respectively. Notice that some sections consist of two or three tubes in parallel.

where $B = 2\Phi_m\sqrt{k_B/(2\pi m)}$. To estimate the requirements on the pumping lines we have to assume an ideal pump, which means approximating $P_n/\sqrt{T_n} \simeq 0$. This may appear to be a rather modest approximation since the temperature of the charcoal pump, T_n, is much higher than the temperature of the evaporator, T_0, and P_n is presumably lower than P_0. We will soon return to this assumption and show that it is not as trivial an assumption it may seem. By rearranging equation 2.17, we find that the pumping lines have to be designed in such a way that:

$$\sum_{i=1}^{n} \frac{1}{K_f(l_i/r_i)\, r_i^2} \leq \frac{P_0}{\sqrt{T_0}B}. \tag{2.18}$$

The required cooling power of our sorption coolers was 200 μW which corresponds to $\Phi_m = 2.2 \times 10^{-5}$ g/s at $T_0 = 0.4$ K, and the vapour pressure of ^{3}He gives $P_0 = 3.7$ Pa. The geometric sum on the left side of equation 2.18 therefore has to be $\leq 654\,\mathrm{cm}^{-2}$. As shown in table 2.5, the sorption coolers used in our experiment was designed with a geometric sum of $232\,\mathrm{cm}^{-2}$; the capacity of the pumping lines is therefore significantly higher than what is required.

The lowest achievable temperature and the cooling power can be estimated by assuming a residual heat load, $\dot{Q}_0$, from the pumping lines themselves, wires and 4 K radiation. We estimate the residual heat load to be 22 μW from the pumping lines, 0.9 μW from wires and $\leq$ 1 μW from 4 K radiation. Equation 2.18 was solved numerically[†] to create figure 2.14 (dashed line). In the same figure we have also included the measured cooling power (■) of the sorption cooler.

2.3.3 BEST-FIT OF THERMAL MODEL TO EXPERIMENTAL DATA

The pumping speed of the charcoal pump is determined by the temperature at which the charcoal is operated and the available surface area. Figure 2.15 shows the adsorption isotherms

[†]MathCad 13's ROOT function uses the Ridder and Brent method (see for example Press *et. al.* [65].)

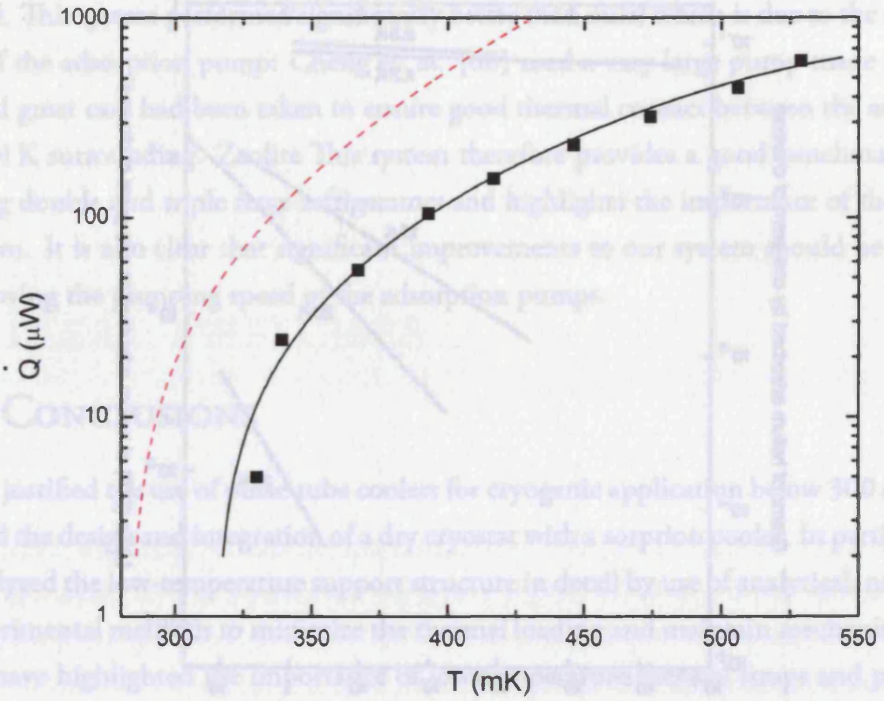

Figure 2.14: Measured cooling power (■), theoretical cooling power assuming an ideal pump (dashed line), and a best fit corresponding to $P_n(T_0) = 2.83P_0(T_0)$. The theoretical calculations assume $\dot{Q}_0 = 24\ \mu W$.

of ^{3}He on activated charcoal. It is clear from this figure that the charcoal pump should contain approximately 10 g of charcoal per gram of helium. The importance of achieving a good thermal contact between the charcoal and the base plate is also obvious; the charcoal pump will quickly lose in adsorption efficiency at temperatures above 4 K. For example, a mass flow $\Phi_m = 2 \times 10^{-5}$ g/s will result in a heat load on the charcoal pump of the order of $\Phi_m/L_3 \simeq 300\ \mu W$. This heat is conducted through the heat switch to the base plate. It is however not just the on-conductance of the heat switch which determines the temperature of the charcoal: the thermal contact between the charcoal and the heat switch relies on the thermal conductivity of the vapour and the charcoal itself, both of them are rather poor conductors. Therefore, the temperature of the charcoal is probably significantly greater than the temperature one measures with a thermometer attached to the charcoal pump. This is the most likely explanation of why the measured cooling power is significantly smaller than the theoretical estimate.

It is difficult to estimate the pumping speed of the charcoal pump without further information about the temperature of the charcoal inside the pump. It is, however, possible to fit equation 2.17 to the measured cooling power by adjusting the value of P_n. It turns out that the best result is achieved if P_n is allowed to be a function of the mass flow of gas. Since the temperature of the evaporator, T_0, is also a measure of the mass flow, we choose $P_n =$

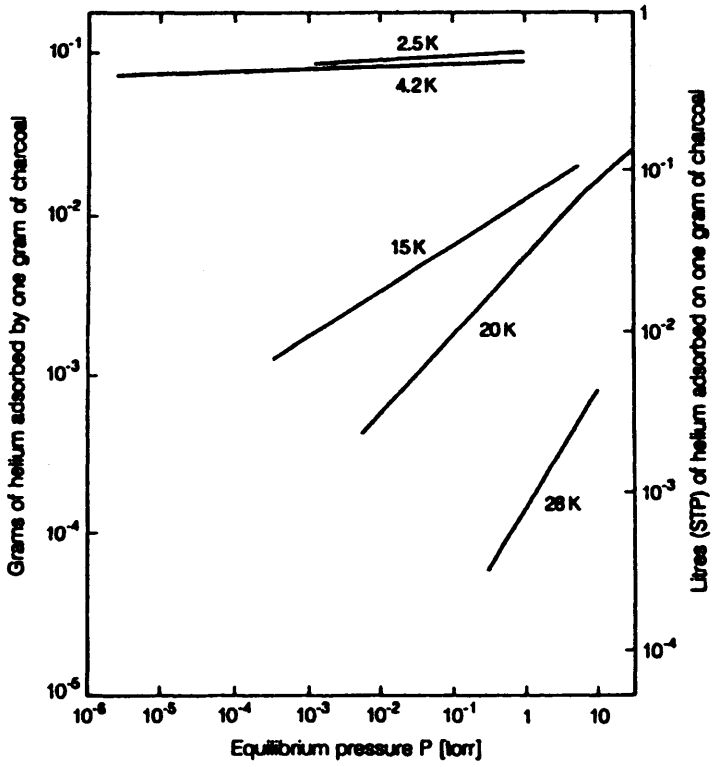

Figure 2.15: Adsorption isotherms of ^{3}He on activated charcoal as a function of the helium-gas pressure. [25]

$P_n(T_0)$. The solid line in figure 2.14 represents such a best fit where $P_n(T_0) = 2.83P_0(T_0)$. We now see that the assumption $P_n/\sqrt{T_n} \simeq 0$ from above is not representative of a real system. Indeed, it is clear that the mass flow through the system must be more than an order of magnitude lower than that of which the pumping lines are capable. Therefore, the performance of these coolers is limited by the pumping speed of the charcoal pump, not by the pumping conductance of the tubes. Of course, there are two factors contributing to the elevated temperature of the charcoal: the thermal impedance between the charcoal and the pump, and the thermal impedance of the heat switch connecting the pump to the 4 K base plate. In our experiment, the temperature of the pump was approximately 1 K hotter than the base plate with a heat load of 0.5 mW to the evaporator. Although it seems more likely that the thermal impedance between the charcoal and the pump is dominating here, a better heat switch may improve the situation slightly.

The pumping speed of various adsorption pumps have been measured [66, 67] for the purpose of optimizing the performance of ^{3}He coolers. A single stage ^{3}He cooler [68], designed to test the practical limits of sorption coolers, reached 190 mK and achieved a cooling power of 600 μW at 255 mK when operated from a base temperature of 1.56 K. From a base temperature of 4.2 K, it reached 225 mK with zero heat load and 270 mK at 600 μW

heat load. This system performed significantly better than ours, which is due to the different design of the adsorption pump: Cheng *et. al.* [68] used a very large pump made from zeolite, and great care had been taken to ensure good thermal contact between the adsorbent and the 4 K surrounding. Zeolite This system therefore provides a good benchmark when designing double and triple stage refrigerators and highlights the importance of the pumping system. It is also clear that significant improvements to our system should be possible by improving the pumping speed of the adsorption pumps.

2.4 CONCLUSIONS

We have justified the use of pulse-tube coolers for cryogenic application below 300 mK, and described the design and integration of a dry cryostat with a sorption cooler. In particular we have analysed the low-temperature support structure in detail by use of analytical, numerical and experimental methods to minimize the thermal loading and maintain mechanical rigidity. We have highlighted the importance of low-temperature thermal straps and presented important measurements on their performance in various configurations.

A thermal model for predicting the cooling power of ^{3}He sorption coolers have been discussed and compared with experimental results. We have shown that such coolers are limited by the pumping speed of the charcoal pump, and that the most likely explanation to this is the thermal impedance between the charcoal and the outside of the pump, and between the pump and the 3 K base plate. A comparison of our measurements with other systems suggest that significant improvements on the existing design should be possible. As we shall see in chapter 4, such improvements could also benefit the performance of the condensation pumped dilution refrigerator.

3 Heat Switches

In this chapter, a selection of heat switches which could be used for operation below 1 K will be discussed. Based on the requirements for operating the MDR in a continuous mode, we will argue that the gas-gap heat switch is the most feasible option. A number of different gas-gap heat switches were built and tested in the temperature range from 300 K to 300 mK and the results are compared with a theoretical model. We also discuss problems associated with excessively long switch-off times, and present a design which has proven particular successful.

In addition to the need for a gas-gap heat switch for operation with the MDR, it is also essential to have a heat switch for pre-cooling of large thermal loads. A novel design of such a heat switch will be described, and experimental results obtained from a prototype is presented. It distinguishes itself from any existing design in that it offers an unprecedented short distance between the conductors. We also suggest a more advanced version of this prototype which has great potential for many applications.

3.1 Introduction

As was discussed in section 1.4, our design of a miniature dilution refrigerator requires two heat switches to allow each of the two sorption coolers to be recycled independently of the other. It is crucial that each sorption cooler can be recycled without degrading the performance of the system as a whole. This places a number of requirements on the performance of the heat switches:

1. Considering the cooling power of the sorption cooler (chapter 2: figure 2.14) and the condensation efficiency (chapter 4: figure 4.16), the on-conductance should be at least 5 mW/K in order to ensure a reasonable ^{3}He circulation rate. This would correspond

to a temperature difference of 40 mK with 200 μW heat load. With a still power $P_S = 200$ μW, the condenser will operate at 470 mK.

2. A low off-conductance is required to allow one sorption cooler to recycle without a significant increase of the condenser temperature. A reasonable target is 10 μW/K. This would correspond to an increased heat load on the condenser of approximately 10% during the recycle period where the cold head warms up to a temperature as high as 5 K.

3. The heat switch must be able to switch between on and off-states on a reasonable time-scale. Given a duty cycle of about 8 h and a recycle time of about 2–3 h, the switch-off time should be limited to about an hour or so.

4. Thermal loading on the cold head due to operation of the heat switch must be negligible in comparison with the overall heat load. Heat dissipation or conductive loading should be limited to about 10–20 μW.

In principle there are four potential candidates for the heat switch: mechanical, superconducting, gas-gap or the liquid-gap heat switch. The mechanical heat switch has the obvious advantage of a zero off-conductance, but is limited in its applicability by a rather poor on-conductance. The gas-gap and the liquid-gap heat switches on the other hand both benefit from a very high on-conductance but have the disadvantage of a rather high off-conductance. The off-conductance of a gas-gap heat switch can however be made negligible if designed properly and carefully machined. The superconducting heat switch can, in some applications, be very powerful with both a high on-conductance and low off-conductance. Its main disadvantage is usually a rather impractical design with large magnetic fields which would require shielding.

3.2 OVERVIEW OF DIFFERENT HEAT SWITCH TECHNOLOGIES

In this section we give a brief description of different heat switch technologies in order to find the most suitable choice for our application. Section 3.2.4, on mechanical heat switches, also contains an important discussion on metal contact impedances which is referred to repeatedly elsewhere in this thesis.

3.2.1 SUPERCONDUCTING HEAT SWITCHES

A superconducting heat switch consists of a magnet coil and a metal strip, operating at a temperature below its superconducting transition temperature, T_c. With zero magnetic

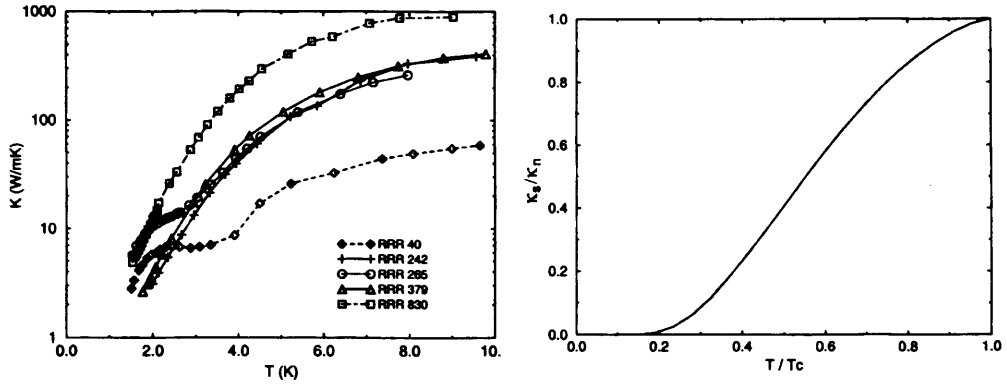

Figure 3.1: Measured thermal conductivity of superconducting Niobium (left) and the thermal conductivity ratio as a function of the reduced temperature (right) [74].

Material	T_c (K)	B_c (mT)	Type
Aluminium (Al)	1.18	10.5	I
Niobium (Nb)	9.3	198	II
Titanium (Ti)	0.39	10	I
NbTi	10	15000	II
Zinc (Zn)	0.85	5.3	I
Lead (Pb)	7.2	80.3	I
Indium (In)	3.4	20	I
Tin (Sn)	3.7	22	I

Table 3.1: Superconducting transition temperatures and critical fields for a number of metals suitable for use in superconducting heat switches.

field, the heat switch is in its superconducting off-state. The heat transport through the metal strip is dominated by phonons and is therefore very low, at least for $T \ll T_c$. A current through the solenoid generates a magnetic field, just large enough to drive the metal into its normal state. Therefore, the ratio of the normal thermal conductivity, κ_n, to the superconducting thermal conductivity, κ_s, is a figure of merit of how suitable a material is as a heat switch. Since thermal transport is dominated by electrons in the normal state and by phonons in the superconducting state: $\kappa_n/\kappa_s \propto 1/T^2$. For example κ_n/κ_s for Indium and Lead below 1 K have been measured to $26/T^2$ K^2 and $34/T^2$ K^2 respectively [69, 70]. Aluminium [71, 72] and Zinc [73] have also been used in many heat switches.

In order to allow the two sorption coolers to recycle independently, the heat switch has to remain in its superconducting state at a temperatures as high as 5 K. This means that only Nb, NbTi or Pb could be used (table 3.1). Being a type II superconductor, NbTi has a very high critical field† and would therefore require an impractically large magnet.

†In table 3.1 the maximum critical field, $B_c(0)$, is given. The actual critical field is a function of temperature: $B_c(T) = B_c(0)\,[1 - (T/T_c)^2]$.

Unfortunately it turns out that neither Niobium nor Lead are particular useful at such high temperatures. For example, figure 3.1 shows the measured Niobium thermal conductivity and κ_s/κ_n for different values of RRR[†]. It is clear that, even for temperatures around $T_c/2$, the thermal conductivity remains rather high. Although Lead has a steeper κ_s gradient [75], it also has a lower T_c which, in the end, makes Lead no more useful than Niobium at 5 K.

We conclude that, due to the required temperature range of operation, the on-off ratio would be unacceptably low for any superconducting heat switches.

3.2.2 GAS-GAP HEAT SWITCHES

The gas-gap heat switch utilisers the high vapour pressure of ^{3}He gas at low temperatures to create a thermally conducting medium in between two conductors. The gas pressure inside the switch is controlled by an external charcoal pump with a heater. Such heat switches have been designed for a large number of applications [76–79] and are particular useful in the high-temperature regime where the mean-free path is much shorter than the distance between the conductors. In the low-temperature regime, where the mean-free path is limited by the vapour pressure curve, their efficiency drops significantly. However, it is relatively easy to compensate for this by simply increasing the surface area of the conductors, thus gas-gap heat switches have been used for operation down to 0.4 K [80–82] and in passive mode (see section 3.5) down to 0.25 K [83].

The real advantage of the gas-gap heat switch is its simplicity and reliability: no moving parts, no magnetic field and an operation procedure which is easily computer automated. On the downside, they will usually suffer from a rather high off-conductance associated with the metal (stainless steel or titanium) shell which separates the two conductors. For our application, however, the thermal path through the shell can be intercepted by means of a thermal link to an intermediate stage: for example, the still provides hundreds of micro-Watt of cooling power at 0.7 K which can be used to effectively eliminate the residual load through the tube. Alternatively, a low conductivity dielectric such as Vespel^{TM} tube could be used [83]. The on and off-conductance of these switches will be discussed in more detail in section 3.3.

3.2.3 LIQUID-GAP HEAT SWITCHES

The basic design of a liquid helium heat switch is essentially the same as for the gas-gap heat switch. For operation at temperatures around 2 K, one can take advantage of superfluid

[†]The Residual Resistivity Ratio, RRR, is the ratio between the 300 K and 4 K electrical conductivity. It is used as a measure of the material purity: the higher RRR, the purer material.

^{4}He as a conducting medium instead of ^{3}He gas. Close to T_λ, the thermal conductivity of the superfluid is extremely high, and even exceeds that of very pure copper down to temperatures around 0.5 K. However, the very small vapour pressure of ^{4}He would make it virtually impossible to switch off when operated at temperatures below 1 K. Therefore, the usefulness of these switches is limited to the temperature range 1–2.2 K. A number of such heat switches have been described in literature [77, 79, 84].

For temperatures below 0.5 K, liquid ^{3}He could be used. Unfortunately, its thermal conductivity (7×10^{-3} Wm^{-1}K^{-1} at 0.4 K [85]) is nowhere near as high as that of ^{4}He; in fact, it is about an order of magnitude below that of stainless steel. At 0.4 K, the thermal conductivity of liquid ^{3}He is, however, still a factor of two larger than gaseous ^{3}He.

There are two main concerns about a liquid ^{3}He heat switch. Firstly, it may take a very long time to switch off due to the temperature of operation. More importantly though, to condense and cool the required amount of liquid would dissipate a significant amount of heat. The required on-conductance could be met using a distance between the conductors of 0.5 mm and a surface area of 5 cm^2, which would give a total liquid volume of 250 mm^3. Condensing this amount of liquid would dissipate at least 0.2 J. It is not straightforward to control the condensation accurately enough to make this dissipation negligible (it would have to take about an hour). Despite this, the liquid ^{3}He heat switch must be considered as a possible candidate: for example, if the distance between the conductors could be made very small, the amount of liquid and thus the dissipated heat could be reduced. In section 3.5, we show a method for minimizing the distance between the conductors which, in principle, also could be used to realize a liquid ^{3}He heat switch.

Only one reference to a liquid ^{3}He heat switch has been found in literature – Roach *et. al* [82] found that the on-conductance of their switch (tested down to 1 K) was about a factor of 3 below that you would expect from thermal conductivity measurements. They conclude that other factors of the design (such a solder joints) may play an important role and that the final result is not necessarily much better than what can be achieved using ^{3}He vapour. At temperatures around 0.3 K, the Kapitza resistance (see section 4.3.3)is also likely to play an important role.

3.2.4 MECHANICAL HEAT SWITCHES AND THERMAL CONTACT RESISTANCE

In a mechanical heat switch, physical contact between two metals is maintained or broken by an externally applied force. In general, large clamping forces can be applied manually from outside the cryostat. Such heat switches have been very common in applications which require a zero off-conductance and/or pre-cooling of large thermal loads: for example, Calorimetry (heat capacity measurements) and the operation of an ADR. Since the

on-conductance is limited by thermal impedance of a pressed metal contact, mechanical switches are less effective at low temperatures. For our purpose, the operation also has to be reliable and fully automatic. Before we discuss the design of a mechanical heat switch and evaluate its suitability for our application, we give a brief description of the thermal impedance in metal-metal contacts. This discussion is important, not only for mechanical heat switches, but for the design of almost any cryogenic system.

The thermal contact resistance is attributable to several factors, the most notable being that contact between two surfaces is made only at a few discrete locations rather than over the entire surface area. This is supported empirically by findings that the thermal conductance of pressed contacts is dependent upon the applied force and not on the area of contact nor on the apparent contact pressure [86]. As the applied force is increased, surface deformation of the material occurs. The initial area of contact increases and, as the material deforms further, contact occurs at new locations. Additionally, the presence of oxides contributes to the phenomenon since an oxide layer generally adds to the thermal resistance. At low temperatures, each oxide layer acts as an additional boundary resistance, and the problem is compounded because of the acoustic mismatch between the layers (Kapitza resistance). Further, the thickness of the oxide layer is often a function of time. Estimating the contact resistance from theoretical models [87, 88] is not a trivial task since the actual area of contact must be calculated, hence most data in the field are empirical.

Copper, aluminium and brass contacts are improved if the samples are gold plated [89, 90]. Gold prevents oxidation and because it is soft, it also deforms more easily and thus helps to increase the surface area. It is common to first deposit a layer of nickel on the copper substrate before depositing the gold; this is because gold bonds better to nickel than it does to copper. Any such interposers should however be avoided since an additional metal interface will create a small temperature gradient and make the thermal contact worse. At liquid helium temperatures, a thin layer of indium or Apiezon^{TM} grease can help to improve the contact [91]. In the case of a bolted metal-metal contact, where the force is generally very high, and at low temperatures (below 4 K) the conductance would be dominated by the transports of electrons. In such a situation it is not necessarily a good idea to apply grease or other dielectrics since they could only improve the phonon transport and may actually impede the electron transport [92]. At temperatures below 2 K, the best contacts are made from bolted, flat, clean and gold plated copper parts. Indeed, it is claimed that for such a 'dry' joint the resistance can be almost as small as a bulk, continuous part [41]. In conclusion, dielectric interposers may improve a poor (phonon dominated) contact at temperatures above 2 K but will most likely make matters worse in a good (electron dominated) contact a lower temperatures.

The best mechanical heat switches for operation above 2 K appear to be made of soft In-Cu contacts [93]. The conductance of such switches show a $T^{2.5}$ dependence, suggesting a phonon-dominated thermal transport. At 2 K and below, Cu-Cu and Au-Au contacts have shown better performance with electron-dominated $T^{1.4}$ contacts [94]. A linear temperature dependence of Au-Au joints has also been reported [95]. The Cu-Cu measurements by Berman et. al. [94] also showed that the load dependence is not necessarily linear:

$$G = 60 \times 10^{-6} L^{0.75} T^{1.4} \tag{3.1}$$

where L is the load in kg applied at room-temperatures, and G the thermal conductance in W/K. According to equation 3.1, a clamping force of several kN would be required to meet our criteria. This is a very large clamping force, and at least an order of magnitude higher than what is used in most designs described in literature. To make matters worse, the conductance is known to decrease by about a factor of 3 when the joint is opened and closed at cryogenic temperatures [93]. A large clamping force is also more likely to cause problems with vibrations and heat dissipation as it opens and closes.

We conclude that, although an advanced design of a mechanical heat switch could probably meet our requirements, liquid and gas-gap heat switches appear to be easier and more reliable technologies. We chose to focus on the latter option, mainly because of concerns regarding heat dissipation, but also because other authors [82] have suggested that a liquid-gap heat switch does not perform significantly better than a gas-gap.

3.3 THERMAL MODEL OF THE GAS-GAP HEAT SWITCH

3.3.1 MEAN-FREE PATH

Gas conduction is divided into three different regimes: molecular, laminar and a transition region between the two. With the distance between the conductors, δ, and the mean-free path, l, they are defined as:

$l/\delta < 0.01$ In the laminar region, the conductivity is nearly independent of pressure. This is generally the preferred region for operation of gas-gap heat switches as it offers the highest conductance.

$0.01 < l/\delta < 1$ The transition region is difficult to model and one generally has to extrapolate from the two other regions.

$l/\delta > 1$ In the molecular (or Knudsen) region the conductivity of the gas is proportional to pressure. We will also refer to it as the low-temperature region, as it only becomes

important at temperatures where the SVP (saturated vapour pressure) curve puts an upper limit to the pressure of the gas[†].

The mean-free path is given by

$$l = \frac{k_B T}{\sqrt{2}\pi d^2 P}, \tag{3.2}$$

where d is the molecular diameter and P is pressure. Figure 3.2 shows the mean-free path of the ^{3}He molecules in a heat switch. At high temperatures, the mean-free path is of course constant since the molar density (proportional to P/T) is constant in a heat switch. However, at temperatures below 0.7 K, the molar density will decrease rapidly since the vapour pressure puts an upper limit to the number of molecules in the vapour phase. Machining tolerances and assembling procedures restrict δ to somewhere between 0.1 mm and 0.5 mm. In general, a heat switch operating at 0.3–0.4 K will therefore always be in the transition region where the thermal conductivity is difficult to estimate.

3.3.2 HEAT TRANSPORT IN THE LAMINAR REGIME

The thermal conductivity is defined by

$$\boldsymbol{J} = -\kappa \nabla T, \tag{3.3}$$

where $\boldsymbol{J}$ is the heat current density. In the laminar regime, and at moderate pressures, the thermal conductivity relates to the viscosity, η, as

$$\kappa = \frac{1}{3}\rho v l c_v = \eta c_v, \tag{3.4}$$

where v is the average velocity, ρ is the density and $c_v = 3R/2$ for a monoatomic gas. Viscosity measurements of helium gas can therefore be used to get accurate values of the thermal conductivity. To take into account that the molecules have a distribution in velocity and that not only the reference molecule but also all others are in motion, one has to introduce a extra coefficient:

$$\kappa = \epsilon \eta c_v, \tag{3.5}$$

[†]Although vapour and gas are frequently used interchangeably, there are important differences between the two. Firstly, vapour refers to gaseous matter in a state of equilibrium with identical matter in a liquid or solid state below its boiling point. More importantly though, the ideal gas approximation is actually not valid for a vapour since the phase is close to its condensation point. Despite this, we will follow what appears to be common practise and apply the ideal gas approximation for heat switches even when the pressure is close to the SVP .

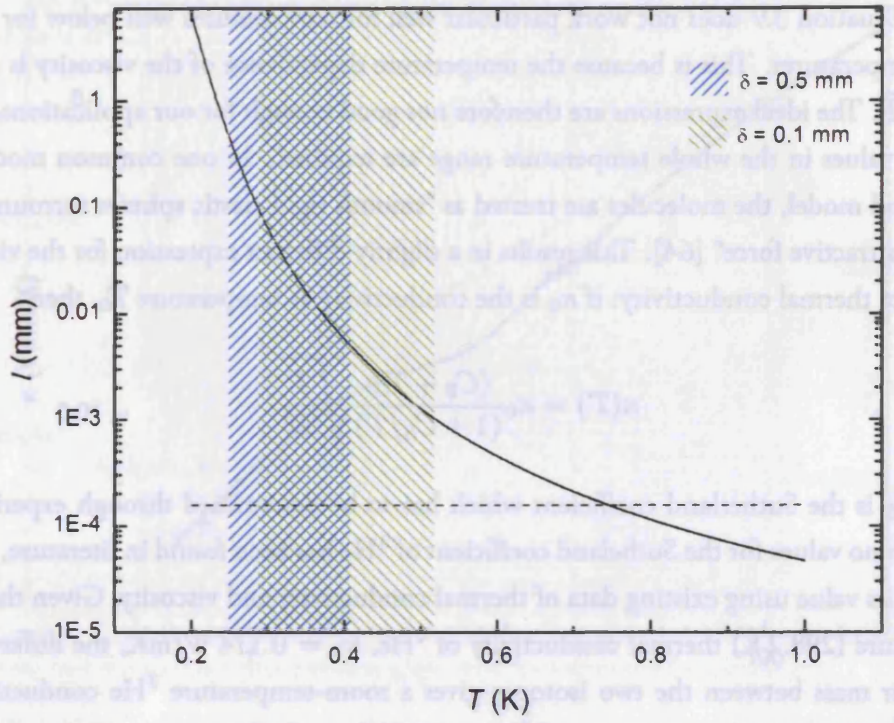

Figure 3.2: At temperatures below 0.7 K, the mean-free path increases exponentially (solid line) due to the decreasing vapour-pressure of ^{3}He. At higher temperatures it is constant (dashed line). The shaded areas illustrate the transition regions for a heat switch with $d =$ 0.5 mm and $d = 0.1$ mm respectively.

where $\epsilon = (9\gamma - 5)/4$ [61]. For a monoatmic gas, the heat capacity ratio $\gamma = 5/3$, hence $\epsilon = 2.5$.

Of course, the thermal conductivity can also be expressed explicitly by assuming a Boltzmann distribution of particles with mass m and mean velocity

$$v = \sqrt{\frac{8k_B T}{\pi m}}. \tag{3.6}$$

Inserting equations 3.6 and 3.2 in 3.4, and using $\rho = P/RT$ gives

$$\kappa(T) = \epsilon \frac{1}{d^2} \sqrt{\frac{k_B^3 T}{\pi^3 m}}. \tag{3.7}$$

This shows that $\kappa \propto \sqrt{T}$ and independent of pressure. This equation is qualitatively correct but does not consider non-ideal molecular interactions. To make it agree with the room temperature conductivity of ^{4}He (0.174 W/mK), we have to choose $d = 1.93$ Å.†

†The molecular diameter varies depending on how it is calculated or how it is measured: Dushman [64] gives values for the helium ranging from 1.69 Å to 2.66 Å.

Equation 3.7 does not work particular well for temperatures well below (or above) room-temperatures. This is because the temperature dependence of the viscosity is not actually $\sqrt{T}$. The ideal expressions are therefore not good enough for our applications, where accurate values in the whole temperature range are required. In one common model, the Sutherland model, the molecules are treated as "smooth rigid elastic spheres surrounded by fields of attractive force" [64]. This results in a slightly different expression for the viscosity, and hence thermal conductivity: if κ_0 is the conductivity at temperature T_0, then

$$\kappa(T) = \kappa_0 \frac{(C_S + T_0)}{(1 + C_S/T)} \sqrt{\frac{T}{T_0^3}} \tag{3.8}$$

where C_S is the Sutherland coefficient which has to be determined through experiments. Although no values for the Sutheland coefficient of ^{3}He has been found in literature, we can estimate its value using existing data of thermal conductivity and viscosity. Given the room temperature (298.2 K) thermal conductivity of ^{4}He, $\kappa_0 = 0.174$ W/mK, the difference in molecular mass between the two isotopes gives a room-temperature ^{3}He conductivity of $\kappa_0\sqrt{4/3}$. Viscosity measurements of ^{3}He at 20 K from Becker *et. al.* [96] provide the low-temperature data through equation 3.5. Using equation 3.8, the Sutherland coefficient could be then determined to $C_S = 7.95$. Quantum mechanical effects will influence the molecular interaction at the low-temperature end, and so the Sutherland model can not be used below 10 K or so. See Fokkens *et. al.* [97] for experimental data and a discussion of the theory at low temperatures. Figure 3.3 shows the thermal conductivity of ^{3}He in the whole temperature range (between 4 K and 20 K, a more or less arbitrary interpolation has been applied).

Figure 3.3 will provide the basis for calculating the on-conductance in the laminar regime. However, the molecular regime also has to be considered in order to define a complete model for gas-gap heat switches.

3.3.3 HEAT TRANSPORT IN THE MOLECULAR REGIME

The thermal conductance is defined as $G \equiv \kappa A/\delta$, where A is the surface area of the conductors. In the molecular regime, where κ is ill-defined, it can be estimated using [81, 98]

$$G = \frac{A\alpha}{4} \frac{\gamma + 1}{\gamma - 1} \sqrt{\frac{2R}{\pi MT}} P, \tag{3.9}$$

where M is the molar weight and $\alpha \leq 1$ is the accommodation coefficient. The value of α varies depending on the materials, surface conditions and temperatures. For example,

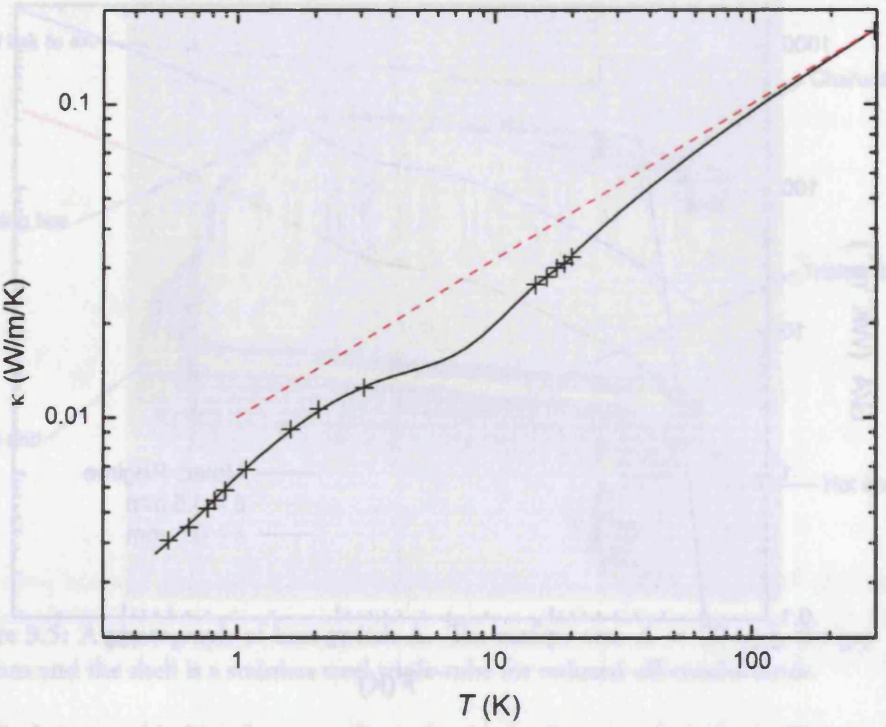

Figure 3.3: Thermal conductivity of ^{3}He gas. Measured conductivity data below 4 K [97], data around 20 K calculated from measured viscosity [96], and room-temperature data calculated from measured ^{4}He conductivity [64]. The ideal-gas conductivity with $\kappa \propto \sqrt{T}$ is also included for comparison (dashed line).

when estimating the conduction through the residual gas in a liquid helium cryostat, the upper limit is $\alpha = 1/3$ [99]. But at much lower temperatures, a monolayer of helium may cover most of the surfaces and in which case, $\alpha \approx 1$ [81]. The temperature of the gas, T, is ill-defined since there is no chance for the molecules to thermalize. Nevertheless, since the temperature difference between the conductors is generally small, we will approximate T with the average temperature of the two conductors.

In figure 3.4, we have plotted G/A for both laminar and molecular regions (using $\alpha = 1$ in equation 3.9). It represents the theoretical limit of any gas-gap heat switch since the Kapitza resistance and conductor impedances are not included. The dotted lines illustrate the corresponding transition regions, given by figure 3.2. Note how the conductance in the molecular region is independent of δ.

3.3.4 OFF-CONDUCTANCE

In general, the off-conductance of a gas-gap heat switch is limited by three factors: (i) conduction through the stainless steel shell, (ii) conduction through any residual gas and (iii)

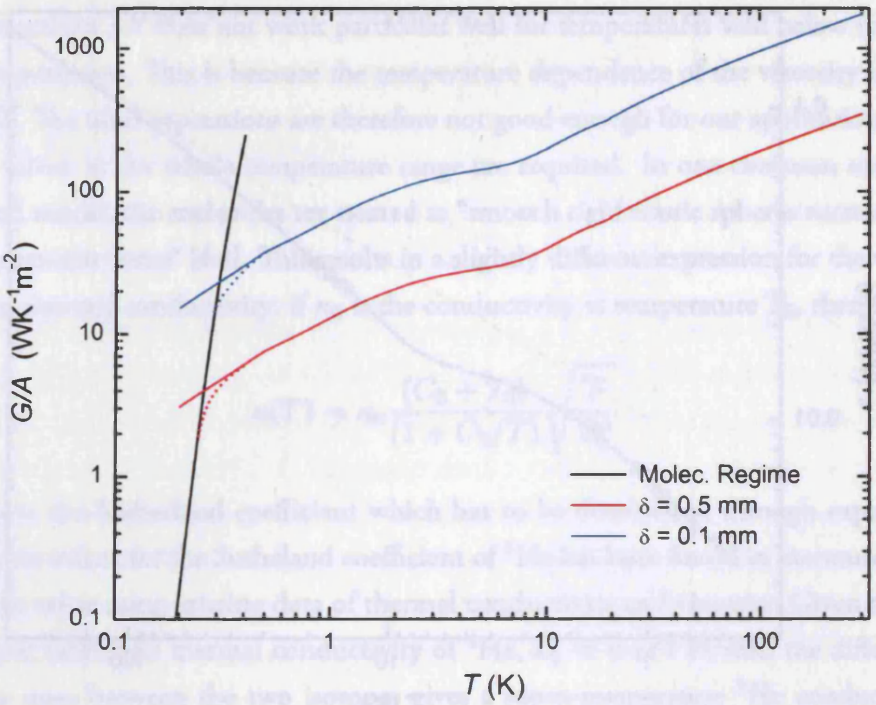

Figure 3.4: Thermal conductance divided by the surface area of an ideal heat switch. Solid lines are calculated values in the molecular region and the laminar region, dotted lines indicate the transition regions.

thermal radiation. For heat switches operating below 4 K, the thermal radiation is negligible and if the heat switch is properly switched off, so should the conduction through any residual gas. Thus, the off-conduction of the heat switch is given by

$$G_{\text{off}} = \frac{A_{\text{T}}}{L_{\text{T}}(T_1 - T_0)} \int_{T_0}^{T_1} \kappa_{\text{SS}}(T)\, dT\,, \tag{3.10}$$

where A_{T} is the tube cross-section, L_{T} the tube length, T_0 the cold end temperature, T_1 the hot end temperature and κ_{SS} the thermal conductivity of stainless steel.

3.4 A HEAT SWITCH FOR OPERATION BELOW 0.5 K

3.4.1 DESIGN

We have built and tested a number of heat switches between 0.3 K and 4 K. They were all built with cylindrical conductors and $\delta \simeq 0.5$ mm, with surface areas ranging between 4 cm^2 and 20 cm^2. Some of them had a shell made from a single stainless steel tube, whilst others had a 'triple-tube' (tube-in-tube) to reduce the off conductance. Here we will only consider the most advanced version (figure 3.5) with the largest surface area (20 cm^2) and a

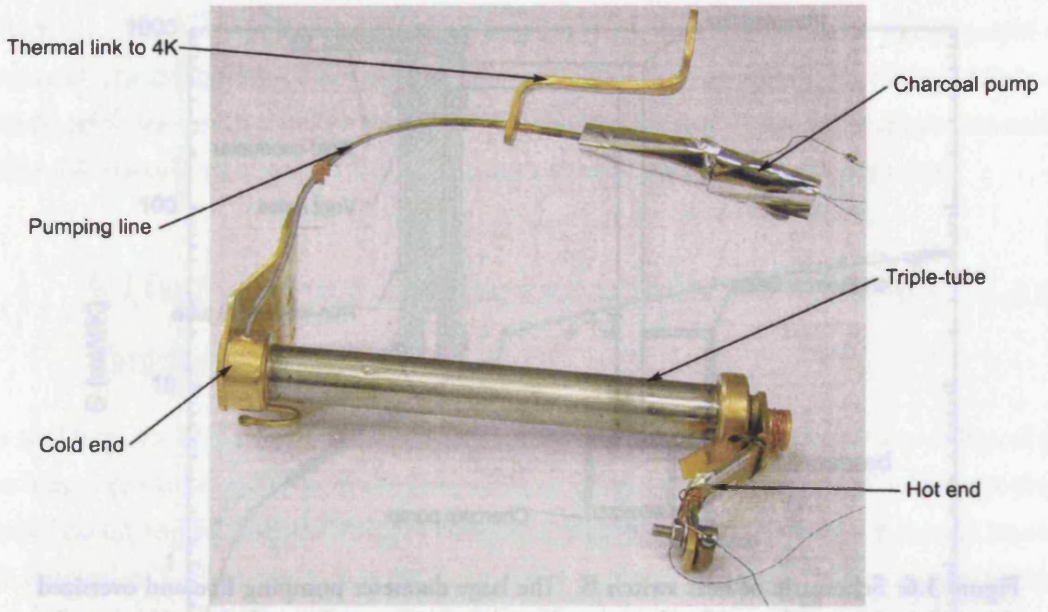

Figure 3.5: A photograph of heat switch 𝔸. The surface area $A = 20\,\mathrm{cm}^2$, the gap $\delta = 0.5\,\mathrm{mm}$ and the shell is a stainless steel triple-tube for reduced off-conductance.

triple-tube: 120 mm long $\varnothing 12 \times 0.1\,\mathrm{mm}^2$. The pumping line, a 10 cm long $\varnothing 2 \times 0.2\,\mathrm{mm}^2$ stainless steel capillary, connects the cold end of the heat switch to a charcoal getter. From now on we will refer to this design as heat switch 𝔸.

It quickly became apparent that the main problem with all the heat switches we tested was not to meet the required on-conductance, but to turn them off on a reasonable time-scale. It proved extremely difficult to ensure that all the ^{3}He inside the heat switch was pumped out. For this reason, we tried a number of different designs of the charcoal pump. The 'standard' design was a single pellet ($\sim$ 40 mg) of charcoal inside a small copper cylinder. We increased the amount of charcoal from one to two pellets, and following suggestions from Smith *et. al.* [80] we also sliced the pellets up into small sections. To ensure a better thermal contact, the charcoal was also glued to the inside of the pump using Stycast 1266.

The problems associated with the residual gas inside the switch eventually forced us to compromise the on-conductance, and instead build a switch specifically designed for minimizing the switch-off time. In this design, referred to as heat switch 𝔹 and shown in figure 3.6, the internal impedance and the pumping impedance were reduced by: (*i*) increasing the distance between the conductors to $\delta = 1\,\mathrm{mm}$, (*ii*) introducing 'vent holes' in the conductors, (*iii*) increased the pumping line diameter to 9 mm, and (*iv*) using an oversized ($\sim$ 400 mg) charcoal pump. Rather than trying to achieve the on and off- conductance requirements, this heat switch was built to find out wether or not it was at all possible to evacuate the switch completely at 0.4 K

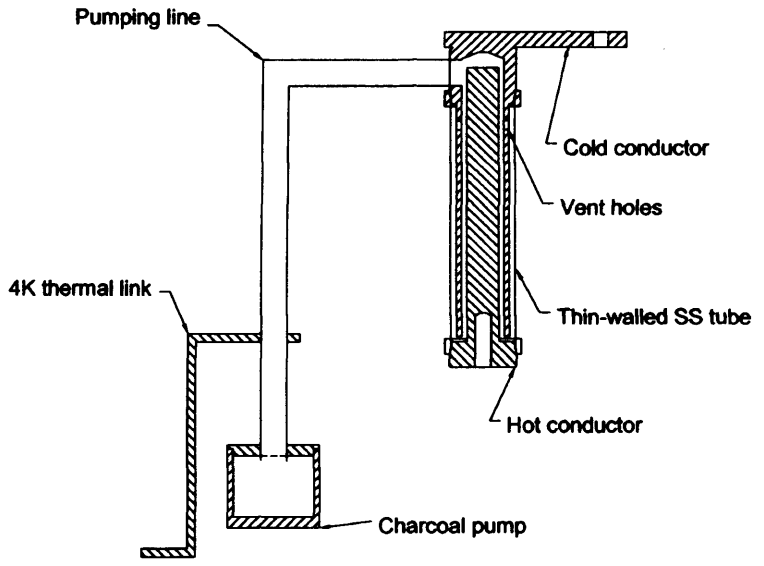

Figure 3.6: Schematic of heat switch 𝔹. The large diameter pumping line and oversized charcoal pump together with a large conductor separation and vent holes minimizes the pumping impedance.

3.4.2 EXPERIMENTS

A double stage ^{3}He-^{4}He CRC sorption cooler was integrated with a CryoMech PT405 pulse-tube cooler. To avoid any serious temperature gradient close to the 'hot' thermometer, the heater (a 20 kΩ resistor) was mounted on a separate copper block and then bolted to the heat switch. This allows the heater to be properly heat-sunk on a safe distance from the thermometer. In order to eliminate the lead resistance, the heater is wired with three leads. Ruthenium-Oxide thermometers were used, calibrated against a Lakeshore germanium thermometer (see Appendix B for a discussion on low-temperature thermometry).

The system was first cooled to 0.9 K using the ^{4}He side of the sorption cooler. To make sure no residual gas is present in the heat switch, an off-conductance test was carried out before the on-conductance test. Once the on-conductance test was finished, the system was left to warm up to 4.2 K to ensure any residual gas is pumped out from the heat switch. This may appear to be an excessive precaution but, as will be obvious from the discussion of our results, residual gas may be prevalent at temperatures as high as 2 K. The system was then cooled to 0.3 K using the ^{3}He side of the sorption cooler. Again, the off-conductance test was carried out before the on-conductance test.

A simple way to test the switch-off time is to leave the switch at 0.3 K with a small power applied to the heater. Due to the very small heat capacity of the conductors at these temperatures, the hot end of the heat switch quickly warms up to a temperature given by its off-conductance. We used this method to study the performance of both heat switch 𝔸 (using two different charcoal pumps) and heat switch 𝔹.

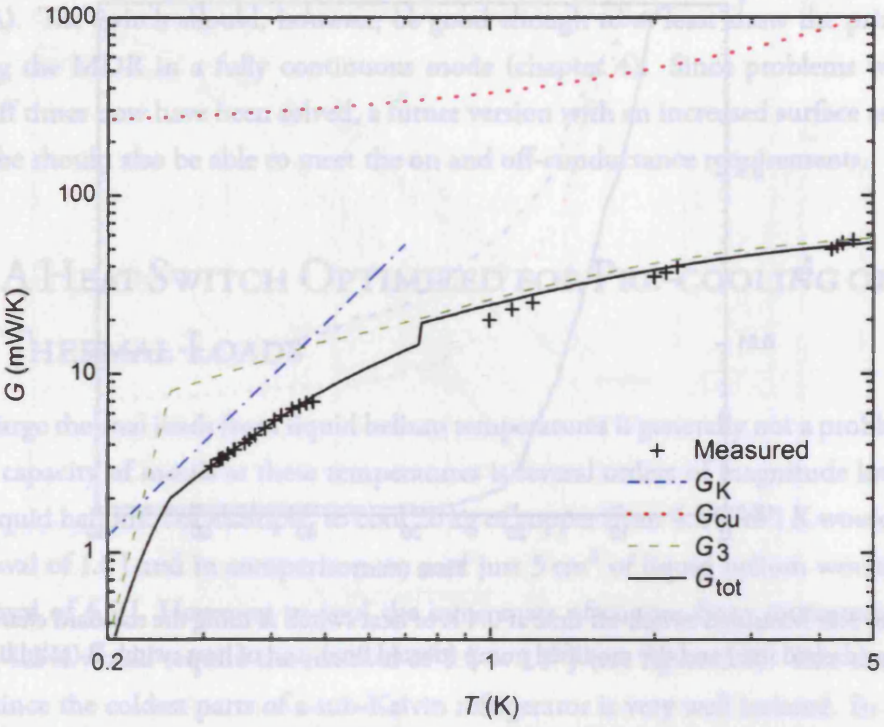

Figure 3.7: The contribution to the overall conductance (solid line) from ^{3}He gas (dashed line), copper conductors (dotted line) and Kapitza resistance (dash-dotted line).

3.4.3 Results

The measured on-conductance of heat switch 𝔸 as a function of the average conductor temperature is shown in figure 3.7. In order to make the data fit the theoretical curve in the low-temperature end, we have had to assume that a thin layer of ^{3}He covers the surfaces of both conductors. This means that Kapitza resistance will be prevalent at temperatures below 0.7 K where some of the gas has condensed (figure 3.2). The contribution to the overall conductance, G_{tot}, from the ^{3}He gas, G_3, the copper conductors, G_{cu}, and Kapitza resistance, G_K, are also shown. The overall conductance is given by: $G_{tot}^{-1} = G_3^{-1} + G_{cu}^{-1} + G_K^{-1}$. The Kapitza coefficient was used as a free parameter to make the data below 0.7 K fit the thermal model; this way the Kapitza coefficient was determined to be $a_K = 0.0065\,\mathrm{K^4m^2/W}$, which is in reasonable agreement with measurements from literature [85]. At 0.4 K, we have $G_{tot} = 5.5$ mW/K which meets the requirement for operation with the MDR.

The off-conductance of 𝔸 at 0.4 K was measured to 0.9 μW/K, slightly higher than the theoretical value of 0.7 μW/K. This is most likely because of uncertainties in the shell thickness or in the thermal conductivity values of stainless steel. Together with the measured on-conductance, we find an on/off ratio at 0.4 K of about 6100. The off-conductance, measured with the hot end at 5 K and the cold end at 0.4 K was measured to 6.4 μW/K (theoretical value is 5.0 μW/K) which also meets our requirements.

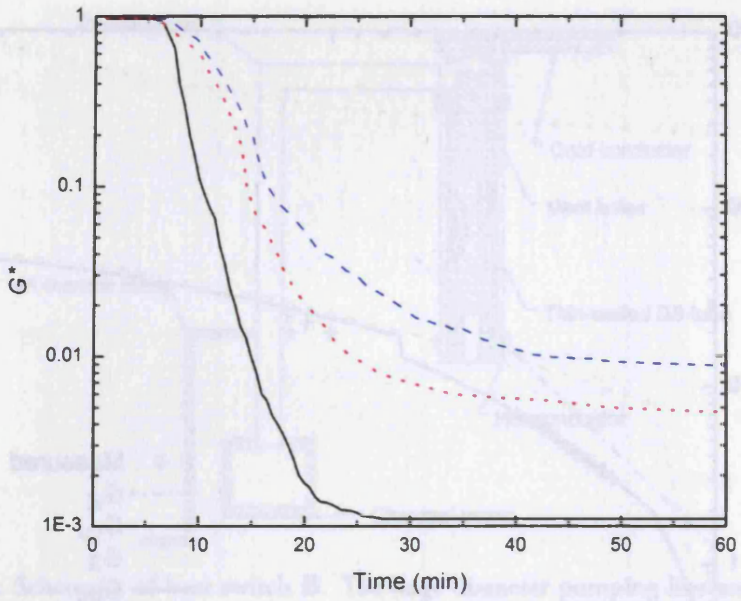

Figure 3.8: Measured switch-off time at 0.4 K of heat switch 𝔸 using the standard charcoal pump (dashed line) and the modified pump (dotted line), and of heat switch 𝔹 (solid line).

Heat switch 𝔸 never switched off properly. With its original charcoal pump, the off-conductance was limited by the residual gas even after 4–5 hours. When we installed a larger pump in which we had sliced each charcoal pellet into thin discs and glued them to the inside wall of the pump using Stycast 1266, we noticed some improvement. However, if the cold end was heated up, it was obvious that a significant amount gas was still inside the switch, probably adsorbed on the conductor and then released as it warmed up. If the conductor was allowed to warm up from 0.4 K to 2 K, the conductance increased by more than a factor of 10.

Heat switch 𝔹 with its reduced impedance and larger pump performed significantly better — its conductance was virtually identical to the measured off-conductance after less than 30 min. Figure 3.8 shows how the conductance decreases with time for the different designs. Since heat switch 𝔸 and 𝔹 have different on and off-conductance, the measured conductance, G, has been normalized by: $G^* = (G - G_{ss})/G_0$, where G_{ss} is the conductance of the stainless steel shell and G_0 is the conductance measured just before it is being switched off. This way, $G^* = 0$ corresponds to a perfect off state and $G^* \simeq 1$ to its on state.

Even switch 𝔹 showed some sign of residual gas inside it: when the conductor was warmed up from 0.4 K to about 2 K, the off-conductance increased by about 50%. Therefore, unless the charcoal pump can be operated at a temperature below 3 K, it seems unlikely that a gas-gap heat switch will be able to switch off completely. Neither the on-conductance, nor the off-conductance of heat switch 𝔹 are good enough to meet our requirements for operation with the MDR (they were both found to be about a factor of two worse than heat

switch A). The switch should, however, be good enough to at least show the principle of operating the MDR in a fully continuous mode (chapter 4). Since problems with long switch-off times now have been solved, a future version with an increased surface area and a triple-tube should also be able to meet the on and off-conductance requirements.

3.5 A Heat Switch Optimized for Pre-cooling of Large Thermal Loads

To cool large thermal loads from liquid helium temperatures is generally not a problem since the heat capacity of metals at these temperatures is several orders of magnitude lower than that of liquid helium. For example, to cool 20 kg of copper from 4.2 K to 1 K would require the removal of 1.8 J and in comparison, to cool just 5 cm^3 of liquid helium would require the removal of 6.9 J. However, to cool the same mass of copper from room temperature down to 4.2 K would require the removal of 1.5×10^6 J (see figure 3.9). This can be very tedious since the coldest parts of a sub-Kelvin refrigerator is very well isolated. In sorption coolers of the kind described in chapter 2, the heat transport at high temperatures relies on the rather inefficient circulation of gas within the cooler itself. In general, some kind of heat switch must be used to help in cooling down a large mass. For example, the CMB experiment QUAD uses a passive gas-gap heat switch with cylindrical conductors; even so it takes 6–7 days to cool the 10 kg heavy focal plane from room temperature to liquid helium temperatures.

One common way to speed up the pre-cooling is to use a mechanical heat switch. For example, SCUBA2 uses such a switch, operated manually from outside the cryostat. Passive gas-gap heat switches [83] (with cylindrical conductors) for operation down to 0.25 K are now also under development for use with continuous ADR systems [38].

In a passive gas-gap heat switch there is no control of the charcoal temperature. Instead of using an external pump, the charcoal is simply glued inside the shell onto the hot conductor. As the hot end cools and reaches a temperature below about 11 K, the gas is adsorbed and the heat switch automatically switches off.

In an attempt to shorten the cooling down time without compromising the simplicity and automatic operation of the gas-gap heat switch, we have built and tested a new type switch specifically designed for cooling large thermal loads. The conventional gas-gap design with cylindrical conductors and a large surface area has the disadvantage of a relatively large, typically 0.3–0.5 mm, conductor separation. It is difficult to decrease the distance between the conductors much further since the machining of the parts and soldering the

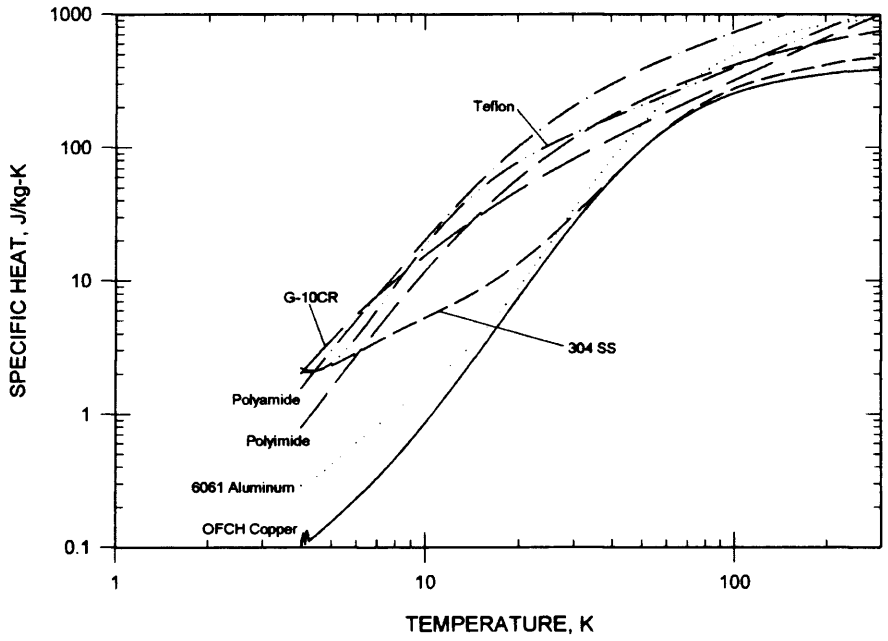

Figure 3.9: Specific heat of some common material. [58]

assembly together becomes significantly more difficult. It is however possible to take a different approach to this problem and minimize the distance between the conductors but pay less attention to the surface area.

3.5.1 DESIGN

Figure 3.10 (a) shows the principle schematic of a heat switch in which the distance between the conductors is created as a result of the different thermal expansion coefficients of copper and stainless steel. At room temperatures, the two conductors are in contact with each other but will separate as the system cools down. With the dimensions given in figure 3.10 (a), the distance between the conductors will be less than 30 μm at 4 K (figure 3.11 shows how the distance varies as a function of temperature). Such a short distance would be practically impossible to achieve with cylindrical conductors, thus a surface area $0.5/0.03 \simeq 17$ times smaller than in a conventional heat switch is required to achieve the same on-conductance. Of course, the surface area can easily be increased without compromising the simplicity of the design too much; either by simply extending the base conductor or by using two rod-shaped conductors with several slots, as shown in figure 3.10 (b). The two conductors could easily be manufactured from a single copper rod, for example by wire roding. This way the tolerances could be met easily, and a large number of 'teeth' could be introduced; the on-conductance would then be limited by the copper conductors even at LHe temperatures.

It is easy to see how the distance between all contact surfaces in (b) will be the same

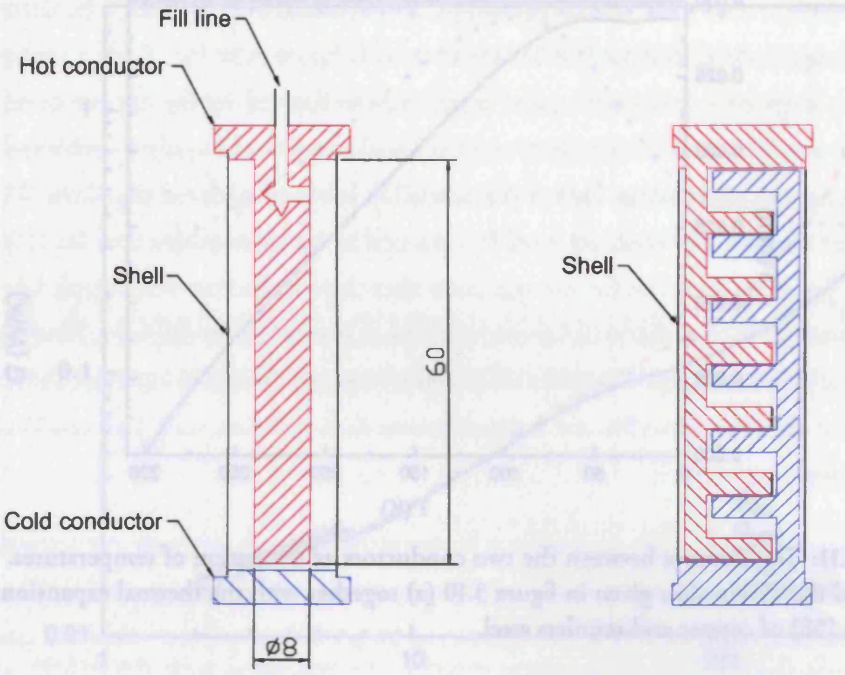

(a) Prototype (b) Advanced version

Figure 3.10: Schematics of thermal contraction gas-gap heat switches. Figure (a) shows the prototype built and tested during this project, and figure (b) shows a more advanced conductor design which takes better use of the full height of the heat switch.

as in (a) as the system cools down. Of course, a conductor separation too small would not be beneficial since the mean-free path of the helium molecules would become longer than the distance between the conductors. However, in accordance with figure 3.2, the mean-free path is less than 1 μm so the criteria of $l \ll d$ is easily fulfilled; it would be enough to fill the heat switch with a room-temperature pressure of 1 atm.

We have built a first prototype, figure 3.10 (a), to show the suitability of this design, and to compare it with our thermal model. If the heat switch assembly was soldered together, the conductor distance would be bigger than that given in figure 3.11 since the materials would expand when they are heated up. Although this could be avoided by using a vice to prevent the assembly from expanding during the soldering phase, we chose a safer and easier option: the copper conductors and the shell were simply glued together using Stycast, cured at room temperature. Of course, such an assembly is unlikely to survive repeated thermal cycling since the different thermal expansion coefficients will eventually crack the glue. For our purpose, however, a single thermal cycle would be enough in order to demonstrate the feasibility of the design. We tried two different types of glue: Stycast 1266 and Stycast 2850 FT. Both of them are commonly used in cryogenics; the former is slightly stiffer and clear in colour, whilst the latter contains carbon making it softer and black. The heat switch was

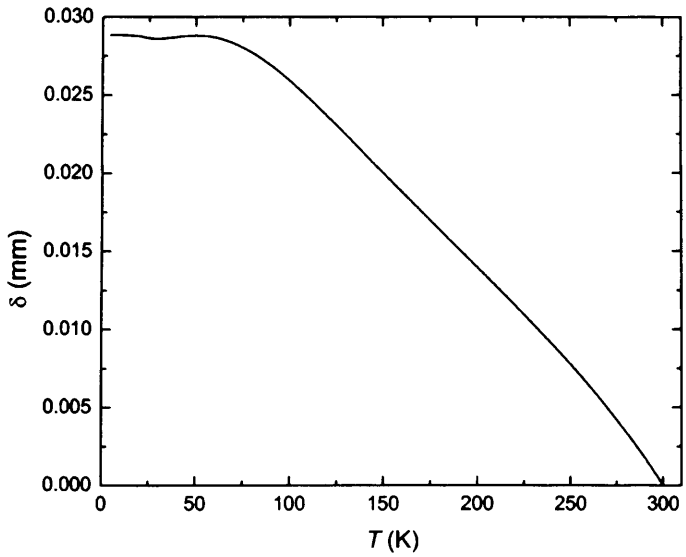

Figure 3.11: The distance between the two conductors as a function of temperatures. We have used the dimensions given in figure 3.10 (a) together with the thermal expansion coefficients [58] of copper and stainless steel.

charged at room temperature with 1 atm of ^{3}He gas.

3.5.2 EXPERIMENTS

The heat switch was mounted in a liquid helium cryostat together with a heater on the hot end of the switch and one thermometer at each end. The thermal on-conductance was measured at 300 K, 77 K (LN_2), 4.2 K (LHe) and 2 K (pumped LHe). The thermometers were silicon diodes, calibrated against a Lakeshore RhFe sensor. The heater, a 1 kΩ resistor operated in a three-wire configuration, was used in the whole temperature range. The same experiment was performed twice. In between the two measurements, the heat switch was cycled 10 times between room temperature and LHe temperatures in order to check the tolerance of the glue to thermal shocks.

3.5.3 RESULTS

The measured conductance as a function of the average conductor temperature is shown in figure 3.12. The contribution to the overall conductance, G_{tot}, from the ^{3}He gas, G_3, and the copper conductors, G_{cu}, are also shown. The overall conductance is given by: $G_{\text{tot}}^{-1} = G_3^{-1} + G_{\text{cu}}^{-1}$. The heat switch was tested down to 2 K, a temperature too high for any of the gas to condense, thus Kapitza resistance can be ignored in the following analysis.

In order to make the data fit the thermal model at 300 K we have had to assume a room-temperature separation of 5 μm. This is a very realistic value considering that the

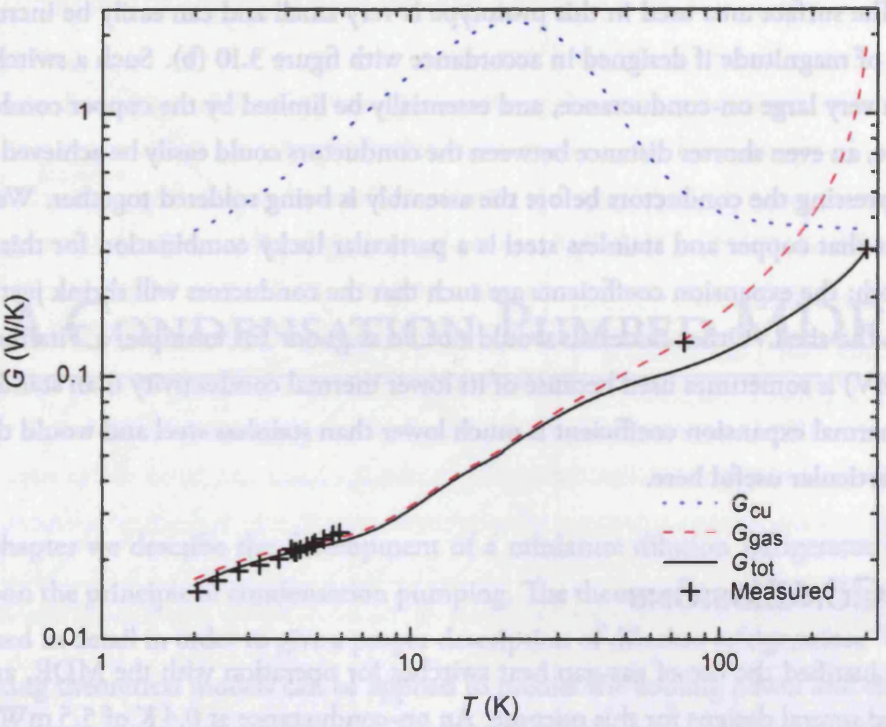

Figure 3.12: Measured conductance and contributions to the overall conductance from ^{3}He gas and copper conductors. As one would expect, the room-temperature conductance is limited by the thermal conductivity of copper, whilst the low-temperature conductance is given by that of ^{3}He.

conductor surfaces are not perfectly flat. Another minor parameter was necessary to tweak in order to make the theoretical curve match the low-temperature end: the surface area was increased from 0.5 cm^2 to 0.55 cm^2. This too can be explained by assuming the effective surface area to be somewhat larger than the theoretical area — basically, the hot conductor in figure 3.10 (a) actually sees a slightly larger area than what has been assumed. With the exception of the 77 K data point, the measurements must be considered to be in remarkably good agreement with the theoretical model. In fact, given uncertainties in the thermal conductivity of OFHC copper, it is rather surprising to find such good agreement between measurements and theory at room temperature.

Both Stycast 1266 and Stycast 2850 FT worked well, but it was necessary to apply multiple (4–6) layers of glue to prevent leakage. With a single layer of glue, the assembly developed leaks already after one cycle. Of the two different glues, 2850 FT appeared to work best: small cracks were visible in the 1266 Stycast after a few cycles although they never gave rise to a leak, probably because of the multiple layers. In hindsight, we should perhaps not be surprised to find 2850 FT to be better for this application since it (by design) has a thermal expansion coefficient similar to that of metals.

The surface area used in this prototype is very small and can easily be increased by an order of magnitude if designed in accordance with figure 3.10 (b). Such a switch would achieve a very large on-conductance, and essentially be limited by the copper conductivity. Of course, an even shorter distance between the conductors could easily be achieved by simply compressing the conductors before the assembly is being soldered together. We should point out that copper and stainless steel is a particular lucky combination for this type of heat switch: the expansion coefficients are such that the conductors will shrink just slightly less than the shell. Other materials would not be as good: for example, a Titanium alloy (Ti-6Al-4V) is sometimes used because of its lower thermal conductivity than stainless steel but its thermal expansion coefficient is much lower than stainless steel and would therefore not be particular useful here.

3.6 CONCLUSIONS

We have justified the use of gas-gap heat switches for operation with the MDR, and built and tested several designs for this purpose. An on-conductance at 0.4 K of 5.5 mW/K with an on/off ration in excess of 6000 has been achieved. Although both these values fulfill our requirements, problems with a very long switch-off times prevent these switches from operating satisfactorily. An alternative design, specifically built to eliminate this problem has been tested successfully and demonstrated how the switch-off time can be shortened to less than 30 min.

A novel gas-gap heat switch particular useful for operation in passive mode and for pre-cooling of large thermal loads have been presented. A prototype has confirmed its potential and shown excellent agreement with our thermal model. A more advanced version, which takes better use of the switch geometry in order to increase its surface area, has also been proposed as part of future work.

4 A Condensation Pumped MDR

In this chapter we describe the development of a miniature dilution refrigerator (MDR), based upon the principle of condensation pumping. The theory of liquid ^{3}He-^{4}He mixtures is discussed in detail in order to give a proper description of dilution refrigeration. We show how existing theoretical models can be applied to predict the cooling power and the lowest achievable temperatures of a condensation pumped MDR. Measurements of the cooling power are presented and analysed to estimate the performance of the heat exchangers and the ^{3}He circulation rate. We have also measured the condensation efficiency and how the system performs when tilted. Finally, we demonstrate how the system can be operated continuously below 100 mK by means of two ^{3}He sorption coolers and gas-gap heat switches.

4.1 Introduction

Dilution refrigerators are today the most important cryogenic technology for temperatures between 300 mK and 2 mK. With an unparallel cooling power and a continuous cryogenic cycle, they have become the preferred method of cooling in applications ranging from material sciences and the study of superfluid phenomena to detector development and astronomy. The dilution refrigerator is arguably the workhorse of cryogenics and has been for the last 30 years. Many important improvements have been made since the technology was first proposed, in particular the development of low-temperature heat exchangers which reduce the heat leak to the coldest parts of the system without impeding the circulation rate of ^{3}He. Today the most advanced systems are commercially available from Leiden Cryogenics, but less powerful machines can be purchased from Janis Research Company and Oxford Instruments. Traditionally, the dilution refrigerator requires a liquid helium cryostat for optimal performance. Recently however, it has been shown that very powerful dilution refrigerators can be coupled to pulse-tube coolers to create a cryogen-free operation: for example,

the dilution refrigerator built for SCUBA 2 achieves a cooling power of 20 μW at 25 mK, operating from a CryoMech PT410 [100].

So far, the development of dilution refrigeration has followed a path towards increased cooling power and lower temperatures. Naturally, this has led to rather bulky, complicated and expensive systems mainly suitable for laboratory use. Recent development in low noise detector arrays, primarily for astrophysical applications, will require temperatures below 100 mK with tough constraints on size, weight and reliability. In general, these applications require a cooling power of only a few micro-Watt: for example, the CMB experiment QUAD uses a triple stage sorption cooler which operates at 250 mK with a heat load of approximately 1 μW. Astronomy, and possibly many other, applications could therefore benefit from a dilution refrigerator where the cooling power has been compromised to achieve a system which is more convenient to use, more reliable and still able to reach temperatures below 50 mK.

A particular class of dilution refrigerators, based upon the principle of condensation pumping, was discussed in section 1.4. Due to their limited cooling power, such systems have not attracted much attention in the past. For astronomy applications, where low temperatures are generally more important than high cooling powers, they could potentially become very important. Condensation pumping allows for a naturally continuous cycle of the ^{3}He. As the ^{3}He is cycled internally, large pumping lines and room-temperature pumps are avoided and so the size, weight and complexity of the system is reduced dramatically. In the absence of any fine capillaries, moving parts or cold O-rings, the refrigerator also becomes mechanically very reliable, has no risk of blockages and is unlikely to develop cryogenic leaks.

Several condensation pumped dilution refrigerators have been built in the past [50–56]. However, none of these systems are both cryogen-free and fully continuous in operation.

4.2 THERMODYNAMIC PROPERTIES OF ^{3}HE-^{4}HE MIXTURES

In this section, a general description of liquid ^{3}He-^{4}He mixtures is presented. In particular we discuss the physical reason for why such a mixture separates at low temperatures, and how the limited solubility of ^{3}He in ^{4}He can be explained. Before we discuss how all this relates to dilution refrigerators (section 4.3), we also describe the fundamentals of osmotic pressure.

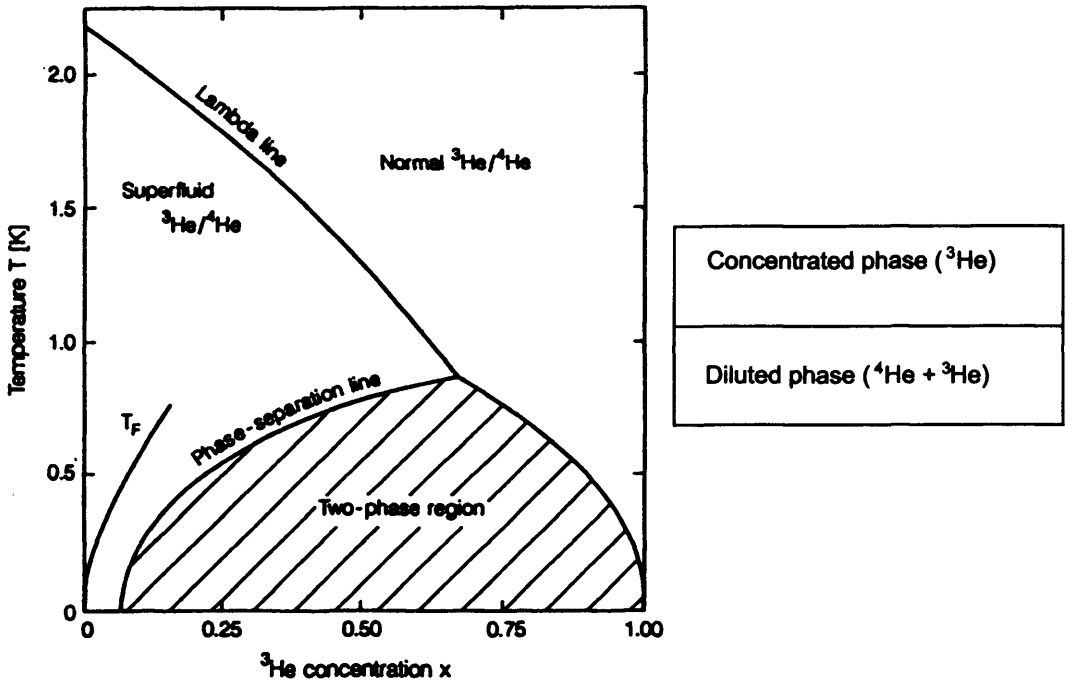

Figure 4.1: ^{3}He-^{4}He phase diagram [41]. As the mixture separates, a ^{3}He rich layer is formed on top of a heavier ^{4}He rich layer. At $T = 0$, the top layer is virtually 100% ^{3}He, whilst the bottom layer contains about 6.6% ^{3}He.

4.2.1 PHASE SEPARATION

At temperatures above 2.2 K, a mixture of liquid ^{3}He and ^{4}He behaves essentially like a classic fluid or in some respect, because of its low density, almost like a classic gas. The total pressure above the liquid is the sum of the ^{3}He and the ^{4}He partial vapour pressures, the specific heat is the sum of the two components and the thermal conductivity is approximately that of pure ^{3}He or pure ^{4}He liquids. At lower temperature though, the picture changes dramatically.

Pure liquid ^{4}He, with a nuclear spin $I = 0$, undergoes a superfluid transition at $T_\lambda = 2.177$ K due to a Bose-Einstein like condensation in momentum space. Pure liquid ^{3}He on the other hand, with $I = 1/2$, is a Fermi liquid and thus obey Fermi statistics and the Pauli principle. This prevents ^{3}He to undergo a superfluid transition until much lower temperatures.[†]

In a mixture with n_3 and n_4 moles of ^{3}He and ^{4}He, the concentration of the two isotopes are expressed as[‡] $x_3 = n_3/(n_3 + n_4)$ and $x_4 = n_4/(n_3 + n_4)$. The Lambda-line in

[†]At 0.94 mK, at saturated vapour pressure, the weak attraction between two ^{3}He molecules allows them to pair up much like two electrons in a metal. This forms a boson particle which then undergoes a transition into a superfluid state.

[‡]We will consistently use subindex 3 and 4 to indicate ^{3}He and ^{4}He quantities, subindex C and D refers to the concentrated and the diluted phase. For example μ_{3D} refers to the partial chemical potential of ^{3}He in the diluted phase.

figure 4.1 shows how the superfluid transition of ^{4}He is suppressed as x_3 is increased. This effect can be understood with a simple model in which the liquid behaves like a mixture of ideal Bose and Fermi gases, suggested by Bennemann and Ketterson (the BK model) [101]. The ideal gas mixture is confined to a more or less constant volume by the cohesive forces between the atoms and with a constant total number density. This model predicts that the Bose condensation temperature varies as $T_\lambda \propto (1 - x_3)^{2/3}$ which is qualitatively similar to T_λ of the real liquid.

As a mixture with $x_3 = 0.5$ is cooled down from $T_\lambda = 1.25\,\mathrm{K}$, it reaches the phase-separation line at 0.75 K. At this point the liquid starts separating which results in a lighter layer of ^{3}He-rich liquid floating on top of the ^{4}He-rich phase. As the temperature decreases further, ^{3}He atoms move from the diluted ^{4}He layer to the concentrated ^{3}He layer. Eventually, at $T = 0$, the concentrated layer contains almost 100% ^{3}He whilst there is a ^{3}He residual of 6.6% left in the diluted phase. If the BK model discussed above was applied, the liquid would never separate at all. A mixture of Ideal Bose and Fermi gases at constant volume would remain mixed even when the entropy $S = 0$ at $T = 0$. This is because the BK model does not take into account the interaction between molecules.

4.2.2 LANDAU–POMERANCHUK THEORY

The Landau-Pomeranchuk (LP) model introduces an effective mass $m_\mathrm{D}^* = m_\mathrm{D}^*(x_\mathrm{D})$ where x_D is the ^{3}He concentration in the diluted phase. The effective mass incorporates the interaction between ^{3}He and ^{4}He atoms, and so the ^{3}He atom can be treated as a quasiparticle which only interacts with other quasiparticles. Thus, the superfluid ^{4}He background acts as a 'mechanical vacuum' which contains the quasiparticles at a pressure equal to the osmotic pressure Π. The osmotic pressure is discussed in section 4.2.3 but for the time being, assume $\Pi \propto x_\mathrm{D}$.

Phenomenologically, the reason for introducing m_D^* can be understood with a classical hydrodynamic model. Here the weak dependence of x_D on m_D^* is ignored. A sphere of volume Ω moving through an non-viscous surrounding with density ρ has an additional mass $\delta m = \rho\Omega/2$ due to the inertia of the back-flow around it. Essentially, δm is a result of the dynamic pressure (or Bernoulli pressure): $\rho u^2/2$ associated with a body travelling at velocity u, but see Ebner [102] for more details. Hence, for a single ^{3}He atom moving through the superfluid ^{4}He:

$$\delta m_3 = \frac{1}{2}\rho_4\Omega_3\,. \tag{4.1}$$

With $\Omega_3/\Omega_4 \approx 4/3$ and $m_4/m_3 = 3/4$ equation 4.1 yields

$$\delta m = \frac{1}{2}\rho_4 \frac{4}{3}\Omega_4 = \frac{2}{3}m_4 = \frac{8}{9}m_3 \Rightarrow m_3^* \approx 1.9 m_3 \,. \tag{4.2}$$

More accurate estimates [103] found $m_3^*(0) = 2.28 m_3$ and $m_3^*(0.066) = 2.4 m_3$. This weak dependence of x_D on m_3^* is due to the interaction between the quasiparticles: as the number density and hence the osmotic pressure increases, the partial volume of ^{3}He decreases more rapidly than that of the ^{4}He solvent.

The explanation to the solubility at $T = 0$ of ^{3}He in ^{4}He is straight forward. Because ^{3}He is the lighter of the two isotopes, it has the largest zero-point motion and will therefore occupy a larger volume. A single ^{3}He atom will therefore find itself closer to its surrounding atoms in the diluted phase, resulting in a larger binding energy. This can also be expressed in terms of the chemical potentials μ_{3C} and μ_{3D} for ^{3}He in the concentrated and diluted phase respectively. Here it is important to distinguish between the chemical potential of pure liquid helium $\mu_3 \equiv G_3 \equiv H_3 - TS_3$ and the *partial* chemical potential $\mu_{3D} = (\partial G_D/\partial n_3)_{T,P}$, where G is the Gibbs function and H is the molar enthalpy. If L_3 is the molar latent heat of vaporization for pure ^{3}He at $T = 0$, then $\mu_{3C} = \mu_3 = -L_3$. Empirically, $L_3/k_B = 2.473$ K. The amount of energy required to remove one ^{3}He atom from the concentrated phase to vacuum is $|\mu_{3C}|/N_A$ where N_A is Avogadro's constant. At $T = 0$ and $x_D = 0$, ^{3}He atoms will move from the concentrated phase to the diluted phase since $\mu_{3D} < \mu_{3C}$.

The first two ^{3}He atoms to cross the boundary will fill the lowest energy state, ϵ_{3D}, with antiparallel spin. Due to the Pauli principle, additional Fermi particles have to occupy increasingly higher states and their relative binding energy will decrease. The Fermi energy $k_B T_F$ depends on x_D. All states with energy smaller than $k_B T_F$ are occupied at $T = 0$, and thus [104]

$$k_B T_F(x_D) = \frac{\hbar^2}{2m_3^*}\left[\frac{3\pi^2 x_D}{v}\right]^{2/3} , \tag{4.3}$$

where v is the average volume per helium atom. Therefore, if both both v and m_3^* are assumed to be independent of x_D, $T_F \propto x_D^{2/3}$.

Eventually, when $\mu_{3C} = \mu_{3D}$, a thermodynamic equilibrium is reached and it is not energetically favorable for more ^{3}He molecules to cross the boundary. This equilibrium, which of course corresponds to a number density of $x_D = 0.066$ is shown in figure 4.2. The chemical potential of ^{3}He, if treated as an ideal Fermi gas at $T = 0$, can be written as

$$\mu_{3D}(x_D) = -\epsilon_{3D}^*(x_D) + k_B T_F(x_D) \,, \tag{4.4}$$

where the effective binding energy, ϵ_{3D}^*, has to be used rather than just the binding energy

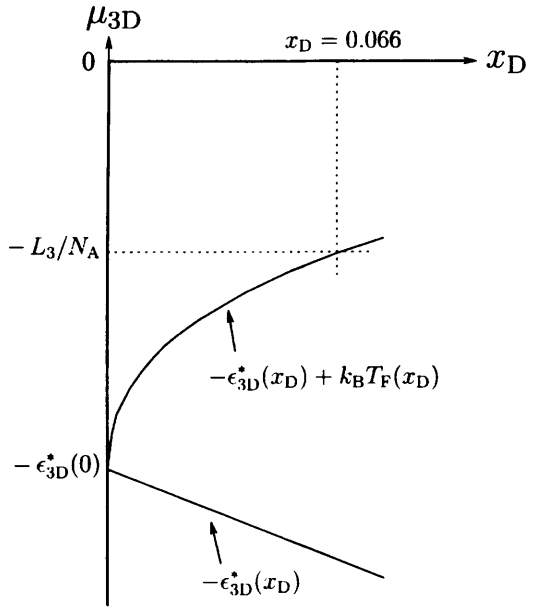

Figure 4.2: Chemical potential of a ^{3}He atom in pure ^{3}He and in a mixture of ^{3}He and ^{4}He as a function of the ^{3}He concentration.

of a single ^{3}He molecule in pure ^{4}He, $\epsilon_{3D}/k_B = 2.785\,\mathrm{K}$. The reason for introducing ϵ^*_{3D} is to take into account the interaction between the quasiparticles. This is necessary since as $x_D \rightarrow 0.066$, the mixture is not sufficiently dilute for the LP theory to strictly apply. By making the following linear assumption, this interaction can be accounted for [105]:

$$\epsilon^*_{3D}(x_D)/k_B \approx \epsilon_{3D}/k_B + (2.3\mathrm{K})x_D\,. \tag{4.5}$$

The importance of the quasiparticle interactions can be seen in figure 4.2; the slope of the bottom line, $-\epsilon^*_{3D}(x_D)$, would be horizontal if this effect was ignored.

The analogy of ^{3}He in diluted ^{4}He could obviously be applied to the ^{4}He atoms in the concentrated phase (Zharkov-Silin theory [106]). Empirically the binding energy of a ^{4}He atom in ^{3}He is $\epsilon_4/k_B = 6.61\,\mathrm{K}$, to be compared with that of pure ^{4}He: $L_4/k_B = 7.16\,\mathrm{K}$. Clearly the binding to ^{4}He is stronger than to ^{3}He. The exponential decrease of the ^{4}He concentration as $T \rightarrow 0$ can be understood if Boltzmann statistics is applied. Although the ^{4}He quasiparticles are presumably bosons, at low temperatures the concentration is extremely low. For Bose-Einstein statistics to apply, the particles must be *indistinguishable*; that is their separation must be small in comparison to their deBroglie wavelength. Due to the low concentration this is not the case, thus they are *distinguishable* so Boltzmann statistics apply. The equivalent expression to equation 4.4 then becomes [107]

$$\mu_4(T, x_4) = -\epsilon_4 + k_B T \log_e \left[(T^*_4/T)^{3/2} x_4\right]\,. \tag{4.6}$$

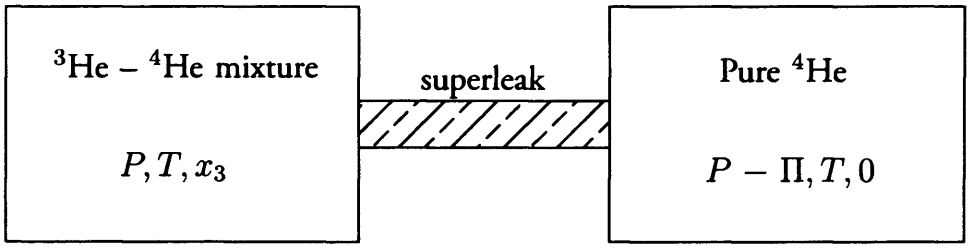

Figure 4.3: Definition of the osmotic pressure $\Pi(P, T, x_3)$. The two vessels are connected by a superleak and have the same ^{4}He chemical potential μ_4. [107]

The temperature T_4^* is defined as (compare with the definition of the Fermi temperature T_F, equation 4.3): $k_B T_4^* = (2\pi\hbar^2/m_4^*)/v^{2/3}$. Equating $\mu_{4C} = \mu_4 = -L_4$ and ignoring the small effect of the osmotic pressure on ^{4}He yields [107]:

$$x_4 = (T/T_4^*)^{3/2} \exp\left[(\epsilon_4 - L_4)/k_B T\right] \simeq 0.85 T^{3/2} \exp\left(-0.56/T\right) . \qquad (4.7)$$

This is the ^{4}He concentration along the right hand side of the phase separation line in figure 4.1.

4.2.3 OSMOTIC PRESSURE

For the understanding of how ^{3}He circulates in a dilution refrigerator, the concept of the osmotic pressure is essential. The definition of the osmotic pressure, Π, at pressure P is illustrated in figure 4.3. The two vessels are connected by a superleak and have the same ^{4}He chemical potential $\mu_4(P, T, x_3) = \mu_4(P - \Pi, T, 0)$. Physically Π corresponds to the pressure of the ^{3}He quasi particle gas and it acts in the same way as the fountain pressure due to phonons and rotons.

If the fountain pressure is ignored, it can be shown (see for example Lounasmaa [85] or Ebner and Edwards [108]) that the osmotic pressure in the diluted liquid is given by:

$$\Pi_D = \frac{1}{v_4} \int_0^{x_{3D}} \frac{x_3}{1 - x_3} \left(\frac{\partial \mu_{3D}}{\partial x_3}\right)_{P,T} dx_3 , \qquad (4.8)$$

where v_4 is the molar volume of ^{4}He. For and ideal solution, that is for helium mixtures in the classic regime where $T > T_F$ and $x_3 < 0.03$, the partial chemical potential for ^{3}He in the diluted liquid can be written as (see appendix A.1)

$$\mu_{3D}(T, x_{3D}) = \mu_3(T) + RT \ln x_{3D} \qquad (4.9)$$

Since $x_{3D} \ll 1$, equation 4.8 then becomes

$$\Pi_D = \frac{RTx_{3D}}{v_4}. \tag{4.10}$$

Thus, for low concentrations, the osmotic pressure is close to the value predicted by the ideal gas law. But equation 4.8 is not valid at temperatures typical for the lowest parts of a dilution refrigerator where the Fermi gas is degenerated. To find an expression for the osmotic pressure in the mixing chamber, equation 4.8 can be used. This time, however, together with the chemical potential of an ideal Fermi gas given by equation 4.4. After ignoring higher order terms:

$$\Pi_D = \frac{2}{5}\frac{RT_F x_{3D}}{v_4}, \tag{4.11}$$

which is valid for $T \lesssim 0.1$ K. The fundamental difference between equation 4.10 and 4.11 is that the latter is temperature independent. Of course, this is a result of the limited solubility of ^{3}He in ^{4}He. In next section, these equations are used to show how this influence the circulation rate, and hence the cooling power, of a dilution refrigerator.

4.3 DILUTION REFRIGERATORS

4.3.1 ^{3}HE CIRCULATION RATE

In a dilution refrigerator, the mixing chamber and the still can be seen as two chambers separated by a superleak. The superleak is non-ideal since it is possible for ^{3}He molecules to move through the superleak by working against the viscous forces of the interconnecting tubes. The flow rate of ^{3}He from the mixing chamber to the still is therefore dictated by the osmotic pressure difference between the two chambers, and the flow impedance of the tubes. Equation 4.10 and 4.11 with subindex M and S for the mixing chamber and the still yields

$$\Pi_M - \Pi_S = \frac{R}{v_4}(0.4T_F x_M - T_S x_S). \tag{4.12}$$

If ^{3}He molecules are removed from the still by pumping, the ^{3}He concentration in the still will decrease. With a powerful pump, x_S can be very low, typically $\ll 1\%$. Given equation 4.12, and given $T_M < 0.1$ K, the maximum pressure difference is about 3 kPa which corresponds to the hydrostatic pressure of a column of liquid ^{4}He more than 1 m tall. The significant outcome of this is that the still can be positioned well above the mixing chamber which allows for the slim and tall design, typical to the dilution refrigerator. Multiple heat exchangers can then easily be inserted in between the still and the mixing chamber.

If the pumping of ^{3}He from the still is halted, the osmotic pressure in the still will slowly increase until eventually $\Pi_M - \Pi_S = 0$. According to equation 4.12, this correspond to $x_S = 1.6\%$ for $T_S = 0.7\,K$. Therefore, since $x_S \leq 1.6\%$ and $x_M \geq 6.5\%$, the liquid in the still is always heavier than the liquid in the mixing chamber. Convection due to gravitational instability may therefore occur and effectively stop the dilution refrigerator from operating. This problem can be avoided by inserting a flow impedance in the still tube, which will dampen any convection. In practise, such a flow impedance may exist naturally in the heat exchangers if suitable tube diameters have been chosen.

The ^{3}He circulation rate in a condensation pumped DR is rather moderate in comparison with that in a conventional DR. With use of a powerful pumping systems and large diameter pumping lines, circulation rates of several 100 μmol/s is relatively easy to achieve. As is shown in section 4.3.3 however, a circulation rate of only a few μmol/s is enough to achieve the required cooling power for our applications. Under such conditions, the impedance of the heat exchanger can be rather high without compromising the flow rate. Viscous heating, which is only prevalent at very low temperatures ($T \lesssim 10\,mK$) can also be neglected. A more important factor is the efficiency of the condensation pump. No data is available from literature on the required surface area of the condenser, or how the condensation pump efficiency depends on the temperature. As a starting point, however, we can assume that the inner surfaces of the condenser is coated with a thin layer of liquid ^{3}He at all times. Due to the thermal impedance (Kapitza resistance) between the liquid ^{3}He and the metal surface, the vapour will condense at a temperature slightly higher than the temperature of the condenser. The higher the circulation rate, the larger surface area will be required in order to cancel out this effect. Kapitza resistance is discussed in section 4.3.3 and the required surface area for our applications will be estimated in section 4.4.2.

In a conventional DR, the circulation rate can be measured directly at room temperatures. In an MDR, however, there is no method of measuring this quantity directly since the system is sealed. Theoretically, the circulation rate is given by the power applied to the still, P_S:

$$\dot{n} = \frac{P_S}{L_{3D}(T_S, x_S)}. \tag{4.13}$$

Given the cooling power of the sorption cooler, measured in section 2.3.2, a reasonable value of P_S would be in the order of 200–400 μW. Radebaugh [109] has calculated the latent heat of diluted ^{3}He and found: $L_{3D} \simeq 24\,J/mol$ for $T_S = 0.7\,K$ (in comparison, for pure ^{3}He: $L_3(0.7\,K) = 33.1\,J/mol$). Thus we find that we can expect a circulation rate $\dot{n} = 8$–17 μmol/s. A larger still power would exhaust the ^{3}He buffer rather quickly and also make the condensation pump operate at a very high temperature. Of course, this calculation does not take into account the pumping speed of the condenser. As will be shown in section

4.4.1, the true circulation rate can therefore only be determined after comparing a theoretical model of the MDR cooling power to experimental data.

4.3.2 COOLING POWER ESTIMATES

The first law gives the cooling power, $\dot{Q}$, in the mixing chamber:

$$\dot{Q} = \dot{n}_3[H_{3D} - H_3]\,, \tag{4.14}$$

where $\dot{n}_3$ is the molar circulation rate of ^{3}He. The enthalpy of ^{3}He in the concentrated and diluted phase can, in principle, be estimated by integration of experimental values for the specific heat. For pure ^{3}He below 40 mK and at constant saturated vapour pressure [110], $C_3 = 2.7RT$ and hence:

$$H_3(T) = H_3(0) + 11T^2\,. \tag{4.15}$$

Due to lack of experimental data, a theoretical estimate is necessary for the diluted phase. For $T \ll T_F$, the ^{3}He quasiparticle gas can be treated as a weakly interacting Fermi gas with an effective mass m_3^*. In analogy with the LP theory discussed in section 4.2.2, the specific heat of the diluted mixture per mole of ^{3}He can be written [41]

$$C_{3D} = N_A k_B \frac{\pi^2 T}{2T_F} = 0.745 \frac{m_3^*}{m_3} \left(\frac{v}{x_{3D}}\right)^{2/3} T\,, \tag{4.16}$$

after using the equation for the Fermi temperature (4.3). In thermal equilibrium $\mu_3 = \mu_{3D}$, therefore $H_3 - TS_3 = H_{3D} - TS_{3D}$ which together with equation 4.15 yields:

$$H_{3D} = H_3(0) + 11T^2 + T\int_0^T (C_{3D} - C_3)/T'\,dT' = H_3(0) + 95T^2\,. \tag{4.17}$$

Finally, substituting 4.17 and 4.15 into 4.14 yields

$$\dot{Q}(T) = 84\dot{n}_3 T^2\,. \tag{4.18}$$

Of course, this expression does not take into account the enthalpy of the pure ^{3}He returning to the mixing chamber from heat exchangers. Equation 4.18 therefore corresponds to the cooling power of a dilution refrigerator with ideal heat exchangers or a dilution refrigerator operated in a single-shot mode. In order to find the cooling power of a continuous dilution refrigerator, the enthalpy balance in the mixing chamber should be written as

$$\dot{Q} + \dot{n}_3[H_3(T_0) - H_3(T_M)] = \dot{n}_3[H_{3D}(T_M) - H_3(T_M)]\,, \tag{4.19}$$

where T_M and T_0 is the temperature of the mixing chamber and the temperature of the returning ^{3}He respectively. Following the same steps as above gives

$$\dot{Q}(T) = \dot{n}_3(96T_M^2 - 12T_0^2)\,. \tag{4.20}$$

Not surprisingly, estimating the cooling power is now a matter of estimating the efficiency of the heat exchangers.

4.3.3 CONTINUOUS HEAT EXCHANGERS

Conventional dilution refrigerators have a combination of a continuous heat exchanger at the high temperature region and a number of step heat exchangers at the low temperature region. The reason for this is the increasing importance of the Kapitza resistance with lower temperatures. The Kapitza resistance, defined as

$$R_K \equiv \frac{\Delta T}{\dot{Q}}\,, \tag{4.21}$$

where ΔT is the temperature step at a given heat load $\dot{Q}$, is the thermal boundary resistance occurring between a solid and liquid helium due to the acoustic mismatch. Since only phonons can transfer heat between the liquid and the metal, the efficiency of the heat transport will depend on the acoustic properties near the interface. The acoustic mismatch model [111, 112] is in reasonable agreement with experimental results below 0.2 K which is also where the Kapitza resistance is most noticeable.

Phenomenologically, the acoustic mismatch model is similar to that of light reflecting at an interface between two materials of different refraction indexes. Using Snell's law the transmission coefficient, t, can be expressed in terms of the acoustic impedances Z_h and Z_s for helium and the solid respectively: $t = 4Z_hZ_s/(Z_h + Z_s)^2$. It turns out that only a small fraction ($t = 2 \times 10^{-3}$) of the incoming phonons will enter the solid. Without going into further details, the essential result is [41, 85]:

$$R_K = a_K \frac{1}{AT^3}\,, \tag{4.22}$$

where A is the surface area of contact and a_K is a constant depending on the materials in contact and the surface conditions. For a helium-metal contact below 0.3 K, the value of a_K is approximately 1–5 $\times 10^{-2}$ m^{2}K^4/W [41, 85].

The general approach to minimize the effect of Kapitza resistance is to increase the surface area. For this reason, a number of step heat exchangers are introduced, operating

in series down to the lowest temperatures. Each of them is built from a copper block with sintered copper/silver inside to provide a good thermal contact between the counterflow of concentrated and diluted liquids. Experiments have shown that the Kapitza resistance of sintered metals built from fine silver powder is proportional to T^{-2} rather than the usual T^{-3}. This is a significant advantage at low temperatures and is an important reason for the success of the modern heat exchangers developed by Frossati [113]. As a result, temperatures below 3 mK can be achieved [113–115] and the current world record is 1.75 mK. At these temperatures, the performance is limited by viscous heating ν, an effect which increases with decreasing temperatures ($\nu \propto T^{-2}$). The only way to reduce this effect would be to increase the dimensions of the tubes where the cold ^{3}He liquid flows. It can be shown that at these temperatures, the minimum temperature of the mixing chamber depends on the diameter of the tubes as: $T_{\min} \propto d^{-1/3}$ [116]. Thus, to lower the temperature from 2 mK to 1 mK, the dimensions would have to be increased by at least a factor of eight. It is easy to see how the system would become significantly more expensive, complicated and impractical to use.[†]

The design, modelling and implementation of step heat exchangers are rather complicated as well as expensive. For the purpose of an MDR operating at temperatures down to 50 mK, a continuous heat exchanger alone is sufficient. Indeed, temperatures as low as 22 mK has been achieved [117] using a long (150 cm) continuous heat exchanger. In addition to their simple design, they also benefit from a smaller volume which saves expensive ^{3}He and cooling-down time. Therefore the following analysis will be restricted to a tube-in-tube, continuous counterflow heat exchanger.

A very useful model for estimating the efficiency of both continuous and step heat exchangers have been developed by Frossati [113, 118] and later improved by Takano [119] (see Appendix B). The latter version of this model can (in the case $R_K \propto T^{-3}$) be written as

$$\dot{Q}/\dot{n} = \frac{(\gamma_D - \gamma_C)\left[\gamma_D (f-1) - \gamma_C\right]}{\gamma_D (f-1) - \gamma_C (f+1)} T_M^2 , \tag{4.23}$$

where γ_D and γ_C are the enthalpy coefficients of diluted and concentrated ^{3}He. The dimensionless factor f contains both $\dot{Q}/\dot{n}$ and the mixing chamber temperature T_M:

$$f = \exp\left(\frac{A/a_K}{\dot{n}\gamma_D\gamma_C}\left[(\gamma_D - \gamma_C)\, T_M^2 - 2\dot{Q}/\dot{n}\right]\right) . \tag{4.24}$$

Here, A is the total surface area of the inner tube. Equation 4.23 and 4.24 are valid for a

[†]If lower temperatures are required it is better to couple a nuclear demagnetization stage to the dilution refrigerator. This method can be used to achieve temperatures in the micro-Kelvin range.

perfect continuous heat exchanger with the Kapitza resistance proportional to T^{-3}. In this model, viscous heating and lateral heat conduction are absent and all of the heat removed from the incoming pure ^{3}He is absorbed by the returning dilute ^{3}He in ^{4}He. The perfect continuous counterflow heat exchanger is a model with powerful simplifications over earlier models [120, 121]. Whilst other models include explicit terms for viscous heating and lateral heat conduction, the perfect heat exchanger replaces these with a single parameter for the residual heat leak to the mixing chamber, $\dot{Q}_0$. Furthermore, the geometry of the heat exchanger is represented by their total surface area only. By comparing the model with experimental data, $\dot{Q}_0$ can be determined and used as a measure of the heat exchanger efficiency. This way the perfect heat exchanger model has been used successfully in the development of actual machines [113, 115].

4.4 DESIGN OF THE MDR

In the case of an MDR which relies on a sorption cooled condenser, there is a limit on the circulation rate of ^{3}He. In order to keep the condenser at a temperature well below that of the still, the heat load $\dot{Q}_c$ from the condenser should be less than 400 μW. Given the cooling power of a standard CRC sorption cooler, this heat load would correspond to a condenser temperature of approximately 400 mK. Hence, the circulation rate should be less than $\dot{n} = \dot{Q}_c / L_{3D} = 10\,\mu\text{mol/s}$.

4.4.1 HEAT EXCHANGER CALCULATIONS

In order to design the continuous heat exchanger, we now turn to equations 4.23 and 4.24. Numerically solving these equations turns out to be difficult because physical and non-physical solutions are very close to each other for certain values of T_M and $\dot{Q}$. Essentially, the problem origins in the exponential behaviour of f. The logarithmic version of these equations is therefore easier to use:

$$\dot{Q}/\dot{n} = \left(\frac{\gamma_D}{2} - \frac{\gamma_C}{2}\right) T_M^2 - \frac{\gamma_D \gamma_C}{2} \frac{g\dot{n} a_K}{A}, \tag{4.25}$$

where

$$g = \ln\left(\frac{(\gamma_D + \gamma_C)\left[(\gamma_D - \gamma_C)\, T_M^2 - \dot{Q}/\dot{n}\right]}{(\gamma_D - \gamma_C)\left(\gamma_D T_M^2 - \dot{Q}/\dot{n}\right)}\right). \tag{4.26}$$

Results from heat capacity measurements [110, 122, 123] give the numerical values $\gamma_C = 23\,\text{J/K}^2\text{/mol}$ and $\gamma_D = 107\,\text{J/K}^2\text{/mol}$.

The lowest achievable temperature is dictated by the surface area of the heat exchangers, the ^{3}He circulation rate and the Kapitza resistance. In a continuous heat exchanger, the area on the ^{3}He concentrated side is approximately the same as on the diluted side. Therefore, A can be taken to be the total area of either side. It follows from this assumption that a_K is the sum of the two Kapitza resistance coefficients, one between the pure liquid ^{3}He and the heat exchanger wall and another between the wall and the diluted liquid. According to Takano [119] it is commonly believed that a thin film of ^{4}He coats all surfaces of the heat exchanger, causing a_K of the concentrated side to be the same as that of the diluted side. Hence, a_K can be taken to be twice the value for the dilute liquid. The Kapitza resistivity, a_K, between a diluted liquid and CuNi has been measured to be 0.01 m^2K^4/W and constant in the temperature range 10–200 mK [85].

With $\dot{Q} = \dot{Q}_0 = 0$, equation 4.25 gives the base temperature $T_0^2 = 5.7\dot{n}a_K/A$. Thus, with no heat leak, the lowest achievable temperature can be made arbitrarily small by decreasing the circulation rate. Of course, in reality there will always be a small contribution from viscous heating and lateral heat conduction in the heat exchangers and the connecting tubes, resulting in $\dot{Q}_0 \neq 0$.In figure 4.4 we have used equation 4.25 with $A = 40\,cm^2$ and $a_K = 0.02\,m^2K^4/W$ to estimate the lowest achievable temperature as a function of the circulation rate.

It is worth pointing out that at temperatures $\gtrsim 3T_0$, where $\dot{Q}/\dot{n}$ is large, the cooling power is less dependent of the heat exchanger's surface area. In this regime, equation 4.25 reduces to the familiar expression: $\dot{Q} = (\gamma_C - \gamma_D)\,\dot{n}T^2$. This is because the heat load from the returning ^{3}He becomes small in comparison with the external heat leak. This is illustrated in figure 4.5 where the cooling power, given by equation 4.25, is plotted for $\dot{n} = 10\,\mu mol/s$ and compared with the high-temperature approximation. Here A and a_K are kept to the same values as used in figure 4.4. The comparison is made for the ideal case when $\dot{Q}_0 = 0$ and for a non-perfect heat exchanger with a residual heat leak $\dot{Q}_0 = 1\,\mu W$.

We can conclude that a dilution refrigerator using a circulation rate of less than 10 μmol/s, and a heat exchanger with a surface area of only 40 cm^2 would be enough for our purposes. A base temperature below 50 mK and several micro-Watt of cooling power at 100 mK can be expected.

4.4.2 DESIGN DETAILS

Figure 4.6 shows two pictures of the MDR built during this project. The left picture shows the principle components whilst the right picture shows the MDR together with its radiation shield and suspended with Kevlar. In this section we will describe the design of each component of the MDR.

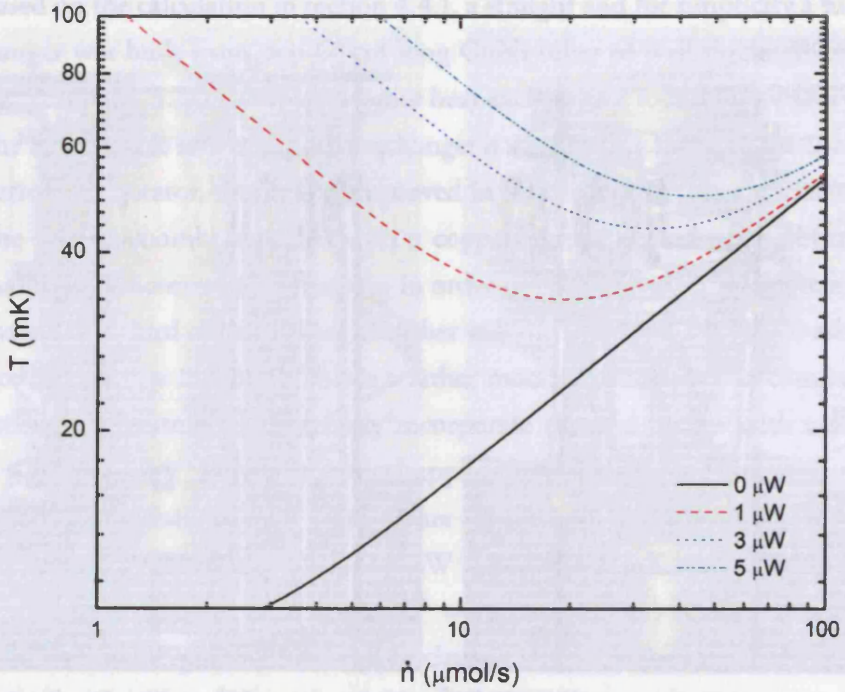

Figure 4.4: Lowest achievable temperature as a function of the ^{3}He circulation rate for various heat loads: 0 μW (black), 1 μW (red), 3 μW (blue) and 5 μW (green).

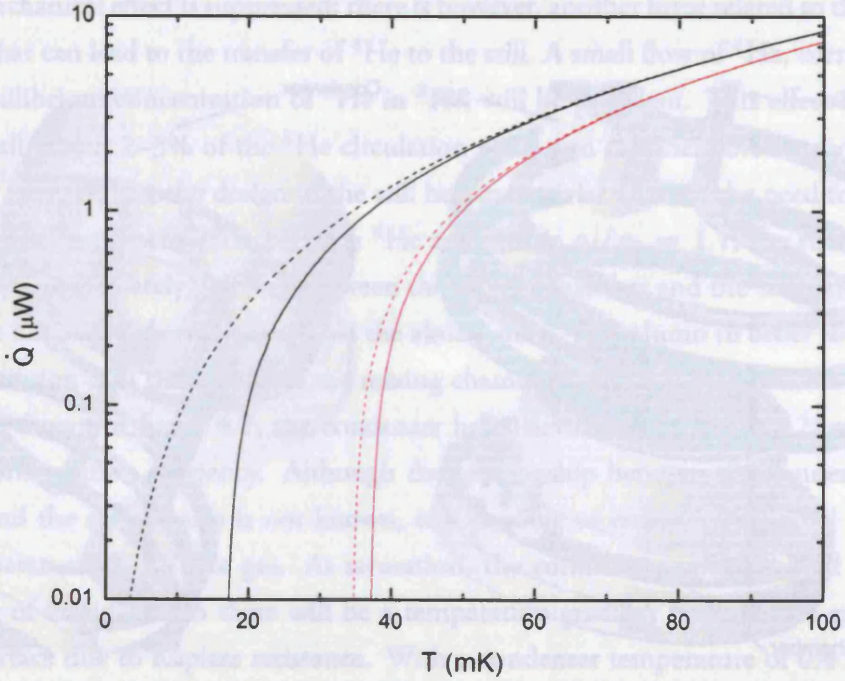

Figure 4.5: A comparison of the cooling power, for $\dot{n} = 10$ μmol/s, as predicted by the perfect heat exchanger model (solid lines) with that predicted by the high-temperature approximation: $\dot{Q} = (\gamma_C - \gamma_D)\,\dot{n}T^2$ (dashed lines). Black curves are for $\dot{Q}_0 = 0$ and red curves are for $\dot{Q}_0 = 1$ μW.

Figure 4.6: Two pictures of the MDR developed during this project. The left picture shows the principle components of the MDR, and the right picture shows the MDR with its radiation shield suspended with Kevlar

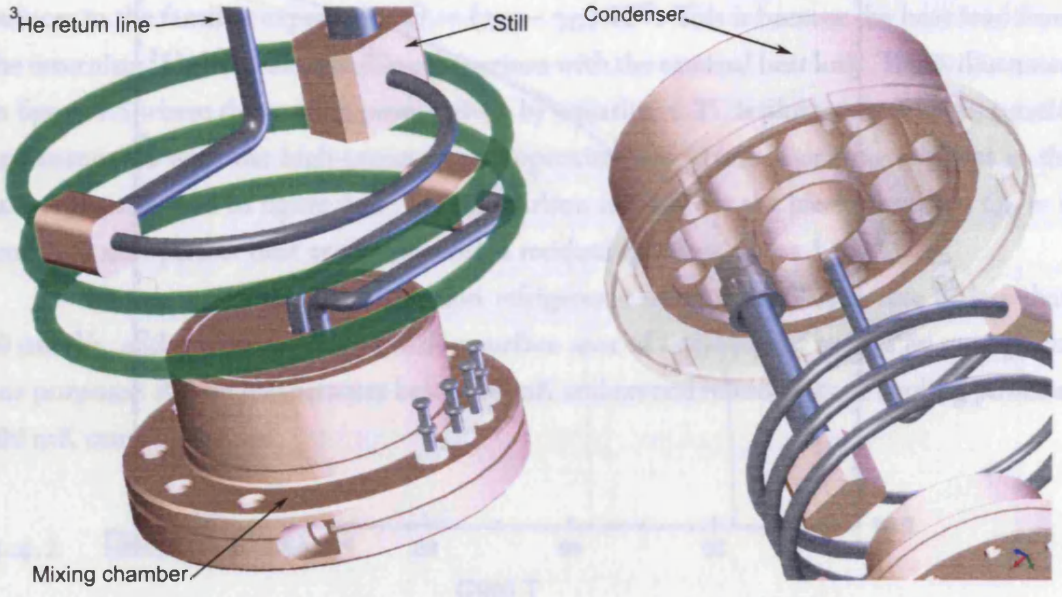

Figure 4.7: The left figure shows how the heat exchanger (green) connects to the mixing chamber, the still and the ^{3}He return line by two split blocks. The right figure shows the developed surface of the condenser.

Based on the calculation in section 4.4.1, a straight and for simplicity a tube-in-tube heat exchanger was built from two 60 cm long CuNi tubes of wall thickness 0.2 mm and diameter 2.3 mm and 3.3 mm. This gives the heat exchanger a total surface area of 43 cm^2. Because the total surface area of the heat exchanger is the limiting factor in the cooling power of the dilution refrigerator, this can be improved in future designs (see section 6.3).

The mixing chamber is filled with a copper mesh soldered to the bottom of the mixing chamber to increase its surface area in order to limit the effect of Kapitza resistance. Approximately one third of the mixing chamber volume is occupied by the mesh, resulting in a surface area $A_M = 200\,cm^2$. This is a rather modest surface area in comparison with most dilution refrigerators which usually incorporate sintered metals with a surface area of several square meters. For astrophysical applications where a cooling power of only a few micro-Watt at a relatively high temperature is sufficient, a much smaller surface area is acceptable. Assuming a heat load of $\dot{Q} = 5\,\mu W$ at $T_M = 100\,mK$ and the mixing chamber surface area A_M given above, and given $\Delta T = a_K \dot{Q}/(T_M A_M)$ where a_K is the Kapitza resistivity between the liquid and the copper chamber, we find $\Delta T = 5\,mK$. Here we used the resistivity for Cu-dilute ^3He: $a_K = 0.02\,m^2K^4/W$ [85].

Unlike conventional DR systems, in a condensation pumped dilution refrigerator the still is the hottest part and so the superfluid film flow is naturally suppressed. At least the thermomechanical effect is suppressed; there is however, another force related to the osmotic pressure that can lead to the transfer of ^4He to the still. A small flow of ^4He, corresponding to the equilibrium concentration of ^4He in ^3He, will be prevalent. This effect is however rather small (about 2–3% of the ^3He circulation rater) and can therefore be considered as negligible [52]. Hence, the design of the still becomes trivial without the need for any film burner. Since the density ratio between ^4He and ^3He is $\rho_4/\rho_3 = 1.7$, the still should be positioned approximately half way between the mixing chamber and the condenser. This is to balance the pure ^3He column against the almost pure ^4He column in order to assure the phase separation is in the middle of the mixing chamber.

As shown in figure 4.7, the condenser has a developed surface of 125 cm^2 for increased condensation efficiency. Although the relationship between the condensation efficiency and the surface area is not known, it is possible to estimate the actual condensation temperature of the ^3He gas. At saturation, the condenser surface should be coated by a layer of liquid and so there will be a temperature gradient between the gas and the copper surface due to Kapitza resistance. With a condenser temperature of 0.4 K we have $a_K = 0.01\,m^2K^4/W$. Assuming a heat load on the condenser $P_{Cnd} = P_S = 500\,\mu W$, and given equations 4.21 and 4.22 we find $\Delta T = 6\,mK$. This means that the condenser should be capable of rather large circulation rates before the Kapitza resistance becomes important.

If the ^{3}He circulation rate is limited by the condensation efficiency, the temperature of the condenser should be a more significant design criteria than the surface area. This highlights the significance of using a powerful sorption cooler and minimizing the thermal impedance between the ^{3}He buffer and the condenser.

The mixing chamber is suspended by thin Kevlar strings. The total cross-section area of all these 20 mm long strings is approximately 0.7 mm^2. With thermal conductivity data from literature [124], the resulting heat load on the mixing chamber should be less than 0.01 μW.

The radiation shield is mounted on the condenser as shown in figure 4.6. Obviously it would have been better to have the shield anchored to the still since this would have reduced the heat load on the ^{3}He sorption cooler. From a practical point of view, however, this would have been more complicated and not much of a benefit since the 4 K radiation heat load is small in comparison to the heat load from the condenser.

The total volume of the dilution unit and its components is given in table 4.1, together with other important dimensions. The total amount of liquid inside the MDR is 10.1 cm^3 of which 50% (by volume) is pure ^{3}He. The liquid-to-gas ratio for ^{4}He and ^{3}He is 886 and 662 respectively. Therefore, the volumes of liquid ^{4}He and ^{3}He (as measured at 1 K) correspond to 4.4 L (STP) of ^{4}He gas and 3.3 L (STP) of ^{3}He gas.

Finally, in order to cool the mixing chamber from room temperature to 4 K, a piece of AGOT graphite mounted between the mixing chamber and the condenser acts as a passive heat switch. This avoids the use of any exchange gas which would have required Indium O-rings and an extra capillary for gas inlet/outlet. The graphite slab is 30 mm long with a cross-section area of 20 mm^2. With thermal conductivity data of graphite from literature [125], the residual heat leak should be less than 0.1 μW during operation. We see that this heat load is dominating over the Kevlar by about an order of magnitude, but is still small enough not to affect the cooling power or the lowest achievable temperature of the system.

4.5 INITIAL TESTS IN A LHE CRYOSTAT

The experimental work of the MDR is divided into three sections: initial tests carried out in a liquid helium cryostat (this section), a far more detailed study using a larger ^{3}He buffer and a pulse-tube cooler (section 4.6), and the realization of a fully continuous operation (section 4.7).

Length of HE	600 mm
Diameter of HE inner tube	2.3 mm
Diameter of HE outer tube	3.3 mm
Surface area of HE	43 cm^2
Volume of HE concentrated side	2.73 cm^3
Volume of HE diluted side	2.54 cm^3
Volume of still	0.34 cm^3
Volume of m.c.	4.5 cm^3
Surface area of m.c.	200 cm^2
Surface area of condenser	125 cm^2
Total volume of ^{3}He liquid	4.98 cm^3 (0.137 mol)
Total volume of ^{4}He liquid	5.13 cm^3 (0.183 mol)
Volume of ^{3}He gas (STP)	3.30 L
Volume of ^{4}He gas (STP)	4.44 L
Molar ratio $n_3/(n_3 + n_4)$	0.428
Total internal volume of MDR	50.4 cm^3
Equiv. room-temperature pressure	155 bar

Table 4.1: A selection of important design parameters of the continuous MDR.

4.5.1 EXPERIMENT

During the first phase of the experiments, the prime purpose was to gain a fundamental understanding of the behaviour of the system and important experience which could be used to integrate the MDR with a pulse-tube cooler. The main target was to verify that the design of the dilution system was fundamentally sound and that dilution cooling could be observed. Therefore a ^{3}He sorption cooler already available to the group was used. It was too small to study the system on a long time-scale but adequate to achieve temperatures below 100 mK for a short period of time. The most basic information such as cool-down time, cycle procedures and information about the performance of the sorption cooler was attained.

The MDR was mounted together with a double stage CRC sorption cooler in a Janis liquid helium cryostat. Initially the assembly included an expansion volume mounted on the 4.2 K base plate which allowed the system to be completely sealed and self-contained with no capillaries linked to room temperatures. The expansion cylinder was necessary to reduce the gas pressure inside the system since the dilution unit alone would not have been able to sustain the pressure at room temperatures. However, this arrangement proved to be very impractical at such an early stage since it did not allow for any changes of the gas mixture (the mash). It became clear that the theoretical estimate of the ^{3}He/^{4}He ratio was incorrect and that the total amount of mash was over-estimated. A successful cooling was achieved only after the expansion cylinder had been removed and a room temperature connection

had been installed. This more flexible arrangement proved invaluable in determining the correct ^{3}He to ^{4}He ratio and amount of mash. From now on, all the described experiments refers to this later arrangement.

Two calibrated thermometers from Lakeshore acted as a calibration standard in all experiments carried out in the liquid helium cryostat. All other thermometers were calibrated against either of these two; one germanium thermometer for temperatures down to 50 mK and one RuOx thermometer for temperatures down to 300 mK. A large number of silicon diodes were also used at higher temperatures, calibrated against a Lakeshore RhFe thermometer.

The MDR was suspended with Kevlar to thermally isolate it from the 4.2 K base plate. A copper thermal link allowed the condenser to be coupled to the sorption cooler evaporator. Good results were achieved only after this link had been gold plated and made from a high conductivity, C103 (OFHC), copper. The thermal connections to the condenser and the evaporator were bolted, 'dry' joints without any dielectric interposers (see section 3.2.4 for a more detailed discussion on thermal contact resistance).

4.5.2 RESULTS

A large number of cycles were performed with small changes to the ^{3}He/^{4}He mixture in order to investigate how critical these parameters were. The essential outcome of these tests were that the system appeared to work well as long as the amount of mash was correct within $\pm 5\%$. The cooling power at 100 mK did not change at all in this range. Outside a $\pm 10\%$ range, however, two different behaviors were observed:

1. Too much mash resulted in violent temperature oscillations at the still, which appeared to propagate down to the mixing chamber. At $t = 26$ hours in figure 4.10 the still temperature dropped from 1.7 K to 0.7 K in less than 10 s. At the same time, the mixing chamber temperature dropped by about 80 mK, the condenser temperature increased by 150 mK and the ^{3}He charcoal pump increased by 600 mK. Together, this indicates a sudden increase of the circulation rate, which allowed the mixing chamber to cool either because of dilution cooling or because of cold liquid arrived to the mixing chamber from the condenser. Either way, no consistent dilution cooling could be observed under these conditions. Although the physics behind the oscillations have not yet been clarified, they were most likely a result of condensing too much mash so that the level of liquid rose well above the still. They disappeared all together once the ratio of ^{3}He/^{4}He and the amount of mash was correct.

2. Too little mash resulted in that the still operated at a much too high temperature.

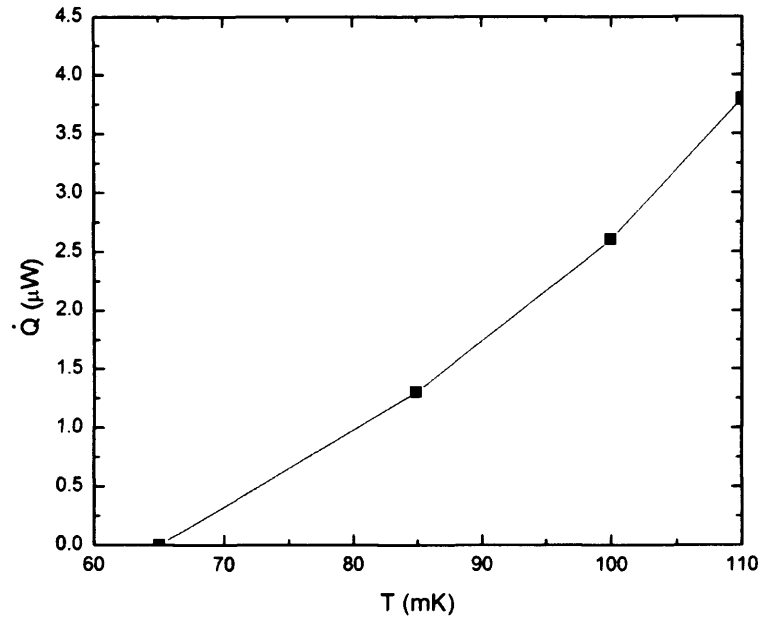

Figure 4.8: Measured cooling power of the MDR in a LHe cryostat

This was interpreted as not enough liquid was available to fill the tubes all the way up to the still. With no liquid in the still, the heat capacity would have been very low and so the power to the still warmed it up very quickly. No dilution cooling at all was observed under these conditions.

Figure 4.9 shows a successful cool-down starting from 4.2 K. The ^{4}He charge cooled the dilution unit and the mash down to $\sim$ 0.9 K, at which temperature virtually all the gas condensed. Once the ^{4}He buffer was exhausted, the mash was cooled by evaporation of ^{3}He. The mixing chamber was left to cool to a temperature below 0.6 K before approximately 200 μW of power was applied to the still heater. The mixing chamber then slowly cooled and eventually reached 65 mK. At that point the ^{3}He buffer was exhausted and the cycle was over.

Initial cooling power tests were also performed but had to be limited to only a few data points due to the short duty time. The measured cooling power is shown in figure 4.8.

In conclusion, these initial tests confirmed that the dilution unit was working as expected with approximately 3 μW of cooling power at 100 mK. The lowest temperature achieved was 65 mK but the temperature was still decreasing when the ^{3}He buffer was exhausted. The graphite heat switch appeared to work well, although it was never clarified if the residual heat leak during operation was as low as estimated (< 0.1 μW). This last point will be clarified in section 4.6.

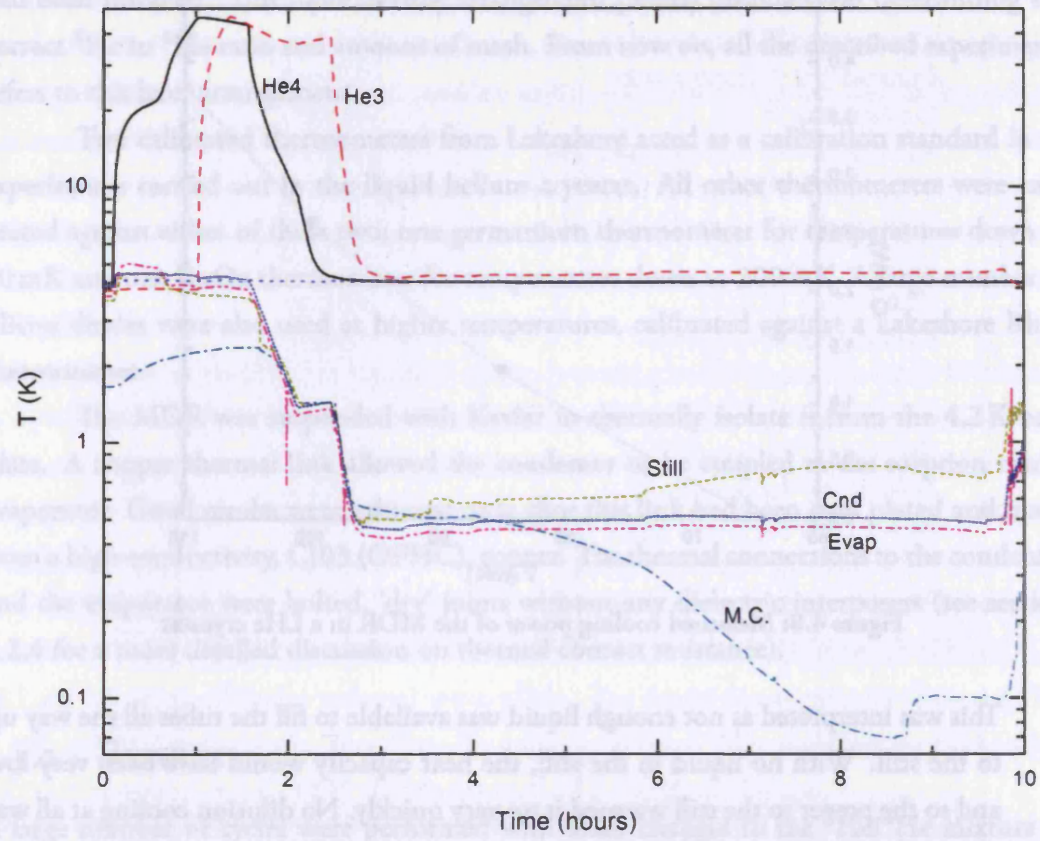

Figure 4.9: Cool-down of the MDR from 4.2 K in a liquid helium cryostat. The figure shows the temperature of the still, mixing chamber (M.C.), condenser (Cnd), ^{3}He charcoal pump (He3), ^{4}He charcoal pump (He4) and the ^{3}He evaporator (Evap).

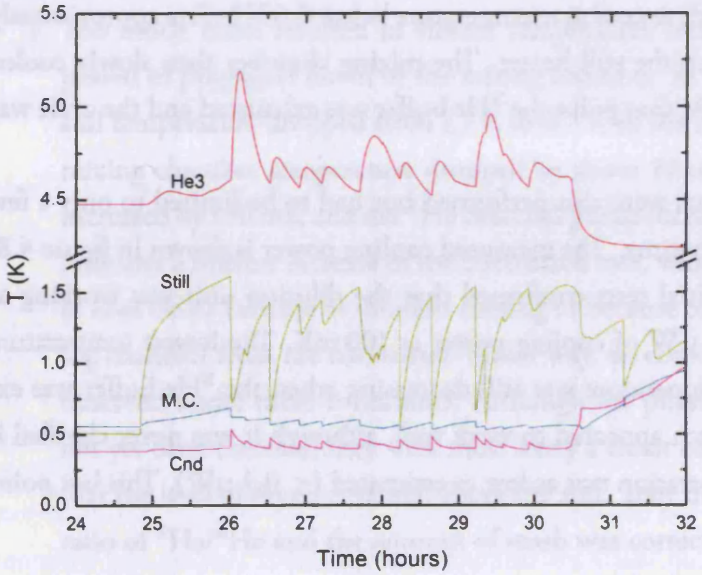

Figure 4.10: Observed temperature oscillations of the still, a result of too much mash being condensed.

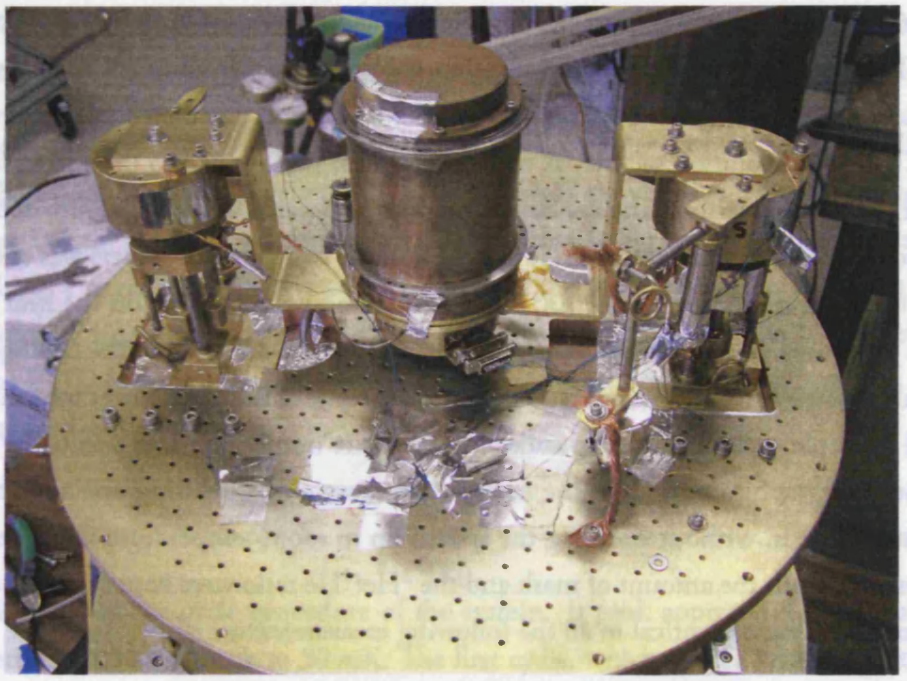

Figure 4.11: A picture of the experimental setup for semi-continuous operation in a PTC.

4.6 DETAILED TESTS IN A PTC CRYOSTAT

4.6.1 EXPERIMENT

Given the positive results from the initial tests, a more thorough investigation was justified. For this purpose, a larger ^{3}He buffer was required in order to operate below 100 mK for several hours. On this time scale, all the ^{3}He in the mixture can circulate through the system and return to the mixing chamber.

In accordance with figure 4.11, the dilution unit was thermally coupled to the two evaporators by means of two 150 mm long OFHC copper links, each with a cross-section area of 160 mm^2. Both sorption coolers where mounted in the PTC cryostat described in chapter 2.

The MDR therefore operated in a semi-continuous mode. That is, although the MDR itself is continuous in operation, it will only function for as long as the ^{3}He buffer of the sorption cooler lasts. This is essentially the same setup used by Edel'man [50, 51]. It may seem counter-intuitive to use a continuous MDR in a single-shot operation; if only a short duty cycle is required, one could argue that a single-shot MDR would be a better option since such a system can reach lower temperatures. As will be shown in chapter 5, however, there are complications with pre-cooling the mash in a single-shot MDR which can shorten the operation time significantly. Further more, the semi-continuous operation allows us to test the dilution unit on its own before introducing any heat switches. In this scheme, the

MDR could also take advantage of the combined cooling power of both sorption coolers.

There was enough ^{4}He in the sorption coolers to liquify and cool the ^{3}He in the evaporators as well as all the mash in the MDR to 2 K. The mixture then cooled from 2 K to about 0.7 K by evaporation of ^{3}He, at which point heat was applied to the still in order to initiate the ^{3}He circulation. The condensation pump operated at 400–450 mK depending on the power to the still. The total amount of ^{3}He in the two sorption coolers was enough to operate the mixing chamber below 100 mK for 10–20 hours depending on the heat load to the still. Of course, in semi-continuous mode there is a trade-off between the cooling power at 100 mK and the run-time of the system. Therefore, some of the high-power measurements required multiple cycles in order to collect an adequate number of data points. With one exception (the graphite test) all of the measurements were made during one and the same cold-down. That is, without warming the system up to room-temperature in between two measurement. Both the amount of mash and the ^{3}He/^{4}He ratio were kept constant and the cycle procedures were identical in all the following measurements:

1. In two separate cool-downs, two different graphite heat switches were used. After the first cool-down, the cross-section of the graphite was reduced from 40 mm^2 to 20 mm^2. By comparing the lowest attainable temperatures, it was possible to determine wether or not the performance of the MDR was limited by the graphite.

2. The cooling power of the system was measured for two different still loads: P_S = 225 μW and 625 μW. The lead resistance of the mixing chamber heater was eliminated by a 3-wire configuration, and the heater current was measured.

3. In order to evaluate the condensation efficiency, the cooling power was measured as a function of the condenser temperature. We used P_S = 225 μW and kept the mixing chamber temperature constant at 95 mK by using a heater. The temperature of the condenser was increased in steps and stabilized by controlling the temperature of the ^{3}He charcoal pump and by a heater on the condenser.

4. The lowest attainable temperature as a function of the still load was also measured. We found that it was relatively easy to get false data points unless the system was left to stabilize for a long time. For low vales of P_S, it could take several hours before a data point could be taken. The system stabilized on about the same time scale as the ^{3}He completes one full cycle.

5. The conductance of the thermal link which connects the condenser to the evaporators was measured using a heater on the condenser and thermometers position at each end of the link.

6. Tilt tests were performed in order to investigate the possibility of using the MDR as part of an astronomy experiment on a telescope.

7. Both the first and the second stage of the PTC give rise to temperature oscillations. These oscillations propagate through the system all the way down to the mixing chamber, but the significance on these oscillations have so far not been explored in detail. Using a signal analyser, the analog output of the mixing chamber sensor (a germanium RTD) was integrated for 45 min in an attempt to measure the 1.4 Hz peak from the PTC. Higher frequency harmonics had to be ignored due to a low-pass filter in the read-out electronics.

4.6.2 RESULTS

Figure 4.12 shows the cycle procedure of the system. It took approx 4.5 hours to recycle the system from 50 mK back to 50 mK. The first cycle, which started with all parts of the system at 4 K, was somewhat shorter and took less than 2 hours. The cool-down from room temperature to 4 K took about 24 hours.

The measured cooling power for two different still loads is shown in figure 4.13, and in more detail in figures 4.14 and 4.15. The theoretical model (equation 4.25) was fitted to the data in figure 4.13; it is clear that a residual heat leak $\dot{Q}_0 = 1.1$–1.55 μW was prevalent. In part this was due to the non-perfect heat exchanger but earlier measurements in a LHe cryostat (figure 4.8) suggest that vibrations originating from the PTC may have impeded the performance slightly: despite the fact that the still power was smaller in the wet cryostat, the cooling power at 110 mK was about 1 μW higher than in the PTC cryostat. Nevertheless, temperatures below 50 mK and a cooling power of several micro Watt at 100 mK was achieved.

The best fit is done in such a way that it agrees with the lowest achievable temperature. As can be seen in figure 4.13, the fit deviates from the data at the high-temperature end. Although this model has been used with some success at temperatures as high as 200 mK [119], we believe that at least two factors may be responsible for why the theoretical line deviates. Firstly, the temperature is measured on the outside of the mixing chamber which means that the actual cooling power was higher than what the measurements show. Secondly, the entropy coefficients, γ_D and γ_C, can only be used in the linear (entropy and hence heat capacity) regime. Strictly speaking they are only valid for temperatures below 50 mK, although for our purposes, they are useful up to about 100 mK. At temperatures around and above 200 mK however, the heat capacity of both diluted and concentrated ^{3}He is almost constant with temperature. The cooling power is therefore almost linear at high temperatures, and

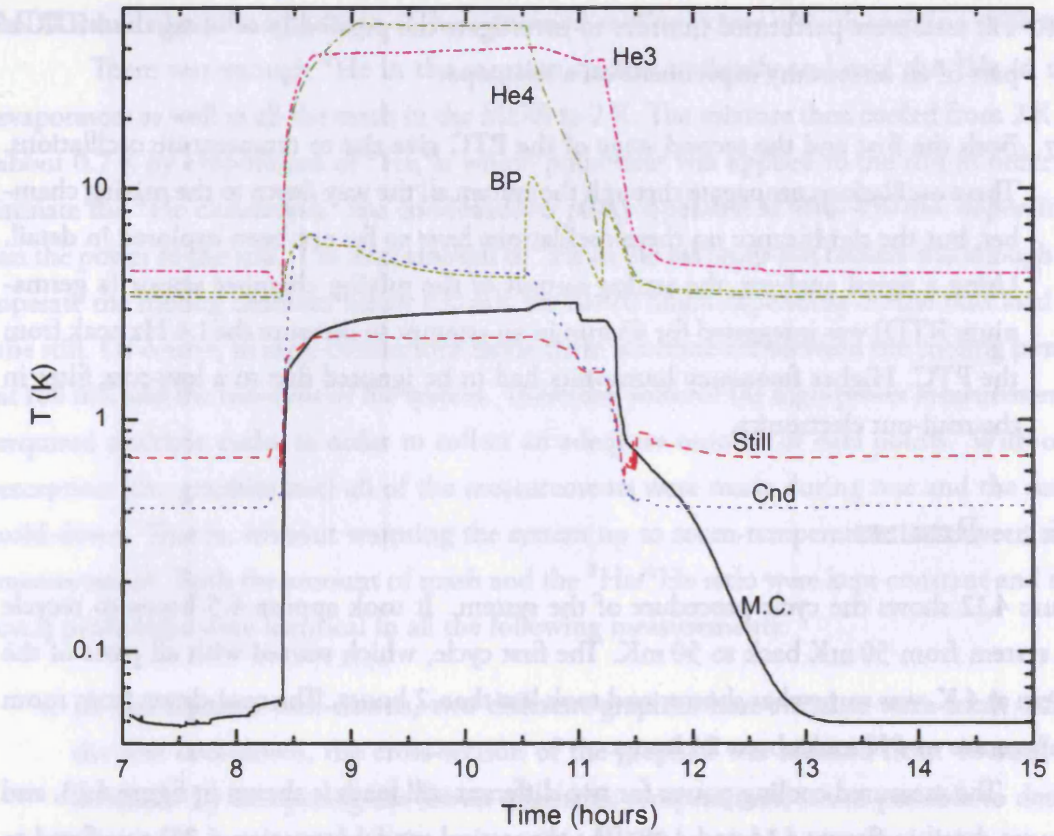

Figure 4.12: To recycle the system from 50 mK back to 50 mK takes about 4.5 hours. The graph shows the temperature of the mixing chamber (M.C.), the still, the condenser (Cnd), base plate (BP), the ^{4}He charcoal pump (He4) and the ^{3}He charcoal pump (He3).

so the theoretical model is not valid anymore. This is not of any concern here since we are primarily interested in operating the system at $T \leq 100$ mK. We will however, return to this issue in chapter 5 where high-temperature calculations are more important.

In the first successful cool-down, where the larger cross-section graphite was used, the system reached 48.5 mK. In the next cool-down, with a reduced cross-section, the system reached 48 mK. The difference is so small that it can not be be ruled out that the result could have been influenced by something else than the graphite: for example, the temperature of the mixing chamber may vary as much as 0.3 mK during one and the same cycle. It is also questionable wether or not we can trust the stability of the thermometer down to this accuracy. Nevertheless, the conclusion is that the graphite has no appreciable affect on the lowest attainable temperature of the system. Therefore, the MDR must be limited by the efficiency of the heat exchangers.

The temperature dependence of the condensation efficiency is shown in figure 4.16. During our experiments, with $P_S \leq 625\,\mu$W, the condenser temperature, T_C, was always less than 440 mK. The temperature gradient across the thermal link between the condenser

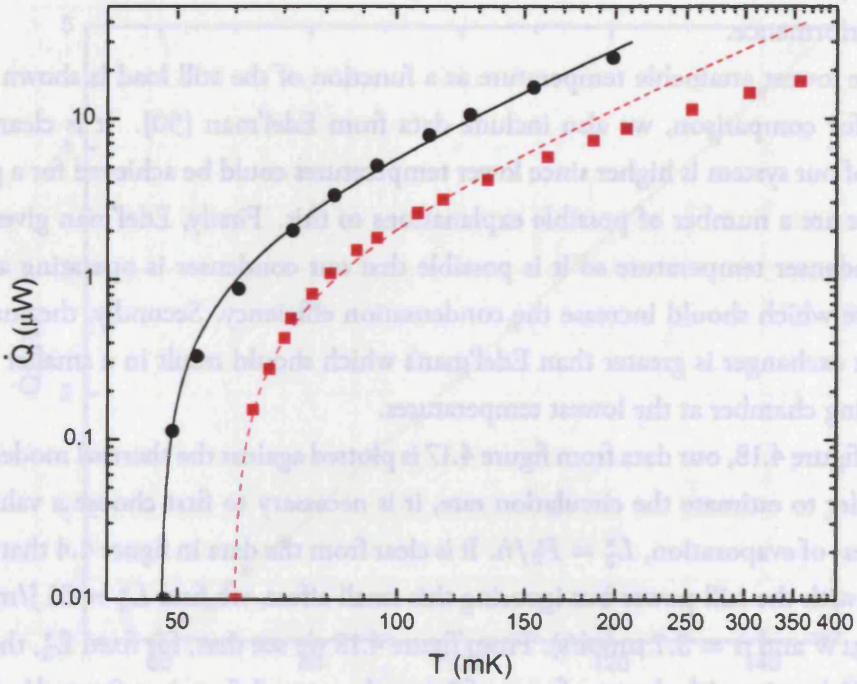

Figure 4.13: Measured cooling power with $P_S = 225\,\mu W$ (■)and $P_S = 625\,\mu W$ (•). A best fit of the data gives $\dot{Q}_0 = 1.1$, μW, $\dot{n} = 3.7$ μmol/sec for $P_S = 225\,\mu W$ (dashed line) and $\dot{Q}_0 = 1.55$, μW, $\dot{n} = 8.5$ μmol/sec for P_S=625 μW (solid line).

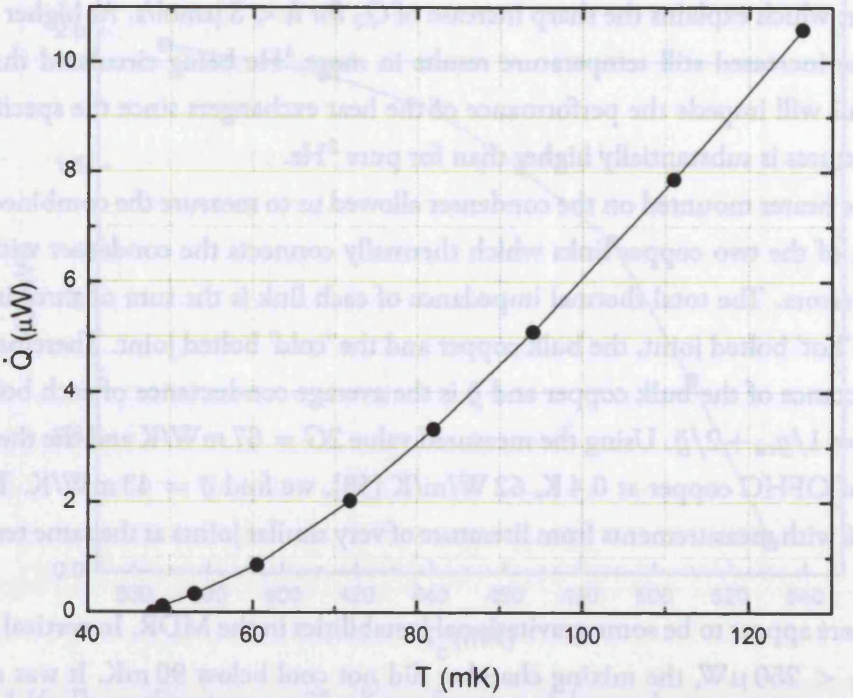

Figure 4.14: Measured cooling power using 625 μW to the still

and the evaporator was less than 30 mK; the system must therefore have been close to its optimal performance.

The lowest attainable temperature as a function of the still load is shown in figure 4.17, and for comparison, we also include data from Edel'man [50]. It is clear that the efficiency of our system is higher since lower temperatures could be achieved for a given still load. There are a number of possible explanations to this. Firstly, Edel'man gives no data on the condenser temperature so it is possible that our condenser is operating at a lower temperature which should increase the condensation efficiency. Secondly, the surface area of our heat exchanger is greater than Edel'man's which should result in a smaller heat leak to the mixing chamber at the lowest temperatures.

In figure 4.18, our data from figure 4.17 is plotted against the thermal model in figure 4.4. In order to estimate the circulation rate, it is necessary to first choose a value for the effective heat of evaporation, $L_3^* = P_S/\dot{n}$. It is clear from the data in figure 4.4 that L_3^* varies somewhat with the still power but ignoring this small effect, we find $L_3^* = 61$ J/mol (using $P_S = 225$ μW and $\dot{n} = 3.7$ μmol/s). From figure 4.18 we see that, for fixed L_3^*, the residual heat leak ($\dot{Q}_0$) varies with almost a factor of 3 over the range $1.5 < \dot{n} < 3$ μmol/s. This, and the fact that $\dot{Q}_0$ increases with $\dot{n}$ for $\dot{n} > 3$ μmol/s, has a simple explanation. In analogy with the cold vapour from a ^{3}He sorption cooler, the ^{3}He molecules which flow from the mixing chamber to the still absorb some of the heat conducted by the tubes and the liquid, and so reduces the heat leak to the mixing chamber. For low values of $\dot{n}$, this effect will become less efficient which explains the sharp increase of $\dot{Q}_0$ for $\dot{n} < 3$ μmol/s. At higher flow rates though, the increased still temperature results in more ^{4}He being circulated through the system. This will impede the performance of the heat exchangers since the specific heat of ^{3}He in mixtures is substantially higher than for pure ^{3}He.

The heater mounted on the condenser allowed us to measure the combined conductance, $2G$, of the two copper links which thermally connects the condenser with the two ^{3}He evaporators. The total thermal impedance of each link is the sum of three impedance terms: the 'hot' bolted joint, the bulk copper and the 'cold' bolted joint. Therefore, if g_{cu} is the conductance of the bulk copper and $\bar{g}$ is the average conductance of each bolted joint, then $1/G = 1/g_{cu} + 2/\bar{g}$. Using the measured value $2G = 67$ mW/K and the thermal conductivity of OFHC copper at 0.4 K, 62 W/m/K [58], we find $\bar{g} = 43$ mW/K. This agrees within 10% with measurements from literature of very similar joints at the same temperature [126].

There appear to be some gravitational instabilities in the MDR. In vertical operation and for $P_S < 250$ μW, the mixing chamber did not cool below 90 mK. It was enough to tilt the cryostat ±5° to eliminate this problem. Another successful approach was to increase

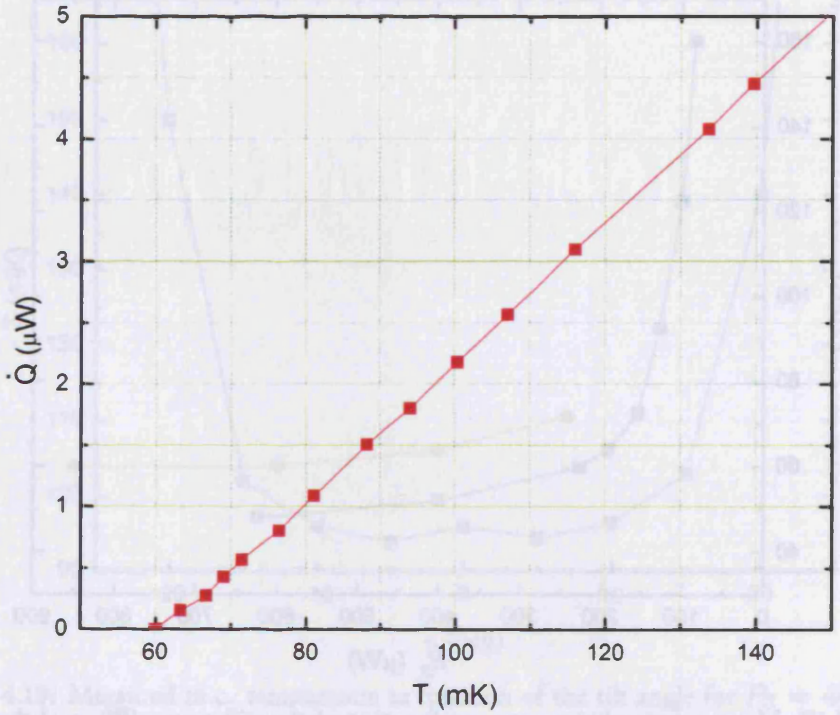

Figure 4.15: Measured cooling power using 225 μW to the still

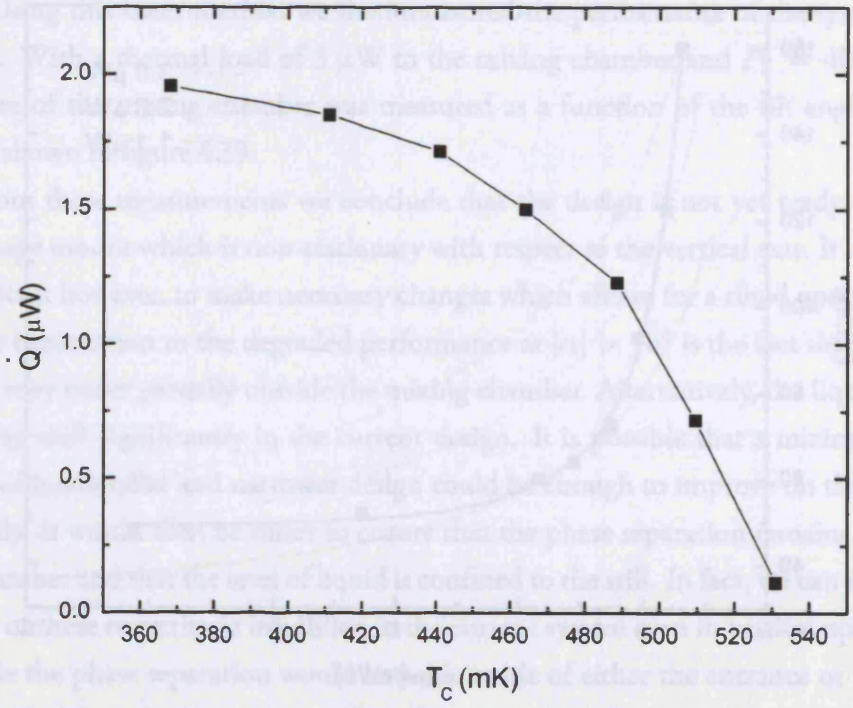

Figure 4.16: The cooling power at 95 mK as a function of the condenser temperature using $P_S = 225\,\mu W$.

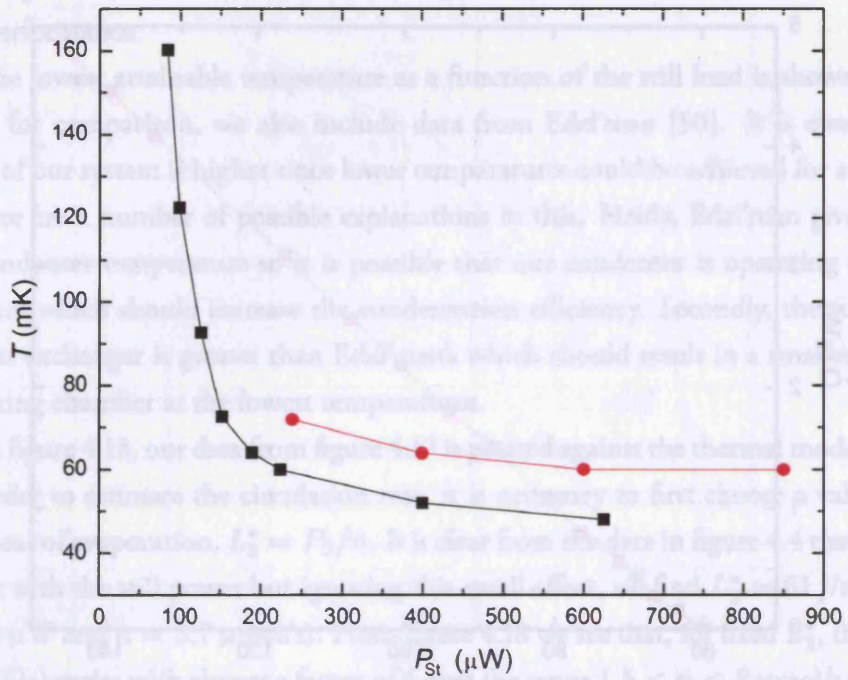

Figure 4.17: Measured circulation rate as a function of the still power (■), and the same data from Edel'man (•) [50].

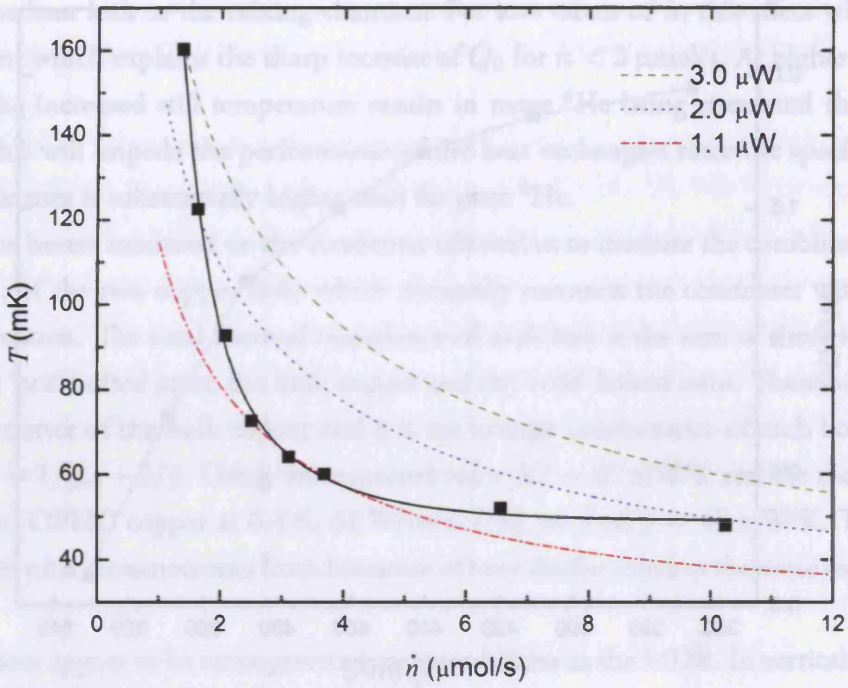

Figure 4.18: Measured circulation rate in comparison with the thermal model. It is clear that the residual heat leak increases with decreasing $\dot{n}$.

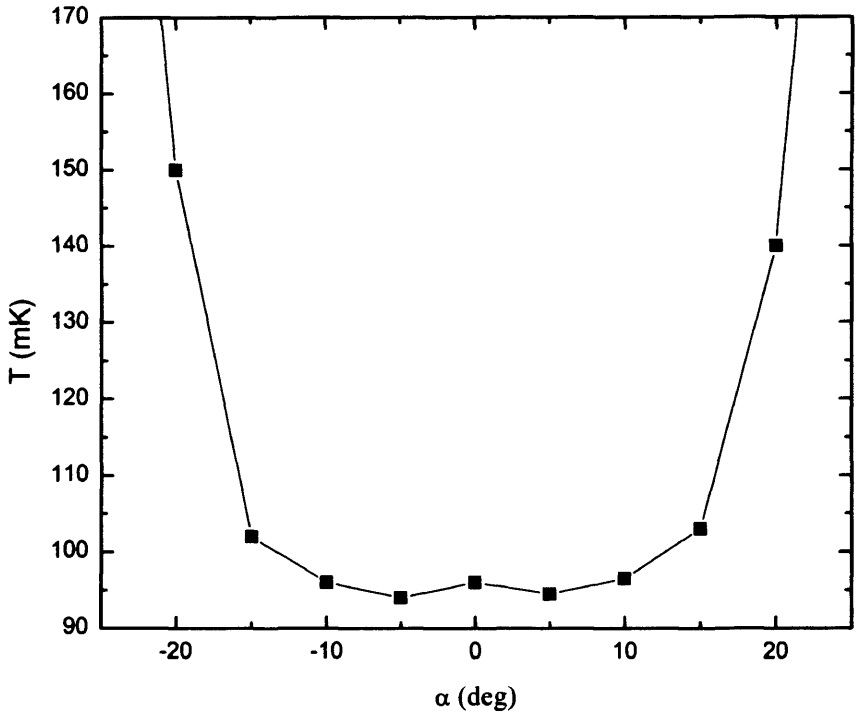

Figure 4.19: Measured m.c. temperature as function of the tilt angle for $P_S = 400\,\mu W$, $\dot{Q} = 3\,\mu W$. Note that optimal performance requires $\alpha \neq 0$.

the amount of mash with about 5% and at the same time increase the still power to $P_S \geq 400\,\mu W$. Using this latter method we then measured the performance of the system under larger tilts. With a thermal load of $3\,\mu W$ to the mixing chamber and $P_S = 400\,\mu W$, the temperature of the mixing chamber was measured as a function of the tilt angle, α. The results are shown in figure 4.19.

From these measurements we conclude that the design is not yet ready to operate on a telescope mount which is non-stationary with respect to the vertical axis. It should not be too difficult however, to make necessary changes which allows for a tilted operation. The most likely explanation to the degraded performance at $|\alpha| > 15°$ is the fact that the phase separation may occur partially outside the mixing chamber. Alternatively, the liquid level in the still may shift significantly in the current design. It is possible that a mixing chamber and a still of much taller and narrower design could be enough to improve on the situation substantially. It would then be easier to ensure that the phase separation remains inside the mixing chamber and that the level of liquid is confined to the still. In fact, we can not be sure that either of these two criteria is fulfilled in the current system even in vertical operation. If for example the phase separation would be just outside of either the entrance or the exit of the mixing chamber, the system may still perform as expected under vertical operation. On the one hand, a thermal lag between the phase separation and the mixing chamber would

develop, but on the other this may only result in a smaller than expected cooling power. It is possible that it would make the optimization of the system easier if the volume of the still and the mixing chamber were increased.

4.7 MDR IN CONTINUOUS OPERATION

4.7.1 EXPERIMENT

The semi-continuous results correspond to the best possible performance of the system. The on-conductance of the heat switches can only be less than that of the solid copper link. Therefore, the results presented in section 4.6 provide a good benchmark when evaluating the continuous operation described here. The two solid copper links which connect the condenser to the evaporator were replaced by two heat switches, as shown in figure 4.20. Throughout these experiments, no extra power was applied to the mixing chamber (i.e. $\dot{Q} = \dot{Q}_0$).

Two different cycle procedures have been tested. The first method is essentially identical with the cycle used for the semi-continuous operation. In this method the charcoal pumps are heated up and cooled down rapidly to achieve a fast cycle. As seen in figure 4.12, cooling down the charcoal pumps dissipates a significant amount of heat on the base plate. It turns out that such power dissipation from the sorption cooler has a devastating effect on temperature stability of the mixing chamber. In an attempt to improve on the temperature stability, the second method therefore involved reducing the power dissipation by extending the cycle over a longer time. This was done by careful control of the heat switches which connect the pumps to the base plate. These gas-gap heat switches can be kept partially switched on by balancing the temperature of the charcoal getter right in the transition region between adsorption and desorption. In general, these heat switches are fully switched off for getter temperatures below 9 K and fully switched on at temperatures above 10 K. By adjusting the getter temperature with a precision of about 10 mK, a very good control of the pump temperature could be achieved.

4.7.2 RESULTS

It is clear from figure 4.12 that power dissipation problem is most severe when the ^{4}He charcoal pump cools down from 45 K. This is because the ^{4}He pump is the largest pump with greatest heat capacity. As it cools down, the temperature of the base plate increases to above 10 K. This will effect the cooling power of the other sorption cooler since the adsorption efficiency of charcoal is a strong function of temperature. As a result of the decreased cooling

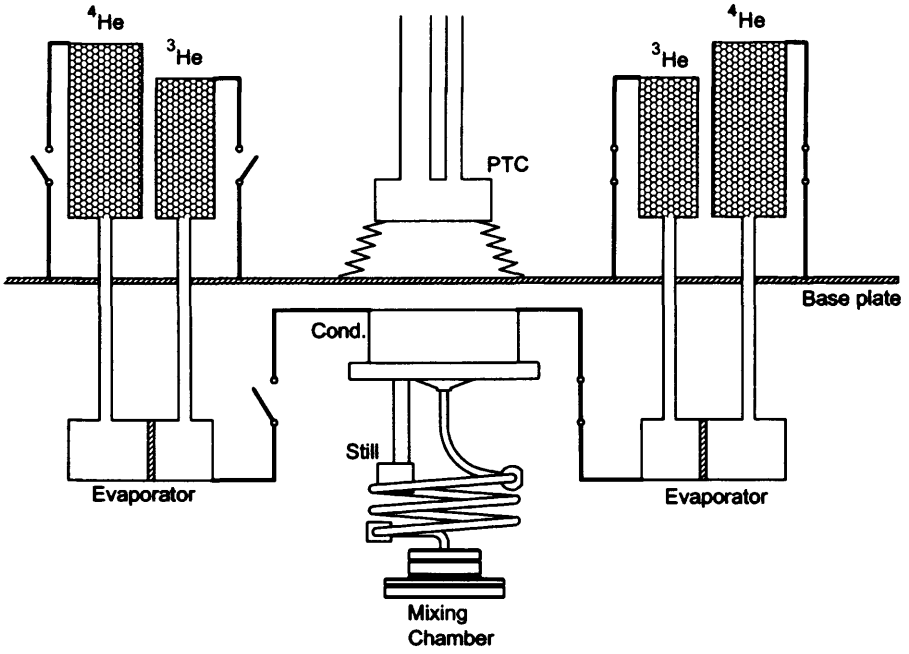

Figure 4.20: Principle schematic of the MDR operating in continuous mode. With the individual heat switches opened and closed as shown above, the left sorption cooler is being recycled whilst the right one is used to keep the condenser cold.

power, the condenser temperature will increase and therefore the ^{3}He circulation rate in the MDR will decrease.

Figure 4.21 shows the result of the extended cycle where the pumps were heated and cooled more slowly. Just a slow cycle, however, was not enough to cancel out the decreased circulation rate. Therefore this method was combined with an increased power to the still. The power to the still was temporarily increased as the charcoal pumps cooled down in order to compensate for the decreased circulation rate. The success of this combined method is illustrated in figure 4.22, where the temperature stability of the two different cycle procedures are compared. With the combined method, the mixing chamber temperature increased by less than 100 μK as the ^{4}He pump cooled down.

Due to the low on-conductance of the heat switch, the condenser was operating at a rather high temperature. As a result, the operating temperature of the mixing chamber was limited to above 90 mK. Nevertheless, the principle of using heat switches to operate the MDR in a fully continuous mode has been successful demonstrated. As was discussed in chapter 3, it should be possible to improve the heat switches further and therefore reach yet lower temperatures.

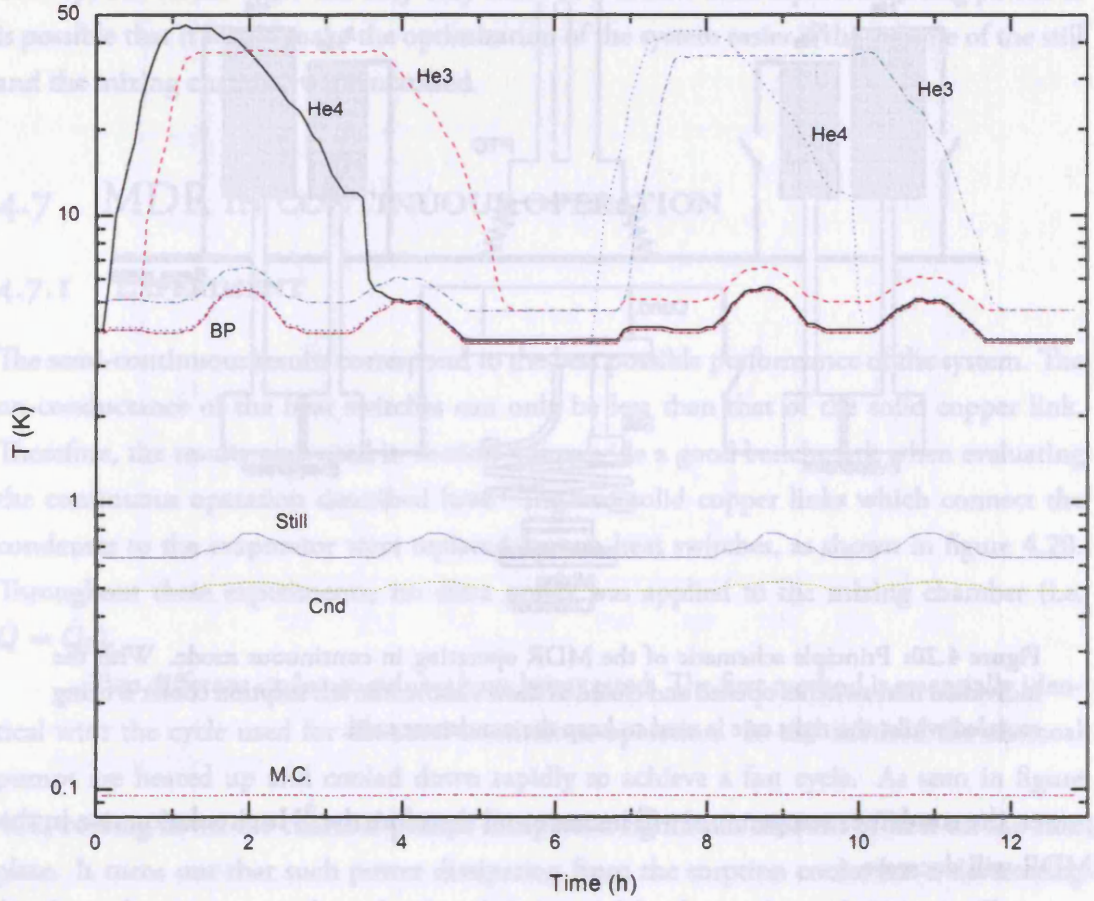

Figure 4.21: Continuous operation of the MDR.

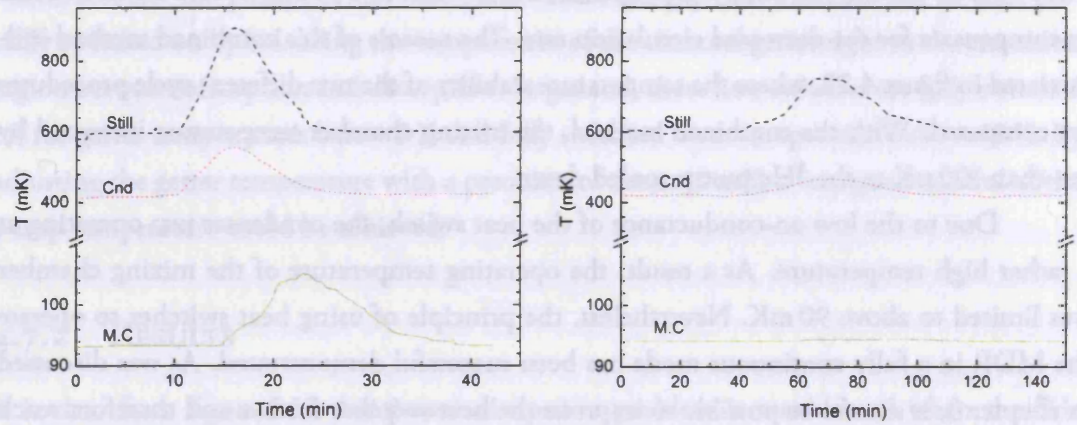

(a) Quick cycle (b) Slow cycle

Figure 4.22: A comparison of the two different cycle procedures. The figures show the temperature stability of the mixing chamber as the ^{4}He pump cools down.

4.8 SOFTWARE CONTROL

An electronic box for thermometry readout and heater controllers have been under development for some time at Cardiff AIG. This electronic was developed for thermometry readout in a earlier CMB experiment (QUAD). An updated version of this DAQ box will be used in another CMB experiment (CLOVER), and we have integrated it with a software control package for operation of the MDR. The DAQ unit features a SNAP[†] chip which allows the user to control all channels by means of a Java XML code. Since the SNAP technology is compatible with a standard IP socket (internet), the XML code can be uploaded remotely to the electronic box from an FTP client. This offers a very convenient way to operate and monitor the entire MDR system remotely. The XML code we wrote for controlling the MDR includes the following features:

1. Automatic control during the cool-down from room temperature to 4 K. The charcoal pumps are kept at a temperature above 25 K which prevents the helium gas to be adsorbed by the charcoal. The gas will circulate inside the sorption coolers which improves the thermal contact between the most isolated parts (evaporator, condenser, mixing chamber) and the base plate. The cool-down time of the system is therefore shortened significantly.

2. A short ^{4}He cycle to condense the remaining mash inside the MDR. Both ^{3}He and ^{4}He charcoal pumps are cooled down simultaneously which rapidly cools the condenser to a temperature of about 1 K. At this temperature, the mash is fully condensed and the system is now ready for its first proper cycle.

3. Automatic night-time cycles of the sorption coolers ensure the system is available for tests during day time.

This cycle scheme, for a semi-continuous operation, is described in more detail in figure 4.23.

4.9 CONCLUSIONS

We have development a miniature dilution refrigerator (MDR) based upon the principle of condensation pumping. Cooling power measurements have been compared with a thermal model to estimate the efficiency of the heat exchanger and the ^{3}He circulation rate. Operating temperatures below 50 mK have been achieved with up to 7 μW of cooling power at 100 mK.

[†]Simple Network Application Platform from ImSys: see for example http://www.imsys.se

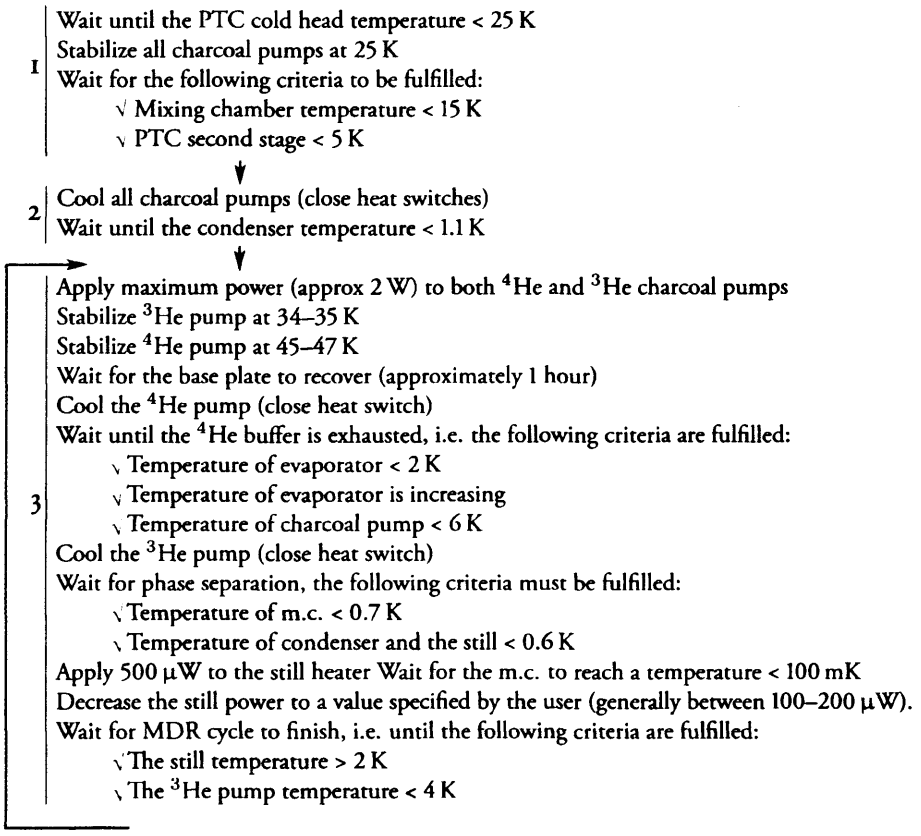

Figure 4.23: The MDR cycle scheme is split into a cool-down from room temperature (1), a quick condensation cycle (2) and a full cycle from 4 K to 50 mK (3).

The MDR has been characterized in detail with measurements of the condensation efficiency, temperature stability, tilted operation and lowest attainable temperature as a function of the still power.

Unlike the original version of this cooler, our system can be operated in a continuous mode to achieve temperatures below 100 mK indefinitely. In particular, we have developed a method of operation which minimizes the heat dissipation from the sorption coolers. This method was used to improve the temperature stability at 100 mK and showed that one of the two sorption coolers can be cycled without impeding the performance of the other.

The MDR has been integrated with a pulse-tube cooler to create a cryogen-free system. Control software for automatic operation from room-temperature down to 50 mK has been written. The entire system can be operated and controlled remotely through a standard web browser or FTP client.

It is clear that the condensation pumped MDR has great potential to become very important for astronomy applications, in particular where infrastructure is limited and where a remote and autonomous operation is essential. Ground based and balloon-borne missions are prime examples of where this kind of cryogenic system is likely to find its first use. In

fact, work is already ongoing to use this system in a CMB experiment (CLOVER) which is to be commissioned in Atacama. CLOVER will cool large TES detector arrays in three separate cryostats; two of which (97 GHz and 150 GHz) will operate below 100 mK.

An MDR system could potentially find applications outside astronomy, in particular where low temperatures are more important than high cooling powers. Examples of where an MDR could be used instead of a conventional dilution refrigerator or an ADR are X-ray spectroscopy and detector developments. Such systems dissipate very little heat and could benefit from a relatively cheap, small, reliable and easy to use system which could be mounted in a standard liquid helium cryostat or a double stage pulse-tube cooler. The user would not have to worry about stray magnetic fields, a limited run-time, leaks, blocks or complicated installation procedures.

5 A Single-shot MDR

In this chapter we present a feasibility study on a single-shot dilution refrigerator which piggy-backs on a double-stage ^{3}He-^{4}He sorption cooler. We calculate the requirements of the ^{3}He buffer and the expected run time below 100 mK. We also describe the design and testing of a prototype, and compare the results from cooling power and duty cycle measurements with a thermal model. Finally, we give suggestions on how to improve the current design in order to realize a powerful system for use in astronomy and other detector applications.

5.1 Introduction

For many experiments, a single-shot operation is sufficient provided the base temperature can be maintained for several hours. For example, many of the ^{3}He sorption coolers used in astronomy today operate at 300 mK for typically 24–48 hours [26, 34, 127, 128], but coolers with a duty cycle as long as 15 days have been constructed for balloon experiments [129]. To recycle these systems takes several hours which result in a duty cycle efficiency of typically 80–90%. There are huge advantages with such single-shot systems in that they are significantly less complicated, cheaper and generally more reliable than their continuous counterparts.

Single, double and triple stage sorption coolers, described in section 1.3.3, have been very popular for some time now. A number of commercial systems are available (Chase Research Cryogenics, Oxford Instruments, VeriCold, Janis) for operation around 300 mK. According to figure 1.15, the cooling power of the dilution refrigerator is higher than the sorption cooler for temperatures as high as 350 mK, and almost five times more powerful at 300 mK. One could then argue that a single-shot dilution refrigerator should be used instead of sorption coolers even at such high temperatures. The enthalpy difference between liquid

and gaseous ^{3}He is, however, much higher than the enthalpy difference between concentrated and diluted ^{3}He. This means that although the sorption cooler is less powerful, it is still much more efficient. For a given duty cycle, the sorption cooler therefore require much less ^{3}He than a single-shot dilution refrigerator do. The dilution refrigerator is more powerful because its cooling power is limited by the enthalpy difference between concentrated and diluted ^{3}He; whilst in a sorption cooler it is limited by the circulation rate[†].

The advantage of a single-shot dilution refrigerator is that it does not require a heat exchanger, which allows it to reach very low temperatures. Limited by viscous heating (see section 4.3.3) only, temperatures below 10 mK could in principle be achieved relatively easily. The duty time at such a low temperature would, however, be very low since most of the ^{3}He would be used during the cool-down phase. Therefore, the main goal of the system described in this chapter, was to achieve and maintain an operating temperature around 0.1 K with a cooling power of the order of a micro-Watt. Larger cooling powers would make the system impractically large for most astronomy applications. Fortunately, the power dissipated by detectors is very low — an array of several hundred TES detectors dissipate typically tens of nano-Watt. Hence the refrigerator must compensate for only the parasitic heat flux delivered to the low-temperature cell through mechanical support structure, vibrations, etc., which can be reduced to a fraction of 1 μW [130, 131]. For example, PLANCK will use a dilution refrigerator with only 0.2 μW of cooling power to operate an array of 48 bolometer at 0.1 K [45].

As with sorption coolers, single-shot dilution refrigerators can be operated by a charcoal pump. In principle, one could for example replace the third stage of the sorption cooler in figure 1.11 with a dilution stage. This creates a system no more complicated than a standard sorption cooler, but capable of much lower temperatures or longer operating times. From now on, we will refer to such a design as a single-shot MDR (ssMDR) to distinguish it from the continuous MDR described in chapter 4.

Any conventional dilution refrigerator can be operated in single-shot mode by simply disabling the ^{3}He return line, thus allowing the system to reach a lower temperature for a short period of time. Very few dilution refrigerators specifically designed for operation in a single-shot mode have been described in literature. Apart from Roach *et. al.* [47, 48, 82, 132] which have been working on a micro-G version for space, no attempts appear to have been made to build a miniature system utilizing sorption pumps which could be used for astronomy. Nor have any commercial products been introduced on the market.

[†]Strictly speaking, there is of course no such thing as a 'circulation rate' in a single-shot system. For simplicity we will ignore this and use the same notation, $\dot{n}$, to express the molar flow rate in ^{3}He sorption coolers and single-shot dilution refrigerators.

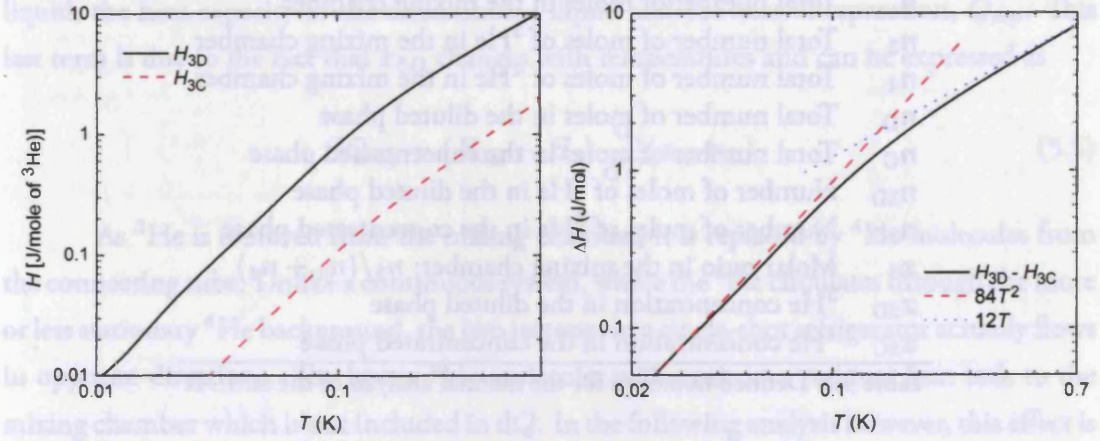

Figure 5.1: Enthalpy of concentrated ^{3}He and diluted ^{3}He along the coexistence curve (left), and ΔH together with high and low-temperature approximations (right).

5.2 THERMAL MODEL

In chapter 4 we gave a detailed overview of the theory of dilution cooling. From this we see that the cooling power of the ssMDR is given by equation 4.18 for $T \lesssim 0.1$ K. In a single-shot system, the cooling power is dictated by the required run-time. Thus the emphasis will instead be on how to ensure the ^{3}He in the concentrated phase is used most efficiently. That is, how to ensure that as little ^{3}He as possible is wasted during the cool-down to 100 mK.

Since the high and low-temperature regimes are equally important for this analysis, we can not rely on the same enthalpy expressions used in chapter 4. The entropy coefficients (γ_D and γ_C) were used in chapter 4 in the low-temperature approximation: $\Delta H = (\gamma_D - \gamma_C)T^2$. They can, however, only be used in the linear entropy and hence heat capacity regime. Indeed, strictly speaking, they are only valid for temperatures below 50 mK, although for our purposes they are useful up to about 100 mK. At temperatures around and above 200 mK, the heat capacity of both diluted and concentrated ^{3}He is almost constant with temperature. The cooling power is therefore almost linear at high temperatures, and so the theoretical model used in chapter 4 is no longer valid.

In this section, we will rely on experimental data (figure 5.1), originally from Radebaugh [109] but here taken from Lounasmaa [85]. These data can be differentiated to get values for the heat capacities since for a reversible process: $C_P = (\partial H/\partial T)_P$. Figure 5.1 shows the enthalpy of the diluted and concentrated ^{3}He along the coexistence curve. We have also plotted ΔH together with the low-temperature approximation $(\gamma_D - \gamma_C)T^2$. For clarity, a linear fit to the high-temperature region is also included.

Before discussing the dilution refrigerator, consider a sorption cooler in which n_0 moles of ^{3}He have been condensed at temperature T_0. Some of the liquid will be used

n	Total number of moles in the mixing chamber
n_3	Total number of moles of ^{3}He in the mixing chamber
n_4	Total number of moles of ^{4}He in the mixing chamber
n_D	Total number of moles in the diluted phase
n_C	Total number of moles in the concentrated phase
n_{3D}	Number of moles of ^{3}He in the diluted phase
n_{3C}	Number of moles of ^{3}He in the concentrated phase
x_3	Molar ratio in the mixing chamber: $n_3/(n_3 + n_4)$
x_{3D}	^{3}He concentration in the diluted phase
x_{3C}	^{4}He concentration in the concentrated phase

Table 5.1: Defined notations for the thermal analysis of the ssMDR

as the liquid cools by evaporation from T_0 down to temperature T. For example, as the temperature changes with dT' at temperature T', a fraction dn of the ^{3}He will evaporate:

$$dn = -\frac{c_v(T')}{L_3(T')} n \, dT' . \tag{5.1}$$

Separation of n and integration yields:

$$\frac{n(T)}{n_0} = \exp\left(-\int_T^{T_0} \frac{c_v(T')}{L_3(T')} dT' \right) . \tag{5.2}$$

Using data for the latent heat and specific heat [133] and assuming a condensation temperature $T_0 = 2\,\mathrm{K}$, we find $n(0.3\,K)/n_0 = 0.751$. Thus, almost 25% of the liquid has been used. If, however, the condensation temperature is 1 K we find $n(0.3\,K)/n_0 = 0.927$ so less than 8% of the liquid will be used. Now, an equivalent analysis can be done for the single-shot dilution refrigerator. This means calculating how much ^{3}He will be removed from the mixing chamber as the mixture cools down.

To do this we will use the notations defined in table 5.1. It is assumed that the mixing chamber has already been cooled by a ^{3}He evaporator to a temperature, T_0, at which phase separation has occurred in the mixing chamber. To calculate the amount of ^{3}He being used as the mixing chamber cools from T_0 to T_1, we start with the following equation:

$$-dn_3 = \frac{dQ}{H_{3D} - H_3} , \tag{5.3}$$

where dQ is the amount of energy required to remove dn_3 moles of ^{3}He from the mixing chamber:

$$dQ = (C_{3D}\, n_{3D} + C_3 n_{3C})\, dT + dQ_{sep} . \tag{5.4}$$

Equation 5.4 consists of three terms which take into account the heat capacity of the diluted

liquid, the heat capacity of the concentrated liquid and the heat of separation, Q_{sep}. This last term is due to the fact that x_{3D} changes with temperatures and can be expressed as

$$dQ_{sep} = (H_{3D} - H_3)\frac{d}{dT}(x_{3D}n_D)\,. \tag{5.5}$$

As ^{3}He is removed from the mixing chamber, it is replaced by ^{4}He molecules from the connecting tube. Unlike a continuous system, where the ^{3}He circulates through the more or less stationary ^{4}He background, the two isotopes in a single-shot refrigerator actually flows in opposite directions. The hotter ^{4}He molecules will result in a residual heat leak to the mixing chamber which is not included in dQ. In the following analysis however, this effect is ignored and the ^{4}He molecules are assumed to be cooled by the ^{3}He which move up the tube towards the still. This should be a moderate simplification since, at low temperatures, the heat capacity of liquid ^{3}He is several orders of magnitude higher than that of ^{4}He. Further to this, and in analogy with the perfect heat exchanger model discussed in chapter 4, viscous heating and lateral heat conduction through the liquid and the tube is ignored.

Solving equation 5.3 analytically is difficult because the number of moles of ^{3}He in the upper as well as in the lower phase changes with temperature. Numerically, we can use a program to iterate from T_0 to T_1 in small temperature steps of ΔT. At each temperature, the concentration and number of moles in the concentrated and diluted phase can be evaluated. The amount of heat, ΔQ, required to decrease the temperature ΔT can then be calculated for each step. This gives the number of ^{3}He molecules, Δn_3, which need to be removed. The amount of ^{3}He in the concentrated phase is then decreased accordingly. With n_{3D} and n_{3C} being the number of moles of ^{3}He in each phase, and Δn_{3D} being the number of moles which separates from the diluted phase:

$$-\Delta n_3 = \frac{C_{3D}n_{3D} + C_3 n_{3C}}{H_{3D} - H_3}\Delta T + \Delta n_{3D}\,. \tag{5.6}$$

Ignoring the molar difference between ^{3}He and ^{4}He, the total number of moles of liquid in the mixing chamber can be assumed to be constant with temperature:

$$n = n_3 + n_4 = n_D + n_C\,. \tag{5.7}$$

At any temperature, we also have

$$n_3 = x_{3D}n_D + x_{3C}(n - n_D)\,. \tag{5.8}$$

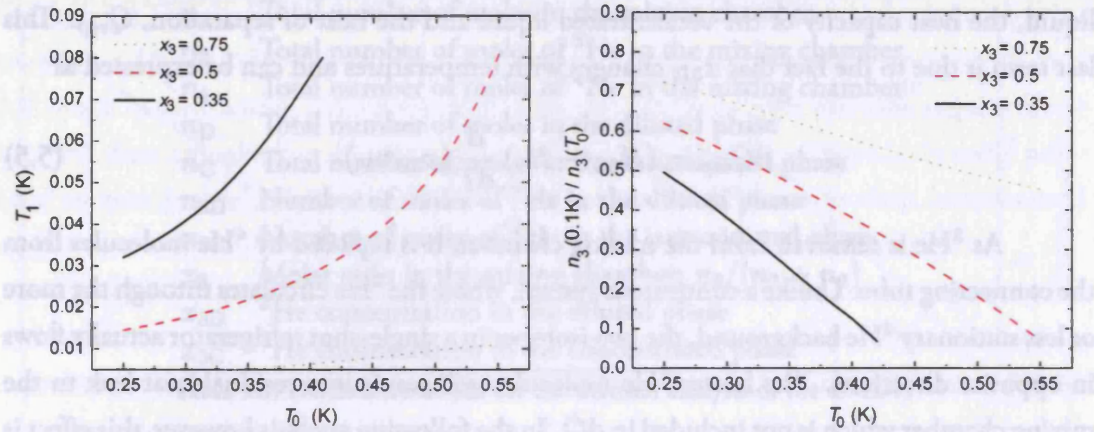

(a) Lowest attainable temperature

(b) Fraction of ^{3}He available at 0.1 K

Figure 5.2: Calculated performance of the ssMDR. Figure (a) shows the lowest attainable temperature, T_1, as a function of the initial temperature, T_0, to which the mixing chamber was cooled by a ^{3}He sorption cooler. Figure (b) shows how much ^{3}He is available for operation at 100 mK. For example with $x_3 = 0.5$ and $T_0 = 0.3$ K, 55% of the initial amount of ^{3}He is left once the mixing chamber has reached $T_1 = 0.1$ K

Using equations 5.7 and 5.8, it is straightforward to show that

$$n_{3D} = \frac{n_3 - x_{3C} n}{x_{3D} - x_{3C}} x_{3D}\,, \tag{5.9}$$

$$n_{3C} = \left(n - \frac{n_{3D}}{x_{3D}} \right) x_{3C}\,. \tag{5.10}$$

Solving equation 5.6 numerically for various values of the initial temperature, T_0, yields figure 5.2. Solutions have been plotted for three different values of x_3. Note that x_3 is the initial ^{3}He molar ratio of the mash: $n_3(T_0)/\left[n_3(T_0) + n_3(T_1)\right]$. We can now see the importance of the initial temperature; a 50% mixture will have almost 3 times more ^{3}He available at 0.1 K with $T_0 = 0.3$ K in comparison with $T_0 = 0.5$ K. In fact, in a 50% mixture, temperatures below 50 mK can only be achieved for $T_0 < 0.5$ K. We also conclude that much can be gained from using a rather high ^{3}He ratio. For example, if we assume $T_0 = 0.5$ K, a factor of 2.5 more ^{3}He will be available at 0.1 K with $x_3 = 0.75$ in comparison with $x_3 = 0.5$. This is because the heat capacity of diluted ^{3}He is much higher than that of concentrated ^{3}He. With a lower initial temperature however, the benefit is less significant.

With a 50% mixture and $T_0 = 0.3$ K temperatures below 20 mK can be achieved, if only for a very short time. Alternatively, more than 50% of the ^{3}He would be available for operation at 100 mK. Given a required cooling power, $\dot{Q}$, and duty cycle, t, one can readily calculate the number of moles of ^{3}He, n_3, with which the system need to be charged. For

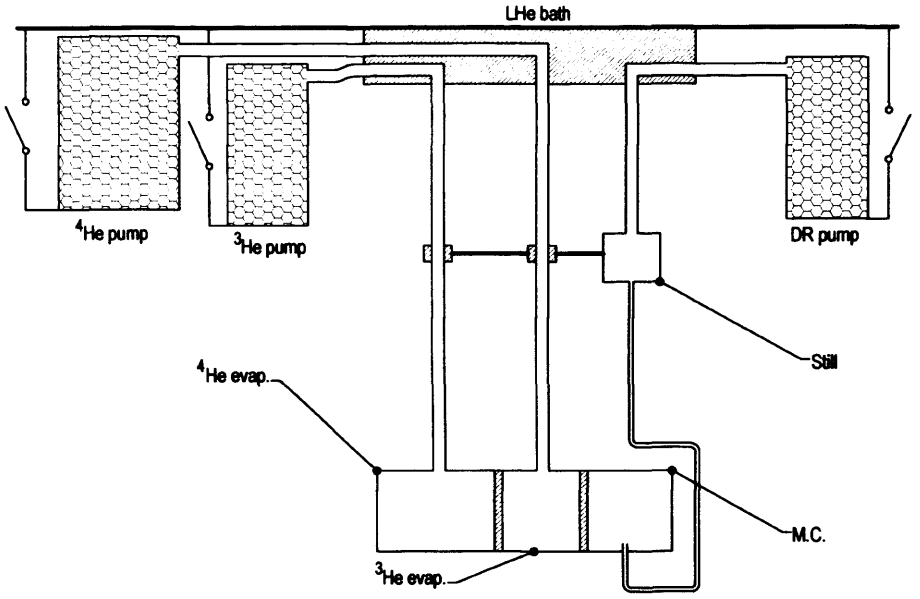

Figure 5.3: Principle schematic of the ssMDR, operated in a LHe cryostat. A double stage ^{3}He-^{4}He sorption cooler cools the mixing chamber to a temperature below 0.4 K. The still is used to thermally intercept conductive loading through pumping lines

example, with $x_3 = 0.5$, $\dot{Q} = 1\,\mu$W, $t = 12$ hours, $T_1 = 0.1$ K and $T_0 = 0.3$ K we have

$$n_3 = \frac{\dot{Q}t}{\Delta H(T_1)} \frac{n_3(T_0)}{n_3(T_1)} = 0.23\,mol\,. \tag{5.11}$$

This corresponds to 5.8 L (STP) of ^{3}He gas. If x_3 was increased to 0.75, this figure could be decreased to about 4.7 L.

5.3 ssMDR Design

Figure 5.3 shows the overall schematic of the ssMDR, mounted in liquid helium cryostat. Figure 5.4 shows two photographs of the system. The mixing chamber is in direct thermal contact with the ^{3}He/^{4}He evaporator. This arrangement has the obvious advantage of that it makes it easy to pre-cool the mash to a temperature at which dilution cooling can be initiated. On the other hand, it means that the residual heat leak will be dominated by conduction through the sorption cooler's pumping lines. To minimize this heat leak, a thermal link connects to the still half way up the pumping lines.

The still acts as a thermal buffer for a 0.7 K radiation shield and cryogenic wires. Thermometry and heater wires (in total 10 of 5 cm long ⌀0.07 mm manganin) conduct less than 0.1 μW. The double stage refrigerator looks rather different to how it is presented in figure 5.3. As shown in figure 5.5, its pumping line assembly is more complicated and the

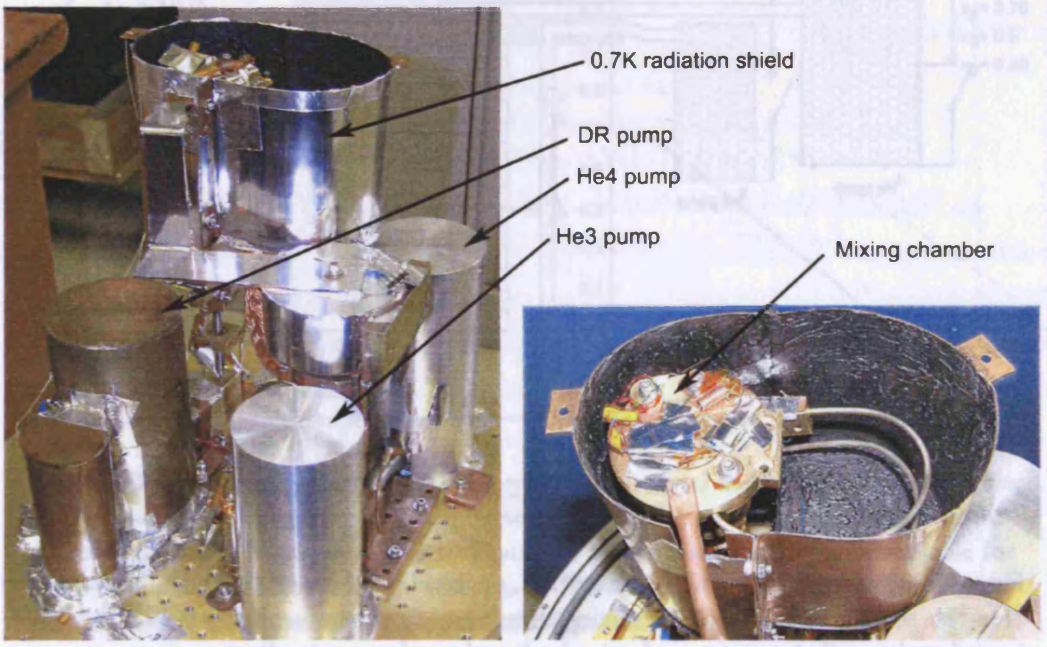

Figure 5.4: Photographs of the ssMDR. Cryopumps, evaporator, thermal link and 0.7 K radiation shield (left), and mixing chamber (right).

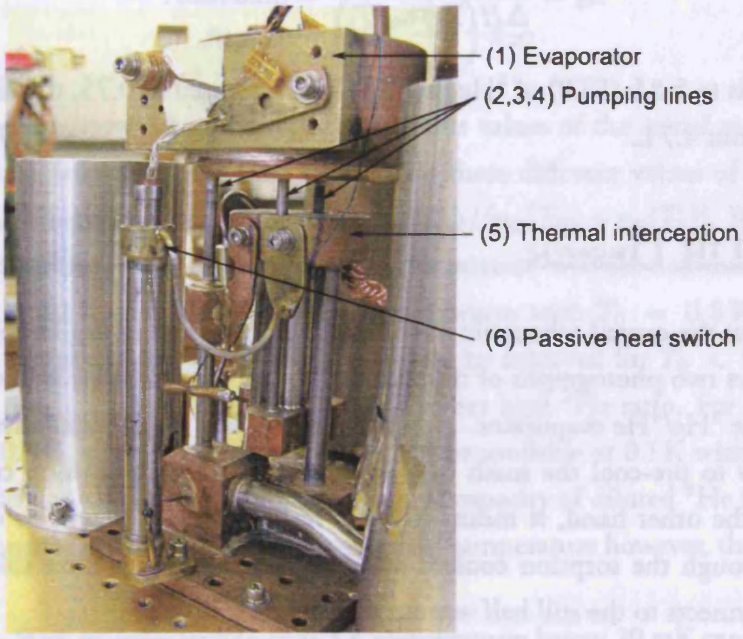

Figure 5.5: The double-stage sorption cooler. The thermal interception point (5) is connected to the still via a copper braid. The passive heat switch has a cold 'foot' which also connects to (5) in order to reduce its off-conductance.

diameter of the various tubes change in diameter. Unfortunately, the design of this particular refrigerator is not ideal for our applications because the thermal load to the evaporator (1) will be quite high. The thermal link from the still intercepts at point (2). Conduction from this point to the mixing chamber is possible through three different tubes (3), (4) and (5). By assuming the temperature of point (2) to be 0.7 K, we find an expected heat leak to the mixing chamber (at 0.1 K) of 2.5 μW.

The passive gas-gap heat switch shown in figure 5.5 (6) was used to help the evaporator and the mixing chamber to cool from room temperature down to LHe temperatures. This heat switch is of a 'tube-in-tube' (or triple-tube) design which results in a three-times longer thermal path between the two conductors when the heat switch is off. The heat leak is reduces further by a thermal link from the still connected half way up the this triple-tube. It operates in a passive mode since the charcoal getter is inside the heat switch itself; it is therefore not possible to control the on/off state of the switch manually. The switch remains in its on-state until the temperature of the hot end drops below 12 K.

The design of the mixing chamber is essentially the same as in the continuous MDR with a copper mesh resulting in a total surface area of 200 cm^2. A 470 mm long, ∅2.2 × 0.125 mm copper-nickel tube, which connects the mixing chamber to the still, enters the mixing chamber from beneath. The length of this tube is probably excessive since most of the conducted heat will be absorbed by the ^{3}He as it flows towards the still. Anyway, its volume is relatively small and the tube is coiled up so it does not take up much space.

The still is a simple copper cylinder without any film burner, connected to the condenser by a ∅6.4 × 0.1 mm stainless steel tube. In a continuous system, any circulating ^{4}He could have a serious effect on the efficiency of the heat exchangers; in a single-shot system, however, the consequences of a superfluid film flow should be limited. On the one hand, an unnecessary amount of ^{4}He will be evaporated from the system. But on the other, the ^{4}He would not impede the dilution cooling in any way since there is no heat exchanger.

The volume of the still is such that it is empty when all the ^{3}He in the mixing chamber is exhausted — that is, the volume of the still equals the total volume of ^{3}He liquid. The volumes of other parts of the ssMDR, and the amount of ^{3}He and ^{4}He liquid, are given in table 5.2.

5.4 EXPERIMENTS

Lakeshore-calibrated germanium and ruthenium-oxide RTDs were used to measure the temperature of the mixing chamber and the still. Silicon diodes, calibrated against a Lakeshore RhFe sensor were used to measure the temperatures of the base plate, the charcoal pumps

Volume of still	6.2 cm^3
Volume of m.c. (excl. mesh)	10.6 cm^3
Volume of tube	1.5 cm^3
Surface area of m.c.	200 cm^2
Total volume of ^{3}He liquid	6.0 cm^3 (0.163 mol)
Total volume of ^{4}He liquid	12.2 cm^3 (0.442 mol)
Volume of ^{3}He gas (STP)	3.9 L
Volume of ^{4}He gas (STP)	10.6 L
Overall molar ratio $n_3/(n_3 + n_4)$	0.27
Molar ratio in m.c.	0.5
Total internal volume of MDR	140 cm^3
Equiv. room-temperature pressure	104 bar

Table 5.2: Design parameters of the ssMDR.

and heat switch getters. All thermometers were operated in a 4-wire configuration. The following experiments were performed in a number of separate cool-downs.

1. A large number of cool-downs were carried out in order to optimize the cycle procedure of the system. The most important aspect of the procedure was to ensure that all the ^{3}He in the evaporator was exhausted before the dilution cooling was initiated. If a significant amount of ^{3}He were to remain in the evaporator, this liquid would have contributed with a non-negligible heat capacity. This would result in an unnecessary amount of the ^{3}He in the mixing chamber being used, and thus shorten the duty time at 100 mK.

2. We measured the cooling power of the refrigerator at several different temperatures. The most useful information from these tests came from comparing the results with the thermal model; in particular we got an estimate of the ^{3}He circulation rate and the parasitic heat load.

3. The power to the still was reduced in order to stabilize the mixing chamber at 100 mK. The purpose of this was to extended the duty time and provided an estimate of the amount of remaining ^{3}He.

5.5 RESULTS

5.5.1 CYCLE PROCEDURES

Figures 5.6 and 5.7 depict the result of a successful cool-down to 73 mK. In this cycle too much ^{3}He had been condensed in the evaporator, and it therefore took several hours from

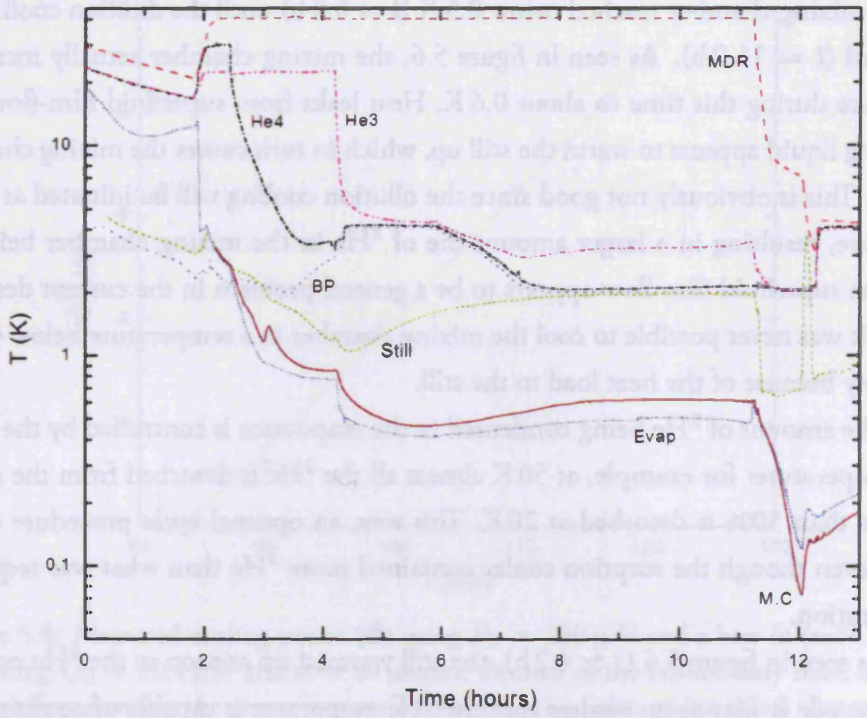

Figure 5.6: In this cycle, the evaporator contained slightly too much ^{3}He which resulted in an unnecessary long cycle time. The ^{3}He buffer is not exhausted until $t = 11$ h, at which point the mixing chamber had warmed up from ~ 0.5 K to ~ 0.6 K. Despite this, the mixing chamber cools down to 73 mK.

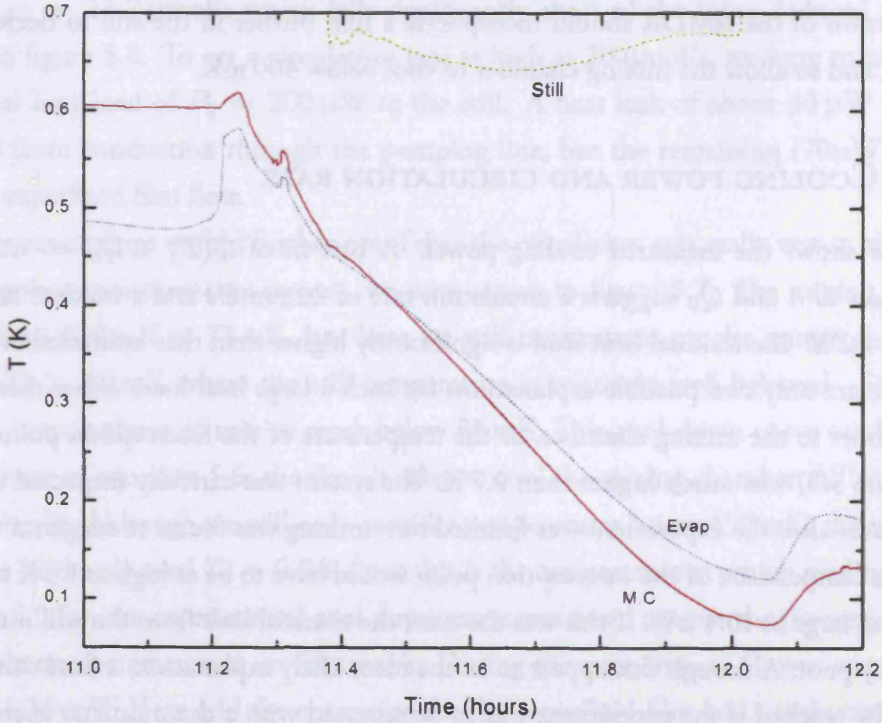

Figure 5.7: The ^{3}He in the mixing chamber was eventually exhausted and the cycle finished.

when the mixing chamber reached below 0.5 K ($t = 5.5$ h) until the dilution cooling could be initiated ($t = 11.2$ h). As seen in figure 5.6, the mixing chamber actually increased in temperature during this time to about 0.6 K. Heat leaks from superfluid film-flow and/or condensing liquid appears to warm the still up, which in turn causes the mixing chamber to warm up. This is obviously not good since the dilution cooling will be initiated at a higher temperature, resulting in a larger amount the of ^{3}He in the mixing chamber being used. In fact, the superfluid film flow appears to be a general problem in the current design. For example, it was never possible to cool the mixing chamber to a temperature below 460 mK, presumably because of the heat load to the still.

The amount of ^{3}He being condensed in the evaporator is controlled by the charcoal pump temperature: for example, at 50 K almost all the ^{3}He is desorbed from the charcoal, whilst less than 50% is desorbed at 20 K. This way, an optimal cycle procedure could be achieved even though the sorption cooler contained more ^{3}He than what was required for our application.

As seen in figure 5.6 ($t \simeq 4.2$ h), the still warmed up as soon as the ^{4}He evaporator was exhausted. It may seem strange that the ^{4}He evaporator is capable of cooling the still whilst the ^{3}He evaporator is not. This is because a superfluid film-flow from the ^{4}He evaporator will effectively provide a thermal link between the evaporator and the still (which is connected half way up the pumping line). This thermal link is broken as soon as the ^{4}He is exhausted; apparently the evaporated ^{3}He gas does not provide a similar thermal link. A future version of the ssMDR should incorporate a film burner in the still to decrease the heat leak, and so allow the mixing chamber to cool below 400 mK.

5.5.2 COOLING POWER AND CIRCULATION RATE

Figure 5.8 shows the measured cooling power. A best fit of $\dot{Q}(T) + \dot{Q}_0 = \dot{n}\Delta H(T)$ with respect to $\dot{n}$ and $\dot{Q}_0$ suggests a circulation rate of 20 μmol/s and a residual heat load $\dot{Q}_0 = 10.4$ μW. The residual heat load is significantly higher than that estimated in section 5.3. There are only two possible explanations for such a large heat load; either there was a thermal short to the mixing chamber, or the temperature of the interception point (point (1) in figure 5.5) was much higher than 0.7 K. The system was carefully inspected at room temperatures after the experiment was finished but nothing was found to suggest a thermal short. The temperature of the interception point would have to be as high as 1.5 K to give a heat leak as large as 10.4 μW. If this was the case, the thermal link from the still must have been pretty poor. Although this appear to be the most likely explanation, a final conclusion can only be reached if the experiment was to be repeated with a thermometer mounted at the interception point.

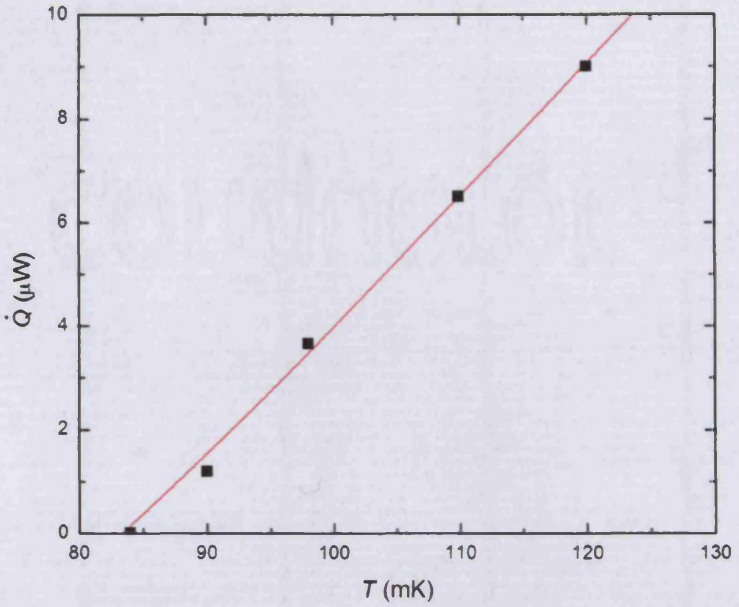

Figure 5.8: Measured cooling power (■) using $P_S = 280\,\mu W$ and a best fit (solid line) suggesting $\dot{Q}_0 = 10.4\,\mu W$ and $\dot{n} = 20\,\mu mol/s$. Because of the limited duty time, it was difficult to ensure that the system was perfectly stable at each data point; this is why several of the data points deviates from the theoretical line.

The applied power to the still heater was $P_S = 280\,\mu W$ during the cooling power experiment. Using $L_{3D} = 24\,J/mol$ (from section 4.3.1), this should give a circulation rate of $P_S/L_{3D} = 11.7\,\mu mol/s$ which falls significantly short of the value deduced from the best fit in figure 5.8. To get a circulation rate as high as 20 μmol/s, we have to assume an additional heat load of $P_0 = 200\,\mu W$ to the still. A heat leak of about 30 μW could be expected from conduction through the pumping line, but the remaining 170μW must be due to a superfluid film flow.

In an attempt to find further proof that the circulation rate really was as high as the cooling-power measurements suggest, we now return to figure 5.7. The mixing chamber cooled from 600 mK to 73 mK, but here we will concentrate on the temperature range $450 > T > 80\,mK$ where the still temperature is relatively well behaved. Starting at 450 mK, it took about 35 min to reach below 80 mK. This cool-down curve can be reproduced by use of equation 5.6: the time it takes to cool the mixing chamber ΔT is given by $\Delta t = \Delta n_3/\dot{n}$. Although we will only consider temperatures below 450 mK, the numerical iterations obviously used $T_0 = 0.6\,K$ since this is the temperature at which cooling started. In figure 5.9 (a), the experimental cool-down curve was fitted against the theoretical curve, using only one parameter: $\dot{n} = 64\,\mu mol/s$. During the experiment, P_S was constant and equal to 1.36 mW. If we add the correction for the superfluid film and conductive loading ($P_0 = 200\,\mu W$), we find that the circulation rate should have been 65 μmol/s. This agrees

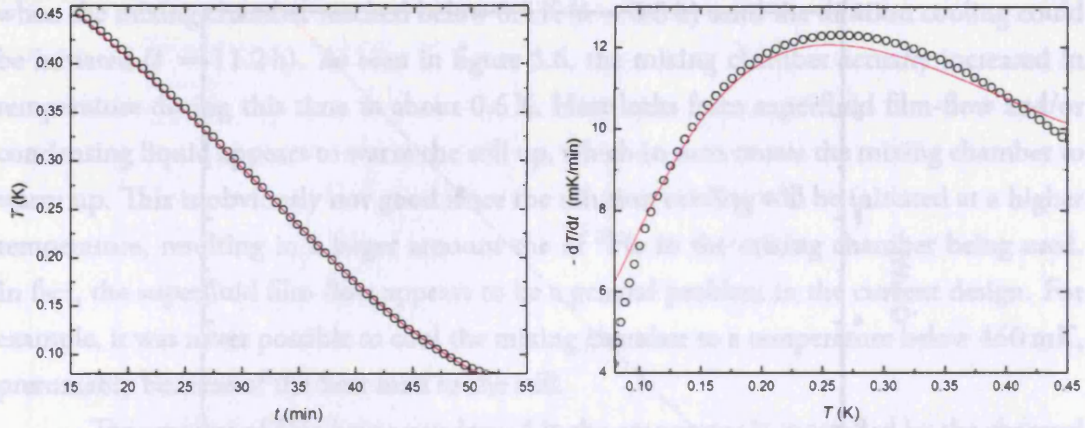

(a) The cool-down from figure 5.7.

(b) The slope of the cool-down curve.

Figure 5.9: A Cool-down using $P_S = 1.36\,\text{mW}$; experimental values (o) and thermal model (solid line). A best fit of the thermal model using a single parameter, $\dot{n}$, suggest a circulation rate of 64 µmol/s. This agrees well with what one would expect from the cooling-power measurements. For more information see text.

well with the theoretical fit and therefore suggest that the excessive heat load to the still really is due to the superfluid film flow. In conclusion, two separate and rather different experiments both suggest a circulation rate significantly higher than what one would calculate from P_S.

Figure 5.9 (b) shows the cooling rate; measured (o) and theoretical fit (solid line). Of course, the absolute values agrees well because $\dot{n}$ was the parameter used in the curve fit. However, it is reassuring to find that the thermal model largely reproduce the same features seen in the experimental data: the cooling rate has a maximum at around 250 mK and decreases faster at lower temperatures than at higher temperatures. This adds credibility to the model and suggest that all the dominant factors have been taken into account.

5.5.3 EXTENDED DUTY CYCLE

To save time, the m.c. can be cooled from T_0 to T_1 using a rather high still power. The still power can then be reduced once T_1 has been reached, this way the duty cycle time is maximized. Figure 5.10 shows a cool-down from $T_0 = 0.5\,\text{K}$ during which the still power was reduced at $T_1 = 0.1\,\text{K}$ in order to stabilize the temperature of the mixing chamber. With $P_S = 100\,\mu\text{W}$, the mixing chamber remained at 100 mK for about $t = 46\,\text{min}$ until the ^{3}He was exhausted.

According to the theoretical prediction, figure 5.2, 19% of the initial amount of ^{3}He should be available for operation at 0.1 K. With values for P_S and P_0 from above, we find a

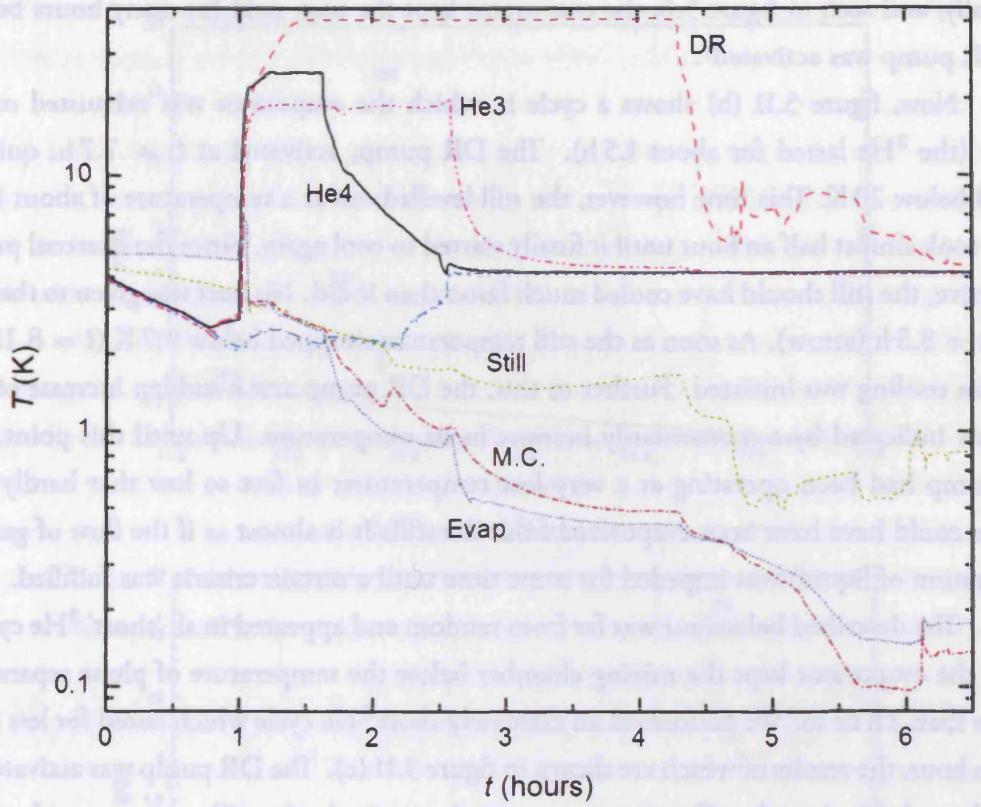

Figure 5.10: The still power is reduced at 100 mK in order to extend the duty cycle.

circulation rate $\dot{n} = 15$ µmol/s. Thus 19% of the ^{3}He should last for about 51 min, which is in remarkable agreement with the experimental value.

The benefit of this method was not great due to the rather large parasitic heat leak to the mixing chamber. If the heat leak had been of a more reasonable value, say 1–2 µW, the circulation rate could have been reduced to a few µmol/s which would have extended the duty cycle to several hours. Nevertheless, the experiment demonstrated the principle of this method and confirmed the accuracy of the thermal model.

5.5.4 Impeded ^{3}He-circulation phenomena

Under certain conditions, the ssMDR behaved as if the ^{3}He circulation was severely impeded. The purpose of this section is to describe the conditions under which this phenomena was observed together with a possible explanation.

We first return to the cycle shown in figure 5.6, but now we concentrate on the temperatures of the still, mixing chamber and the DR pump. Figure 5.11 (a) shows the behaviour of the still as the DR pump cooled down. When the DR pump reached below 20 K, the adsorption was efficient enough to cool the still to a temperature below 0.7 K. Heat was applied to the still at $t = 11.37$ h (arrow) whereby dilution cooling was initiated.

Crucially, and seen in figure 5.6, the evaporator kept the m.c. cold for many hours before the DR pump was activated[†].

Now, figure 5.11 (b) shows a cycle in which the evaporator was exhausted much earlier (the ^{3}He lasted for about 1.5 h). The DR pump, activated at $t = 7.7$ h, quickly cooled below 20 K. This time however, the still levelled out at a temperature of about 1.1 K and it took almost half an hour until it finally started to cool again. Since the charcoal pump was active, the still should have cooled much faster than it did. No heat was given to the still until $t = 8.3$ h (arrow). As soon as the still temperature dropped below 0.7 K ($t = 8.15$ h), dilution cooling was initiated. Further to this, the DR pump saw a sudden increase of the gas flow indicated by a momentarily increase in its temperature. Up until this point, the DR pump had been operating at a very low temperature; in fact so low that hardly any vapour could have have been evaporated from the still. It is almost as if the flow of gas (or evaporation of liquid) was impeded for some time until a certain criteria was fulfilled.

The described behaviour was far from random and appeared in all 'short' ^{3}He cycles, where the evaporator kept the mixing chamber below the temperature of phase separation for less than 2 h or so. We performed an extremely short ^{3}He cycle which lasted for less than half an hour, the results of which are shown in figure 5.11 (c). The DR pump was activated at $t = 7$ h, and this time the effect was even more dramatic. As the still temperature dropped ($t = 7.7$) the DR pump saw a massive heat load; again, this can only be explained by a sudden and very large increase of the ^{3}He evaporation.

Roach *et. al.* [47] observed a very similar phenomena in their micro-G ssMDR. In their experiment, the still cooled to about 0.8 K and remained stable for about an hour until its temperature finally dropped. They concluded that this must be an effect of the very fine pores in the sinter, which they used to confine the liquid to the mixing chamber and the still. By introducing a 'coefficient of sticking', they managed to reproduce this phenomena in their thermal model. Although their model appears to have been very successful in describing many other features of their system, it is to some extent in contradiction with our findings. Fine-pore sinter is not used in our refrigerator, thus the observed phenomena must originate from something else.

We propose that the dilution cooling is instead impeded by the ongoing phase separation in the system. Under certain conditions, superfluid ^{4}He can form regions of normal and superfluid liquids which can remain stable for long times. An example of when this happens is a LHe cryostat which has been cooled by evaporation to a temperature below T_λ. After the pump has switched off and the pressure above the liquid has increased to 1 atm, the temperature of the liquid should quickly reach 4.2 K. This is however, not always what

[†]That is, allowed to cool down to a temperature at which adsorption will start (broadly speaking, this happens at temperatures below 25 K).

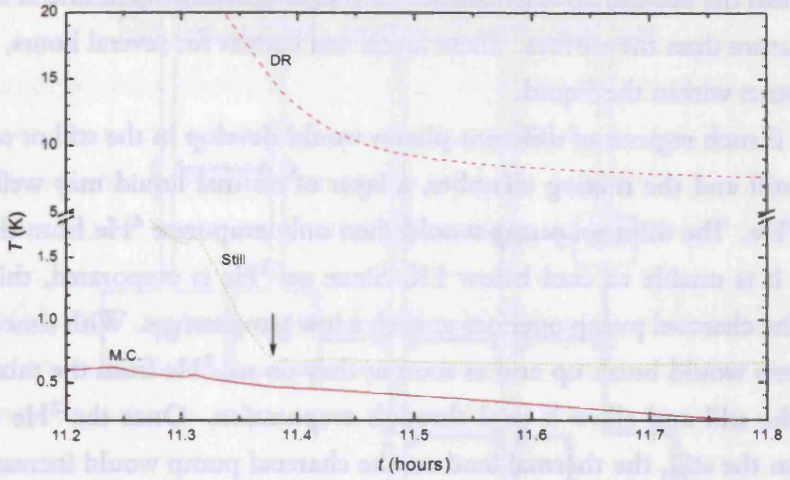

(a) Extended ^{3}He cycle

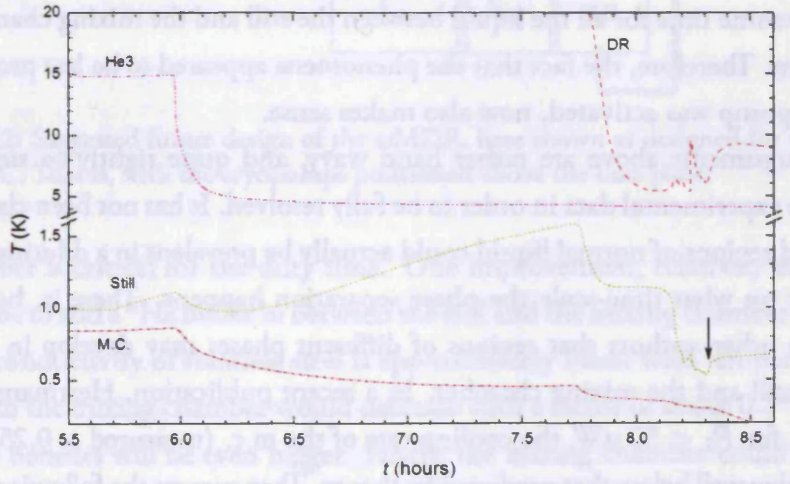

(b) Standard ^{3}He cycle

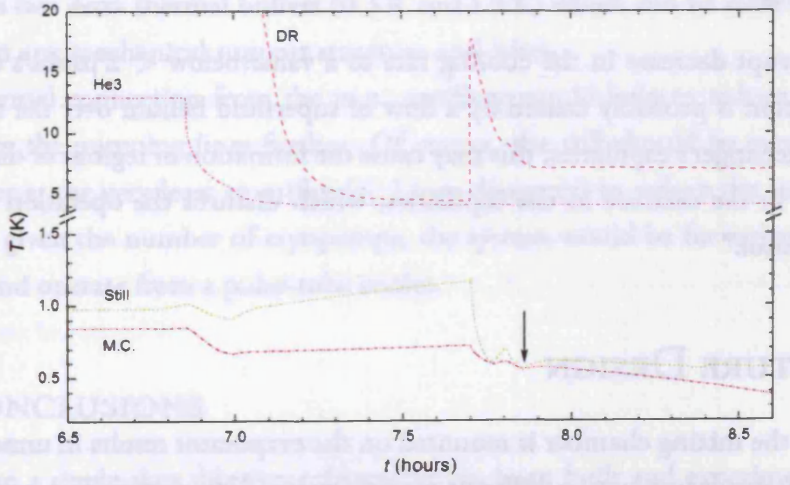

(c) Short ^{3}He cycle

Figure 5.11: The impeded flow of ^{3}He from mixing chamber to still is illustrated in three different scenarios: the mixing chamber has been kept cold for almost 7 h (a), for about 1.5 h (b) and for less than 0.5 h (c). The arrows indicate when the still power was applied.

happens. Instead the bottom layer usually remains in a superfluid state, and at a significantly lower temperature than the surface. These layers can coexist for several hours, despite large thermal gradients within the liquid.

Now, if such regions of different phases would develop in the still or somewhere in between the still and the mixing chamber, a layer of normal liquid may well prevent the transport of ^{3}He. The dilution pump would then only evaporate ^{4}He from the still which explains why it is unable to cool below 1 K. Since no ^{3}He is evaporated, this would also explain why the charcoal pump operates at such a low temperature. With time, the normal-superfluid layers would break up and as soon as they do so, ^{3}He from the mixing chamber could reach the still and allow it cool through evaporation. Once the ^{3}He is allowed to evaporate from the still, the thermal load on the charcoal pump would increase which also agrees with our observations[†]. Presumably the phase separation process is not instantaneous, it should take some time for all the liquid between the still and the mixing chamber to reach an equilibrium. Therefore, the fact that the phenomena appeared to be less pronounced the later the DR pump was activated, now also makes sense.

The arguments above are rather hand wavy, and quite rightly so since this issue requires more experimental data in order to be fully resolved. It has not been clarified wether or not isolated regions of normal liquid could actually be prevalent in a dilution refrigerator, nor is it clear on what time-scale the phase separation happens. There is, however, some support from other authors that regions of different phases may develop in the capillary between the still and the mixing chamber. In a recent publication, Herrmann *et. al.* [52] describe how, for $P_S < 50$ μW, the cooling-rate of the m.c. (measured at 0.25 K) decreases rapidly to a value well below that predicted by theory. They suggest the following explanation to their findings:

> "An abrupt decrease in the cooling rate to a value below < 2 μmol/s during circulation is probably caused by a flow of superfluid helium over the film in heat-exchanger's capillaries; this may cause the formation of regions of different phases in the mixture in the capillaries, which disturbs the operation of the refrigerator."

5.6 FUTURE DESIGN

The fact that the mixing chamber is mounted on the evaporator results in unnecessary conductive heat leaks. It is, however, difficult to avoid such a ^{3}He stage since pre-cooling of the

[†]Unfortunately, Roach *et. al.* [47] do not provide any details regarding the DR pump temperature, which would have allowed for a more detailed comparison with our results.

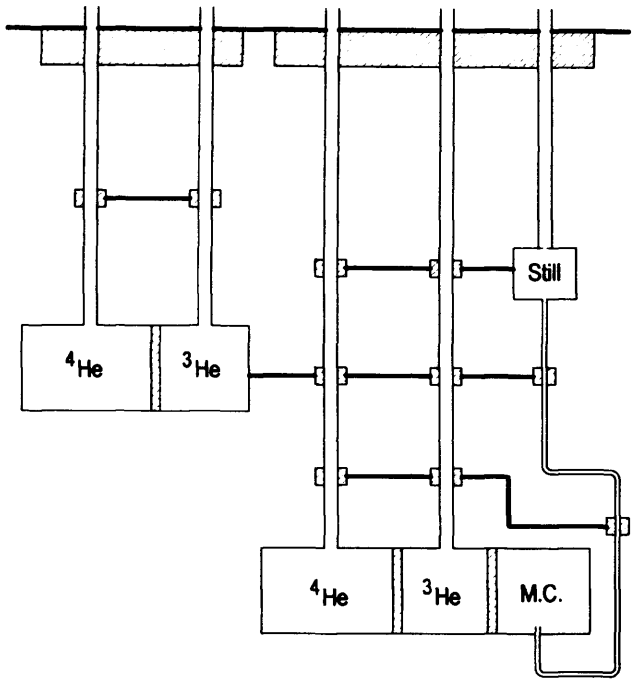

Figure 5.12: Suggested future design of the ssMDR, here shown as designed for operation with a PTC. That is, with the cryopumps positioned above the base plate.

mixing chamber is critical for the duty time. One improvement, relatively easy to implement, would be to add a ^{3}He buffer in between the still and the mixing chamber (figure 5.12). The thermal conductivity of stainless steel is approximately linear with temperature, and so the heat leak to the mixing chamber would decrease with a factor of about $0.7^2/0.3^3 = 5.5$. In reality, the benefits will be even bigger. Firstly, the mixing chamber could be cooled to a lower temperature before the dilution process is initiated. Secondly, the additional ^{3}He stage provides two extra thermal buffers (0.3 K and 1.5 K) which can be used to reduce the heat leak from any mechanical support structure and wires.

A thermal connection from the m.c. capillary would help to reduce the parasitic heat leak from the pumping lines further. Of course, the still should be equipped with a film burner, or at the very least an orifice ($\leqslant$ 1 mm diameter) to reduce the superfluid film flow. Finally, given the number of cryopumps, the system would be far easier and cheaper to assemble and operate from a pulse-tube cooler.

5.7 CONCLUSIONS

A prototype to a single-shot dilution refrigerator has been built and experimentally evaluated. A lowest temperature of 73 mK was achieved and temperatures below 100 mK could be maintained for about 45 min. A poor thermal strap and problems with superfluid film

flow from the still appear to be the most likely explanation to why the current design fails to achieve the expected duty time. A future version should therefore incorporate (*i*) a film burner, and (*ii*) an extra ^{3}He buffer to reduce the heat leak to the mixing chamber.

A thermal model for predicting the behaviour of the system has also been developed and can be used in the design of a future version. It is particular useful for estimating the duty time, given a required cooling power. Although more experimental data is required to investigate the accuracy of this model, it agrees very well with all the data acquired so far.

Under certain conditions the ^{3}He flow in our system was severely impeded, and very similar behaviour has been observed by other authors [47]. The formation of stable regions of different phase, suggested elsewhere [52], could offer an explanation to the observed phenomena.

It is clear that a single-shot MDR could fulfill the requirements for many astronomy experiments, and could also find applications outside astronomy as discussed in section 4.9. The real potential of this design – to achieve much lower temperatures than the condensation pumped MDR – is somewhat defeated by a relatively short duty time at the lowest temperatures. For operation around 0.1 K, however, it cold possibly offer an even more reliable and stable operation than the condensation pumped MDR. Although we have not yet investigated its performance when tilted, the absence of heat exchangers should make it virtually immune to gravitational instabilities.

6 Conclusions and Final Remarks

6.1 Cryogen-free Sorption Coolers

In chapter 2 we described the design of a dry cryostat which later was used to evaluate the continuous dilution refrigerator. In the same chapter, a thermal model for ^{3}He sorption coolers was developed and compared with experimental results. The analysis showed that the cooling power of these refrigerators was limited by the pumping speed of the charcoal pumps. In particular, we concluded that the thermal impedance between the charcoal and the 4K thermal buffer resulted in a reduced cooling power due to the elevated charcoal temperature and its strong temperature dependent adsorption efficiency.

As part of the work on the dry cryostat, thermal contact resistance of clamped metal joints and thermal conductivity of a fiberglass epoxy resin were measured. Here we found that by soldering a copper braid to bolted blocks instead of just clamping the braid, the thermal conductance at 4 K could be increased by about a factor of two. Further to this, the application of Apeizon N grease had a small but noticeable positive effect on the thermal conductance of both these joints. The Bastion epoxy resin was found to be very useful a material for cryogenic support structures between 4 K and 77 K. A comparison with G10 in this temperature range showed that both the thermal conductivity integral and the room-temperature Youngs modulus is about a factor of two higher for the Bastion epoxy resin. As this material is significantly cheaper than G10, it should be regarded as a possible alternative for applications below 77 K.

6.2 Gas-gap heat switches

In chapter 3 we described the design and testing of two different gas-gap heat switches; one for operation below 0.5 K which played a crucial role in the realization of the continuous

dilution refrigerator, and another specifically designed for cooling of large thermal loads. An on-conductance of 5.5 mW/K at 0.4 K, and an on/off ratio in excess of 6000 was achieved. Problems associated with long switch-off times at temperatures below 1 K have been analysed in detail, and a heat switch which proved to be particularly successful in tackling these issues has been described.

A novel heat switch design, based upon the difference in thermal expansion between stainless steel and copper, was also presented. A prototype of this latter switch has been built and tested, and found to agree remarkably well with our thermal model. We have also proposed a more advanced version of this thermal expansion hybrid, which will allow for a copper-limited on-conductance even at liquid helium temperatures; such a switch should be very useful for cooling of large focal planes and detector assemblies typically used in many astronomy experiments.

6.3 CONDENSATION PUMPED DILUTION REFRIGERATORS

In chapter 4 we detailed the design of a cryogen-free condensation pumped dilution refrigerator. The theoretical analysis focused on the efficiency of the heat exchanger, but important considerations regarding the design of the condensation pump, still and mixing chamber were also discussed. In semi-continuous mode, the cooling power was measured between 50 mK and 200 mK for two different still powers (figure 4.14 and figure 4.15). The analysis of these results gave the corresponding ^{3}He circulation rate and heat exchanger efficiency (figure 4.13): for example, at 100 mK and a still power of 625 μW we measured a cooling power of 6 μW, and calculated the circulation rate and residual heat leak to be 8.5 μmol/s and 1.55 μW respectively. The thermal model was found to agree well with experimental results for temperatures below 100 mK, but deviated at higher temperatures. This was explained by two different factors: the assumed (linear) temperature profile of the entropy is not valid above 100 mK, and any thermal impedance in the mixing chamber will become more noticeable with larger heat loads.

The cooling power was measured as a function of the condenser temperature (figure 4.16); these very important results showed that the circulation rate drops quickly at condenser temperatures above 450 mK. Also, if the condenser could be kept at a temperature below 350 mK, for example by using a more powerful sorption cooler, only a small improvement in cooling power would be achieved. This suggests that it is not the ^{3}He circulation rate which limits the performance of our cooler, but rather the heat exchanger efficiency. However, the condensation efficiency was only tested for one still power value and only one type of condenser. A more thorough investigation into the condensation efficiency is therefore justified: for example, it would be interesting to measure the condensation efficiency as

a function of the surface area.

For those astronomy applications where the cryostat moves with the telescope, the cryogenic system must be able to operate under tilt. Our measurements showed that the current design has a strong angle-dependent performance (figure 4.19). The most likely explanation to the unstable behavior at large angles is that the point of phase separation was not perfectly in the middle of the mixing chamber, or that the level of liquid in the still was slightly too high or too low. It is easy to see that a taller and narrower design of both the mixing chamber and the still would result in a system less sensitive to being tilted. It may also be important to consider the geometry of the heat exchanger; local regions with phase boundaries may otherwise form somewhere up the heat exchanger, effectively impeding the ^{3}He circulation rate or produce pockets of cooling and heating. Finally, gravitational instabilities may occur as a result of inadequate impedance in the concentrated return line; this effect is also likely to depend on the tilt angle.

It took about 20 hours to cool the mixing chamber from room temperature to 4 K, and another 4–6 hours to reach 100 mK. A control program which automatically re-cycles the sorption cooler during night time was developed to allow the system to be used efficiently and without any manual input. Typically 10–15 hours below 100 mK could be achieved, depending on the required cooling power. The cooling down time to 4 K was limited by the rather large 4 K base plate; a future version could easily be slimmed down to shorten the turnaround time significantly.

In a dry cryostat, the re-cycle time of the system is longer than in a liquid helium cryostat. This is due to the time it takes for the pulse-tube to recover from the heating of the charcoal pumps. The recovery phase generally lasts for 1.5—2 hours. It should, however, be possible to shorten this to 0.5—1 hour by using a more powerful pulse-tube cooler, and by mounting the sorption cooler straight to the 4 K cold head.

The lowest attainable temperature, about 50 mK, was limited by the efficiency of the heat exchanger; a future version should therefore incorporate a more advanced heat exchanger design. In principle, temperatures below 30 mK would be attainable with a longer continuous (tube-in-tube) heat exchanger: for example, the inner tube could be flattened and coiled up inside the outer tube to reduce the ^{3}He volume and increase the surface area.

The condensation pumped system developed here is already mature enough to be used in many applications. Although we have achieved a fully continuous operation by using gas-gap heat switches, it should be possible to improve on these results by using a system with double condensers. A modified version of the Sivokon cooler, figure 1.17, should therefore be considered for any future work on the continuous system.

6.4 SINGLE SHOT DILUTION REFRIGERATORS

The single-shot dilution refrigerator, presented in chapter 5, piggybacks on a double-stage ^{3}He-^{4}He sorption cooler. We developed a thermal model to predict the run time of the dilution stage; the results (equation 5.11) showed that at least 12 hours at 0.1 K should be possible to achieve, even with a relatively small amount of ^{3}He (0.23 mol). The most important outcome from the thermal model, however, was the prediction of what fraction of the ^{3}He in the mixing chamber will be used as the mixing chamber cools down. In particular, we calculated how the residual ^{3}He depends on the starting temperature and the initial ^{3}He/^{4}He ratio (figure 5.2).

Experimental results from a first prototype were very promising with a lowest temperature of 73 mK. Good agreement between the theoretical and the measured run time was also found. The main problem with the current design is that it has no superfluid film burner; this caused problems during the cool-down phase and limited the run time. It had been anticipated that the sorption cooler would be able to cool the mixing chamber to about 0.3 K, at which temperature the dilution cooling would be initiated. However, superfluid film-flow from the still prevented the sorption cooler from reaching temperatures below 0.6 K (figure 5.6). Since dilution cooling is much less efficient than evaporation cooling at these temperatures, a large fraction of the ^{3}He was used before the mixing chamber reached 0.1 K. Thus, and in agreement with our thermal model, temperatures below 0.1 K could be maintained for less than an hour.

A future version should incorporate a film burner or, at the very least, a small-diameter neck positioned just above the still to reduce the film flow. We have also suggested a slightly different arrangement of the sorption cooler, figure 5.12, which will reduce the conductive heat load through the pumping lines to the mixing chamber. Further to this, the run time could be extended by increasing the ^{3}He/^{4}He ratio: for example, changing this ratio from 50% to 75% will almost double the run time.

Single-shot refrigerators can potentially reach lower temperatures than their continuous counterpart; the trade-off is a more complicated cool-down procedure which must ensure that a large fraction of the initial amount of ^{3}He is available once the mixing chamber has reached the desired temperature. Another condition for the single shot system to be successful is that conductive loading from the pumping lines can be reduced to a minimum; otherwise the prime reason for choosing a single shot system – no residual heat load from the heat exchanger – is quickly defeated. There is, however, a subtle but potentially important difference between a single shot and a continuous dilution refrigerator: with no return line, gravitational instabilities and similar effects related to a tilted operation may be naturally

suppressed. This may well prove to be very important for applications where extreme temperature stability is required even as the system is being rotated and tilted throughout the duty cycle.

At present, there is not enough experimental evidence to suggest that one of the two systems would be better than the other; both remain potential candidates for future astronomy applications. Therefore, although this project has came much further on the development of a condensation pumped design than on a single-shot design, research should continue along both paths.

Appendix A Derivations

A.1 Partial Chemical Potential

The expression for the partial chemical potential: $\mu_i = \mu_i^* + RT \ln x_i$ of component i in an ideal gas mixture can be derived from first principles. Let μ_A^* be the chemical potential for pure i, and x_i the molar fraction of i in the mixture. Given the definition of the Gibbs function: $G \equiv H - TS$, where H is enthalpy, S is entropy, and T is temperature, one finds:

$$dG = dH - TdS - SdT\,. \tag{A.1}$$

The first term in equation A.1, dH, can be expressed in terms of the molar specific heat since $C_P \equiv (\partial H/\partial T)_P$:

$$dH = C_P dT\,. \tag{A.2}$$

The second term in equation A.1, dS, can be expanded if $S = S(T, P)$ where P is the total pressure:

$$dS = \left(\frac{\partial S}{\partial T}\right)_P dT + \left(\frac{\partial S}{\partial P}\right)_T dP \tag{A.3}$$

For a reversible process, $(\partial S/\partial P)_T = C_P/T$, and from Maxwell's relation: $(\partial S/\partial T)_P = -(\partial V/\partial T)_P$. By taking use of that for an ideal gas: $(\partial V/\partial T)_P = R/P$, equation A.3 can be written as:

$$dS = \frac{C_P}{T}dT - R\frac{1}{P}dP. \tag{A.4}$$

Inserting A.2 and A.4 into A.1 and integrate from $T = 0$ yields

$$G(T,P) = \int C_P dT - T\int \frac{C_P}{T}dT - TR\ln P - S(T) + constant\,. \tag{A.5}$$

This can now be written as

$$G(T,P) = G^0(T) - TR\ln P\,, \tag{A.6}$$

with the last term as the only pressure dependent term. With n_i moles of component i, the partial Gibbs function is given by:

$$G_i(T,P) = G_i^0(T) - n_i T R \ln P\,. \tag{A.7}$$

Using the definition of the partial chemical potential

$$\mu_i = \left(\frac{\partial G}{\partial n_i}\right)_{\mathrm{P,T,n_{j\neq i}}}, \tag{A.8}$$

on equation A.7 yields:

$$\mu_i = \mu_i^0 + RT \ln p_i\,, \tag{A.9}$$

where p_i is the partial pressure. Equivalently, the chemical potential for pure i is:

$$\mu_i^* = \mu_i^0 + RT \ln p_i^* \tag{A.10}$$

Eliminating μ_i^0 using A.10 and A.9 yields

$$\mu_i = \mu_i^* + RT \ln \frac{p_i}{p_i^*}\,. \tag{A.11}$$

Since $p_i/p_i^* = x_i$ (Dalton's law), one finally arrives at:

$$\mu_i = \mu_i^* + RT \ln x_i \tag{A.12}$$

♯

A.2 THE PERFECT HEAT EXCHANGER MODEL

The perfect heat exchanger model, used in chapter 4 was initially developed by Frossati [113, 118] and later improved by Takano [119]. Here we present the details of this model, essentially as a summary of how it was described by the latter author. Note that the model discussed here is only valid for a Kapitza resistance proportional to T^{-3}.

At temperatures below roughly 50 mK, the entropies of the two Fermi liquids are $S_C(T) = \gamma_C T$ for pure ^{3}He in the concentrated phase and $S_D(T) = \gamma_D T$ for the diluted ^{3}He. The empirical values of the entropy coefficients are $\gamma_C = 23\,\mathrm{J/K^2/mol}$ and $\gamma_D = 107\,\mathrm{J/K^2/mol}$ [110, 122, 123].

The cooling power in a mixing chamber at temperature T_M is given by the familiar expression:

$$\dot{Q}/\dot{n} = (\gamma_D - \gamma_C/2)T_M^2 - \gamma_C T_C^2/2\,, \tag{A.13}$$

where T_C is the temperature of the pure ^{3}He (the concentrated phase) that leaves the last section of the heat exchanger and enters the mixing chamber.

In a perfect heat exchanger, all the heat given by the concentrated phase is taken by the diluted phase, that is $\mathrm{d}H_C = \mathrm{d}H_D$, or in terms of the enthalpy $\gamma_C T_C\,\mathrm{d}T_C = \gamma_D T_D\,\mathrm{d}T_D$. Therefore, if $\mathrm{d}T/\mathrm{d}x$ is the temperature gradient along the heat exchanger in figure A.1:

$$\gamma_C T_C \frac{\mathrm{d}T_C}{\mathrm{d}x} = \gamma_D T_D \frac{\mathrm{d}T_D}{\mathrm{d}x}\,. \tag{A.14}$$

If the thermal conductivity of the tube itself is ignored, and the thermal impedance between the two liquids therefore is dominated by Kapitza resistance, the power transmitted is given by an expression similar to Stefan's radiation law [118]:

$$\dot{Q} = \frac{A}{4a_K}\left(T_C^4 - T_D^4\right)\,, \tag{A.15}$$

where a_K is the Kapitza coefficient (in units of $\mathrm{m^2K^4/W}$). Therefore, and since the molar circulation rate, $\dot{n}$, is the same in both directions:

$$\dot{n}\gamma_C T_C \frac{\mathrm{d}T_C}{\mathrm{d}x} = \frac{A}{4a_K}\left(T_C^4 - T_D^4\right)\,. \tag{A.16}$$

Given boundary conditions and an expression which relates the temperature profile of the diluted side with that of the concentrated side, equations A.13, A.14 and A.16 can be solved to find the cooling power. A temperature profile relation can be found by first integrating equation A.14:

$$\gamma_C\left[T_C^2(x) - T_C^2(0)\right] = \gamma_D\left[T_D^2(x) - T_D^2(0)\right] \tag{A.17}$$

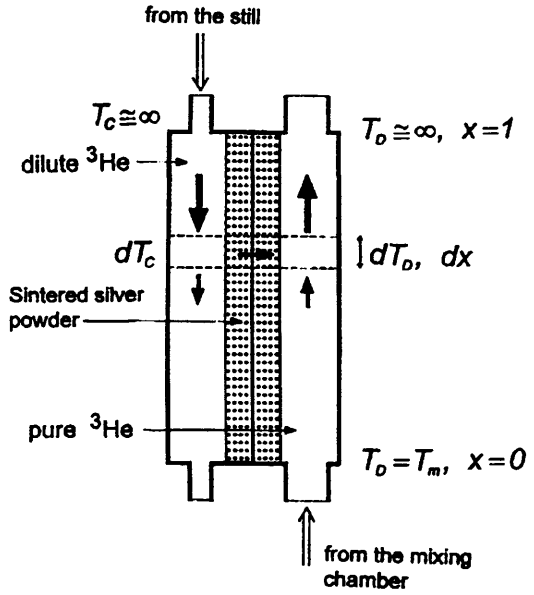

Figure A.1: Illustration of the perfect heat exchanger model. All heat removed from the concentrated liquid is carried away by the diluted liquid. The arrows indicate direction of flow.

Inserting equation A.13 and the boundary condition $T_{\mathrm{D}}(0) = T_{\mathrm{M}}$ into A.17 yields the temperature profile relation:

$$\gamma_{\mathrm{C}} T_{\mathrm{C}}^2(x) = \gamma_{\mathrm{D}} T_{\mathrm{D}}^2(x) + (\gamma_{\mathrm{D}} - \gamma_{\mathrm{C}}) T_{\mathrm{M}}^2 - 2\dot{Q}/\dot{n}\,. \tag{A.18}$$

Finally, using the second boundary condition, $T_{\mathrm{C}}(1) \simeq \infty$, and substituting equation A.18 into equation A.16 yields:

$$\dot{Q}/\dot{n} = \frac{(\gamma_{\mathrm{D}} - \gamma_{\mathrm{C}})\left[\gamma_{\mathrm{D}}(f-1) - \gamma_{\mathrm{C}}\right]}{\gamma_{\mathrm{D}}(f-1) - \gamma_{\mathrm{C}}(f+1)} T_{\mathrm{M}}^2\,, \tag{A.19}$$

where the dimensionless factor f is given by:

$$f = \exp\left(\frac{A/a_{\mathrm{K}}}{\dot{n}\gamma_{\mathrm{D}}\gamma_{\mathrm{C}}}\left[(\gamma_{\mathrm{D}} - \gamma_{\mathrm{C}})\, T_{\mathrm{M}}^2 - 2\dot{Q}/\dot{n}\right]\right)\,. \tag{A.20}$$

‡

Appendix B Low-Temperature Thermometry

B.1 Errors associated with temperature measurements

The following comment, from a very respected scientist, is not a genuine recommendation but us much as it is false it is also true; it illustrates how frustrating low-temperature thermometry can be even for someone very experienced.

> "If you wish to know the temperature of your system, use no more than one thermometer at any one place. Two different thermometers will never show the same temperature" – A.T.A.M. de Waele[†]

Measuring the temperature in a cryogenic system accurately can be an elaborate exercise which generally requires experience, a good understanding of the system and knowledge about potential sources of systematic errors. A well calibrated thermometer is a good start, but not much more. The final accuracy of a thermometer system will depend on a number of factors [134]:

1. Design errors: If the sensor cannot be mounted on or near to the sample, thermal lags and offsets will arise due to thermal conductance. The size of the sensor could also have an effect since the thermal mass of the sensor could bias the temperature of the sample.

2. Installation and environmental errors: The leads need to be properly heat sunk or they will introduce heat load into the sensor. Thermal radiation, magnetic fields and radiation can also affect the measurement.

3. Operation and instrumentation errors: The choice of 2-lead or 4-lead measurements, excitation current and instrument resolution will all affect the accuracy. Grounding errors, RF noise coupling and thermal EMFs can (and probably will) introduce noise to the measurement. Grounding errors are particular common since there are generally many different instruments, cables, computers and pumps attached to the cryostat. Each instrument may have its own grounding and attaching ground straps

[†]From a cryogenic lecture during Helsinki Cryoschool, August 2003

may create additional ground loops. AC signals in the RF frequency range can cause interference through inductive or capacitive coupling. Diodes are particular sensitive to AC interference since noise currents will introduce a shift in measurement. Due to their nonlinear I-V response, this will be seen as a lower measured voltage, i.e. a higher measured temperature.

4. Storage and handling errors: The calibration accuracy of the sensor will degrade over time even if it is not being used due to long-term changes in the material. It will also change through thermal cycling (thermal shocks) and the sensor may be very sensitive to mechanical shocks. A germanium thermometer for example has a delicate internal assembly and its calibration may shift if the sensor is dropped from a height of just a few centimeters. A ruthenium-oxide thermometer on the other hand is much less sensitive to mechanical shocks since it is not piezo-resistive. Hence it does not require any complicated strain-free packaging, it can simply by glued straight into the thermometer mount.

Fortunately, in many applications absolute accuracy is not necessarily very important. For example to measure the thermal conductivity of a material, each thermometer needs to be well calibrated with respect to each other. However, the *actual temperature* of the sample may not be that important if the results will be compared with that of another sample, measured under the same conditions and using the same thermometers. In this case, repeatability would be of much bigger concern than the absolute accuracy of the thermometer system.

B.2 CRYOGENIC SENSORS

There are a large number of different sensors designed for operation over different temperature ranges and for different applications. The description below on RTD and diode sensors is a summary of Lakeshore's sensor characteristics documentation [135] but is available from most cryogenic sensor manufacturers.

Silicon diodes are based on the temperature dependence of the forward voltage drop across a p-n junction. They are very useful for general use down to 1.5 K, they are simple in design, the required read-out electronics is straight forward and they are interchangeable. This means that two diodes from the same manufacturing batch will show very similar behaviour, thus do not require individual calibrations unless high accuracy is needed. Also, a 10 μA excitation current gives a fairly large signal, typically 0.5 V at room temperatures and 1.7 V at LHe temperatures. This makes the lead resistance error small so silicon diodes are

good for two-lead measurements. AC noise-induced temperature errors and thermal EMF can however be prevalent since the excitation current can not be reversed.

Resistance temperature detectors (RTDs) are based on the changing resistance with temperature. A distinction is made between RTDs with a positive temperature coefficient (PTC) and those with a negative temperature coefficient (NTC). The most common PTC RTD is made from platinum which has high accuracy, is interchangeable but only useful above 14 K. NTC RTDs are normally semiconductors with a very strong temperature dependence of resistance. For example, doped germanium can change its resistance four orders of magnitude between 10 K and 0.1 K. This together with an exceptional reproducibility ($\pm$ 0.4 mK) makes germanium thermometers very useful for low temperature applications despite its rather narrow operating range. However, they require individual calibrations and should not be used in high magnetic fields. A good alternative to doped germanium is ruthenium oxide which is useful between 50 mK and 40 K with similar sensitivity to doped germanium. They are interchangeable, very robust and have low magnetic field-induced errors. They are however not as accurate as germanium RTDs due to their poor reproducibility ($\pm$ 15 mK). Unlike diodes, all RTD sensors are immune to thermal EMF since they are AC biased.

Germanium RTDs and silicon diode sensors are examples of secondary thermometers. They need to be calibrated against fixed points in order to be accurate. A primary thermometer on the other hand does not need to be calibrated because its temperature dependence is well defined with an analytical expression. The equation of state for vapour-pressure thermometers, gas thermometers and noise thermometers have no unknown temperature-dependent quantities and hence they are examples of primary thermometers.

Primary thermometers are expensive, slow and far too complicated for most applications. Instead one would use secondary thermometers, calibrated against an internally recognized temperature scale based on primary thermometers and fixed points. The ITS-90 temperature scale range from 10,000 K to 0.65 K and is defined using 17 fixed points and four primary thermometers. Recently, a provisional low-temperature scale (PLTS-2000) based on the melting pressure of ^{3}He has been defined for temperatures between 1 K and 0.9 mK.

The name *secondary* thermometer is somewhat misleading since they are usually several times removed from primary thermometers, even when purchased from well established manufacturers. A more adequate terminology is *primary traceable* calibration. It would be too expensive, even for standards laboratories to upkeep maintenance and equipments to achieve ITS-90 and PLTS-2000. A typical chain of calibration procedures is as follow [136]:

1. The defined temperature scale is transferred from primary thermometers to highly

stable secondary thermometers, such as standards grade platinum RTDs. These thermometers are governed by agencies such as NIST, NPL and PBT.

2. A *working standard* is calibrated for the standards laboratories using these highly stable secondary thermometers. This step provides the laboratory with the possibility to issue calibration certificates for its customers.

3. These working standards then allow the standards laboratories to calibrate ordinary secondary sensors for customer use to a more adequate price.

Recently, a new class of primary thermometers for the low temperature region has been developed [137, 138]. These CBT thermometers use the coulomb blockade phenomenon in a series of two or more normal-metal/insulating layer/normal-metal junctions. They consist of a primary and a secondary thermometer mounted together on a small chip. This makes them significantly cheaper and easier to use in a day-to-day experiment than other primary thermometers. Efforts are also underway to make CBT sensors the scale defining method for 1 K and below. Although this is not yet achieved, they have already found applications and have been commercially realized through Nanoway[†].

[†]See for example http://www.nanoway.fi

References

[1] P. L. Richards and C. R. McCreight. *Physics today*, **58**, 41 (2005).

[2] D. Scott. Cosmic Glows: A CMB Review. In S. Courteau and J. Willick, editors, *ASP Conf. Ser. 201: Cosmic Flows Workshop*, page 403 (2000).

[3] W. Hu and M. White. *Sci. Am.*, **February**, 44 (2004).

[4] A. E. Lange. Detectors for future CMB observatuions. In J. Wolf, J. Farhoomand and C. R. McCreight, editors, *In Proceedings FAR-IR, sub-mm & mm detector technology workshop, NASA/CP-211408, page 1-01* (2002).

[5] M. Griffin. Noise in Electromagnetic Radiation Detection (2006). Postgraduate lecture notes, School of Physics and Astronomy, Cardiff University.

[6] R. V. Sudiwala, M. J. Griffin and A. L. Woodcraft. *Int. J. Infrared Mill. Waves*, **23**, 545 (2002).

[7] J. C. Mather. *Appl. Opt.*, **23**, 584 (1984).

[8] M. J. Griffin and W. S. Holland. *Int. J. Infrared Mill. Waves*, **9**, 861 (1988).

[9] A. L. Woodcraft, R. V. Sudiwala, M. J. Griffin, E. Wakui, B. Maffei, C. E. T. C. V. Haynes, F. Gannaway, P. A. R. Ade, J. J. Bock, A. D. Turner and S. Sethuraman. *Int. J. Infrared Mill. Waves*, **23**, 575 (2002).

[10] D. C. Alsop, C. Inman, A. E. Lange and T. Wilbanks. *Applied optics*, **31**, 6610 (1992).

[11] D. J. Benford, S. H. Moseley and J. A. Chervenak. Mission requirements for ultralow-background large-format bolometer arrays. In J. Wolf, J. Farhoomand and C. R. McCreight, editors, *Proceedings FAR-IR, sub-mm & mm detector technology workshop (NASA/CP-211408)*, pages 3–33 (2002).

[12] M. Linder, N. Rando, A. Peacock and B. Collaudin. Cryogenics in Space - A review of the missions and technologies. *ESA Bulletin*, **107** (2001).

[13] E. I. Mikulin, A. A. Tarasov and M. P. Shkrebyonock. Low temperature expansion pulse-tubes. volume 29, page 629 (Plenum Press, New York, 1984).

[14] A. T. A. M. de Waele. Cryocoolers (12 August 2003). Lecture notes from the European Advanced Cryogenic School in Helsinki.

[15] R. Radebaugh. Development of the pulse tube refrigerator as an efficient and reliable cryocooler. *Proc. of the Institute of Refrigeration, London*, **96**, 11 (2001).

[16] W. R. Smith. *Cryogenics*, **41**, 573 (2001).

[17] P. Neveu and C. Babo. *Cryogenics*, **40**, 191 (2000).

[18] B. Flake and A. Razani. *Advances in Cryogenic Engineering*, **49b**, 1138 (2004).

[19] S. W. K. Yuan and H. H. Jung. Thermal Management of Computer Systems Using Active Cooling of Pulse Tube Refrigerators. *Proc. Pacific Rim/ASME International, Electronic Packaging Technical/Business Conference* (1999).

[20] A. T. A. M. de Waele. *Cryogenics*, **39**, 13 (1999).

[21] B. N. Esel'son, B. G. Lazarev and A. D. Shvets. *Cryogenics*, **3**, 207 (1963).

[22] F. F. Mate, R. Harris-Lowe, W. D. Davis and J. G. Daunt. *Rev. Sci. Instrum.*, **36**, 369 (1965).

[23] M. Fruneau, A. Lacaze and L. Weil. *Cryogenics*, **7**, 135 (1967).

[24] A. D. Shvets. *Cryogenics*, **7**, 294 (1967).

[25] W. Wiedemann and E. Smolic. *Proc. 2nd Int. Cryogenic Eng. Conf.*, page 559 (1968).

[26] R. S. Bhatia, S. T. Chase, S. F. Edington, J. Glenn, W. C. Jones, A. E. Lange, B. Maffei, A. K. Mainzer, P. D. Mauskopf, B. J. Philhour and B. K. Rownd. *Cryogenics*, **40**, 685 (2000).

[27] A. L. Reesink and M. Durieux. *Physica B*, **194-196**, 29 (1994).

[28] R. L. Rusby. *J of Low Temp. phys.*, **58**, 203 (1985).

[29] J. R. Clement, J. K. Logan and J. Gaffney. *Phys. Rev.*, **100**, 743 (1955).

[30] A. L. Reesink and M. Durieux. *Metrologia*, 33, 401 (1996).

[31] L. Duband, L. Hui and A. Lange. *Cryogenics*, 30, 263 (1990).

[32] L. Duband, A. Lange and A. Ravex. *Proc 4th European symp. on space environmental and control systems, Florence, Italy*, page 407 (1991).

[33] J. J. Bock, L. Duband, M. Kawada, H. Matsuhara, T. Matsumoto and A. E. Lange. *Cryogenics*, 34, 635 (1994).

[34] L. Duband. A He^3 adsorption cooler associated with a 2.5 K mechanical cooler. In T. D. Guyenne, editor, *ESA SP-400: Sixth European Symposium on Space Environmental Control Systems*, page 503 (1997).

[35] A. Graziani, G. Dall'Oglio, L. Martinis, L. Pizzo and L. Sabbatini. *Cryogenics*, 43, 659 (2003).

[36] J. P. Pekola, R. J. Schoelkopf and J. N. Ullom. *Physics Today*, 57, 41 (2004).

[37] Task Force on Cosmic Microwave Background Research (TFCR) - Final report (2005). (TFCR provides recommendations to NASA and NSF on future fundings). See for example http://www.nsf.gov.

[38] P. Shirron, E. Canavan, M. DiPirro, M. Jackson, T. King, J. Panek and J. Tuttle. *Cryogenics*, 41, 789 (2001).

[39] P. Shirron, E. Canavan, M. DiPirro, J. Francis, M. Jackson, J. Tuttle, T. King and M. Grabowski. *Cryogenics*, 44, 581 (2004).

[40] C. Brockley-Blatt, I. D. Hepburn, P. Coker, E. Crofts, B. Winter, S. Milward, R. S. Allen, R. Hunt, M. Brownhill, N. Rando and M. Linder. Design and development of space engineering model cryogen free ADR for future ESA space missions. *Proc. Space Cryogenic Workshop, ESA-ESTEC* (2005).

[41] F. Pobell. *Matter and Methods at Low Temperatures* (Springer, Berlin Heidelberg, 1996).

[42] H. London. *Proc. Int. Conf. on Low Temp. Phys, Oxford*, 34, 157 (1951).

[43] H. London, G. Clarke and E. Mendoza. *Phys. Rev.*, 128, 1992 (1962).

[44] P. Das, R. D. B. Ouboter and K. Taconis (Plenum Press, London, 1965).

[45] A. Benoit and S. Pujol. *Cryogenics*, 34, 421 (1994).

[46] K. Madet, A. Benoit and B. Gautier. The archeops cryostat: A dilution refrigerator for a balloon experiment. *Proc. of the 19th international Cryogenic Engineering Conference, Grenoble-France* (2002).

[47] P. R. Roach and B. P. M. Helvensteijn. *Cryogenics*, **39**, 1015 (1999).

[48] P. R. Roach and B. P. M. Helvensteijn. volume 10, page 647 (Kluwer Academic/Plenum Publishers, 1999).

[49] H. London, G. R. Clarke and E. Mendoza. *Phys. Rev.*, **128**, 1992 (1962).

[50] V. S. Edel'man. *Cryogenics*, **12**, 385 (1972).

[51] V. S. Edel'man. *Physica B*, **329-333**, 1574 (2003).

[52] R. Herrmann, A. V. Ofitserov, I. N. Khlyustikov and V. S. Edel'man. *Instrum. Exp. Tech.*, **48**, 693 (2005).

[53] V. E. Sivokon', V. V. Dotsenko, L. A. Pogorelov and V. I. Sobolev. *Low Temp. Phys.*, **19**, 312 (1993).

[54] V. A. Mikheev, V. A. Maidanov and N. P. Mikhin. *Cryogenics*, **24**, 190 (1984).

[55] G. J. Batey, J. P. White, W. D. D. A. F. Simpson and V. A. Mikheev. *Low Temp. Phys.*, **23**, 492 (1997).

[56] Y. M. Bunkov, D. A. Sergatskov, J. Nyki and I. N. Ivoilov. Dilution refrigerator with internal cryogenic ^{3}He cycle. *AIP conf. proc.*, **194**, 397 (1989).

[57] A. L. Woodcraft. *Cryogenics*, **45**, 421 (2005).

[58] E. D. Marquardt, J. P. Le and R. Radebaugh. Cryogenic Material Properties Database. *Proc. 11th Int. Cryocooler Conf., Keystone* (2000). A database is available from http://cryogenics.nist.gov.

[59] Pultruded epoxy/glassfibre rod & sections (2002). Technical documentation from Bastion Glassfibre rod & Sections Ltd., 12 Harvey close, Crowther Industrial Estate, Tyne and Wear, NE38 OAB, UK.

[60] J. E. Shigley and C. R. Mischke. *Mechanical Engineering Design* (McGraw-Hill, 1988).

[61] C. M. Van Atta. *Vacuum science and engineering* (McGraw-Hill, New York, 1965).

[62] R. C. Richardson and E. N. Smith. *Experimental Techniques in Condensed Matter Physics at Low Temperatures* (Addison-Wesley, Colorado, 1998).

[63] D. Walton. *Rev. Sci. Instr.*, 37, 734 (1966).

[64] S. Dushman. *Scientific foundations of vacuum technology* (John Wiley & Sons, New York, 1962).

[65] W. H. Press, S. A. Teukolsky, W. T. Vetterling and B. P. Flannery. *Numerical Recipes in C* (Cambridge University Press, Cambridge, 1992).

[66] V. G. Kolobrodov, L. V. Karnatsevich, T. K. Grigorova and A. N. Skomorokhov. *Low temp. phys.*, **19**, 234 (1993).

[67] D. W. Sedgley, A. G. Tobin, T. H. Batzer and W. R. Call. *J. of Vacuum Sci. & Techn. A*, 5, 2572 (1987).

[68] E. S. Cheng, S. S. Meyer and L. A. Page. *Rev. Sci. Istrum.*, 67, 4008 (1996).

[69] R. H. March and O. G. Symko. *Proc. Grenoble Conf., Int. Institute of Refrigeration*, page 57 (1965).

[70] E. Schuberth. *Rev. Sci. Instrum.*, 55, 1486 (1984).

[71] Y. M. Bunkov. *Cryogenics*, **29**, 938 (1989).

[72] N. S. Lawson. *Cryogenics*, 22, 667 (1982).

[73] M. Krusius, D. N. Paulson and J. C. Wheatley. *Rev. Sci. Instrum.*, 49, 396 (1978).

[74] F. Koechlin and B. Bonin. *Supercond. Sci. Technol.*, 9, 452 (1996).

[75] F. W. Kus. *J. Phys. F*, 11, 1879 (1981).

[76] A. C. Rose-Innes and J. J. Rowland. *Journal of Physics E: Scientific Instruments*, 5, 939 (1972).

[77] A. Kashani, B. P. M. Helvensteijn, F. J. McCormack and A. L. Spivak. Helium liquid- and gas-gap heat switches. *Proc. of 1992 ICC*, 7, 355 (1993).

[78] A. Kashani, B. P. M. Helvensteijn, F. J. McCormack and A. L. Spivak. Helium liquid- and gas-gap heat switches for applications at 2 K. *Proc. of 1993 CEC, Adv. in Cryo. Eng.*, 39, 1657 (1994).

[79] J. P. Torre and G. Chaninin. *Rev. Sci. Instr.*, **55**, 213 (1984).

[80] E. N. Smith, J. M. Parpia and J. R. Beamish. *Physica B*, **284-288**, 2026 (2000).

[81] E. Smith, J. M. Parpia and J. R. Beamish. *J. of Low Temp. Phys.*, **119**, 507 (2000).

[82] P. R. Roach and B. P. M. Helvensteijn. A (He-3)-gap heat switch for use below 2 K in zero g. In *Advances in cryogenic engineering. Vol. 37, pt. B*, pages 923–930 (1992).

[83] P. J. Shirron, E. R. Canavan, M. J. Dipirro, M. Jackson, J. Panek and J. G. Tuttle. Passive gas-gap heat switches for use in adiabatic demagnetization refrigerators. In S. Breon, M. Dipirro, D. Glaister, J. Hull, P. Kittel, V. R. R. Pecharsky, J. Theilacker, S. van Sciver, J. I. Weisend and A. Zeller, editors, *AIP Conf. Proc. 613: Advances in Cryogenic Engineering CEC*, pages 1175–1182 (2002).

[84] W. E. Keller, H. S. Somers and J. G. Dash. *Rev. Sci. Instrum.*, **29**, 530 (1958).

[85] O. V. Lounasmaa. *Experimental Principles and Methods Below 1K* (Academic Press, London and New York, 1974).

[86] R. Berman. *J. Applied Physics*, 27 (1956).

[87] P. Kittel. *Cryocoolers 8* (1995). Plenum Press.

[88] M. M. Yovanovich. *Progress in Areonautics and Astronautics*, **49** (1976).

[89] P. Kittel, A. L. Spivak and L. J. Salerno. *Advances in Cryogenic Engineering*, 37 (1992).

[90] P. Kittel, A. L. Spivak and L. J. Salerno. *Cryogenics*, **34** (1994). ICEC Supplement.

[91] L. J. Salerno, P. Kittel and A. L. Spivak. *Cryogenics*, **34** (1994).

[92] A. Woodcraft. *J. Phys. D: Appl. Phys.*, **34**, 2932 (2001).

[93] J. H. Colwell. *Rev. Sci. Instrum.*, **40**, 1182 (1969).

[94] R. Berman and C. F. Mate. *Nature*, **182**, 1661 (158).

[95] A. M. Mustafa and R. G. Scurlock. *J. Phys. E: Sci. Instrum.*, 7, 430 (1974).

[96] E. W. Becker and R. Misenta. *Z. Physik*, **140**, 535 (1955).

[97] K. Fokkens, W. Vermeer and K. W. Taconis. *Physica*, **30**, 2153 (1964).

[98] S. D. Probert and T. Thomas. *Scientific Instruments*, **41**, 182 (1964).

[99] G. K. White. *Experimental techniques in low-temperature physics* (Clarendon Press, 1968), 2nd edition.

[100] W. Duncan, D. Audley, W. Holland and SCUBA 2 consortium. *Nuclear Instruments and Methods in Physics Research A*, **520**, 427 (2004).

[101] C. V. Heer and J. G. Daunt. *Phys. Rev.*, **81**, 447 (1951).

[102] C. Ebner. *Phys. Rev. A*, **3**, 1201 (1971).

[103] C. Ebner. *Phys. Rev.*, **156**, 222 (1967).

[104] C. E. Kittel. *Introduction to Solid State Physics, 4th ed.* (John Wiley & Sons, Chichester, 1971).

[105] D. O. Edwards, D. F. Brewer, P. Seligmann, M. Skertic and M. Yaqub. *Phys. Rev. Lett.*, **15**, 773 (1965).

[106] V. N. Zharcov and V. P. Silin. *Zh. Eksp. Teor. Fiz. [Sov. Phys.-JETP **10**, 102 (1960)]*, **37**, 143 (1960).

[107] D. O. Edwards and M. S. Pettersen. *Low Temp. Phys.*, **87**, 473 (1992).

[108] C. Ebner and D. O. Edwards. *Phys. Rev.*, **2C**, 77 (1970).

[109] R. Radebaugh. Thermodynamic properies of He^3-He^4 solutions with applications to the He^3-He^4 dilution refrigerator. *Nat. Bur. Stand. (US), Tech. Note*, **362** (1967).

[110] D. S. Greywall. *Phys. Rev. B*, **27**, 2747 (1983).

[111] A. C. Anderson and W. L. Johnson. *J. Low Temp. Phys.*, **7**, 1 (1972).

[112] T. Nakayama. *Progress in Low Temperature Physics*, volume 12 (Elsevier Science Publisher B.V., 1989). Chapter 3.

[113] G. Frossati, H. Godfrin, B. Hébral and G. Schumacher. *Proc. of ULT Hakoné Symp., Japan*, page 205 (1977).

[114] D. I. Bradley, T. W. Bradshaw, A. M. Guénault, V. Keith, B. G. Locke-Scobie, I. E. Miller, G. R. Pickett and W. P. Pratt. *Cryogenics*, **22**, 296 (1982).

[115] G. A. Vermeulen and G. Frossati. *Cryogenics*, **27**, 139 (1987).

[116] J. C. Wheatley. *Am. J. Phys.*, **36**, 181 (1968).

[117] J. C. Wheatley, R. E. Rapp and R. T. Johnson. *J. Low Temp. Phys.*, **4**, 1 (1971).

[118] G. Frossati. *J. Low Temp. Phys.*, **87**, 595 (1992).

[119] Y. Takano. *Rev. Sci. Instrum.*, **65**, 1667 (1994).

[120] R. Radebaugh and J. D. Siegwarth. *Cryogenics*, **11**, 368 (1971).

[121] J. D. Siegwarth and R. Radebaugh. *Rev. Sci. Instrum.*, **43**, 197 (1972).

[122] D. S. Greywall. *Phys. Rev. B*, **33**, 7520 (1986).

[123] J. C. Wheatley. *Progress in Low Temperature Physics*, **6**, 77 (1970).

[124] G. Ventura, M. Barucci, E. Gottardi and I. Peroni. *Cryogenics*, **40**, 489 (2000).

[125] F. J. Shore, V. L. Sailor, H. Marshak and C. A. Reynolds. *Rev. Sci. Instr.*, **31**, 970 (1960).

[126] I. Didschuns, A. L. Woodcraft, D. Bintley and P. C. Hargrave. *Cryogenics*, **44**, 293 (2004).

[127] S. Church, P. Ade, J. Bock, M. Bowden, J. Carlstrom, K. Ganga, W. Gear, J. Hinderks, W. Hu, B. Keating, J. Kovac, A. Lange, E. Leitch, O. Mallie, S. Melhuish, A. Murphy, B. Rusholme, C. O'Sullivan, L. Piccirillo, C. Pryke, A. Taylor and K. Thompson. *New Astronomy Review*, **47**, 1083 (2003).

[128] M. J. Devlin, S. R. Dicker, J. Klein and M. P. Supanish. *Cryogenics*, **44**, 611 (2004).

[129] S. Masi, E. Aquilini, P. Cardoni, P. de Bernardis, L. Martinis, F. Scaramuzzi and D. Sforna. *Cryogenics*, **38**, 319 (1998).

[130] M. Frank, L. J. Hiller and J. B. Legrand. *Rev. Sci. Instrum.*, **69**, 25 (1998).

[131] D. Y. Akimov. *Instrum. Exp. Tech.*, **5**, 575 (2001).

[132] P. R. Roach and B. Helvensteijn. Development of a compact dilution refrigerator for zero gravity operation. In *Advances in cryogenic engineering. Vol. 35B - Proceedings of the 1989 Cryogenic Engineering Conference, Los Angeles, CA, July 24-28, 1989. New York, Plenum Press*, pages 1045–1053 (1990).

[133] J. Wilks. *The properties of liquid and solid helium* (Clarendon Press, Oxford, 1967).

[134] Lakeshore Cryotronics inc., manufacturers documentation, *appendix e: temperature measurements system* (2005). See for example http://www.lakeshore.com.

[135] Lakeshore Cryotronics inc., manufacturers documentation, *appendix b: sensor characteristics* (2005). See for example http://www.lakeshore.com.

[136] Lakeshore Cryotronics inc., manufacturers documentation, *appendix a: overview of thermometry* (2005). See for example http://www.lakeshore.com.

[137] J. P. Pekola, K. P. Hirvi, J. P. Kauppinen and M. A. Paalanen. *Phys. Rev. Lett.*, 73, 2903 (1994).

[138] T. A. Knuuttila, K. K. Nummila, W. Yao, J. P. Kauppinen and J. P. Pekola. *Physica E*, 3, 224 (1998).